Universitat de Barcelona
Departament d'Electrònica

Characterisation of $CuInS_2$ films for solar cell applications by Raman Spectroscopy

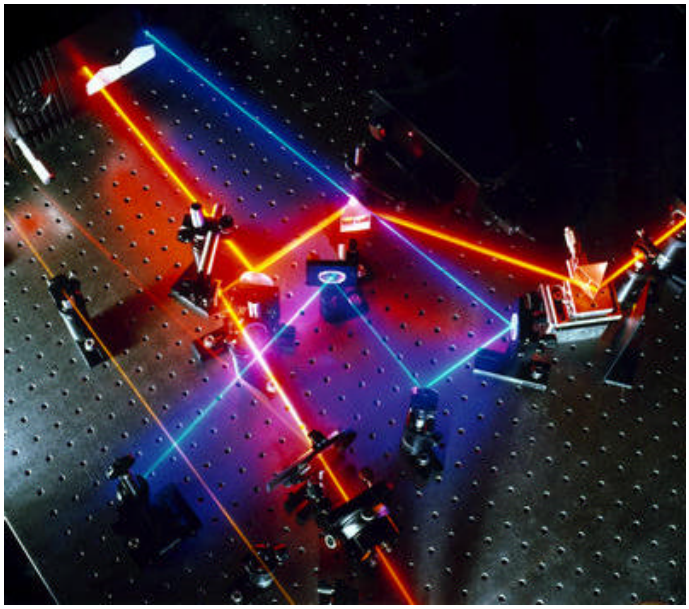

Jacobo Álvarez García

Universitat de Barcelona

Facultat de Física
Departament d'Electrònica

Characterisation of $CuInS_2$ films for solar cell applications by Raman Spectroscopy

Memòria presentada per optar al grau de Doctor en Ciències Físiques.

Programa de Doctorat: Enginyeria i Tecnologia Electrònica.
Bienni: 1998-2000
Barcelona, Febrer de 2002
Autor: *Jacobo Álvarez García*
Director: *Dr. Alejandro Pérez Rodríguez*

El Dr. ALEJANDRO PÉREZ RODRÍGUEZ, professor titular de la Facultat de Física de la Universitat de Barcelona,
CERTIFICA:
Que la memòria titulada: **"Characterisation of $CuInS_2$ films for solar cell applications by Raman Spectroscopy"**, que presenta Jacobo Álvarez García per a optar al grau de Doctor en Ciències Físiques, ha estat realitzada sota la seva direcció.

Barcelona, 25 de febrer del 2002

Dr. Alejandro Pérez Rodríguez.

Contents

Preface

Motivation

In the recent years, photovoltaics has become an active field for the basic research and technology. Hitherto, the economical aspects have limited the expansion of the photovoltaics industry, despite its environmental interest. The development of new materials has opened new perspectives for the production of low-cost and high efficient devices. From the economical point of view, these characteristics are essential in order to consolidate photovoltaic energy.

One of the most promising thin film photovoltaic technologies is based upon the use of $CuInS_2$ as photovoltaic absorber material, and has already demonstrated efficiencies up to 10.2% in the mini-module scale. $CuInS_2$ presents good optoelectronic properties, due to its well-suited bandgap to the solar spectrum, and its high optical absorption coefficient. However, the possibility to precisely control, modify and optimise the film properties relies on the knowledge of the properties of the films. Despite this, the physico-chemical properties of the thin film $CuInS_2$ absorber layers commonly used for the production of solar are still rather limited. Furthermore, the vibrational properties of these films had not been systematically investigated yet. This lack of experimental data, together with the necessity for developing characterisation tools for this thin film technology, led our group to undertake the present work.

Raman spectroscopy has proved itself as an useful tool for the characterisation of semiconductors. On the other hand, it provides a direct information about the vibrational properties of crystalline materials. Besides, its non-destructive character offers the possibility to implement this technique in an industrial production line for quality assessment. Therefore, special efforts have been devoted to interpret the Raman spectra of the films on the basis of their

crystalline structure, and to study the effect of the variation of the properties of the films upon their Raman spectra.

This work has been performed at the Electronic Department of the University of Barcelona, in the framework of the European Project [1] "*SULFURCELL: Efficient Thin Film Solar Cells Based on* $CuInS_2$", in collaboration with: Hahn-Meitner Institut (Berlin); University of Oxford; Ente per le Nuoce Tecnologie, l' Energia e l'Ambiente (ENEA); Vakuumtechnik Desden GmbH (VTD), and Vereinigte Glasswerke GmbH (VEGLA).

Objectives

The main objective of this work has been the characterisation of polycrystalline $CuInS_2$ films for solar cell applications by means of Raman Spectroscopy. The films were grown either by coevaporation or by a sequential process, under different growth conditions. The effect of the main parameters, such as the growth stoichiometry and temperature, upon the Raman spectra has been investigated in detail. The introduction of *Ga* in the films, as an alloying element, has been also studied. On the other hand, the interpretation of the Raman spectra of the films has made necessary to deepen in the physico-chemical properties of the material. Therefore, other experimental techniques, such as X-Ray Diffraction, have been used in order to achieve an accurate knowledge of the crystalline properties of the films.

Structure

This work is divided into five chapters. The first two chapters provide an introduction to photovoltaics and Raman spectroscopy. Chapter one gives a general overview about the current status of photovoltaics, emphasising the different technologies that are being used to fabricate solar cells. Since most of the experiments presented in this work are related to Raman spectroscopy, I considered convenient to include a chapter dealing with the theory of inelastic scattering of light by matter and Raman Spectroscopy.

The three following chapters constitute the nucleus of the work, in which the most relevant experimental results are presented, modelled and interpreted. Chapter three faces the problem of understanding the Raman spectra of the films, which has required deepening into their physico-chemical properties. This chapter provides an explanation for the occurrence of additional bands in the spectra of some of these films, which had not been identified yet. The interpretation of these bands is based on experimental results and is supported by a dynamical model of the crystalline structure responsible for the apparition of the bands. The detailed characterisation of the polycrystalline films is presented in chapters four and five. In chapter four, the dependence of the Raman spectra of coevaporated films on the growth temperature and stoichiometry is presented. On the other hand, chapter five focuses on the analysis of sequentially grown films, which are especially interesting for large-scale applications. This chapter presents the analysis of "baseline" $CuInS_2$ films, together with the effect of the incorporation of *Ga* on the structural properties of the films. Finally, the main conclusions of this work are summarised.

1. Photovoltaics

1.1. Photovoltaic energy

Hitherto, the Sun is the largest potential source of energy available for the human being. The Earth receives from the sun $1.7 \cdot 10^{17}$ W of energy, from which about 40% is reflected back to the space. Despite the absorption of part of the radiation in the atmosphere, the amount of energy received in one hour would still be enough to cover the energy requirements of the whole world for one year. There are several classes of systems that try to take profit of this energy. The Federal Energy Administration of USA separates the solar energy into six classes of systems [2]: solar heating and cooling of buildings, solar-thermal electric power, photovoltaic power, wind conversion, bioconversion and ocean thermal-gradient power. The economical viability of all these systems depends on the investment made in their development, as well on the price of fossil fuels, which up to now constitute the cheapest way to produce energy. However, the intensive use of fossil fuels raises a number of problems for mid and long term. Acid rains, global warming and greenhouse effect are typical examples of the environmental problems related to the combustion of fossil fuels. On the other hand, in the future it will be necessary to replace exhaustible resources with appropriate alternatives that allow covering the energetic necessities of the growing population. Other alternatives, like nuclear energy, have been considered in the last decades, but many countries have refused to take the serious risks that nuclear fission reactors suppose. The management of the nuclear residues is an additional problem with no easy solution.

Under these conditions, there is nowadays a growing interest for renewable energy sources, such as solar energy. Capital investments on these new technologies have led to a strong increase of the energy produced, approaching

their competitiveness to conventional technologies. Probably, if these systems are still not competitive is because of the low prices of fossil fuels. While many of these technologies are close to maturity (windmill, solar thermodynamic electricity, etc.) photovoltaics is still an emerging technology, and an important long-term decrease in costs is expected.

Photovoltaic effect was discovered by the French physicist Edmond Becquerel [3, 4] in 1839, whereas studying the behaviour of solids in electrolytes. He observed that when metal plates (silver or platinum) immersed in a solution where exposed to light, a small voltage and current were produced. The first report of photovoltaic effect in solids [5] was not recorded until 1878. Five years later, Fritts fabricated the first thin selenium solar cell [6], forecasting the potential of this energy source. The advances in solid state electronic technology in the fifties lead to the fabrication of the silicon solar cell, developed in the Bell Telephone Laboratories by Chapin, Fuller and Pearson [7]. The first silicon solar cell had an efficiency of 6%. This discovery was the beginning of the active research in high efficient and low cost photovoltaic devices. The market areas of the first commercialised cells in the fifties corresponded to small-scale uses, such as telephone repeaters requiring tens of Watts. The first impacts were realised for space applications. The satellite Vanguard I was launched in 1958, containing a small six silicon cell panel, providing about 5 mW of power. Two months after the Vanguard launch, the USSR launched a much larger solar-powered satellite, which worked for over two years. Since then, practically all spacecrafts have been powered by solar cells. The limitations in the fossil-fuel resources and the oil embargo in 1973 turned the industry to support the terrestrial requirements. During the last decades of the 20th century, the technology and industry developed extensively, with module shipment exceeding 200 MW/year and installations of remote and central power stations producing hundreds of megawatts. While silicon technology achieved efficiencies close to the theoretical limits, new approaches were investigated in order to reduce the high costs involved in crystalline cells. Therefore, since the eighties an intense activity in the research of new materials for the production of

large-scale high efficiency cells took place. As a result, new emerging technologies have penetrated in the photovoltaics market, which up to some years ago was absolutely dominated by crystalline silicon technologies. Among these technologies, amorphous silicon (a-Si), polycrystalline and multicrystalline silicon (p-Si), II-VI compounds, and copper indium diselenide (CISe) have already achieved commercial maturity.

1.2. The solar cell

A solar cell is an electronic device designed for converting the irradiated Sun light into electricity. The simplest way to achieve this is by constructing a p-n homojunction, although there are other structures, such as Metal/Seimconductor (MS), Metal/Insulating/Semiconductor (MIS) and complex heterojunctions that have been used or are still used as solar cells. The operation of the usual photovoltaic cell involves four different steps. First, the photons with energy greater than the fundamental gap of the material are absorbed, thus generating electron/hole pairs. These photogenerated carriers diffuse then to the edge of the depletion region of the junction, where they are separated and swept by the internal electrical field of the junction. Finally, the separated carriers are collected via ohmic contacts with grid structures.

The details of the electrical behaviour depend on the type of cell, and the electronic properties of the material. The efficiency of the cell can be expressed in terms of the short circuit current (I_{SC}) and the open circuit voltage (V_{OC}) of the device, once the fill factor is defined:

$$FF = \frac{V_M \cdot I_M}{I_{SC} \cdot V_{OC}} \qquad \textbf{[Eq. 1. 1]}$$

Here, V_M and I_M represent the voltage and the current intensity for the conditions of maximum output power of the device. Therefore, the cell efficiency (h) defined as the ratio of the generated power with respect to the power of the incident radiation (P_{in}), may be written as:

$$h = \frac{FF \cdot V_{OC} \cdot I_{SC}}{P_{in}} \qquad \textbf{[Eq. 1. 2]}$$

The integrated power of the incident light depends on the angle of incidence of the radiation and on the atmospheric conditions. These differences are taking into account by defining the "air mass" (AM) conditions at a concrete location. Under AM0 conditions (normal incidence without atmosphere) the value of the integrated incident power is 137 mW/cm^2, and this value decreases to about 100 mW/cm^2 on the surface of the Earth under AM1.5 conditions.

Equation **[Eq. 1.2]** expresses the dependence of the cell efficiency on three electrical parameters. In order to correlate them with fundamental properties of the material, one should know more about the electrical properties of the junction, i.e., the I(V) curve of the device under illumination conditions. In the general case of an heterojunction, the light-generated current can be calculated for the steady-state using the diffusion transport equation for minority carriers and the charge conservation relations, and setting the appropriate boundary conditions. Generation and recombination rates have to be included in the previous equations. Restricting us to bulk-recombination in the quasi-neutral region, and considering a p-type absorber, the current equation is derived:

$$J = \frac{e \cdot a(l) \cdot G_0(l)}{1 + \frac{1}{a(l) \cdot L_n}} - \frac{e \cdot D_n \cdot n_i^2}{L_n \cdot N_A}\left[e^{\frac{eV}{kT}} - 1\right], \qquad \textbf{[Eq. 1. 3]}$$

where $G_0(l)$ designates the incident photon flux, $a(l)$ is the coefficient of absorption at a wavelength l, N_A is the concentration of dopants, n_i is the intrinsic carrier concentration, and D_n and L_n are the diffusion coefficient and the diffusion length for the minority carriers, respectively. The first term is just the total light generated current in the absorber, while the second one is the forward-bias injected electron current for one side of a junction. The total current is obtained after integrating the current density for all the useful wavelengths. This equation can be written in a more general form, which

constitutes an example of an ”ideal” solar cell equation in which the dark diode current is added linearly to the light current:

$$J = J_0 \cdot \left[e^{\frac{eV}{kT}} - 1 \right] - J_L \qquad \textbf{[Eq. 1. 4]}$$

Unlike indirect bandgap semiconductors, direct bandgap ones collect appreciable amount of light in the depletion layer. In this case, the common assumption is that the photogenerated minority carriers suffer no recombination in the depletion region because they are swept out rapidly by the large electric field. With this assumption, the expression for J_L becomes:

$$J_L = e \cdot \Gamma_0(l) \cdot \left(1 - e^{-a \cdot W_{dp}(V)}\right) + \frac{e \cdot \Gamma_0(l)}{1 + \frac{1}{a(l) \cdot L_n}} \cdot e^{-a \cdot W_{dp}(V)} \qquad \textbf{[Eq. 1. 5]}$$

where W_{dp} corresponds to the total length of the depletion region in the p-type material. The total current is now the sum of the current generated in the quasi-neutral region and that from the p-region depletion layer. The equation has become a slowly varying function of the bias voltage. This just reflects some of the problems when dealing with real devices. In the general case, the different assumptions employed for deducing the previous equations have to be reconsidered.

On the other hand, considering a simple ideal solar cell equation, it can be derived some useful relations between the fundamental electric parameters. The *I(V)* curve of the device may be expressed as:

$$I = I_L - I_0(T)\cdot\left(e^{\frac{eV}{AkT}} - 1\right) \qquad \textbf{[Eq. 1. 6]}$$

In the above equation the diode ideality factor (*A*) has been introduced. The open circuit voltage is written as:

$$V_{OC} = \frac{A\cdot k\cdot T}{e}\cdot\ln\left(\frac{I_L}{I_0(T)}\right) \qquad \textbf{[Eq. 1. 7]}$$

These equations already give some insight in the relationship between the material properties and the device performance. Since the diode saturation current (I_0) is proportional to the square of n_i, the V_{OC} depends in a linear way on the energy gap of the material. However, choosing a material with a high bandgap reduces the number of photons that can contribute to the total photogenerated current, thus decreasing I_L. This leads to one of the more fundamental questions concerning photovoltaics, which is the maximum efficiency achievable with a solar cell device, and the optimum material for being used as solar cell. This question has been widely studied during the last decades. Detailed Balance Theory has been applied to calculate the limiting theoretical conversion efficiency of photovoltaics solar cells when only radiative recombination losses are taken into account, since the first studies appeared in the early sixties [8]. The theory consists on establishing a balance between the number of electrons extracted from a cell per unit time as electrical current, and the difference between the number of photons absorbed and those emitted from the device. Araujo et al. [9] have recently found an absolute limit of the efficiency for single junction and multijunction devices. Considering the Sun as a blackbody at 5759K, they found an absolute maximum efficiency for single junction cells of 40.8%, for an optimum gap of 1.06eV. This maximum efficiency was found to be independent on the concentration of the sunlight, providing that the angle of emission of radiative photons is strictly restricted to

the angle of the illumination photon flux. For AM1.5 illumination conditions, under direct normal irradiance without any concentrator system, the maximum efficiency was found [10] to be 32.5%, for an optimum bandgap of 1.13eV. It should not be possible to overcome these limits, even with the utilisation of innovative ideas, such as quantum wells devices. In the case of multijunction devices, the same authors [10] found an absolute limit of 85% efficiency, for a system with infinite number of junctions under AM1.5 conditions.

Besides this fundamental approach to the problem of the determination of the maximum efficiency achievable, other estimations have been done using empirical data obtained from real devices. Shah et al.[11] compared different approaches based on the gap dependence of the electrical parameters of the solar cell. The predicted results were compared with experimental ones, obtained from different absorbers. It was found that the semi-empirical relation found by Green [12], could reproduce the experimental results for p-n single junctions:

$$I_0\left[\frac{mA}{cm^2}\right]=1.5\cdot 10^8\cdot e^{\frac{-E_g}{kT}} \qquad \textbf{[Eq. 1. 8]}$$

Therefore, the open circuit voltage can be written as:

$$V_{OC}=\frac{K\cdot T}{e}\cdot\ln\left(\frac{I_L}{1.5\cdot 10^8\left[\frac{mA}{cm^2}\right]}\right)+\frac{E_g}{e} \qquad \textbf{[Eq. 1. 9]}$$

Finally, the device efficiency may be computed. In this case, an optimum bandgap around 1.5 eV was found for AM1.5 conditions, and a maximum efficiency slightly below 30%. The maximum efficiency decreases slowly

between 1.1 and 1.5 eV, and therefore materials with this bandgap range are considered suitable for solar cell applications. In general, one would wish to use materials with bandgaps as high as possible, which allow achieving higher open circuit voltages. The material absorption coefficient and the free carrier diffusion length are also important parameters. Materials with direct bandgap absorb most of the photons closer to the depletion region of the device, and the diffusion lengths required for the photons to contribute to the external current is much lower. However, the utilisation of high quality single crystals, such as the case of silicon, makes possible very large diffusion length. In fact, Auger recombination process is the mechanism limiting the efficiency of silicon real devices. In the case of thin film technologies, economics becomes a primordial aspect. The total cost of the cell is inversely proportional to the efficiency of the device, but increases with the amount of raw material required, and with the number of technological steps to be implemented in the production plant. In this case, the optimal solution is the use of polycrystalline materials, which can be produced much cheaply. In the case of polycrystalline heterojunction cells, it is especially difficult to describe properly the different aspects of its electrical behaviour. This is due to the existence of different effects related to surface and interface defects present at the grain boundaries, such as surface recombination of carriers and pinning of the Fermi level. Diffusion of atoms in the interfaces can also take place, modifying the interface properties, where tunneling of carriers may also occur. Despite these complexities, some common characteristic parameters can be defined. With these requirements, there are several materials that are now being used as solar cells. They can be divided into group IV, III-V and II-VI materials.

1.3. Solar cell technologies

1.3.1. Single-crystal technologies

Silicon has been and continues to be the foundation of the photovoltaics industry. Silicon present several advantages comparing with other photovoltaic materials. Firstly, their properties are well known and the technological aspects of the growth of crystalline silicon have been profusely studied during the development of the electronic industry. Moreover, silicon comprises about the 20% of the Earth's crust, which makes this element a good choice for large productions. Despite the indirect bandgap of silicon (lower than optimum), single junction devices provide excellent results in terms of efficiency. In fact, the major limitation of silicon has been the cost, rather than the performance. During the last decades, the industry research activity in this area has been guided towards the cost reduction and the optimisation of the device performance.

Since the first crystalline silicon cell in 1954 developed in the Bell Telephone Laboratories with 6% efficiency, a great number of changes have been introduced in order to improve the performance of these cells [13]. First design improvements and the reduction of series resistance lead in 1961 to an average efficiency of 11%. In 1972 Lindmayer and Allison developed the "violet" cell in COSMAT laboratories. In these n/p cells the junction depth was reduced from conventional 400 nm to 150 nm, eliminating a region of almost constant impurity concentration at the front surface, which inhibited the acceleration of minority carriers towards the junction. This structure, together with changes in the contact grid and the addition of a TaO_5 antireflective coating increased the AM0 efficiency of these cells to 13.5%. In 1972 Mandelkorn and Lamneck of NASA Lewis Research Center introduced a p^+ layer into the back of the silicon wafer. The electric field created by the impurity gradient helped minority

carriers generated in the base of the cell to go towards the junction and thus improved the red response. This development was an important step towards the fabrication of thinner cells, providing good results with cells 100 to 200 μm thick. Two years after the development of the Violet Cell, the COSMAT laboratories achieved 15% efficiency with a new device, in which selective etching of the front surface practically eliminated reflection losses, due to the light-trapping pyramids formed at the surface. The performance of ultrathin (50 to 100 μm) space solar cells was later enhanced by the introduction of the back surface reflector in 1977 by Scott-Monck. In 1982 Green combined the old MIS type cell with a n/p homojunction (MINP). An insulating SiO_2 film of 20Å-30Å thick was placed between the n-doped region and the grid metallic contact in order to reduce surface recombination, and therefore to increase the open-circuit voltage. Two years later, Green improved the MINP cell reducing the front metallisation area (PESC cell). The most efficient crystalline cell up to date is the PERL (Passivated Emitted and Rear Locally diffused) type. The cells are made from high quality float zone material, and the device include invert pyramid non-reflecting surface, a thin oxide layer on front and back surfaces and small front and back contact areas with local n^+ and p^+ diffusions. A scheme of the PERL cell is shown in *Figure 1.1*:

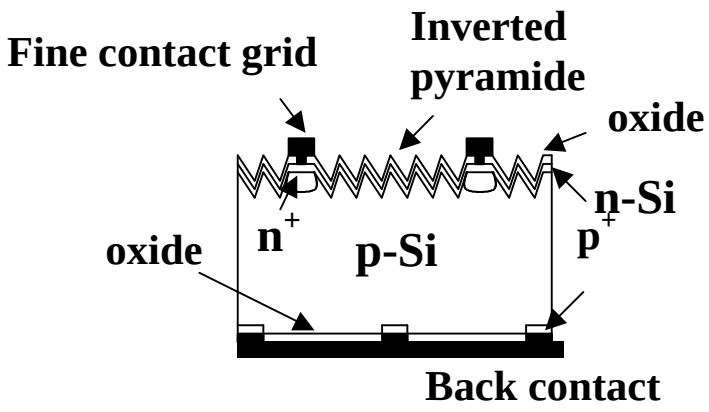

Figure 1. 1. Scheme of a silicon PERL solar cell

The efficiencies achieved with crystalline silicon [14] in the laboratory scale are above 24%, close to the theoretical estimated limit for this material if one takes into account that the efficiencies of Si devices are limited by Auger recombination. The necessity of higher efficiency and radiation-resistant cells for space applications led to the investigation of alternative materials. III-V semiconductors such as GaAs, GaAlAs, GaInAsP, InAs, InSb and InP have near-optimal characteristics, and these can be adjusted in a controlled way. The utilisation of these materials for optoelectronic devices has increased the knowledge about them, which has had a direct repercussion in the quality of the III-V solar cell devices. These materials are well-suited for space applications, and the major industry installations are directed towards them. The high cost of the cells, including materials, manufacturing and processing costs, hinders the application of these technologies to terrestrial applications. However, III-V materials constitute the basis of the highest efficient cells. While single-junction cells are constrained by the second law of thermodynamics to efficiencies below ~30%, the utilisation of multiple junction devices allows for much higher limit efficiencies. Tandem cells or multiple junction cells are designed in such a way that part of the incident light is not absorbed at the top cell, but passes through it and is utilised by the bottom device [15]. This allows using the solar spectrum more effectively, and increased efficiencies can be obtained. Several approaches as the two-terminal tandem, three-terminal cascade cell or the four terminal-connection cell have been successfully employed, obtaining efficiencies above 30%. A three junction mechanically stacked (InGaP/GaAs/InGaAs) cell has been recently developed by Japan Energy Co, Sumitomo Co. and Toyota Technological Institute, achieving 33.3% efficiency [16]. Some alternatives have also been tried in order to take profit of the good performance of these cells for terrestrial applications. An alternative to reduce costs is the utilisation of concentrator lenses and mirrors. In this case, the concentration of the light is accomplished by less costly optical components. Moreover, most solar cells operate with higher efficiencies under increased irradiance conditions, as can be deduced from **[Eq. 1.9]**. The main disadvantages of these systems are the optical losses in the focusing lenses and concentrator systems, and the fact that

these systems are not able to effectively use the diffuse component of the incident sunlight, which constitutes around the 20% of the total available radiation.

1.3.2. Thin film and polycrystalline technologies

The major cost factor for the Si cells is the production of high crystalline quality single crystals. This is a common problem of all of the crystalline technologies when they are designed for terrestrial applications. Even crystalline silicon technologies, despite the good performance of the cells, have serious bottlenecks with respect to large-scale applications, from both an economical as well as from an ecological point of view. This constitutes a major barrier to the widespread use of photovoltaic energy conversion. Recently, attention has been directed toward less energy-intensive processes, which sacrifice the crystalline order and better device performance for the benefits of lower energy production and reduced costs. Thin film technologies allow obtaining large area productions, minimising the production costs and the energy pay-back time. Among these technologies, one should point out polycrystalline and amorphous silicon technologies, II-VI polycrystalline (CdTe) and $CuInSe_2$ thin films, which are already commercialised by different companies.

Multicrystalline, polycrystalline, microcrystalline and amorphous Si

As a convention, materials with crystal grain size between 10 cm and 1 mm are referred to as multicrystalline, while those with grain size between 1 mm and 1 μm are designated as polycrystalline. Grain sizes between 1 μm and 100 nm correspond to microcrystalline materials, and materials with smaller grain sizes

are considered as nanocrystalline materials. In the case of amorphous materials, long-range ordering does not exist at all.

Amorphous silicon (a-Si) is an alternative technology that has already achieved relevance in the industry. a-Si:H is an amorphous material with native bandgap of 1.7 eV that can be varied over tenths of eVs by changing the growth conditions and the concentration of *H*. The loose of crystalline order increases the absorption coefficient (due to the structural disorder of the material, the quantum mechanical selection rules for optical transitions do not act in the same way), which makes the material very suitable for solar cell applications. Therefore, it is feasible to fabricate a-Si:H thin film solar cells with thickness down to 1 μm. Photoconductivity in a-Si produced by silane discharge was first investigated by Chittick et al [17], who showed that the properties of the material differed from those of the material grown by evaporation or sputtering. Lewis et al [18] explained the role of hydrogen in the semiconductor. The compensation of dangling Si bonds was shown to reduce the density of gap states in the a-Si:H alloy over its unhydrogentated analogue. a-Si:H contents between 10% and 40% of hydrogen. Moreover, a-Si:H can be deposited using low cost deposition techniques.

First a-Si:H solar cells were fabricated in 1974 with efficiencies of 5.5% using a Schottky barrier cell [19]. Nowadays, a great number of a-Si:H cells with efficiencies exceeding 10% have been reported, but very few are confirmed at the same efficiency after some hours of operation. Indeed instability is the main drawback of the a-Si:H cells. The instability of the cells when exposed to light was first observed by Staebler-Wronski [20]. The effect of the incident light is to increase the number of dangling bonds, producing metastable states in the bandgap that move the Fermi level towards mid-gap with increasing defect population. The degradation of the cell performance takes place mainly in the first 48-72 hours of operation, independently of the cell configuration, whether Schottky, MIS or p-i-n. However, the effect of this degradation on the performance of the final device depends on the configuration of the cell. The

degradation becomes manifest by a drastic reduction in the fill factor leading to a reduction of the cell efficiency in a range between 10%-50%. First cells adopted the simple form of metal/semiconductor junctions. Severe stability problems related to this design promoted the introduction of the p-i-n structures, presenting much better stability and reproducibility, and also better efficiencies. Most current cells are based on this design (*Figure 1.2*). Further engineering design lead to the apparition of the a-Si:H tandem cells, constituted by different stacked layers.

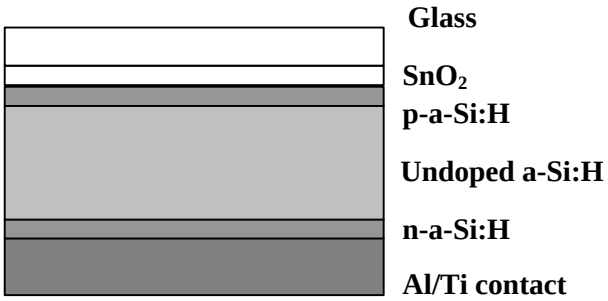

Figure 1. 2. Example of a-Si based solar cell, with a p-i-n configuration.

Additional improvements occurred by introducing impurity gradients in the films and with the introduction of Ge and C in the material, in order to control the band gap across the films. On the other hand, although cell and module engineering have minimised the Staebler Wronski Effect, the stability issue remains a major research. Stabilised a-Si:H cells achieve efficiencies around 13% only for triple junction cells.

While the efficiencies obtained with microcrystalline silicon (μc-Si) cells are still limited (around 8%), heterojunctions of a-Si:H and μc-Si have recently reached efficiencies [21] over 20%. In this case, good performance is achieved but

considerable design sophistication is needed. Moreover, stabilised efficiencies over 12% have been confirmed for micromorph tandem cells (consisting of a μc-Si bottom cell and an a-Si:H top one), obtained by low-temperature deposition techniques [22].

Polycrystalline and multicrystalline silicon present absorption coefficients lying between those of the crystalline and the amorphous silicon. At present, important efforts have been undertaken in order to try to combine the good electronic transport properties of crystalline silicon with the production advantages of thin film technology. Bulk polycrystalline silicon cells have been reported with efficiencies exceeding 17% by Rohatgi et al [23]. However, it is up to now still difficult to make good cells on substrates other than single crystal or polycrystalline silicon wafers. Moreover, the low deposition rates and the high deposition temperatures constitute a further limitation.

II-VI thin film technologies

CdTe is probably the most studied II-VI binary material for photovoltaic applications. Its bandgap of 1.5eV is well-suited to terrestrial applications, and its direct gap results in a high absorption over the whole spectra. The first efficient polycrystalline this film cells based on CdTe were reported by Cusano [24]. The initial CdTe/CdS thin film device is attributed to Bonnet, who fabricated 5% cells by evaporating CdS on a CdTe film [25]. Matsumoto reported the production of CdTe-based cells with efficiencies over [26] 10%, which made possible the commercialisation of these cells with modules around 6% efficiency. The technological advances in the close-space vapour transport deposition technique lead to the fabrication of a 15.8% cell onto a borosilicate glass substrate, which was reported by Ferekides and Britt [27]. Additional studies showed that the Na provided by cheaper soda-lime substrates acts as a minority-

carrier lifetime killer. However, efficiencies around 15% on these substrates have already been reported.

Most of the higher efficiency CdTe-based cells produced at the present involve a chloride treatment at high temperatures. Although the exact mechanisms that enhance the cell efficiency have not been determined yet, it has been demonstrated that this treatment improves the morphology of the films and densifies them, increases grain size and favours the formation of an interfacial CdS_xTe_{1-x} alloyed region through the interdiffusion of the chemical species. The necessity for the chloride treatment is one of the research topics which should be clarified in order to better understand the properties of the cells. It constitutes an intermediate step which increases the cost of the cells, having also negative consequences from the environmental point of view. The most serious problem of CdTe is the metallic back contact. Although gold contacts provide good results due to its high work function, they are a too expensive solution. Other problems of CdTe-based technology are related to scale-up problems, device stability and environmental problems due to the utilisation of *Cd*. Recently, Hanafusa et al. [28] reported a CdS/CdTe solar cell with an area of 1376 cm^2, and 10.5% efficiency.

Copper Indium Diselenide thin films

Chalcopyrite (I-III-VI_2 and II-IV-VI_2) compounds have received great interest in the field of photovoltaics, mainly Cu ternary compounds. Among them, $CuInSe_2$ (CISe), $CuInS_2$ (CIS) and $CuInTe_2$ (CIT) have well-adapted direct bandgaps, possibility of n-type and p-type doping (except possibly CIT), extremely good stability, high absorption coefficients, and lattice and electron affinity well-suited for common window layers (ITO, ZnO...).

In addition to their intrinsic properties, chalcopyrite materials can be alloyed between themselves to further optimise their characteristics. The most widely-used family of chalcopyrite materials for photovoltaics is the Cu-III-VI_2 one, from which it is possible to obtain a wide range of bandgaps and crystalline properties of the quaternary material (see *figure 1.3*). Up to now, $Cu(In,Ga)Se_2$ is the alloy which has provided better results. However, as it may be seen in the figure, there are a great number of candidate materials which deserve attention, and many of them, such as $CuInS_2$ and $CuGaSe_2$ are now under investigation.

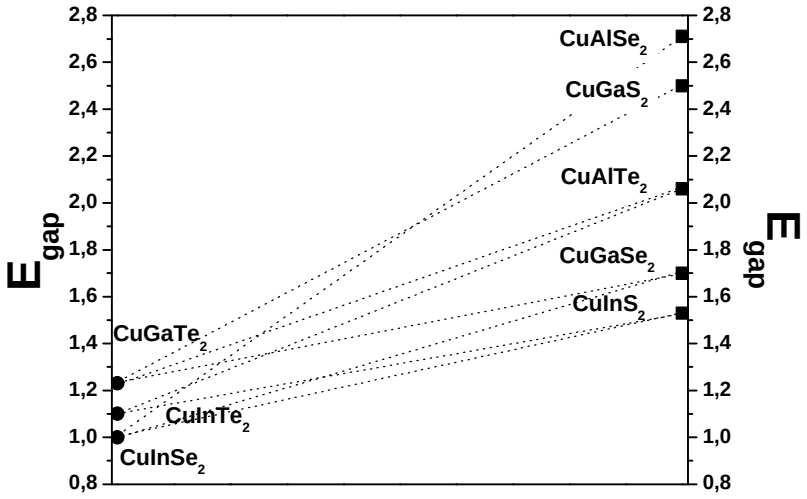

Figure 1. 3. Cu-III-VI_2 chalcopyrite materials candidates for being use as absorbers.

Thin film technology based on CISe appeared at the end of the seventies. In 1982 a CISe/CdS cell was confirmed, with efficiencies greater [29] than 10%. Incorporation of *Ga* and *S* in the CISe compound made possible to reach champion efficiencies [30] over 18%. Furthermore, these devices show excellent stability. The design commonly used for CISe based cell is depicted in *Figure 1.4*. The heterojunction is in fact so complex, that several approaches have been used to model its electrical behaviour. The first CISe-based cells used a thick CdS window layer, which was responsible for the important electronic losses in these early devices, due to the recombination at the CdS/absorber interface [31]. The introduction of a highly doped ZnO window layer, together with the thickness decrease of the CdS layer, increased the band bending in the absorber and decreased the recombination rate of electrons at the heterointerface such that in the actual state-of-the-art, it is accepted that recombination at the interface does not limit the V_{OC} of the device. Probably the recombination at the space charge region in the bulk of the absorber constitutes the dominant electronic loss mechanism in high efficiency devices [32].

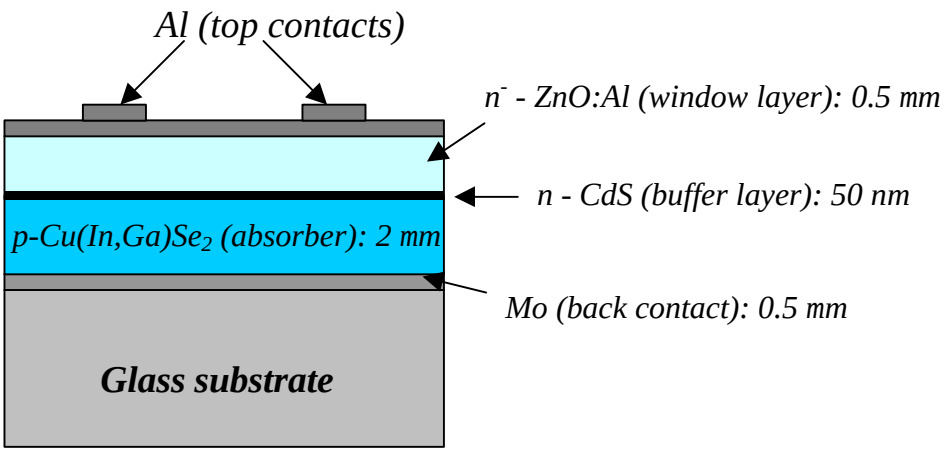

Figure 1. 4. Scheme of a typical configuration for a CISe-based solar cell.

There are several aspects of the chalcopyrite-based solar cells that are not totally understood. For example, it is generally accepted that the presence of *Na* in appropriate amounts (≈0.1%) in the CISe films improves the device performance [32]. The benefits of the *Na* are probably a result of manifold consequences. Moreover, the formation of $NaSe_x$ compounds during the formation of the film slows down the growth of the CISe grains, facilitating the incorporation of *Se* and widening the existence range of the α (chalcopyrite) phase of the CISe compound in the equilibrium phase diagram [33]. The diminishment of the number of V_{Se} defects and the *Na*-promoted oxygenation and passivation of grain boundaries are other mechanisms influencing the properties of the resultant absorbers [34]. Therefore, it is necessary to control the incorporation of *Na* in the absorbers, which is either externally introduced or through the utilisation of soda-lime glass substrates. Another example of the complex physical problems concerning these devices is the influence of the surface phases. Several authors have reported the presence of a chalcopyrite-related crystalline phase in the surface of the CISe films, and it is assumed to have some influence in the electronic response of the device [35, 36].

Best CISe-based cells are obtained with the utilisation of $Cu(In,Ga)(S,Se)_2$ pentenary absorbers. *Ga* and *S* are added in order to tune the gap of the absorber. Typically, about 30% of *Ga* is added to the CISe ($CuIn_{0.7}Ga_{0.3}Se_2$) in order to increase the energy gap of 1.02eV of the CISe up to 1.2 eV. As a consequence, the open-circuit voltage of the cells increases, achieving values above 0.7 V without decreasing cell efficiency. High *Ga* contents increases (E_g - eV_{OC}). This is due to either unfavorable band alignment or Fermi level pinning. In addition to the effect upon the bandgap, the incorporation of *Ga* has similar effects that the introduction of *Na*. The existence of the α phase is substantially widened, decreasing the sensitivity of the cell performances to stoichiometric deviations. The *Ga* addition also increases the free carrier density, increasing the conductivity one order of magnitude [37], which has been explained in terms of defect physic considerations [38].

Sulphur constitutes another alloying element commonly employed in the commercial cells. The incorporation of *S* in the films promotes the surface segregation of CuS, which must be removed by an additional step in the industrial process. Despite this drawback, the improvement in the open circuit voltage achieved is in the range [39] of 100 mV. This increase is mainly attributed to a passivation of recombination centers, which strongly affects the electrical transport properties of the material.

Finally, the annealing of the samples in O_2 atmosphere results also positive, and is also a step currently introduced in the production lines [40]. Oxygen seems to passivate the V_{Se} defects present at grain boundaries, reducing the recombination probability of the photogenerated carriers, as well as the band bending at the grain boundary [41].

The most positive aspects of this technology are the high stability of the devices, together with the large-area production with performance characteristics similar to those of laboratory devices. For instance, Siemens Solar is nowadays achieving CISe modules with efficiencies [42] over 13%. However, the highly complexity of the pentenary system makes necessary to carefully control the stoichiometry and homogeneity of the absorber film in order to achieve those high efficiencies.

1.4. The “sulfurcell”

1.4.1. Fundamentals

Although big efforts are devoted to the development of thin film photovoltaic technologies, the results achieved up to now are still limited. Further investigations are needed in order to solve many fundamental and technological aspects, and to reduce the production costs for making photovoltaics competitive in front more classical energy production systems. Chalcopyrite materials have already demonstrated to be potential candidates for large-scale productions. However, current technologies based on CISe present some problems. The adjustment of the stoichiometry, the necessity to introduce other alloy elements (*Ga, Na, S*) in order to achieve high efficiencies are important difficulties, which at the same time increase the production costs. Besides, from the environmental point of view, common CISe-based technology involves some steps which one wish to eliminate. *Se* in the absorber is incorporated through the selenization of the metallic precursors in H_2Se atmosphere. This gas is highly toxic and it must be manipulated very cautiously. Even if this step were removed or substituted for another one less problematic, the presence of *Se* in the cells would still be a disadvantage, due to the potential toxicity of this element.

Copper Indium disulphide (CIS) is one of the most promising chalcopyrite absorbers in terms of competitiveness, with other thin film polycrystalline materials. CIS has a bandgap of 1.5 eV, which is well suited for terrestrial and space applications. The substitution of *Se* by *S* avoids one of the most critical steps of the CISe technology, decreasing the production costs. Moreover, the replacement of the *Se* by *S* increases the gap of the material from 1.1 eV to 1.5 eV, thus increasing the open circuit voltage of the cell. In terms of module design, it is possible to reduce the number of interconnects or to reduce the

thickness of the ZnO window layer. Moreover, the final module becomes less sensitive to infrared transmission losses induced by the cover glass. Finally, the higher bandgap favours the device response at higher temperatures, and improves the blue response of the cell. Important progresses in the understanding on the properties of $CuInS_2$ and other chalcopyrite materials have been made during the last decades [43, 44], though a lot of questions are still opened. The device performance has also been improved in the recent years. Cells with total area efficiency of 11.4% have been reported [45], and currently efficiencies up to 12.1% have been achieved [46]. Although this value is still far away from the values obtained for other materials, especially CISe, other considerations must be taken into account. First, one should keep in mind that the difference in the efficiency between different materials is much less important when dealing with modules. For instance, although CIS submodule technology has started very recently, efficiencies up to 9.2% have already been reported [47] (the best sub-module fabricated up to now achieves an efficiency of 10.2% [48]). This may be compared with the submodule efficiency of other materials as $Cu(In,Ga)(Se,S)_2$ (14.7%), CdTe (10.6%) or unstabilised a-Si (12%). Moreover, CIS devices show excellent stability and can be produced with low energy consumption. From the technological point of view, the absorbers can be produced in a much more reproducible way than CISe ones. This is so because the performance of the CIS devices seems to be not affected by the outdiffusion of Na from the glass [49]. This avoids the requirement for the utilisation of *Na* diffusion barriers or the fair control of the incorporation of *Na*, as in the case of CISe films. Moreover, by selecting *Cu*-excess growth conditions high quality and stable CIS films are obtained, and therefore cell performance is insensitive to local stoichiometry variations during growth. This constitutes an important difference with respect to CISe technology, in which the stoichiometry of the film must be carefully controlled. It is expected to be possible to produce modules using Rapid Thermal Process (RTP) which ensures a very fast formation of the absorbers. This would decrease the cycle time of the process, in comparison with other technologies.

CIS cells are designed following similar procedures that those used for other chalcopyrite materials. The heterojunction is constituted by the p-type CIS absorber, the ZnO:Al window layer and a CdS buffer layer, which is placed in between the CIS and the ZnO layers. From the electrical point of view, the configuration window/absorber forms an heterojunction presenting the advantage that a great part of the photocurrent is generated at the surface of the absorber, where the electric field is maximum.

The details of the functioning and the electronic device properties are still not clear. Recent results suggest that the dominant recombination mechanism in CIS cells change from tunnelling assisted recombination at the dark to thermal activated recombination under illumination [50]. R. Klenk discussed some of the different aspects of diverse chalcopyrite cells [51], emphasising the differences between CISe and CIS cells, in terms of their respective band diagrams (see *Figure 1.5*):

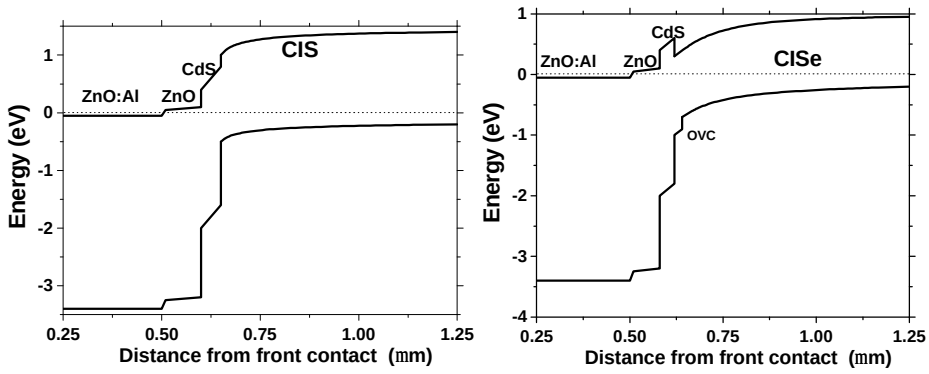

Figure 1. 5. Band diagrams for the $CuInS_2$ and $CuInSe_2$ based solar cells.

In the case of the CISe diagram, the presence of a spike in the conduction band enhances the inversion at the interface, and the absorber is inverted from p-type to n-type close to the interface. As a result, the interface recombination is very inhibited, even though the recombination velocity maybe high. Furthermore,

bulk recombination is dominant in CISe cells. The situation in high bandgap chalcopyrite materials, such as CIS is quite different. As can be appreciated in the band diagram, the band line-up is not in favour of an inverted interface, and the presence of a cliff results in higher interface recombination probability. Experimental results based on j(V) curves measurement have shown that the dominant recombination mechanism at the dark is tunnel-assisted [50, 52] over an energetic barrier of around 1.3 eV. In view of the band cliff, it is therefore necessary to accommodate at least part of the band offset by the introduction of a buffer layer. Despite the limitations mentioned above, active area efficiencies of almost 13% have been obtained with these devices, which may be explained because of a lower interface recombination velocity, because of Fermi level pinning due to interface charged states, or by the existence of an inverted interface (despite the band cliff).

1.4.2. Baseline technology

During the development of the SULFURCELL European project [53], a baseline technology has been established for the production of CIS-based solar cells [54]. Many of the technological steps are analogous to those from the CISe technology, but there are some important differences, as already stated above. The full process involves several steps. The optimisation of each step has been possible due the support of different characterisation tasks. Different glass substrates may be appropriate for architectural applications. The type of glass must be carefully selected for reducing costs without degrading the absorber properties. Glass substrate interacts with the absorber through the outdiffusion of *Na* and mismatch of the thermal expansion coefficient related (which might cause adhesion failure problems). In the case of the CIS-based cell, floated soda-lime has shown to have adequate thermal expansion coefficient, and not affect the properties of the film. The first step of the process is the cleaning of the glass, which is a critical step for avoiding problems with the coatings (holes,

adhesion failure...). The second step is the coating of the glass with the back contact of the cell. Molybdenum is used as back contact due to its high conductivity and corrosion resistance. Molybdenum is deposited by DC Magnetron sputtering, with a typical thickness around 1 μm. Once deposited, the back contact is pattering by laser scribing. The following step is the deposition of the metallic precursors of the absorber (*Cu* and *In*) by DC Magnetron sputtering. Usually, a *Cu/In* ratio between 1.2 and 1.8 is selected because of the beneficial effects of the *Cu*-excess. The formation of a secondary *Cu*-chalcogenide phase during the growth process is believed to reduce the formation of defects by chemical growth assistance, enhancing the ion mobility, reactivity and sulphur incorporation. The sulphurisation of the precursors is performed in a vacuum chamber using commonly vapour S. Sulphur pressure determines the pressure in the chamber. Sulphurisation using other gases such as H_2S, may be used. The last avoids the problem of vapour sulphur condensation in the pumps, but otherwise does not significatively affect the device performance [55]. Baseline sulphurisation process consists on a Rapid Thermal Process (RTP) in which the precursors are heated up to 500-600ºC in about one minute time, with the aid of halogen lamps, and then maintained to that temperature for about two minutes more [56]. Substrate temperature can be monitored by using thermocouples. After that time, the absorber has been formed and the substrates are cool down. As a result of the stoichiometry of the precursors, Cu-excess segregates at the surface in the form of CuS. Therefore it is necessary to introduce an additional step for the removal of the CuS. However, the high quality films obtained under these conditions and the wide window for the process justify this technology, in spite of the need to introduce an additional step. Despite the toxicity of KCN, a solution of this compound in water is a very fast and effective way to remove the Cu-excess, mainly due to the very different etching rates between CuS and CIS. Other alternatives to the KCN treatment are under development, and a suitable and less hazardous system would be very positive in terms of environmental impact of the whole process [57, 58]. The only effect of the chemical treatment is an increase in the film roughness, but it does not cause the degradation of the crystalline quality of it.

The extremely bad performance of p-type CIS / n-type ZnO cells makes necessary to introduce a buffer layer in the heterostructure. As in the case of CISe based cells, CdS is up to now the best alternative in terms of efficiency of the final device. The high toxicity of Cd and the chemical products used for the chemical bath deposition of the layer have promoted important investigations towards the substitution of this layer by a suitable alternative. However, up to now the results obtained with other buffers are still limited. Cadmium is believed to have some direct influence in the surface properties of the absorber. As a matter of fact, best buffer-free cells have been obtained after a pre-treatment of the absorber in a cadmium acetate solution, giving rise to efficiencies [59] up to 6%. Other approaches [60], specially $In(OH)_xS_y$ have already shown promising results [61], but are still under development. CdS is deposited on the top of the CIS by using the Chemical Bath Deposition technique, with a bath containing thiourea and cadmium acetate. The thickness of the buffer layer is around 50 nm. Before depositing the ZnO window layer, the absorber scribing process is performed. ZnO is used as transparent contact, and is deposited by RF Magnetron Sputtering. As the other deposition techniques, RF- Magnetron Sputtering allows to extend the production in the laboratory scale to industrial size productions. Close to the metallic contacts, ZnO is doped with Al. The doping of the high resistivity ZnO material is performed by co-sputtering an Al_2O_3 target under the appropriate conditions, therefore introducing Al in the ZnO crystalline structure. Finally, the *Al/Ni* metallic front contacts are deposited by e-Gun Deposition and the cells are scribed and encapsulated with EVA copolymer. A scheme of the whole process is given in next figure:

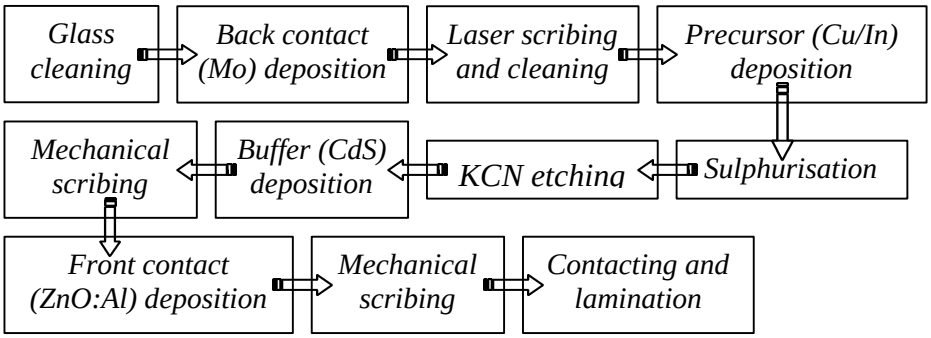

Figure 1. 6. Scheme of the different steps of the baseline sequential process.

2. Raman spectroscopy

2.1. Fundamentals of the Raman effect

The study of the interaction between the radiation and the matter was started by Rayleigh in the last decades of the past century. Rayleigh [62] showed that the intensity of the light scattered by particles suspended in a medium of different permitivity was frequency dependent, and found for the first time the relation $I_S \propto \lambda^{-4}$. This is know as Rayleigh's law, and provides an explanation for the blueness of the sky. After the work of Rayleigh, different studies appeared related to thermal induced light scattering density fluctuation in fluids. It was well-known that homogeneous fluids scatter light quite strongly, especially when they reach its critical temperature, a phenomenon known as opalescence [63]. This problem was explained by Smoluchowski [64], who suggested that the density of the media fluctuated due to the thermal motion of the molecules in the fluid. While other progresses were made in the understanding of scattering induced by thermal fluctuations, Brillouin [65] predicted the scattering of light by long wavelength elastic sound waves. In 1923 Raman [66] observed for the first time the inelastic scattering of light when studying the light scattering processes by benzene. It was found that the light scattered spectra contained sharp bands symmetrically disposed in pairs around the incident frequency, with shifts identical to the frequency of some infrared vibrational lines. At about the same time, Landsberg and Mandelstam [67] found independently a similar result in quartz crystals. The theory of the inelastic light scattering process by a system with two quantum energy levels had already been theoretically described by Smekal [68] in 1923, and nowadays is known as the Raman Effect. It is now well-established that the Raman effect is a consequence of the spatial and temporal fluctuations in the electronic contributions to the electric susceptibility. In the case of light scattering by collective excitations, such as lattice vibrations,

plasmons or magnons, the fluctuations result from the modulation of the electric susceptibility.

Macroscopic Theory

From the macroscopic point of view, Raman scattering by collective excitations may be interpreted as a nonlinear interaction of the incident and scattered electromagnetic waves with the collective excitations. Macroscopic theory [69, 70] provides important theoretical results, mainly the scattering cross-section of the Raman process.

Let $\vec{E}_I(\vec{r},t)$ be the electric field associated to the incident radiation, which we will consider to be monochromatic with frequency w_I and wave-vector $\vec{k}_I$. The incident radiation may interact with a periodic excitation in the media, whose amplitude can be described by a time and space dependent sinusoidal wave $X(\vec{r},t)$:

$$\vec{E}_I(\vec{r},t) = \vec{E}_I^0 \cdot cos(\vec{k}_I \cdot \vec{r} - w_I \cdot t) \qquad \textbf{[Eq. 2. 1]}$$

$$X(\vec{r},t) = \sum_q X^0(q,t) \cdot cos(\vec{q} \cdot \vec{r}) \qquad \textbf{[Eq. 2. 2]}$$

We will assume also that the medium is in thermal equilibrium, and therefore the Fourier amplitudes of the excitation are randomly distributed, and their phases fluctuate on a time scale characteristic of the thermal excitation processes. In this way, the statistic average of the fluctuation amplitude may be considered as a Dirach Delta-function in the reciprocal space:

$$< X^{*}(q,W)\cdot X(q,W') >=< X^{*}(q)\cdot X(q) >_{W}\cdot d(W-W') \qquad \textbf{[Eq. 2. 3]}$$

We will consider the polarizability induced in the media as a result of the presence of the incident electric field, which may be described by the polarization vector $\vec{P}$. Assuming a linear response, and in the absence of any excitations in the medium, we have:

$$\vec{P}(r,t)=e_0\cdot\vec{c}(w_I)\cdot\vec{E}_I(r,t), \qquad \textbf{[Eq. 2. 4]}$$

where $\vec{c}(w_I)$ is the susceptibility tensor characterising the macroscopic medium.

Furthermore, the presence of an excitation in the medium described by $X(\vec{r},t)$ results in a modulation effect of the wavefunctions and energy levels. From a macroscopic point of view, this modulation may be described by an additional contribution to the susceptibility tensor. Expanding $\vec{c}(w_I)$ in a series of Taylor up to first order we obtain:

$$\vec{c}=\vec{c}_0+\vec{c}'\cdot X \qquad \textbf{[Eq. 2. 5]}$$

As a result, we obtain three contributions to the total polarizability:

$$\vec{P}_0 = e_0\cdot\vec{c}_0\cdot\vec{E}_I \qquad \textbf{[Eq. 2. 6]}$$

$$\vec{P}_1=\vec{P}_{AS}+\vec{P}_S=\sum_q e_0\cdot\vec{c}'\cdot\left\{\vec{E}_I^{\,o}\cdot X^{o}(q,t)\cdot e^{i\left[(\vec{q}+\vec{K}_I)\cdot\vec{r}-w_{AS}\cdot t\right]}+c.c.\right\}+$$
$$+\sum_q e_0\cdot\vec{c}'\cdot\left\{\vec{E}_I^{\,0}\cdot X^{0}(q,t)\cdot e^{i\left[(\vec{q}-\vec{K}_I)\cdot\vec{r}+w_S\cdot t\right]}+c.c.\right\} \qquad \textbf{[Eq. 2. 7]}$$

where “c.c.” means “conjugate complex”.

The first contribution arises from the zero order susceptibility term, and gives rise to the Rayleigh elastic dispersion. The other two contributions arising from the coupling of the excitation and the electric field describe the scattered light that has changed its frequency. These two contributions are referred to as Stokes and Anti-Stokes radiation fields, and are described by their respective frequencies and wave-vectors:

$$\vec{K}_{AS} = \vec{k}_I + \vec{q}$$
$$\vec{K}_S = \vec{k}_I - \vec{q}$$
$$w_S = w_I - W$$
$$w_{AS} = w_I + W \qquad \textbf{[Eq. 2. 8]}$$

The above equations describe the properties of the inelastically scattered light. In the Stokes process, the incident photon is scattered while a quantum of excitation with energy $\hbar W$ is created in the crystal. In the Anti-Stokes process, a quantum of excitation is annihilated and therefore, the frequency of the scattered phonon increases. Due to the strong analogy between both components of the scattered light, we will restrict ourselves to the study of the Stokes radiation. In this case, the cross-section intensity corresponding to the rate of photons that are inelastically scattered per solid angle and frequency is given by:

$$\frac{d^2 s}{d\tilde{W} \cdot dw_S} = \frac{w_I w_S^3 V n_S \; r \left| e_0 \hat{e}_S \cdot \vec{\vec{c}}\,'(w_I, -w_S) \cdot \hat{e}_I \right|^2}{(4\pi e_0)^2 c^4 n_I} \cdot \left\langle X(q) \cdot X^*(q) \right\rangle_{w_S} \qquad \textbf{[Eq. 2. 9]}$$

In the previous equation, n_s and n_I are the refractive indexes of the scattering and initial media, respectively, and r is the scattering volume. The tensor $\vec{\vec{c}}\,'$ is

commonly referred to as second order Raman tensor. The contraction of the tensor $\vec{c}'$ with the polarization unitary wave-vectors of the incident and scattered radiation ($\hat{e}_I$ *and* $\hat{e}_S$, respectively) determines the existence of the "selection rules", which are given by the crystal symmetry. Selection rules provide an explanation for the existence of experimental configurations in which the scattered intensity is zero.

It should be mentioned that the cross-section scattering intensity given by **[Eq. 2.9]** is proportional to the scattering volume r, but not to the total volume of the crystal (V). One should take into account that the factor (V) appearing in the numerator of the above expression is cancelled by a factor *1/V* arising from the spectral power given by $\left\langle X(q)\cdot X^{*}(q)\right\rangle_{w_S}$, as will be shown later. Another interesting feature is the fourth power law of the scattered light. Considering that under the usual experimental conditions $w_S \approx w_I$, the cross-section is approximately proportional to the fourth power of the frequency of the incident light.

The expression for the cross-section provided by the Macroscopic Theory is valid only for excitation wavelengths far away from electronic resonance conditions. For excitation energies close to the energy gap it is observed a strong increase in the scattering cross-section, whose correct description requires the more sophisticated Microscopic Theory [69, 71]. This phenomenon is the so-called "Resonant Raman Effect", and is characterised by an increase in the scattered light intensity which may be even of various orders of magnitudes. Even in this special case of resonance, the intensity of the scattered light is much lower than the intensity of the Rayleigh dispersed light. Typically, only 1 of each 10^7 photons suffers the inelastic scattering process.

On the other hand, the Fluctuation-Dissipation theory provides a simple way for calculating the spectral power appearing in the expression for the Raman

scattering cross-section. The Fluctuation-dissipation theory relates the statistical average of the product of the generalised force and its conjugated variable, with the imaginary part of the transfer function. Let $F(t)$ be the fictitious force that couples to the excitation amplitude $X(r)$. For such case, the Hamiltonian of the interaction may be expressed as:

$$H = -X(r) \cdot F(t) \qquad \textbf{[Eq. 2. 10]}$$

In the case of the molecular vibrations, the effect of the effective fictitious force upon each molecule $f(t)$ may be described as a set of *N* independent harmonic equations, with natural frequency w_0 and damping constant g. The fictitious force may be considered as a constant force, with a Fourier spectrum consisting on a single component with frequency w. Therefore, the equation that described the dynamical behaviour of the system are given by:

$$\begin{aligned} &\ddot{x} + g \cdot \dot{x} + w_0^2 \cdot x = f(t) \\ &\ddot{\bar{X}} + g \cdot \dot{\bar{X}} + w_0^2 \cdot \bar{X} = N \cdot \bar{f} \end{aligned} \qquad \textbf{[Eq. 2. 11]}$$

In the Linear Response Theory, one may define the Linear Response Function characteristic of the system $G(q,w)$, as the mathematical function relating the spectral components of the fictitious force and the amplitude of the excitation:

$$\bar{X}(q,w) = G(q,w) \cdot \bar{F}(w) \qquad \textbf{[Eq. 2. 12]}$$

In order to find the Linear Response Function for this particular case, one should solve the equation **[Eq. 2.11]** by applying the Fourier transformation, leading to:

$$G(w) = \frac{1}{-w^2 + ig \cdot w + w_0^2} \qquad \textbf{[Eq. 2. 13]}$$

Now, one should consider one of the expressions of the well-established Fluctuation-Dissipation Theorem:

$$\left\langle X^{*}(q)\cdot X(q)\right\rangle_{w}=\frac{\hbar}{p}\cdot(n(w)+1)\cdot Im\{G(w)\} \qquad \textbf{[Eq. 2. 14]}$$

Therefore, known the function $G(w)$, its imaginary component is given by:

$$Im\{G(w)\}\approx\frac{p\cdot L(w)}{2\cdot N\cdot w_0}\;;\quad where\;\; L(w)=\frac{g/2p}{(w-w_0)^2+\left(g/2\right)^2} \qquad \textbf{[Eq. 2. 15]}$$

This results indicates that the spectral power is inversely proportional to the number of particles (and therefore, to the volume of the system), and confirms that the cross-section of the Raman scattering process does not depend on the total volume of the crystal, but only on the scattering volume. Moreover, the Raman cross-section is maximum for $w=w_0$, being the scattered intensity modulated by an almost Lorentzian factor $L(w)$. Notice also that the Stokes cross-section is affected by a factor $(n(w)+1)$, where $n(w)$ is the phonon occupation number, which is given by the Bose-Einstein distribution. For the Anti-Stokes process the result of the calculation is similar, being the only difference the appearance of a factor $n(w)$, instead of the factor $(n(w)+1)$. Therefore, the Anti-Stokes process is only possible in a medium in which at least a fundamental excitation already exists.

On the other hand, the kinematics properties of the first order Raman scattering by phonons in a perfect crystal are governed by the momentum and energy conservation rules **[Eq. 2.8].** Momentum conservation leads to an important consequence with respect to the phonons experimentally available by Raman scattering experiments. Considering the excitation wavelengths used under usual experimental conditions (visible light), it results that the wave-vector of

the incident light is about 10^6 cm^{-1}, which is two or three orders of magnitudes below the typical size of the Brillouin Zone of the crystal. Therefore, for a perfect crystal, even the maximum wavelength phonon that may take part in the process occurring in a backscattering experiment corresponds to a zone-centre phonon.

2.2. Group Theory and determination of the normal modes

Group theory in crystals

Group theory is used in a large number of physical and chemical problems involving atoms, molecules and crystals. The determination of the vibrational normal modes of a molecule is only one example of the several applications provided by group theory. In crystal physics, group theory is used for instance, for determining the symmetry properties of the wavefunction of the electrons subjected to the periodic electric field of the crystal, or to find an expression for the potential energy of an impurity in a crystal site. In the case of Raman spectroscopy, group theory provides a direct method for classifying the vibrations of the crystal, and is very useful to predict the experimental configurations for which a Raman peak is allowed or forbidden ("selection rules").

We will consider now the symmetry properties of the crystal hamiltonian $H(\vec{r})$. All the symmetry operations leaving the Schrödinger equation unchanged, which are defined by the symmetry characteristics of the potential $V(\vec{r})$ in the Schrödinger equation, define the group of interest. Crystal space group (***G***) is defined by a set of translational operations and additional symmetry operations, leaving $V(\vec{r})$ invariant. A representation of a group is defined in terms of square matrices having the same multiplication properties as the operators of the group. The construction of a representation of a group may be done by applying the ***n*** symmetry operations of the group to a function $a(\vec{r})$ being solution of the Schrödinger equation. Consider for example the effect of an arbitrary operation of the group *X*, upon the Schrödinger equation:

$$\hat{H}(X\cdot\vec{r})\cdot a_j(X\cdot\vec{r}) = E\,a_j(X\cdot\vec{r}) \equiv E\cdot\tilde{a}_j(\vec{r}) \qquad \textbf{[Eq. 2. 16]}$$

Since by definition the hamiltonian remains invariant after the application of the symmetry operation *X*, it follows that the transformed function $\tilde{a}_j(\vec{r})$ is also a solution of the Schrödinger equation. The set of ***n*** transformed functions $\tilde{a}_j(\vec{r})$ forms a set of basis functions of the group, and it may be considered as the components of a ***n***-dimensional vector. If we now apply a symmetry operation of the group on this vector, the resultant vector may be expressed in terms of a linear combination of the initial set of functions. The matrices relating the basis functions constitute a reducible representation of the group ***G***. Since the number of possible basis functions to be chosen is infinite, the number of reducible representations of a group is also infinite. This leads to the mathematical problem of finding the finite number of irreducible representations of a group, which posses the fundamental properties of it. When the matrices of a reducible representation are brought into as near to diagonal form as possible they are said to be completely reduced, and the submatrices constitute the irreducible representations of the group ***G***.

Translational symmetry of the crystal may be expressed in terms of a generic translation vector defined in terms of the primitive vectors of the crystal lattice:

$$\vec{R}_n = n_1\cdot\vec{a}_1 + n_2\cdot\vec{a}_2 + n_3\cdot\vec{a}_3 \qquad \textbf{[Eq. 2. 17]}$$

The translations in a crystal, denoted by $T(\vec{R}_n)$ form an abelian group (G), once the product operation between two translations is defined as [72, 73]:

$$T(\vec{R}_n)\bullet T(\vec{R}_m) = T(\vec{R}_{n+m}) \qquad \textbf{[Eq. 2. 18]}$$

In addition to the translations, there are other symmetry elements in a crystal that leave $V(\vec{r})$ unchanged. Those are specific rotations, rotoinversions, reflections by a plane, pure inversion, glide planes and screw axis. Moreover, by constructing all the possible cosets between this set and the translational group *G*, we get different invariant subgroups, which define the crystal space group as [74]:

$$G = G \oplus AG \oplus BG \oplus \ldots \qquad \textbf{[Eq. 2. 19]}$$

The set of operations denoted as {*A, B, C...*} does not always form a group by itself. When the set {*A, B, C...*} forms a group by itself it is referred to as Point Group of the crystal (**G_P**). However, even in the case in which the complex {*A, B, C…*} does not form a group, the cosets {*1/g·G, 1/g·AG, 1/g·BG…*}, regarded as elements, do form a group named *factor group* (the factor *1/g* is a normalisation factor corresponding to the inverse of the order of *G*). Therefore, the order of this group is equal to the number of elements in the complex, and it is possible to find its irreducible representations in the same way as will be shown for the point group of a crystal.

Because of the abelian character of the translational group, matrices representing the operators of the group *G* must commute with each other, and therefore, it is possible to bring each representation to its diagonal form through a single similarity transformation for all of them. This means that a certain basis exists in which all the matrices constituting the representation are diagonal. The set of functions of this new basis, $\{\psi_i(\vec{r})\}$, may be expressed as a linear combination of the transformed wavefunctions being solution of the Schrödinger equation:

$$\psi_i(\vec{r}) = \sum_j c_{ij} \cdot \tilde{\alpha}_j(\vec{r}) \qquad \textbf{[Eq. 2. 20]}$$

It follows from this definition that the effect of the application of a certain translation upon a function $y_i(\vec{r})$ of the basis is just to multiply the function by a certain factor. The result of this is the well-known Block Theorem, through which the representation of the translation operators is expressed by:

$$T(\vec{R}_n)\cdot y_k(\vec{r}) = e^{i\vec{k}\cdot\vec{R}_n}\cdot y_k(\vec{r}) \qquad \textbf{[Eq. 2. 21]}$$

Block Theorem leads to a useful expression for the electronic wavefunction in terms of the wave-vector $\vec{k}$:

$$y_k(\vec{r}) = e^{i\vec{k}\cdot\vec{r}}\cdot u_{\vec{k}}(\vec{r}), \qquad \textbf{[Eq. 2. 22]}$$

where $u_{\vec{k}}(\vec{r})$ is symmetric respect a translation by a lattice vector. Consider now a generic operation of the space group written in terms of a translation $T(\vec{R})$ followed by an arbitrary operation A of the crystallographic point group, which will act upon a basis function of the reduced form of G:

$$A \bullet T(\vec{R}_n) \bullet y_k = A \bullet \left(e^{i\vec{k}\cdot\vec{R}_n}\cdot y_k \right) \qquad \textbf{[Eq. 2. 23]}$$

Notice that if $\vec{k}\cdot\vec{R}_n$ is invariant under the operation A, the translation operation commutes with A. The set of operations leaving $\vec{k}\cdot\vec{R}_n$ invariant forms the wave-vector group $\boldsymbol{G_k}$. In general, when a point group exists, the order of $\boldsymbol{G_k}$ is a factor of the order of $\boldsymbol{G_p}$. The maximum symmetry at a given point of the Brillouin Zone is determined by the symmetry of the crystallographic point group ($\boldsymbol{G_p}$). However, the phonons involved in the first-order Raman scattering processes are those laying in the centre of the Brillouin Zone, and at the G point ($\vec{k}=0$) the groups $\boldsymbol{G_p}$ and $\boldsymbol{G_k}$ coincide.

We will study now the symmetry of the wavefunction at a given point $\vec{k}$ of the Brillouin Zone with respect to the operations of the Point Group of the crystal $\boldsymbol{G_P}$. Unlike the case of the translational group of the crystal, it is not possible to find a similarity transformation which simultaneously reduces all the matrices of the representation of the group $\boldsymbol{G_P}$ into its diagonal form, since the operations of $\boldsymbol{G_P}$ are not commutative in the general case. However, it is still possible to bring the matrices defining the representations of $\boldsymbol{G_P}$ to their as near as possible diagonal form. Such procedure leads to the obtaining of the completely reduced representation of $\boldsymbol{G_P}$. The corresponding submatrices constitute the irreducible representations of the group. Some of the submatrices may occur several times along the diagonal of the reduced matrices. In this case, they may be equivalent if they can be transformed into each other by a single similarity transformation, which is possible if they have the same trace for all the matrices of the group.

The arrangement of the symmetry operations of $\boldsymbol{G_P}$ into classes is very useful for practical purposes. For introducing the concept of class, consider R as an arbitrary operation of $\boldsymbol{G_P}$. Then, a transformation given by $(P^{-1}\cdot R\cdot P)$, where the matrix P denotes a transformation to another system of axes, yields another matrix with the same trace. Moreover, since the effect of this transformation is to permute the atoms in the crystal, $(P^{-1}\cdot R\cdot P)$ must belong also to $\boldsymbol{G_P}$. This fundamental property allows classifying all the operations in $\boldsymbol{G_P}$ into classes. A class in a group is defined in such a way that if A and X are elements of the group, then A and $X^{-1}\cdot A\cdot X$ and A belong to the same class. Obviously, all the elements in a class have the same trace. The order of the point group (g) and the order of the class C_i (h_i) are related by the number of times each element is repeated in the set $\left\{X^{-1}\cdot A\cdot X\,;\,\forall X\in G_P\right\}$. Thus, the class C_i generated by the operation A is formally expressed as:

$$C_i=\frac{h_i}{g}\cdot\sum_{X\in G_P}X^{-1}\cdot A\cdot X \qquad \textbf{[Eq. 2. 24]}$$

Two fundamental properties of the classes are that *i)* they commute between each other, and *ii)* the product of two classes can be expressed as a linear combination of the classes of the group:

$$C_i \cdot C_j = C_j \cdot C_i \qquad \textbf{[Eq. 2. 25]}$$

$$C_i \cdot C_j = \sum_s l_{ij}^s \cdot C_s \qquad \textbf{[Eq. 2. 26]}$$

As a consequence, the matrices corresponding to the representations of the classes, which are defined by the coefficients l_{ij}^s can be diagonalised, provided that they form an abelian group.

The concept of class is especially useful for the determination of the irreducible representations of $\boldsymbol{G_P}$, due to the existence of some important theorems. First of all, it may be shown that the number of inequivalent irreducible representations is equal to the number of classes in the group. Furthermore, the number of times an irreducible representation occurs along the diagonal of the reduced representation is equal to its degree. For each class in the group, the characters of the irreducible representations define the character table of the group. The character table, as well as other important properties of the group may be constructed by using the orthogonality relations, which can be written in a compact way as [75]:

$$\sum_R [G_i(R)_{mn}] \cdot [G_j(R)_{m'n'}]^* = \frac{g}{\sqrt{l_i \cdot l_j}} \cdot d_{ij} d_{mn} d_{m'n'} \qquad \textbf{[Eq. 2. 27]}$$

In the previous equation, $\Gamma_i(R)_{mn}$ denotes the *(m,n)* component of the irreducible representation *i* corresponding to an operation *R* of the group, *g* refers to the order of the group and *l* is the dimension of the matrix. **[Eq. 2.27]**

may be interpreted as follows: for each set of matrices constituting an irreducible representation, any set of elements in a matrix behaves in the same way that the components of a *g-dimensional* vector, being all the vectors orthogonal with each other and with a well defined module $\sqrt{g/l}$. Although the orthogonality relations provide a relationship between all the elements of the representation matrices, generally it is not necessary to use them explicitly. Anyway, it leads to some useful relations expressed only in terms of the traces of the matrices:

1) The sum of the squares of the dimensions of the irreducible representations (l_i) of a group is equal to the order of the group (g):

$$\sum_i l_i^2 = g \qquad \textbf{[Eq. 2. 28]}$$

2) The sum of the squares of the characters of a representation $c_i(R)$ is also equal to the order of the group:

$$\sum_R [c_i(R)]^2 = g \qquad \textbf{[Eq. 2. 29]}$$

3) The vectors whose components correspond to the traces of two different irreducible representations are orthogonal:

$$\sum_R c_i(R) \cdot c_j(R) = g \cdot d_{ij} \qquad \textbf{[Eq. 2. 30]}$$

As already mentioned above, the set of operations {*A, B, C…*} may form the so-called point-group of the crystal. When the point group of the crystal does not exist, it is possible to work analogously with the factor group of the crystal. In

general, the factor group is isomorphic to one of the 32 point groups. Therefore, the irreducible representations are the same that those of one of the point groups.

Normal modes determination

Group theory has several applications in the field of Raman Spectroscopy. The most well-known applications deal with the problem of the determination of the normal mode in a crystal, the classification of the phonons according to their symmetry and the establishment of the so called "selection rules" for each given mode.

The classification of the phonons according to their symmetry can be done in a quite systematic way once the crystal space group has been determined. The application of the different symmetry operations upon the atoms in the unit cell of the crystal leads to the characters of the reducible representation for the zone-centre phonons of the crystal for each class of operation. Then the reducible representation can be decomposed into irreducible representations by using the orthogonality relations given in **[Eq. 2.27]**, with the aid of the character table of the point group of the crystal. The Raman activity of each normal mode, and also the "Selection Rules" may be read directly from the character table of the point group. The activity of the phonons relies on the symmetry properties of the Raman tensor. As discussed in the previous section of this chapter, the Raman scattering cross-section given by **[Eq. 2.14]** is proportional to the contraction of the Raman tensor with the polarisation vectors of the incident and scattered light: $ds \propto \left|\hat{e}_S \cdot c'_{ij} \cdot \hat{e}_I\right|^2$. The representation of the Raman tensor may be decomposed in irreducible representations of the crystallographic point group. Let G_a be an irreducible representation contained in the reducible

representation of the crystal. The symmetry of this tensorial product may be expressed in terms of group theory notation as:

$$G_s = G_v \otimes G_a \otimes G_v^{'}, \qquad \textbf{[Eq. 2. 31]}$$

where G_n and $G_n^{'}$ describe the symmetry of the polarisation vectors. The direct product of the representations in **[Eq. 2.31]** has to contain at least one totally symmetric irreducible representation (A_1 or A_{1g}). By the Matrix Element Theorem, this condition is equivalent to the requirement that the irreducible representation G_a has to be contained in the direct product $\Gamma_v \otimes \Gamma_v^{'}$. Therefore, only the phonons belonging to the irreducible representations transforming like the Cartesian products with the form ***{x², y², z², x·y, x·z, y·z}*** are active in the first-order Raman scattering. Moreover, the transformations properties of the irreducible representation associated with a given phonon lead to an explicit expression for the form of the Raman tensor, which at the same time determines the incident and scattered polarisations that are allowed or forbidden. These constitute the Raman "Selection Rules" for the first-order Raman scattering by phonons, and experimentally are very useful, for example, to distinguish different peaks laying at very close spectral positions.

2.3. Experimental

Since the first light scattering experiments performed by Raman with naked eye, important improvements have been developed in the different parts of the experimental set-up. Nowadays, the experimental set-up for performing Raman scattering experiments consists in four different parts: a light source, an optical system for collecting light, a light dispersive system and a detector. The next figure shows a diagram of the fundamental parts of the experimental system used to perform the Raman measurements.

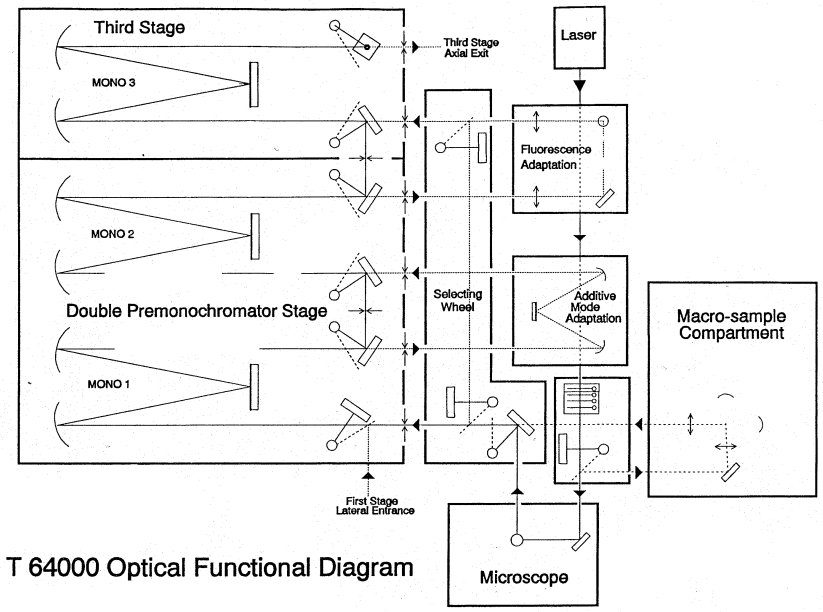

Figure 2. 1. Scheme of the main parts of the Jovin-Yvon T64000 spectrometer.

The previous figure includes the different components of the Jobin-Yvon T64000 spectrometer, which has been used for recording the Raman spectra presented in this work. The laser light may be directed towards a light

microscope by a set of mirrors properly oriented. This allows achieving high spatial resolution, even sub-micronic excitation areas on samples with well-polished surfaces. Alternatively, the laser light may be lead to a chamber where the samples can be placed, in which case the diameter of the excitation area is around 100 microns. The light scattered by the sample is collected, and directed towards an spectrograph, where it is dispersed and finally analysed by a CCD detector. The different components of the T64000 spectrometer will be described in more detail.

Light sources

Usual Raman experiments require a light source capable to produce highly monochromatic light. The apparition and generalisation of the utilisation of lasers sources has provided an easy way to attain this objective, and has lead to the abandonment of the arc discharge lamps. In addition to monochromaticity, the laser light has also the important properties of being coherent, highly directional and the potential capability to produce extremely intense radiation. Continuous lasers are the most extended light sources for Raman experiments. Some of the most used continuous lasers are the Ar^+, the He-Ne and the Kr^+ ones. Each of these produces different lines in the visible range. The operation of the gas lasers is based on the stimulated emission of light by a gas kept at low pressure in a cylindrical cavity. A plasma regime is established inside the cavity through an electric discharge, leading to the ionisation of the atoms in the gas. Under the appropriate conditions of voltage, pressure and current it is possible to achieve the inversion of population between two electronic levels in the atoms. This produces the stimulated emission of light. The emitted radiation is stored at the resonant cavity, as sketched in *figure 2.2*, and the laser emission is achieved when the intensity gain is able to compensate the losses in the cavity.

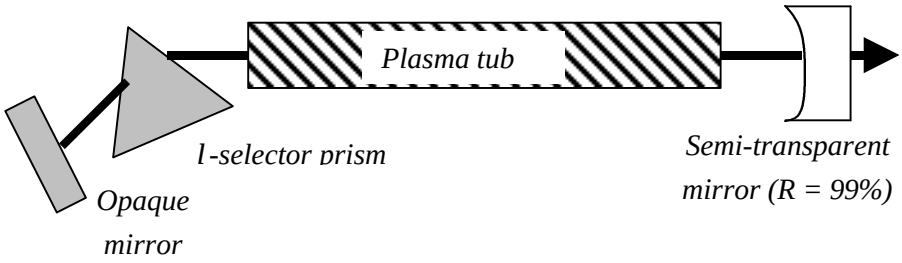

Figure 2. 2. Diagram of the typical configuration of a gas laser.

In the previous figure it can be distinguished the different parts of the laser cavity: the plasma tub (where the light emission is produce), an opaque mirror (that prevents the light to go out from the cavity) and a semi-transparent mirror with a reflection coefficient close to one, which makes possible part of the emitted light to be transmitted outside the cavity.

The light source used for the measurements in the present work has been a Coherent Innova 300 Ar^+ laser. This laser produces intense lines in the blue and green region of the visible spectra, which are listed in the following table. The Raman spectra presented in this work have been obtained using the green line of this laser, at 514.5 nm.

Wavelength (nm)	*Intensity TEM_{00} (W)*
454.5	0.14
457.9	0.42
465.8	0.18
472.7	0.24
476.5	0.72
488.0	1.8
496.5	0.72
501.7	0.48
514.5	2.4
528.7	0.42

Table 2.1. Available visible wavelengths for the Ar^+ laser.

Light Collector system

As already described above, the experimental system offers the possibility for working using a macrochamber or a metallographic microscope (Olympus BH-2) coupled to the optical system. When using a microscope, Raman spectroscopy is sometimes called micro-Raman spectroscopy. Micro-Raman spectroscopy offers some advantages with respect to conventional Raman spectroscopy, mainly the greatest spatial resolution that can be achieved with the aid of the microscope. The lateral resolution of the system is limited by the diameter of the diffracted spot through the optics of the microscope. The measurements presented in this work have been obtained with a 100× objective (NA = 0.95) with an excitation wavelength of 514.5 nm. This gives a diameter for the diffracted spot of 0.6 μm. However, surface roughness results generally

in an increase of the effective illuminated area. It is customary to take 1 μm for the order of magnitude of the lateral resolution of the technique. In the micro-Raman configuration, the laser beam is filtered with a monochromator and then directed towards the microscope by a set of mirrors. The utilisation of a monochromator eliminates any other resonant mode different that the fundamental mode TEM_{00}. The laser beam reaching the entrance of the microscope is there separated by a beam-splitter, consisting in a semi-transparent mirror. The beam falls on the sample, and the backscattered light is collected by the microscope, passes through the beam-splitter and is directed towards the dispersive system. Next figure shows a diagram of the collector system when using the micro-Raman configuration:

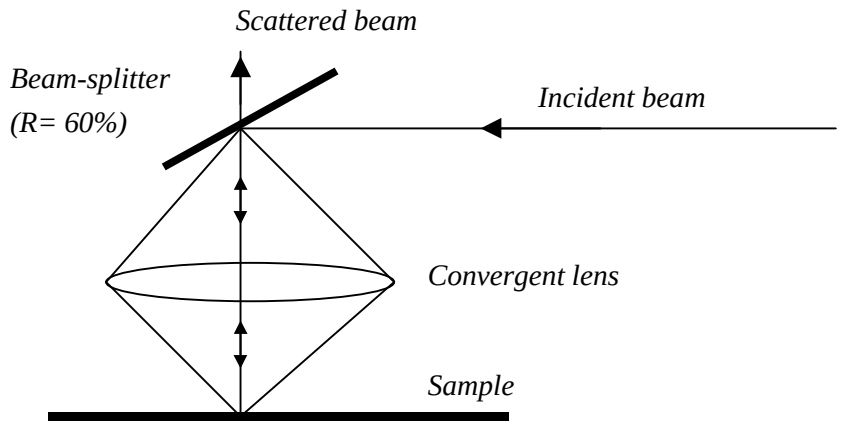

Figure 2. 3. Diagram of the collector system implemented for the micro-Raman configuration.

It should be mentioned that the micro-Raman technique has got some disadvantages with respect to the Macro-Raman configuration. Micro-Raman spectroscopy offers only the possibility for working in the backscattering configuration. When other experimental configurations are required, the macro-chamber must be used. Another significant difference between both configurations is the much lower power density supplied to the sample in the

case of the macro-Raman configuration, due to the larger size of the spot. Therefore, spectral features related to sample heating or sample degradation, which may be important in micro-Raman, may be overcome by using macro-Raman.

Dispersive system

The optical dispersive system of the Jobin-Yvon T64000 consists on three diffraction grids with 1800 lines/mm. The utilisation of the three grids allows for two different configurations in the functioning of the system. In one case, the two first grids are used to select an spectral range [λ_1, λ_2] and to filter the scattered radiation, while the third grid acts as a spectrograph for the dispersion of the beam, which then falls onto the detector. The second possible configuration is the so-called "additive mode", in which the three dispersive grids act on series upon the scattered light. In this case it is possible to achieve a higher dispersion of the scattered light, and therefore a higher spectral resolution. However, this operating mode has got some drawbacks respect the "subtractive mode". First, the higher spectral resolution leads to a reduction of the spectral range, and therefore it is necessary to do at least a second measurement in order to cover the same range. Moreover, the three monochromators disperse the scattered light, and therefore the intensity of the light that the detector receives is much lower. As a consequence, the signal to noise ratio increases, which hinders the study of compounds with low Raman cross-section. *Figure 2.4* shows a diagram of the spectrograph in which can be appreciated the three monochromators described above:

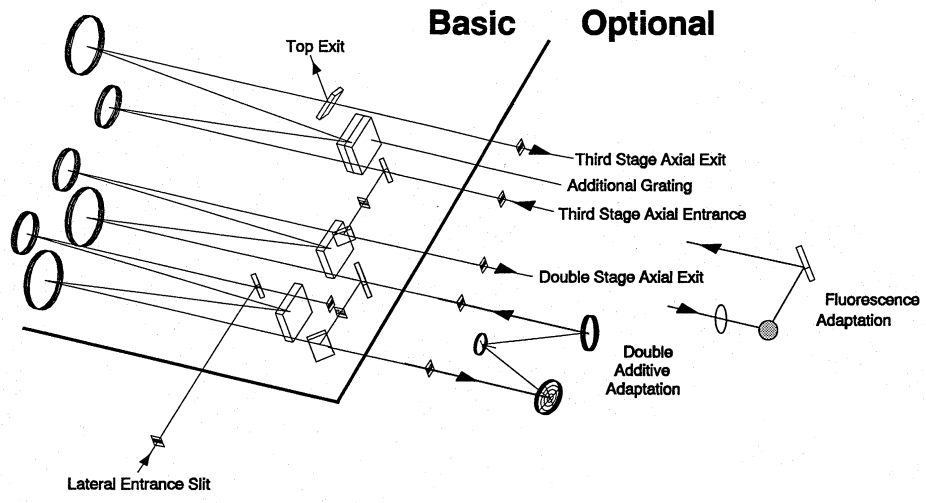

Figure 2. 4. Scheme of the triple-monochromator spectrograph.

A great number of compounds present vibrational modes in the low-frequency range of the spectra, close to the frequency of the Rayleigh scattered light. The old dispersive systems were not able to efficiently separate the scattered light, which made these bands experimentally inaccessible. The development and perfecting of the optical dispersive systems in the last decades has substantially improved the spectral resolution with respect to the old dispersive systems, allowing to study bands at Raman shifts even below 15 cm^{-1}.

Detector

During the last years important developments in the field of the CCDs detectors ("Charge Coupled Device") has lead to the substitution of most of the old single-channel detectors based on fotomultipliers, by new high sensitivity multi-channel CCDs. At the exit of the dispersive stage, the scattered light falls on the different pixels of the CCD depending on the wavelength of the light. The utilisation of the multi-channel detectors allow to record the intensity of all the spectral components of the scattered radiation in a single measurement, reducing drastically the acquisition time for each spectrum with respect to the fotomultiplier detectors.

Raman measurement conditions

The Raman spectra presented in this work have been obtained using the substractive mode of the Jobin Yvon T64000 spectrometer, with a spectral resolution of 0.4 cm^{-1}. In order to achieve the maximum possible spatial resolution, micro-Raman configuration has been used, with a 100× microscope objective (NA=0.95). Therefore, geometrical configuration corresponds to backscattering. Regarding the excitation light, the green light of the Ar^+ laser has been selected (λ=514.5 nm). Plasma lines have been filtered with a pre-monochromator placed at the exit of the laser beam. The green line has given the best signal to noise ration in $CuInS_2$. Otherwise, no resonance enhancement has been observed for anyone of the available wavelengths of the laser. For this wavelength, the penetration depth of the light [76] is around 150 nm. This value must be taken into account when interpreting the results presented on $CuInS_2$ polycrystalline films.

The small scattering volume in $CuInS_2$ results in a small scattering volume, leading to a small scattering cross-section. Due to the bad Raman efficiency of the compound, it has been necessary to use the maximum possible excitation power in order to perform the characterisation of the material. The effect of the power density on the sample has been studied by comparing the Raman spectra of a $CuInS_2$ polycrystalline sample for different excitation powers. Experimental results show that for the micro-Raman configuration with the measurements described above, an excitation power of 1.1 mW constitutes an upper limit, if one wishes to avoid undesirable effects. For higher values of the excitation power, a red shift and broadening of the peaks have been observed. These features are related to anaharmonic effects which manifest as a consequence of the existence of a strong temperature gradient in the sample. Therefore, we have chosen an excitation power of 1.0 mW on the sample, in order to avoid these effects and to obtain the maximum scattered intensity. This value corresponds to a surface power density below 0.06 MW/cm^2.

2.4. Applications of Raman spectroscopy

Raman spectroscopy constitutes a complementary technique to the infrared spectroscopy for the study of the vibrational properties of solids, liquids and gases. Quite often, the experimental availability of the vibrational frequencies requires for the utilisation of both techniques. This is especially true in the case of centrosymmetric compounds, in which the selection rules make Raman-active those modes which are not Infrared-active modes. Therefore, Raman spectroscopy is a very useful tool for the performance of fundamental studies of materials and molecules.

Since the number of vibrational frequencies and their spectral position are a fundamental characteristic of a given material, Raman spectroscopy has been successfully applied to the identification of chemical compounds and chemical phases present in samples. Silicon is by large the most studied electronic material. Its simple structure and the availability of large high quality single crystals made possible to study in great detail the first and second order Raman spectra. Determination of the crystal orientation in Silicon is also possible by analysing the intensity dependence on different experimental polarisation configurations (accuracy up to 2º has been achieved [77]).

In general, polarisation measurements are usually performed on single crystals in order to resolve bands with certain symmetry or for investigating the unknown symmetry of a Raman band. These experiments may be used also to verify if the selection rules hold for a given sample. Moreover, it is well known that the breakage of the polarisation selection rules indicates the existence of defects in the sample, which destroy the crystalline symmetry of the lattice. Due to the fact that the light provided by the laser is already polarised, polarisation experiments can be carried on just with a single polarisator, which selects the polarisation of the light scattered from the sample before reaching the detector.

By convention, it is usual to describe a polarisation experiment using the following notation: $\langle z|xy|z'\rangle$. Unless another specific convention is mentioned, all the symbols in the bracket correspond to directions referred to the crystallographic axis. The directions *z* and *z'* are the directions of the incident and scattered beams, respectively, while *x* and *y* are the directions in which the incident and the scattered light are polarised.

On the other hand, structural and disorder effects may be evaluated in silicon by analysing the broadening and lineshape of the triple degenerate zone-centre phonon. Moreover, in highly damaged crystals selection rules do not hold any more, and a relaxation of the wave-vector conservation rule may be observed. The study of the effect of the implantation dose and damage recovery by post-annealing processes are typical examples in which Raman spectroscopy has been successfully applied [78]. Ion-Implantation processes in other III-V materials have also been investigated, such as the silicon implanted GaAs [79]. Frequency shift and peak broadening may also be useful for the evaluation of residual stresses in heteroepitaxial films [80] or in heteroestructures with different thermal expansion coefficients, such as silicon on insulators [81] (SOI).

In addition to the study of crystalline materials, amorphous, microcrystalline and, more recently, nanocrystalline materials have been also widely studied. The presence of extended defects, such as dislocations or grain boundaries, has been successfully modelled in terms of a "spatial correlation length model", in which the effect of a finite phonon life-time is considered [82]. This gives rise to a red shift and asymmetric broadening of the triple generated zone-centre phonon in *Si*, from which it is possible to estimate the correlation length parameter. This parameter may be interpreted as the characteristic length in which the material can be regarded as having translational symmetry. Raman spectra of amorphous materials have also been investigated. In this case, the breakage of the selection rules leads to Raman spectra resembling the phonon density of states [83].

Another wide field of applicability of Raman spectroscopy has been the characterisation of semiconductor alloys. For binary alloys, the spectra are usually characterised by an unimodal or a bimodal behaviour of the active modes, depending on the type of elements constituting the alloy. The analysis of the spectral features of the bands allows, in general, quantifying the level of strain (degree of relaxation of epitaxial layers), the alloy composition and the coherence length, simultaneously [84, 85]. This has been extensively applied to the analysis of the Si-Ge system [86], III-V alloys, such as In(Al,As) or In(Ga,As), and II-VI alloys, as (Hg,Cd)Te [87]. Raman spectra of superlattices and quantum well structures present also interesting features, which make Raman spectroscopy useful for their characterisation. For example, the position of the folded phonons may be used to determine the superlattice period.

Finally, Raman spectroscopy has also been used for the study of non-semiconducting materials. For instance, superconducting materials, such as YbaCuO's, have been investigated by several authors and interesting superconductor effects upon the electronic and phonon spectra have been reported [88].

3. Spectral features in $CuInS_2$ films

3.1. Raman spectrum of $CuInS_2$ single crystal

$CuInS_2$ is a chalcogenide material belonging to the large group of ternary semiconductors with molecular formula ABX_2. This consists mainly of two major groups: the chalcopyrites ($A^I B^{III} C_2^{VI}$) and the pnictides ($A^{II} B^{IV} C_2^{VI}$). The broad range of optical bandgap and carrier mobility offered by these semiconductors have promoted in the recent years a great number of fundamental studies [89], and have also received considerable attention because of their potential technological applications in photovoltaics, light emitting diodes and nonlinear optical devices. Chalcopyrite materials are the ternary isoelectronic analogues of the II-VI binary compounds. The analogue binary compound for a given chalcopyrite material may be obtained by taking the cation that is situated in the Periodic Table between the *A* and *B* atoms. In the case of $CuInS_2$, the corresponding binary analogue would be $Zn_{0.5}Cd_{0.5}S$. Despite the similarity between the ternary compounds and their analogues, several differences exist in their structural and electronic properties. For example, the ternary materials present an absorption bandgap much lower than their analogues [90] (bandgap anomaly).

The crystal structure of the ternary chalcopyrite belongs to the space group $I\bar{4}2d$ (D_{2d}^{12}), with eight atoms per primitive unit cell. Chalcopyrite structure may be understood as a superlattice of the zincblende structure (T_d^2) with two atoms per unit cell. Because of the two different types of atoms in the unit cell, the volume of the chalcopyrite unit cell is four times larger than the zincblende one. Moreover, in the chalcopyrite cell each anion *C* is tetrahedrally coordinated by two atoms *A* and two atoms *B*, while each cation is coordinated by four anions *C*. There are three significant differences between the chalcopyrite and the

zincblende structures: the existence of two cation sublattices, the tetrahedral distortion and the anion displacement. The presence of two different cations in the structure leads to two different chemical bonds *A*-*C* and *B*-*C*, and in general, the bond lengths are different ($R_{AC} \neq R_{BC}$). As a result of the two types of cations, the tetragonal cell is distorted, and it is commonly defined the tetragonal distortion (*h*) as **c/2a**, where **a** and **c** correspond to the lattice parameters of the tetragonal unit cell. The anion displacement in the chalcopyrite structure is defined in terms of the structural parameter *u*, as:

$$u = \frac{1}{4} + \frac{R_{AC}^2 - R_{BC}^2}{a^2} \qquad \textbf{[Eq. 3. 1]}$$

In an ideal tetragonal cell, $u = ¼$. The bond lengths can be related to these two parameters by the following relations:

$$R_{AC} = a \cdot \sqrt{u^2 + \frac{1+h^2}{16}}$$

$$R_{BC} = a \cdot \sqrt{(u - ½)^2 + \frac{1+h^2}{16}} \qquad \textbf{[Eq. 3. 2]}$$

The following picture (*figure 3.1*) shows the $CuInS_2$ chalcopyrite unit cell, in which the different set of atoms in their corresponding positions can be appreciated.

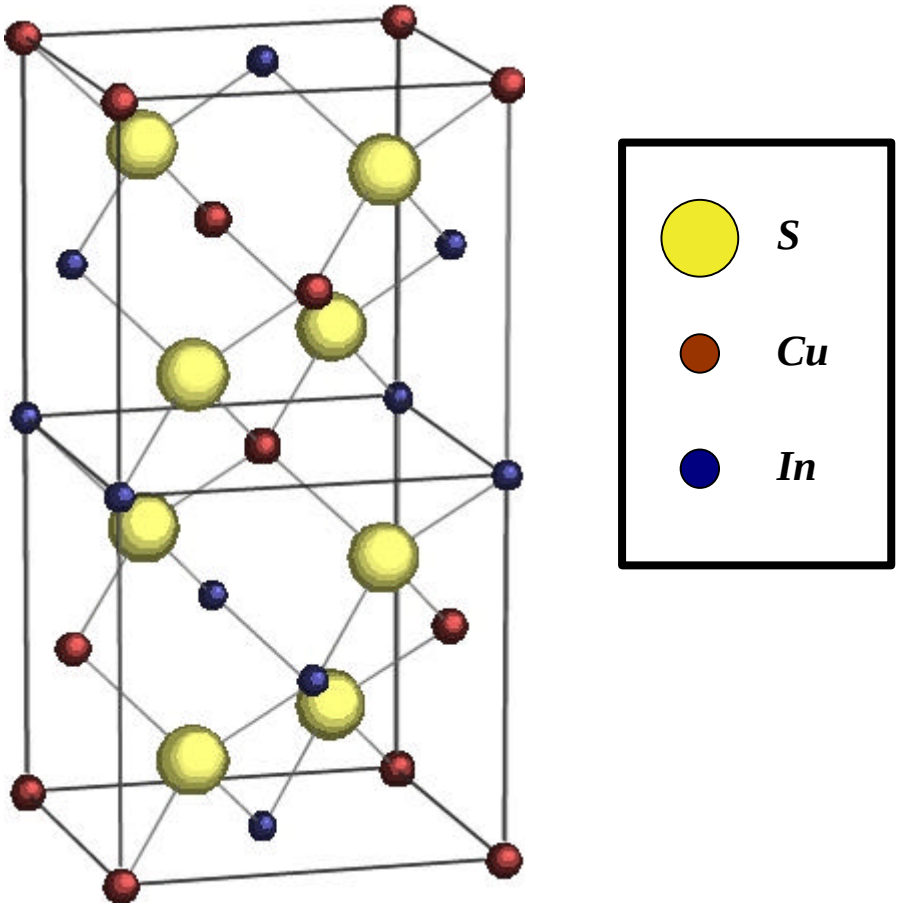

Figure 3. 1. Chalcopyrite body-centred tetragonal cell

The eight atoms per unit cell leads to 24 normal modes at the zone-centre (point G) of the Brillouin zone, and 21 optical phonons. Group theory may be used in order to classify the optical phonons according to their group symmetry. The positions of the basis atoms in the chalcopyrite structure are given by:

A_I : (0,0,0) A_{II} : (0, ½, ¼)
B_I : (½ ½ 0) B_{II} :(½ 0, ¼)
C_I : $(u, \frac{1}{4}, \frac{1}{8})$ C_{II} : $(\bar{u}, \frac{3}{4}, \frac{1}{8})$
C_{III} : $(\frac{3}{4}, u, \frac{1}{8})$ C_{IV} : $(\frac{3}{4}, \bar{u}, -\frac{1}{8})$ [Eq. 3. 3]

In the case of the $CuInS_2$ compound, the atoms of type *A* correspond to *Cu*, the atoms of type *B* to *In* and the atoms of type *C* to *S*. We will consider the case of an ideal chalcopyrite cell in which $u = ¼$. At the point G, the symmetry of the Brillouin Zone is given by the space group of the crystal. The chalcopyrite space group consists of eight symmetry operations, which may be arranged into five classes in the following way:

- Equivalence class: Including the identity operation $\{E|0\}$.
- Class related to the quaternary axis with inversion located along the *Z* axis of the crystal. This class includes the rotoinversion operation $\{S_{4Z}|0\}$ as well as its inverse operation $\{S_{4Z}^{-1}|0\}$
- The two C_2 screw axis placed along the directions *X+Y* and *X-Y* in the crystal give rise to an additional class. In this case, the symmetry operations include a non-lattice translational vector denoted by *f*, with $f = (½, 0, ¼)$: $\{C_{2X}|f\}$ and $\{C_{2Y}|f\}$.
- Class constituted by a C_2 axis along the *Z* axis of the crystal: $\{C_{2Z}|0\}$
- Class formed by two glide planes normal to the crystallographic directions *X+Y* and *X-Y*: $\{s_{XY} \mid f\}$ and $\{s_{X\bar{Y}} \mid f\}$.

In order to find the characters of the reducible representation for the normal modes of the chalcopyrite crystal, we will follow the factor group analysis procedure. Once the operations of the space group have been defined, we will consider the effect of applying each of these operations upon the different atomic displacement coordinates of the crystal basis. Now one should take into account that the positions in the crystal related by a translation of a lattice

vector are equivalent. The following table shows how each atom transforms into another:

	{E|0}	**{S_{4Z}|0}**	**{S_{4Z}^{-1}|0}**	**{C_{2Z}|0}**	**{C_{2X}|f}**	**{C_{2Y}|f}**	$\{s_{x\bar{Y}} \mid f\}$	**{s_{XY}|f}**
A_I	$x_1\, y_1\, z_1$	$\bar{y}_1\, x_1\, \bar{z}_1$	$y_1\, \bar{x}_1\, \bar{z}_1$	$\bar{x}_1\, \bar{y}_1\, z_1$	$x_2\, \bar{y}_2\, \bar{z}_2$	$\bar{x}_2\, y_2\, \bar{z}_2$	$\bar{y}_2\, \bar{x}_2\, z_2$	$y_2\, x_2\, z_2$
A_{II}	$x_2\, y_2\, z_2$	$\bar{y}_2\, x_2\, \bar{z}_2$	$y_2\, \bar{x}_2\, \bar{z}_2$	$\bar{x}_2\, \bar{y}_2\, z_2$	$x_1\, \bar{y}_1\, \bar{z}_1$	$\bar{x}_1\, y_1\, \bar{z}_1$	$\bar{y}_1\, \bar{x}_1\, z_1$	$y_1\, x_1\, z_1$
B_I	$x_3\, y_3\, z_3$	$\bar{y}_3\, x_3\, \bar{z}_3$	$y_3\, \bar{x}_3\, \bar{z}_3$	$\bar{x}_3\, \bar{y}_3\, z_3$	$x_4\, \bar{y}_4\, \bar{z}_4$	$\bar{x}_4\, y_4\, \bar{z}_4$	$\bar{y}_4\, \bar{x}_4\, z_4$	$y_4\, x_4\, z_4$
B_{II}	$x_4\, y_4\, z_4$	$\bar{y}_4\, x_4\, \bar{z}_4$	$y_4\, \bar{x}_4\, \bar{z}_4$	$\bar{x}_4\, \bar{y}_4\, z_4$	$x_3\, \bar{y}_3\, \bar{z}_3$	$\bar{x}_3\, y_3\, \bar{z}_3$	$\bar{y}_3\, \bar{x}_3\, z_3$	$y_3\, x_3\, z_3$
C_I	$x_5\, y_5\, z_5$	$\bar{y}_8\, x_8\, \bar{z}_8$	$y_7\, \bar{x}_7\, \bar{z}_7$	$\bar{x}_6\, \bar{y}_6\, z_6$	$x_5\, \bar{y}_5\, \bar{z}_5$	$\bar{x}_6\, y_6\, \bar{z}_6$	$\bar{y}_8\, \bar{x}_8\, z_8$	$y_7\, x_7\, z_7$
C_{II}	$x_6\, y_6\, z_6$	$\bar{y}_7\, x_7\, \bar{z}_7$	$y_8\, \bar{x}_8\, \bar{z}_8$	$\bar{x}_5\, \bar{y}_5\, z_5$	$x_6\, \bar{y}_6\, \bar{z}_6$	$\bar{x}_5\, y_5\, \bar{z}_5$	$\bar{y}_7\, \bar{x}_7\, z_7$	$y_8\, x_8\, z_8$
C_{III}	$x_7\, y_7\, z_8$	$\bar{y}_5\, x_5\, \bar{z}_5$	$y_6\, \bar{x}_6\, \bar{z}_6$	$\bar{x}_8\, \bar{y}_8\, z_8$	$x_8\, \bar{y}_8\, \bar{z}_8$	$\bar{x}_7\, y_7\, \bar{z}_7$	$\bar{y}_6\, \bar{x}_6\, z_6$	$y_5\, x_5\, z_5$
C_{IV}	$x_8\, y_8\, z_1$	$\bar{y}_6\, x_6\, \bar{z}_6$	$y_5\, \bar{x}_5\, \bar{z}_5$	$\bar{x}_7\, \bar{y}_7\, z_7$	$x_7\, \bar{y}_7\, \bar{z}_7$	$\bar{x}_8\, y_8\, \bar{z}_8$	$\bar{y}_5\, \bar{x}_5\, z_5$	$y_6\, x_6\, z_6$

Table 3. 1. Effect of the space group operations upon each atom in the basis.

Once the table of the transformations has been constructed, the determination of the reducible representation for each atom and for the whole atoms in the basis can be found straightforwardly. The characters for each class may be found by summing all the diagonal elements in the transformation matrix associated to each operation. Obviously, only the atoms remaining unchanged after the application of a given operation contribute to the trace of the matrix. As an example, consider the effect of the identity operation *{E|0}* upon the atoms in the basis. Provided that the identity operation leaves all the atoms at their original sites, one should count *one* for each coordinate of the basis atoms. This gives a character of 24 for the identity class in the reducible representation of the basis of the crystal. Consider now the operation *{C_{2Z}|f}*, that leaves the atoms *A* and *B* invariant, but permute the atoms *C* between themselves. Moreover, the *x* and *y* components of the translation vectors change their sign, while the *z* component remain invariant after the operation. Therefore, one should count *-1* for the four atoms remaining unchanged by the operation

{C_{2Z}|f}, and the total character for the class is *-4*. With these considerations, and operating in the same way for all the symmetry operations, one finds the characters of the reducible representation of the crystal (G_T), as well as the reducible representation for each atom in the basis (G_{Cu}, G_{In}, G_S). The following table summarises the results obtained:

	{E|0}	**{2S_{4Z}|0}**	**{C_{2Z}|0}**	**{2C_2|f}**	**{2s_d|f}**
G_{Cu}	2	2	2	0	0
G_{In}	2	2	2	0	0
G_S	4	0	0	4	0
G_T	24	-4	-4	-2	0

Table 3. 2. Characters of the reducible representation of the chalcopyrite crystal

The following step for determining the symmetry of the zone-centre phonons in the crystal is to decompose the reducible representation into irreducible representations. This can be done easily with the aid of the table of characters for the isomorphic point group of the crystal (D_{2d}), and with the orthogonality relations **[Eq. 2.27]**. The character table (*table 3.3*) of the point group D_{2d} includes five different types of irreducible representations: A_1, A_2, B_1, B_2 and E. Each representation is defined by their characters for each operation. All the representations in the group D_{2d} are single-degenerated, except the representation *E*, which is double-degenerated. Triple-degenerated representations do not exist in the point symmetry group of the crystal, due to the inequivalence of the *X*-*Y* and *Z* directions.

D_{2d}	{E}	$\{2S_4\}$	$\{C_2\}$	$\{2C_2'\}$	$\{2\sigma_d\}$		
A_1	1	1	1	1	1		x^2+y^2, z^2
A_2	1	1	1	-1	-1	R_z	
B_1	1	-1	1	1	-1		x^2-y^2
B_2	1	-1	1	-1	1	Z	xy
E	2	0	-2	0	0	(x,y); (R_x, R_y)	(xz, yz)

Table 3. 3. Table of characters for the point group D_{2d}

Thus, the result for the decomposition of the reducible representations is:

$$\Gamma_{Cu} = 1A_1 \oplus A_2$$
$$\Gamma_{In} = 1A_1 \oplus A_2$$
$$\Gamma_{S} = 1A_1 \oplus 1B_1 \oplus 1E$$
$$\Gamma_{T} = 1A_1 \oplus 2A_2 \oplus 3B_1 \oplus 4B_2 \oplus 7E \qquad \textbf{[Eq. 3. 4]}$$

The expression for Γ_T gives directly the irreducible representations at the centre of the Brillouin Zone. The acoustical and the optical modes are identified with the aid of the character tables. The result is:

$$\Gamma_{opt} = A_1 \oplus 2A_2 \oplus 3B_1 \oplus 3B_2 \oplus 6E$$
$$\Gamma_{ac} = B_2 \oplus E \qquad \textbf{[Eq. 3. 5]}$$

Acoustical modes in the chalcopyrite crystal are frequency split into a double degenerated *E* mode, associated to the equivalent crystallographic directions *X-Y*, and a single-degenerated B_2 mode, corresponding to the direction *Z*.

The correlation method provides a different way to determine the zone-centred phonons of a given crystal. Generally, this method is simpler and faster if the correlation tables between the site groups and the crystal point group are known [91]. In this case, the calculation of the normal modes just requires knowing the site symmetry of each atom in the lattice. Then, the irreducible representations of the site groups of the atoms must be correlated with the irreducible representation of the crystal. Therefore, it is not necessary to apply the symmetry operations upon the atoms in the basis, which greatly simplifies the problem in the cases of complex crystalline structures. In the case of the chalcopyrite structure, the *Cu* and *In* atoms occupy ***a*** Whyckoff sites (site symmetry S_4) and the anions occupy ***d*** sites (site symmetry C_2). With the information given in the tables of the groups the correlation diagram may be constructed:

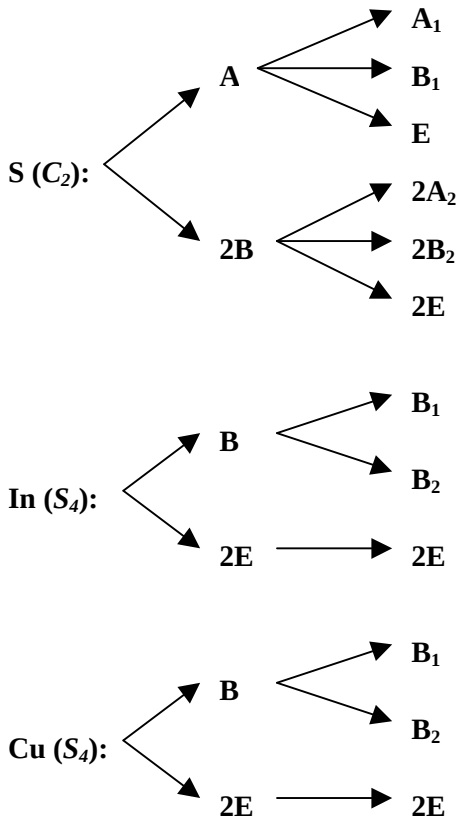

All the chalcopyrite optical modes are Raman active, except the A_2 modes that are "silent" (either infrared-active). Moreover, the B_2 and E modes present LO-TO splitting, due to their polar character. With all these considerations, the total number of different frequencies a priori detectable by Raman spectroscopy in a chalcopyrite compound is *22*. On the other hand, the zone-centre chalcopyrite modes maybe obtained from the folding of the Brillouin Zone of the zincblende structure [92, 93]. In this way, the zone-center modes of the chalcopyrite modes can be classified into three groups [94]. This may be helpful in order to classify and identify the different modes of a chalcopyrite material. Six modes arise from the Γ point, other six modes arise from the point **X** and the other twelve from the point **W** of the zincblende Brillouin Zone. Furthermore, different phenomenological models like the one proposed by Keating [95, 96], have been applied in order to fit the experimental data of chalcopyrite and pnictides compounds [97 - 100].

The determination of all the frequencies of a given chalcopyrite material usually requires the combination of Raman and Infrared spectroscopy. The great number of frequencies existing in each compound makes necessary to perform polarisation measurements on high quality oriented crystals. Koschel and Bettini have studied several chalcopyrite materials, including $CuInS_2$, and reported their corresponding Raman frequencies [101]. We have analysed a $CuInS_2$ high quality single crystal by Raman spectroscopy, in order to compare the data in the literature with our own data. The crystal has been grown by the Iodine Transport Method. Next figure shows the Raman spectrum obtained for this sample at room temperature.

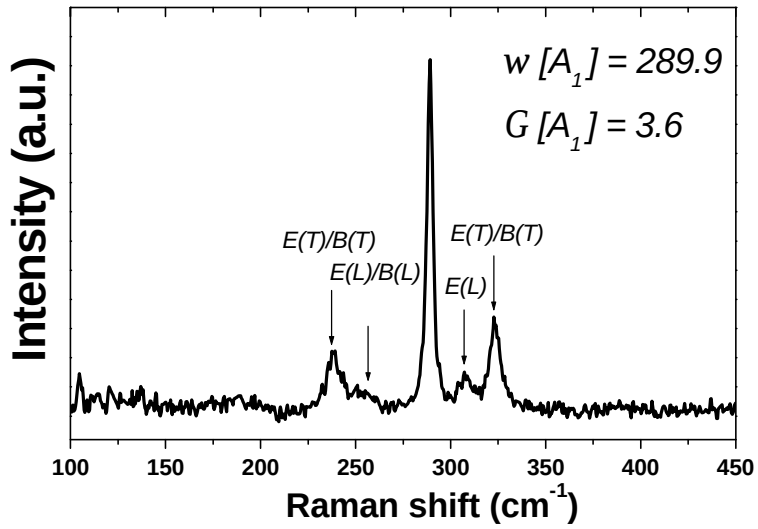

Figure 3. 2. Raman spectrum of a $CuInS_2$ single crystal.

Some remarks may be done on this spectrum. First, the spectrum has been obtained after three scans, recording the scattered light during 400 seconds in each scan. Despite the high integration time used for the measurements and the good quality of the crystal, the absolute number of counts obtained is rather low. This is due to the low Raman scattering efficiency of $CuInS_2$, which may be attributed to its high absorption coefficient (penetration depth for the green light is estimated [102] to be around *150 nm*). The low Raman intensity, together with the large number of bands in the spectra makes very difficult to identify most of the bands reported in the literature. B_1 modes are very low intense, similar to many longitudinal B_2 and E modes. Besides, B_2 and E modes overlap, which makes difficult to separate the corresponding transverse and longitudinal components. Finally, in the low frequency range of the spectra one should take into consideration the superposition of the chalcopyrite bands with those coming up from the excitation of the molecules in the air. The most intense mode in the spectrum corresponds to the totally symmetric vibration A_1, which appears at 290 cm^{-1}. The dominance of this mode in the spectrum is

characteristic of most of I-III-VI_2 chalcopyrite compounds. The frequency of the different modes obtained from the Raman spectra of the single crystal are listed in the following table. In the table it is included the values obtained by Koschel and Bettini [101] from polarisation measurements at 78 K:

Mode		**Koschel et al.**	**Experimental**
$E^{(1)}(L,T)$	$G_5[X_5]$	* / 67	
$B_1^{(1)}$	$G_3[W_2]$	*	
$B_2^{(1)}(L,T)$	$G_4[W_2]$	* / 79	
$E^{(2)}(L,T)$	$G_5[W_4]$	* / 88	
$E^{(3)}(L,T)$	$G_5[W_3]$	* / 140	
$B_1^{(2)}$	$G_3[X_3]$		
$E^{(4)}(L,T)$	$G_5[X_5]$	260 / 244	260 / 245
$B_2^{(2)}(L,T)$	$G_4[W_2]$	266 / 234	260 / 239
A_1	$G_1[W_1]$	294	290
$E^{(5)}(L,T)$	$G_5[W_4]$	314 / 295	308 / *
$B_1^{(3)}$	$G_3[W_2]$		
$E^{(6)}(L,T)$	$G_5[G_{15}]$	339 / 321	* / 324
$B_2^{(3)}(L,T)$	$G_4[G_{15}]$	352 / 323	

Table 3. 4. Raman active frequencies in $CuInS_2$.

Regarding the identification of the modes, it is worth to note that the totally symmetric modes may be easily distinguished by studying the depolarisation ratio of a polycrystalline sample. Moreover, this method avoids possible confusions and is more reliable than the criterion based on the relative intensities of the peaks (for example, in the case of $CuInTe_2$, the A_1 is not dominant) [103]. The depolarisation ratio for a given mode is defined as the

intensity ratio obtained for two different polarisation configurations: vertical-horizontal (*VH*) and horizontal- horizontal (*HH*). The two directions given in brackets refer to the polarisation of the incident light and the analysed scattered light with respect to the sample, respectively [104, 105]:

$$r = \frac{I(VH)}{I(HH)} \qquad \textbf{[Eq. 3. 6]}$$

It can be shown that for any non-totally symmetric mode, the value of **r** for a polycrystalline sample is ¾ independently of the symmetry properties of the mode. In the case of a totally symmetric mode (A_1 or A_{1g}), **r** has typical values between 0 and ¾ being identically zero for cubic crystals, for which the three components of the diagonal of the second-order Raman tensor are equal. In order to verify the symmetry of the mode at 290 cm^{-1}, it has been analysed the depolarisation ratio for a sequentially processed polycrystalline $CuInS_2$ sample. The spectra have been recorded using the macro-Raman configuration, in order to have a big enough spot light onto the sample to excite different grains (grain size in this sample was about 1 μm). The diameter of the beam has been estimated to be around 100 μm. Next figure shows the Raman spectra obtained on this sample for the two different experimental configurations:

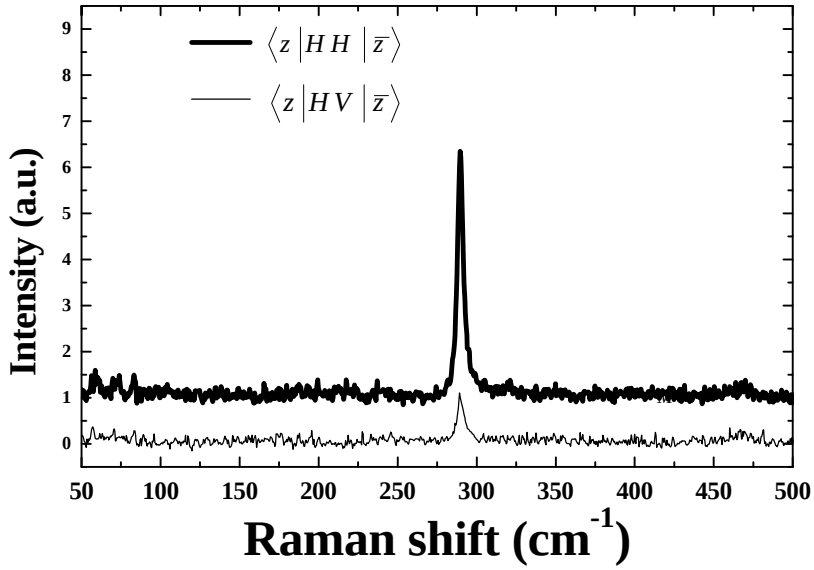

Figure 3. 3. Raman spectra of polycrystalline $CuInS_2$ in the VH and HH configurations.

The strong decrease in the intensity of the A_1 mode confirms the totally symmetric character of the mode. As expected for the tetragonal structure, the depolarisation ratio is above zero ($\rho = 0.19$) due to the different values of the diagonal elements in the Raman tensor. Moreover, it should be noted that the small deviations in the experimental configuration of the polarisators also result in a value of ρ slightly different from zero.

From the experimental results, it seems clear that the characterisation of polycrystalline $CuInS_2$ films by Raman spectroscopy is difficult if one wishes to analyse the behaviour of any other chalcopyrite Raman mode than the A_1 mode. Furthermore, the precise quantification of the spectral features of the rest of the modes would require polarisation measurements in different faces of the crystal, which, at practical level, is not possible in a polycrystalline material with crystal

size around 1 μm. According to this, the present work has paid special attention on the behaviour of the A_1 mode under different growth conditions of the films.

The totally symmetric mode in the chalcopyrite structure involves the alternative movement of all the anions in the *X*-*Y* crystallographic directions, while all the cations in the unit cell remain in rest. Atomic displacement coordinates can be obtained by applying the projector operator associated to the irreducible representation A_1 of the point group, upon the displacement vector:

$$p^{(A_1)}(f_i) = \frac{l^{(A_1)}}{h} \sum_R c_{(R)}^{(A_1)} \cdot R(f_i) \qquad \textbf{[Eq. 3. 7]}$$

The result obtained for the symmetry coordinates for the A_1 vibration is:

$$A_1: \; \boldsymbol{x_5 - x_6 + y_7 - y_8} \qquad \textbf{[Eq. 3. 8]}$$

The previous result indicates that the atom *5* (C_I) moves in the *X* direction, the atom *6* (C_{II}) moves in the -*X* direction, the atom *7* (C_{III}) in the *Y* direction and the atom *8* (C_{IV}) in the -*Y* direction, while all the cations remain at rest (see *figure 3.4*). The symmetry coordinates for the rest of the modes can be obtained by proceeding in a similar way, and have been already reported in the literature [106, 107]. All of them involve the combined movement of cations and anions in different directions.

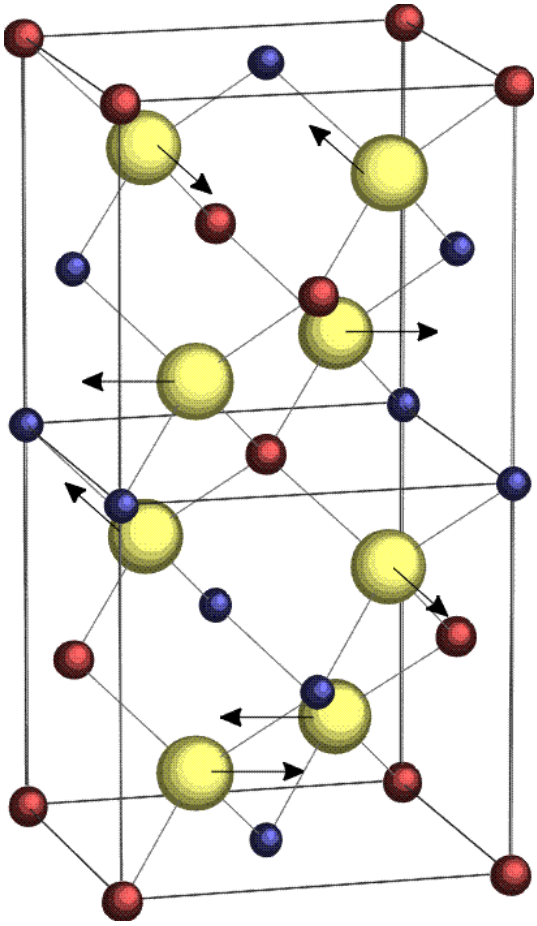

Figure 3. 4. Atomic displacements of the anions corresponding to the A_1 vibration.

The vibrational properties of the chalcopyrite compounds have been discussed by some authors. The simplest analytical approach for describing the dynamical behaviour of the chalcopyrite lattice is provided by the tetra-atomic linear chain model [100]. The normal modes of the linear chain with one atom of *Cu*, one atom of *In* and two atoms of *S* (see figure below) may be related with some of the normal modes of the chalcopyrite crystal.

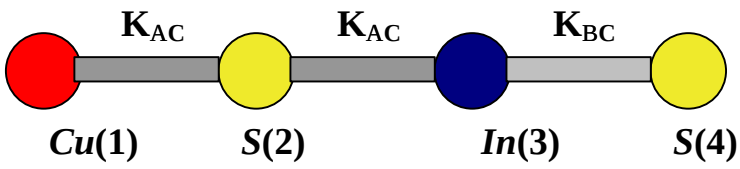

Figure 3. 5. Tetra-atomic linear chain model with two anions and two cations.

The frequency of the normal modes of the tetra-atomic linear chain may be easily obtained by solving the dynamical matrix of the crystal. In general, the dynamical matrix is given by [108, 109]:

$$D\left(\begin{smallmatrix} q \\ jl \end{smallmatrix}\right) = \sum_i f_{ab}\left(\begin{smallmatrix} i \\ jl \end{smallmatrix}\right) \cdot e^{-i\vec{q}\cdot\left[\vec{r}(i)+\vec{X}(j)-\vec{X}(l)\right]} \qquad \textbf{[Eq. 3. 9]}$$

where $\vec{r}(i)$ corresponds to the *i-essim* unit cell of the crystal, $\vec{X}(j)$ and $\vec{X}(l)$ refers to the position of the atoms *j* and *l* in the unit cell of the crystal and f_{ab} is given by:

$$f_{ab}\left(\begin{smallmatrix} i \\ jl \end{smallmatrix}\right) = \frac{1}{\sqrt{M_j \cdot M_l}} \cdot K_{ab}\left(\begin{smallmatrix} i \\ jl \end{smallmatrix}\right) \qquad \textbf{[Eq. 3. 10]}$$

where M_j and M_l are the atomic masses of the atoms *j* and *l*, and K_{ab} are the force constants between the atoms *a* and *b*. At $\vec{q} = 0$, the dynamical matrix is a real matrix, and for the tetra-atomic linear chain is written as:

$$D_{ij}^{q=0}=\begin{pmatrix} \frac{2K_{AC}}{m_A} & \frac{-K_{AC}}{\sqrt{m_A\cdot m_C}} & 0 & \frac{-K_{AC}}{\sqrt{m_A\cdot m_C}} \\ \frac{-K_{AC}}{\sqrt{m_A\cdot m_C}} & \frac{K_{AC}+K_{BC}}{m_C} & \frac{-K_{BC}}{\sqrt{m_B\cdot m_C}} & 0 \\ 0 & \frac{-K_{BC}}{\sqrt{m_B\cdot m_C}} & \frac{2K_{BC}}{m_B} & \frac{-K_{BC}}{\sqrt{m_B\cdot m_C}} \\ \frac{-K_{AC}}{\sqrt{m_A\cdot m_C}} & 0 & \frac{-K_{BC}}{\sqrt{m_B\cdot m_C}} & \frac{K_{AC}+K_{BC}}{m_C} \end{pmatrix} \qquad \textbf{[Eq. 3. 11]}$$

It can be easily verified that the displacement vector *(0 –1 0 1)* is an eigenvector of the dynamical matrix with eigenvalue given by:

$$w^2=\frac{K_{AC}+K_{BC}}{m_C} \qquad \textbf{[Eq. 3. 12]}$$

This normal mode corresponds to the anti-phase motion of the *S* atoms against the corresponding cations, which corresponds to the A_1 vibration in the chalcopyrite three-dimensional lattice. This relation indicates that the frequency of this phonon depends directly on the atomic mass of the anion, which can be easily understood if we notice that only the anions are involved in the movement, while the cations remain at rest. Moreover, because of the dependence on the force constants, the position of this mode directly depends on the atoms surrounding the anions. Although the relation has been obtained using a very simple model, experimental results based on the comparison of different chalcopyrite materials have shown its validity. For example, Matsushita et al. found [110] that the position of the A_1 mode in two chalcopyrite compounds ABC_2 and ABZ_2 can be related by:

$$\frac{w[ABC_2]}{w[ABZ_2]} = \sqrt{\frac{m_Z}{m_C}} \qquad \textbf{[Eq. 3. 13]}$$

Moreover, in the case of chalcopyrites with the same anion and different cations (ABC_2 and XYC_2), the relation between their respective frequencies was found to be:

$$\frac{w[ABC_2]}{w[XYC_2]} = \sqrt{\frac{m_X + m_Y}{m_A + m_B}} \qquad \textbf{[Eq. 3. 14]}$$

Equation **[Eq. 3.14]** just indicates that for cations with higher atomic masses, the corresponding atomic force constant decrease due to the larger atomic distance between the anions and the cations.

On the other hand, Neumann developed [111] a simplified Keating model, neglecting the bond-bending contributions, which lead to analytical expressions for the vibrational modes of the chalcopyrite structure. Neumann found for the A_1 mode a result consistent with **[Eq. 3.12]**:

$$w^2(A_1) = \frac{2\cdot(a_{AC} + a_{BC})}{m_C} \qquad \textbf{[Eq. 3. 15]}$$

Here, a_{AC} and a_{BC} are the bond-stretching constants between the corresponding atoms.

These expression may be useful for the interpretation of the Raman spectra of ternary chalcopyrites [103, 112], or for the interpretation of the vibrational properties of quaternary chalcopyrite alloys [113].

3.2. Chemical properties and polymorphism in $CuInS_2$

The equilibrium diagram of the ternary system Cu-In-S is only partially known, due to its high complexity. Much more experimental work has been devoted to the study of the chemical properties of $CuInSe_2$. However, it is extremely important to have an as accurate as possible knowledge about the chemical phases that may arise as a consequence of stoichiometric deviations. Gibbs phase triangle for the Cu-In-S system at room temperature was reported by Metzner et al [114, 115], and is reproduced in *figure 3.6*:

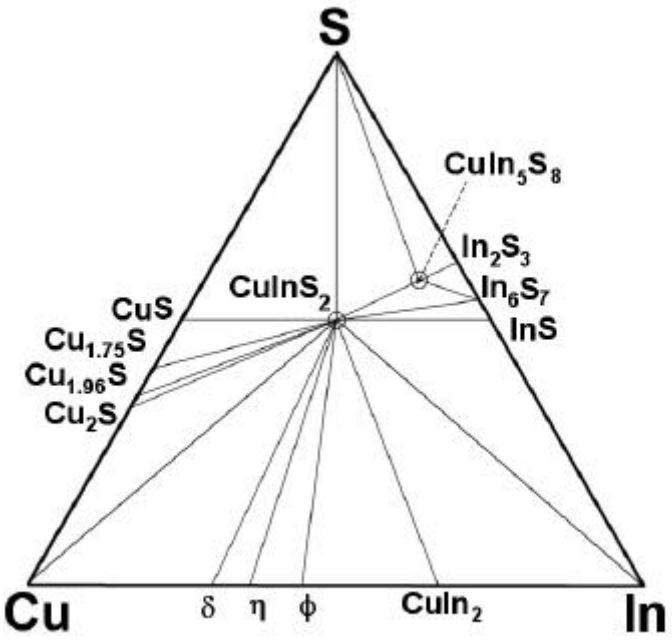

Figure 3. 6. Gibbs diagram of the ternary Cu-In-S system

The Gibbs diagram shows the existence of various quasi-binary lines between the $CuInS_2$ and other phases, indicating the possible coexistence of $CuInS_2$ with other compounds at thermodynamical equilibrium. As can be appreciated in the figure, several binary sulphides and metal phases exist along the boundaries of the diagram. In the Cu-S line, the stable phases at room temperature are found to be CuS, Cu_2S, $Cu_{1.96}S$ and $Cu_{1.75}S$. For the binary system In-S, In_2S_3, InS and In_6S_7 constitute the equilibrium phases. In the case of the Cu-In inter-metallic compounds, the phases δ (Cu_7In_3), η ($Cu_{16}In_9$), ϕ ($Cu_{11}In_9$) and $CuIn_2$ have been reported. Moreover, experimental results indicate [116, 117] that the only ternary compounds that are stable at room temperature are the chalcopyrite phase of $CuInS_2$ and the cubic spinel $CuIn_5S_8$. This is a remarkable difference with respect to the Cu-In-Se system, for which the presence of the so-called "Ordered Vacancy Compounds" (OVC), like $CuIn_3Se_5$ and $CuIn_2Se_{3.5}$, has been reported by several authors [118 - 123]. The formation of these phases in $CuInSe_2$ is due to the extremely low formation energy of the complex defect involving one *In* anti-site and two *Cu* vacancies $(In_{Cu}^{2+} + 2V_{Cu}^{-})$. The periodic repetition of this defect across the crystal leads to the formation of these unusual complex structures [124]. In the case of the sulphur system, it is not clear whether this phase exists, although this possibility has not been completely excluded [125].

In addition to the different equilibrium phases that may form as a result of changes in the stoichiometry of the material, special considerations must be done with respect to the crystalline phase of $CuInS_2$ itself. It is well-established that some ternary tetrahedral semiconductors exhibit order-disorder transitions [126] as a function of the temperature, and this is the case of $CuInS_2$. For temperatures above the transformation temperature T_C (typically [127] between 800-1300 K), the chalcopyrite ordered phase $(I\bar{4}2d)$ reversibly transforms into a zincblende-like structure $(F\bar{4}3m)$. In the disordered structure, the cations *A* and *B* are randomly distributed in the cation sublattice, and the tetragonal cell becomes cubic. This transformation is characteristic of many chalcopyrite compounds, but not all of them present this order-disorder transformation.

When the tetragonal structure is too strained, the energy associated to the entropy gain in the order-disorder transformation ($-T\cdot\Delta S$) is not enough to compensate the destabilising microscopic strain, which is substantially bigger in the disorder phase. As a result, compounds with large anion displacement parameters $(u_c > 0.265)$ or with high tetragonal compression $\left(\frac{c}{a} < 1.95\right)$ melt before this transformation occurs [128]. The transformation temperature for $CuInS_2$ is found to be 1253 K, and the energy gap of the disordered phase is about 0.5 eV lower than the gap of the ordered phase [129]. This temperature is well below the melting point of $CuInS_2$, which is at 1364K. At 1318 K another solid state transformation occurs from the zincblende structure to an hexagonal wurtzite one [116].

Order-disorder transformation is not the only striking feature with respect the structure of $CuInS_2$. Although the $A^{I}B^{III}C^{VI}_2$ compounds normally crystallise in the chalcopyrite structure, other crystalline structures in accordance with the Grimm-Sommerfeld rule may exist (the average number of valence electrons per atom must be 4). Accomplishing this rule, different structures can be obtained by changing the stacking sequence of the cations. For example, chalcopyrite structure may be derived by re-arranging the *Cu* and *In* atoms in the sphalerite structure, into alternate atomic planes following the $[1\,0\,2]$ direction of the cubic zincblende lattice. Cation stacking sequences in the $[0\,0\,1]$ and $[111]$ directions leads to the so-called "Copper-gold" (Cu-Au) and "Copper-Platinum" (Cu-Pt) structures. The names come from the fact that the cations in the corresponding sublattice are arranged as the atoms in the corresponding metallic super-structures. Wei et al. [127] listed the different possible structures derived from the zincblende by re-ordering the cations, and calculated their formation energy for $CuInSe_2$. The apparition of these different types of ordering depends on their formation energy, which are determined by the chemical properties of the atoms in the ABC_2 compound. When the formation energy of one of these cation orderings is not too different with respect to the chalcopyrite one, the crystal growth at $T<T_C$ may result in the formation of

metastable domains into the crystal with different short-range order. In fact, the coexistence of chalcopyrite and Cu-Au ordered domains in $CuInS_2$ and $CuInSe_2$ has been predicted and observed in $CuInS_2$ epitaxial films by several authors [130 - 132], using Transmission Electron Diffraction (TED) and High Resolution Transmission Electron Microscopy (HRTEM). Other cation stacking sequences seem to be much less favourable in these compounds. Theoretical calculations [133] predict that the difference between the formation energy between chalcopyrite and the Cu-Au ordering in $CuInS_2$ and $CuInSe_2$ is only of about 2 meV/atom, which results in a high probability for the formation of Cu-Au domains. In some epitaxial films grown under certain conditions, the Cu-Au ordering has been found to dominate with respect to the chalcopyrite ordering [134, 135]. The crystal structures corresponding to the chalcopyrite $\left(I\bar{4}2d\right)$ and Cu-Au ordered $\left(P\bar{4}m2\right)$ phases of the $CuInS_2$ are depicted in the following figure:

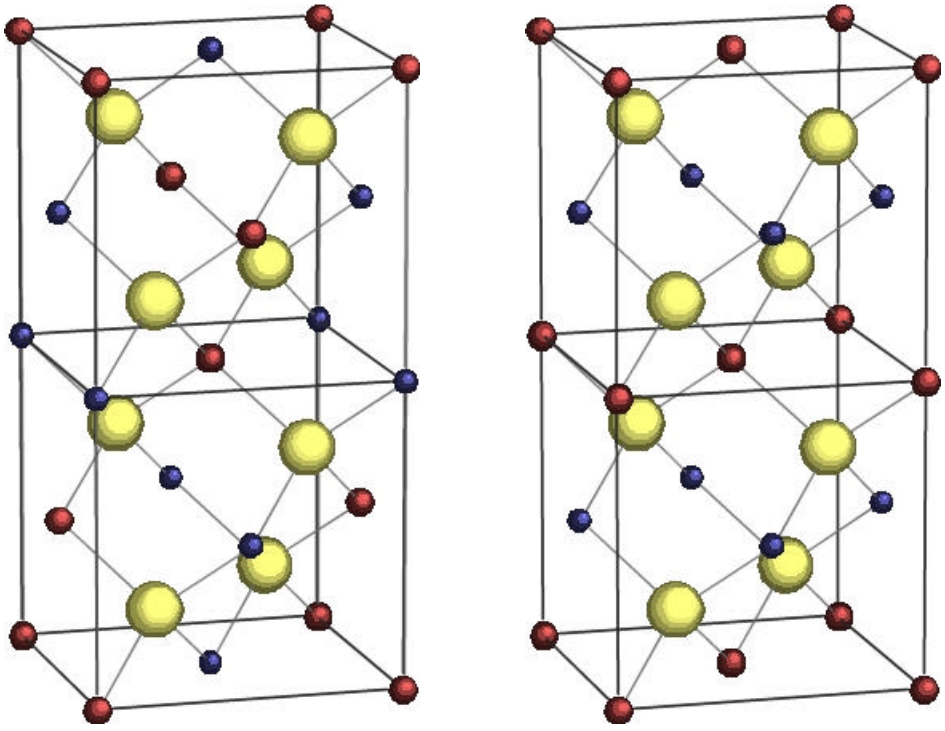

Figure 3. 7. Chalcopyrite (left) and Cu-Au (right) ordered $CuInS_2$ cells.

As shown in this section, the characterisation of polycrystalline $CuInS_2$ may not be straightforward at all. On one hand, stoichiometric deviations may lead to the formation of complex phases in the Cu-In-S ternary diagram, difficult to identify even by XRD. Besides, $CuInS_2$ present intrinsic difficulties related to its complex structural modifications.

3.3. Experimental results

3.3.1. Additional Raman bands in $CuInS_2$

Although the Raman spectra and the vibrational properties of an ideal chalcopyrite $CuInS_2$ single crystal are already well understood, there are some aspects regarding the vibrational properties of $CuInS_2$ films (poly and epi) that have not been explained yet [136]. With the development of the thin film photovoltaic technology, a growing interest appeared in relation to the characterisation of the chalcopyrite materials and related processes. Until only some years ago, most of the few works concerning chalcopyrite thin film characterisation dealt with $CuInSe_2$. This compound presents some properties that are common to the $CuInS_2$ ones. Both crystallise in the chalcopyrite structure, and in the case of the $CuInSe_2$, the A_1 vibrational mode appears at lower frequencies (173 cm^{-1}) due to the larger mass of the anion. For the $CuInSe_2$ technology, it became soon very important to develop experimental techniques in order to control carefully the film stoichiometry, due to its strong influence on the device performance. In 1989 Yamanaka et al. reported [137] the Raman characterisation of $CuInSe_2$ films, including the study of the effect of the chemical composition on the spectra. At that time, they found two important features in the spectra. For films highly *In*-rich, an additional band at about 150 cm^{-1} appeared in the spectrum, while for *Cu*-rich films a band at 183 cm^{-1} was identified. Neither of these bands can be assigned to chalcopyrite zone-centre modes. While the mode at 150 cm^{-1} has been already assigned [138] to an OVC, probably $CuIn_3Se_5$, the origin of the mode at 183 cm^{-1} has not been unambiguously established up to now. In that moment, the complexity of the ternary system made very difficult a clear and univocal assignment of the mode to any crystalline phase.

In a similar way, the study of polycrystalline $CuInS_2$ films lead to the detection of an additional not-chalcopyrite band at 305 cm^{-1}, which was reported by Morell et al [125]. In that study, the presence of this band was found to be characteristic of *In*-rich films, and they assigned this band to the defect spinel compound β-In_2S_3. This assignment is thought to be incorrect [139], because the defect spinel compound has many other intense Raman-active modes [140], which are not visible in the spectra reported in this study.

In our characterisation work, we have found this additional band at about 305 cm^{-1} in samples grown under different conditions. The details of the behaviour of the mode, and its dependence on the growth conditions will be extensively analysed in the next chapter. It will also be shown the importance of this mode for the characterisation of the film structural properties. In fact, the apparition of this mode is always accompanied by a structural worsening of the chalcopyrite phase, as well as a worsening of the final solar cell device. As an example, next figure shows a Raman spectrum of a polycrystalline $CuInS_2$ *Cu*-poor film in which the additional band at about 305 cm^{-1} can be clearly distinguished.

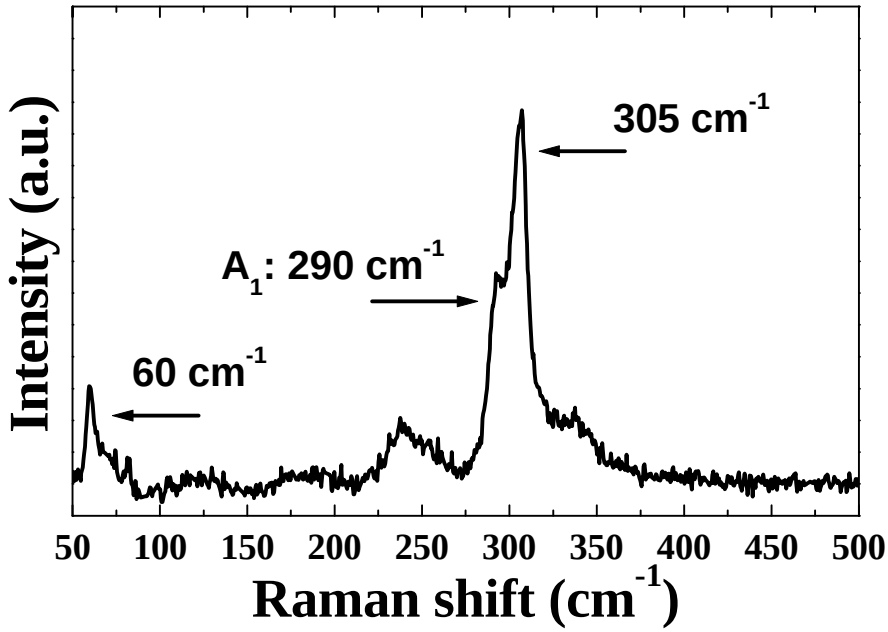

Figure 3. 8. Raman spectra of a polycrystalline Cu-poor film showing the presence of the additional mode at 305 cm^{-1}.

Notice also that together with the band at about 305 cm^{-1}, an additional low-frequency band appears at about 60 cm^{-1}. Both bands may have a related origin, since they have always been observed together. However, it is difficult to establish a reliable correlation between their intensities, mainly due to the low intensity of the low frequency band, and its overlapping with other bands. Anyway, the analysis Raman spectra obtained from different $CuInS_2$ thin films seems to point out a correlation between the intensity of both modes (see next figure).

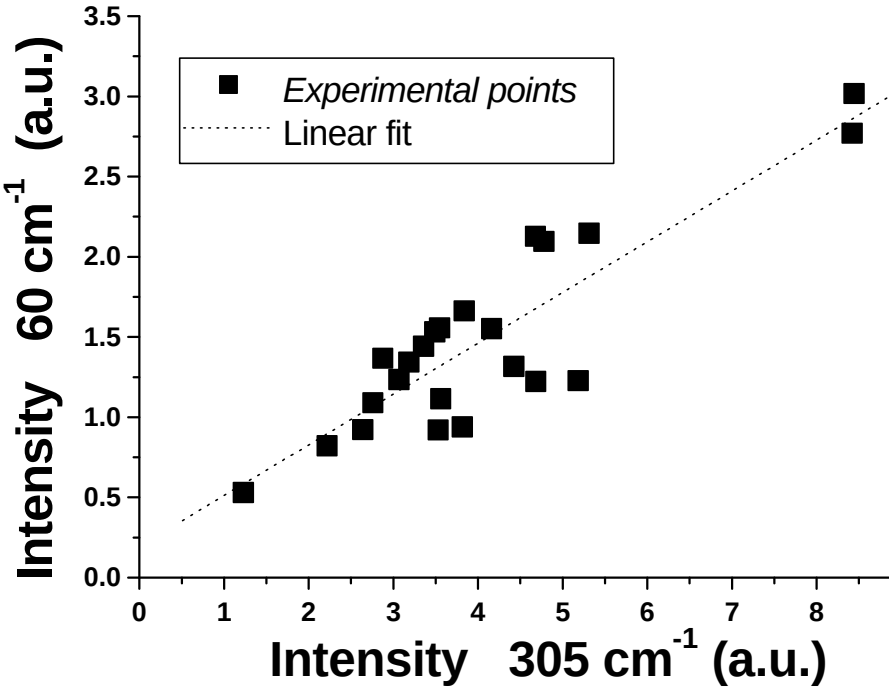

Figure 3. 9. Relation between the maximum intensity of the additional Raman bands in $CuInS_2$ thin film spectra.

Since these additional bands have been detected in $CuInS_2$ and $CuInSe_2$, the same origin has been suggested for both of them. An especial interesting consideration was given by K. Kondo et al [141]. These authors studied polycrystalline samples of $CuInS_2$ and $CuInSe_2$, and compared the frequency ratio between the chalcopyrite A_1 mode and the additional modes appearing in both compounds. The result in both cases was:

$$\frac{w(A_1^{CISe}) = 173\,cm^{-1}}{w'_{CISe} = 183\,cm^{-1}} \approx \frac{w(A_1^{CIS}) = 292\,cm^{-1}}{w'_{CIS} = 307\,cm^{-1}} \approx 0.95$$

This similar frequency ratio was interpreted as a strong indication for a common origin of the additional modes in the two compounds. They tentatively assigned these additional bands to localised phonons involving some defective chalcopyrite structure.

When this moment was started, there existed several interpretations regarding these modes. As already mentioned above, first interpretations [125, 142] in $CuInS_2$ dealt with an origin related to the presence of the defect spinel phase β-In_2S_3. In a similar way, for the case of $CuInSe_2$, the observation of the additional band in *Cu*-rich film was interpreted [137, 143] as an indication of this mode to be related to a *Cu*-rich phase. In the recent years, some authors attributed the presence of these modes to disorder effects in the chalcopyrite structure. For example, S. Shirakata [144, 145] et al. suggested the 183 cm^{-1} mode in $CuInSe_2$ to be related to a sphalerite-ordered phase. Finally, other authors [141, 146] attribute these bands not to crystalline phase, but to a local phonon related to some local arrangement, probably involving an *In*-rich configuration.

3.3.2. Polarisation measurements

Due to the lack of a clear interpretation of these modes, and their importance for the understanding of the structural properties of the $CuInS_2$ films, we have performed a detailed characterisation of the properties of these modes. As will be described in *chapter 4*, our results [147] show that, in terms of the performance of solar cell devices, the 305 cm^{-1} mode in $CuInS_2$ is characteristic of bad quality $CuInS_2$ films. The mode appears in polycrystalline samples grown under *Cu*-poor conditions, but also on *Cu*-rich samples grown at low substrate temperatures. Furthermore, the mode also appears in epitaxially grown $CuInS_2$. The fact that this mode appears in both *Cu*-rich and *Cu*-poor films under certain growth conditions suggests that the origin is not clearly related to a phase with different stoichiometry, but to a phase with different crystallographic structure.

In this sense, it is not clear at all that a well-known *In*-rich phase could be responsible for the apparition of these additional bands. On one hand, the Raman spectra of well-known *In*-rich equilibrium phases (InS, In_2S_3 or $CuIn_5S_8$) are different enough to those experimental observed. Therefore, this hypothesis can be ruled out. Besides, if a more complex phase such as $CuIn_3S_5$ or $CuIn_2S_{3.5}$, is present in our samples, their zone-center phonons should not include a totally symmetric mode appearing at higher frequencies than that of the A_1 of the $CuInS_2$ chalcopyrite phase. Consider as an example the analogy with the ternary system *Cu-In-Se*. As discussed in *section 3.2*, the *In*-excess is accommodated in the chalcopyrite $CuInSe_2$ lattice by the introduction of periodic In_{Cu} anti-sites, which at the same time induce the formation of V_{Cu} that keep the electronic neutrality of the crystal. As a result, a chalcopyrite-related structure is obtained [118] (space group is probably $P\bar{4}2c$), and the reported Raman spectra of these OVC compounds is characterised by a dominant totally symmetric mode appearing at lower frequencies with respect to the A_1 mode of the $CuInSe_2$ chalcopyrite phase [138]. The reason for this is that, despite the $\boldsymbol{In_{Cu}}$ anti-sites should induce a hardening of the anion bonds, the loose of bonds due to the two $\boldsymbol{V_{Cu}}$ introduced for each $\boldsymbol{In_{Cu}}$ anti-site lead to a lowering of the effective force constant for the A_1 mode in this structures. Equation **[Eq. 3.15]** has been used in order to estimate the frequency of the A_1 mode for a chalcopyrite-related structure with a certain number of unoccupied sites, with excellent agreement with the experimental findings in *Cu-In-Se*, *Cu-Ga-Se* and *Cu-In-Te* systems [148 - 150].

In order to gain some insight in the origin and the properties of the mode, polarisation measurements were carried out on epitaxial $CuInS_2$ samples. Samples have been grown at the Hahn-Meitner-Institut of Berlin. They have been obtained by hetero-epitaxial growth of $CuInS_2$ onto [111] oriented *Si* substrates, by co-evaporation of *Cu* and *In* in a low-pressure sulphur atomosphere [151] (about 10^{-5} torr). Substrate temperature during coevaporation was hold at 400ºC. The Si substrates were previously cleaned following an oxidation process in an H_2SO_4 and H_2O_2 solution, and a posterior treatment in

NH_4F for the removal of the oxide layer [152]. Three epitaxial samples with different *In*/(*In+Cu*) contents have been analysed. Micro-Raman spectra of all of the samples show the presence of the additional bands at 305 cm^{-1} and at 60 cm^{-1}, independently of the composition. Moreover, the chalcopyrite bands can also be distinguished, specially the A_1 at about 290 cm^{-1}. *Figure 3.10* shows the not-polarised Raman spectra of these three samples, together with their estimated composition according to EDX analysis.

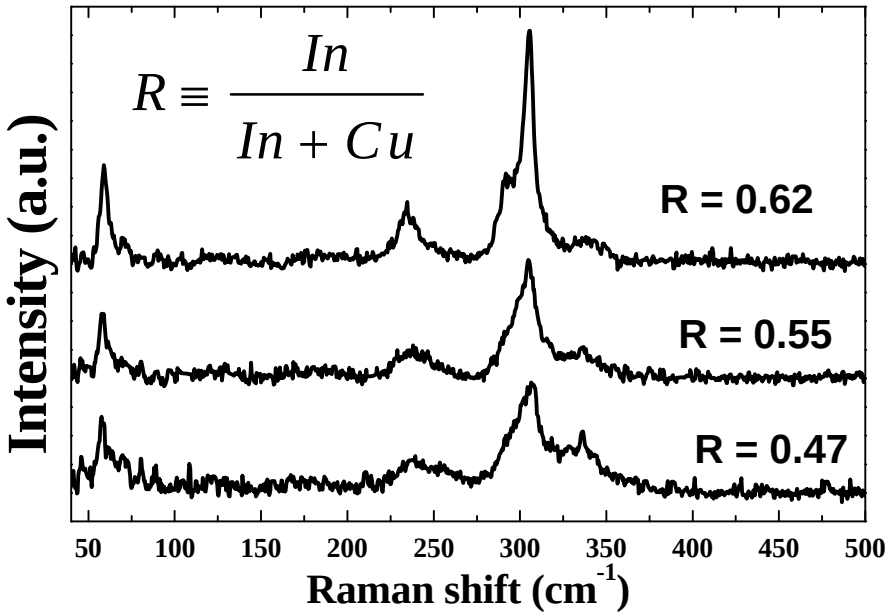

Figure 3. 10. Not-polarised Raman spectra of $CuInS_2$ epitaxial films with different *In/(In+Cu)* contents.

Polarisation measurements have been performed at these samples in different configurations. Let the incident (z) and scattered ($\bar{z}$) directions be defined in reference to the sample orientation. Therefore, respect the $CuInS_2$ tetragonal lattice, the z direction corresponds to the $[221]$ direction. We have chosen two perpendicular directions in the sample plane (x' and y') defined by the

tetragonal directions $[1\bar{1}0]$ and $[11\bar{1}]$, respectively. Selection rules for the A_1 symmetric mode are defined by the corresponding second order Raman tensor, given by:

$$R_{ij}(A_1)=\begin{bmatrix} a & 0 & 0 \\ 0 & a & 0 \\ 0 & 0 & c \end{bmatrix} \qquad \textbf{[Eq. 3. 16]}$$

Therefore, it is clear that the A_1 mode is allowed for the $\langle z|x'x'|z\rangle$ and $\langle z|y'y'|z\rangle$ geometries, while it is forbidden for the $\langle z|x'y'|z\rangle$ and $\langle z|y'x'|z\rangle$ configurations. In *figure 3.11* two micro-Raman spectra performed at the sample with higher *In* content, for an allowed and a forbidden configuration are shown. Similar results have been obtained for the samples with other compositions.

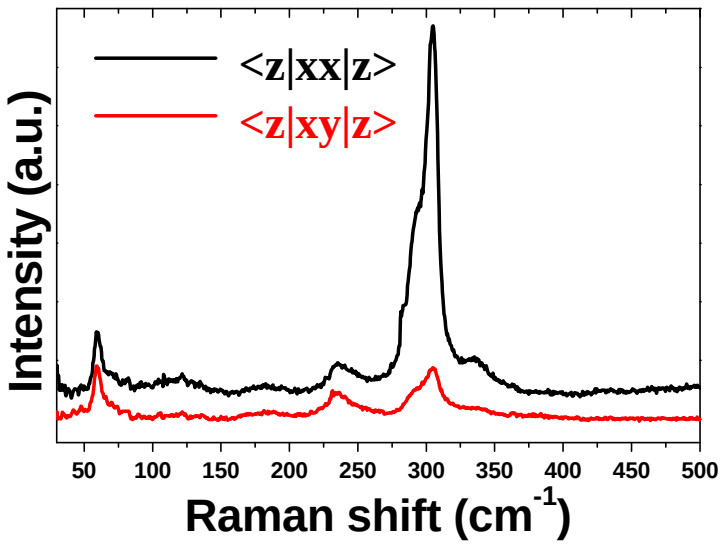

Figure 3. 11. Polarised micro-Raman spectra in two configurations (A_1 -allowed and A_1 -forbidden), for the sample with *In/(In+Cu)* = 0.62

As can be appreciated in the previous figure, the intensity of both the A_1 chalcopyrite mode and the additional band at 305 cm^{-1} strongly decrease in the forbidden configuration. It is worth to notice that although both modes do not completely disappear in the forbidden configuration, the change in the relative intensity of both modes suggests both modes to have the same symmetry. The presence of defects in the material should be responsible for the observation of the forbidden bands. In order to confirm this result, other configurations have been checked. The results are in good agreement with the symmetry assignment to the 305 cm^{-1} mode. Moreover, the totally symmetric character of the mode at 305 cm^{-1} has been corroborated by studying the depolarisation ratio on polycrystalline samples.

On the other hand, *Figure 3.11* shows the existence of a different behaviour of the band at 60 cm^{-1}, which shows almost the same intensity for both configurations. This indicates that the low frequency mode is not totally symmetric.

For comparison, we have performed polarisation measurements on $CuInSe_2$ epitaxial samples. Samples have been grown following the same procedure as that described for the growth of the $CuInS_2$ epitaxial ones using *Se* gas instead of *S*. The results indicate that also in this case, the additional high frequency band at 183 cm^{-1} behaves in the same way that the A_1 chalcopyrite mode at 173 cm^{-1}. This experimental result supports the idea of Kondo [141] et al. that the additional modes in $CuInS_2$ and $CuInSe_2$ have the same origin. *Figure 3.12* shows the micro-Raman spectra for an epitaxial $CuInSe_2$ in two different configurations (A_1 allowed and forbidden). In this figure, the additional band at 183 cm^{-1} is only visible as a shoulder at higher frequencies of the A_1 chalcopyrite mode. Moreover, the line-shape analysis of the peaks clearly indicates the existence of a high frequency contribution.

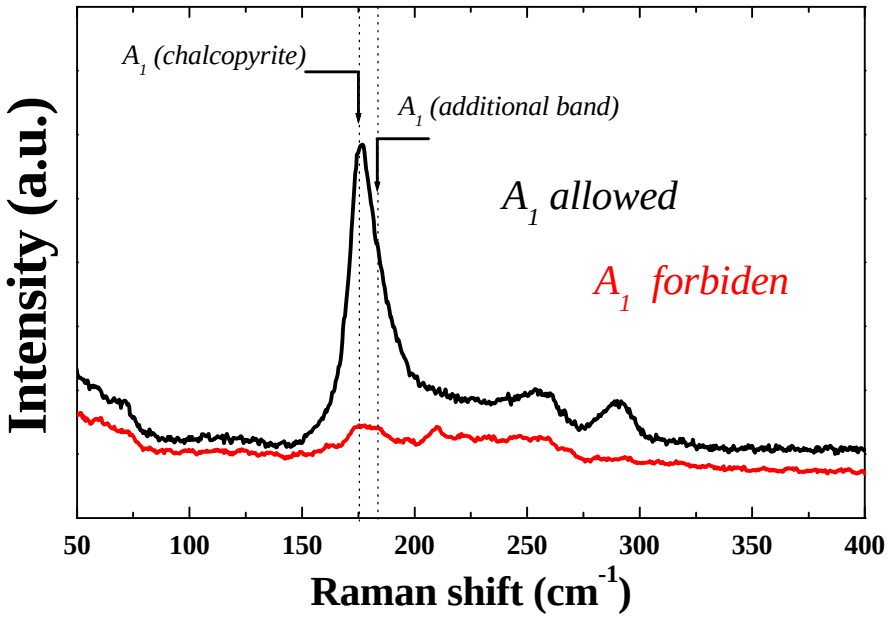

Figure 3. 12. Polarisation micro-Raman spectra on an $CuInSe_2$ epitaxial sample.

The totally symmetric character of the 305 cm^{-1} mode rules out a possible relation of this mode with a zone-centre mode of the sphalerite-like phase of $CuInS_2(Se_2)$.

3.3.3. XRD/Raman measurements

In the previous section of this chapter, the properties of the additional bands in the Raman spectra of $CuInS_2$ and $CuInSe_2$ have been presented, and their symmetry properties have been established. This section presents the experimental results that strongly relate the presence of these modes in $CuInS_2$ with the Cu-Au ordered phase. In order to show this, a bigger set of $CuInS_2$ epitaxial samples have been analysed. Epitaxial samples have been grown on

[111] and [001] oriented *Si* substrates by coevaporation using different growth conditions, i.e. different stoichiometry during growth and substrate temperature, in order to obtain a set of samples with a variation in the relative intensity of the additional Raman modes. As an example, next figure shows the Raman spectra corresponding to two different samples of this set. One of the spectra corresponds to a sample grown under *Cu*-rich conditions (spectrum labelled "***a***") while the other one corresponds to a film grown under *Cu*-poor ones (spectrum "***b***"). In both cases, despite the different growth stoichiometry, the additional Raman modes at 305 cm^{-1} and also the less intense band at 60 cm^{-1} can be discerned. Notice that the relative intensity of the additional bands with respect to the intensity of the chalcopyrite A_1 mode change as a result of the different growth parameters.

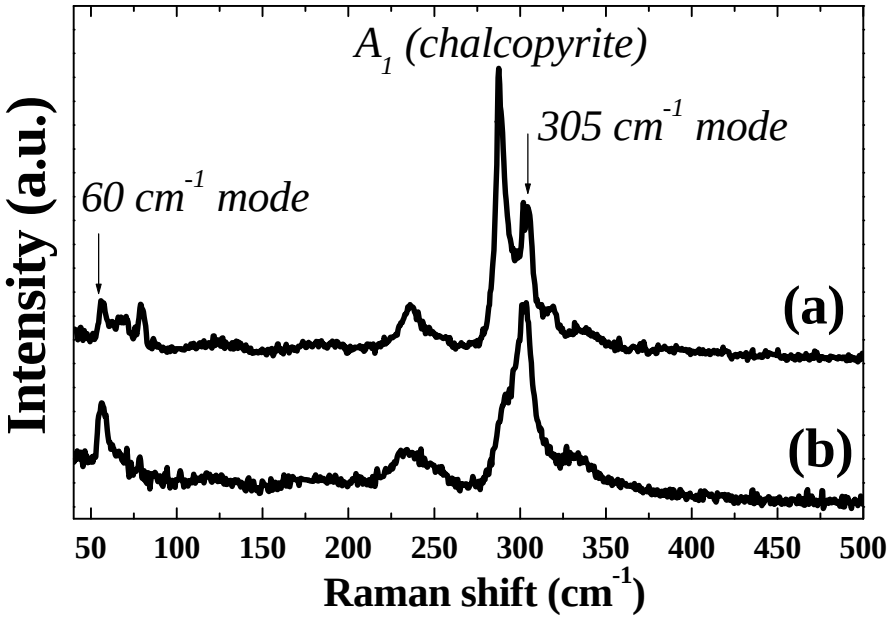

Figure 3. 13. Raman spectra of two $CuInS_2$ epitaxial samples with different growth stoichiometry.

This set of samples has been analysed by different techniques, for the obtaining of experimental evidences for the existence of a direct relationship between the additional modes and the Cu-Au content in the samples. Transmission Electron Diffraction (TED) results will be given first, which show the existence of Cu-Au ordered domains in the $CuInS_2$ epitaxial layers. Afterwards, results based on X-Ray Diffraction (XRD) measurements will confirm the presence of Cu-Au ordering in the samples. Moreover, they will show the existence of a linear correlation between the relative intensity of the additional Raman mode and the estimated amount of Cu-Au ordered phase in the epitaxial films.

TED patterns on epitaxial $CuInS_2$ on [111] oriented *Si* substrates have been obtained with a Philips CM30 Transmission Electron Microscope. The samples have been prepared for cross section TEM observation in several directions. In the next figure, two TED patterns corresponding to two different points of one epitaxial sample of this set are presented. This sample was prepared for its observation in the $[1\bar{1}0]$ direction. The left image shows a chalcopyrite pattern with the reflections at (004), (220), and (112). The presence of Cu-Au ordering is indicated in the right diffraction pattern by the appearance of additional weak spots labelled (002) and (110). These spots are expected for Cu-Au ordering in this zone axis, but not for the chalcopyrite ordering.

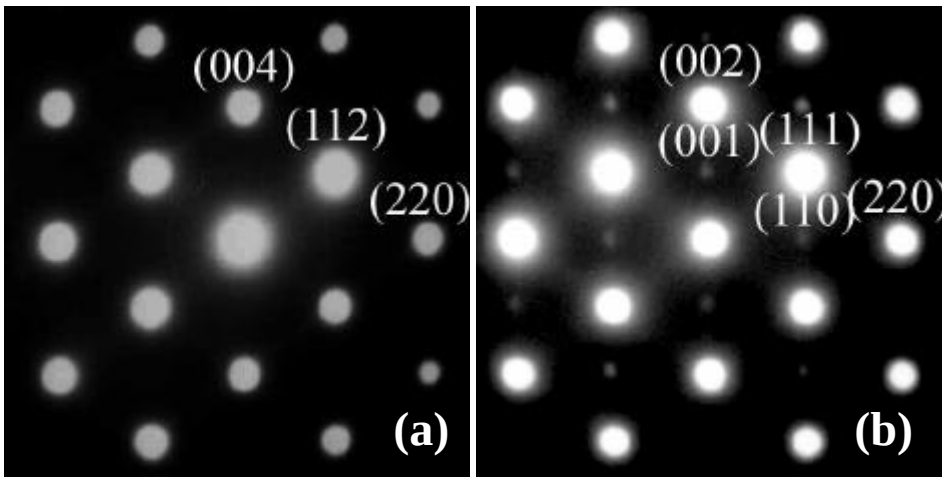

Figure 3. 14. TED patterns on two different points of a $CuInS_2$ epitaxial sample. While left pattern indicates the existence of a single chalcopyrite phase, the right one corresponds to a mixture of chalcopyrite and Cu-Au polytypes of $CuInS_2$.

It is well-known that the observation of additional spots in the TED patterns is sometimes due to the existence of defects in the crystal, which modify the kinematics rules for the electron diffraction. For this reason, several samples were prepared for their observation in different directions. These experiments have shown that single-phase domains with Cu-Au ordering also exist in these samples. Though most of the times the TED patterns indicate the coexistence of both orderings, single-phase domains were also identified. Therefore, it is clear that kinematics effects can not explain the additional spots, and a new crystalline phase must exist in the sample. As an example, consider the following TED pattern (*figure 3.15*) for an epitaxial sample with zone axis parallel to the $[11\bar{1}]$ chalcopyrite direction. In this image, characteristic $\{\bar{1}10\}$ Cu-Au ordering spots are labelled in the image denoted by "CA". Moreover, some of the chalcopyrite allowed spots, which are forbidden for the Cu-Au structure, are not present in the pattern. For example, the $\{101\}$ chalcopyrite planes are not visible in the TED pattern. In the figure one of these spots has

been indicated with a circle at the position where it should appear for a chalcopyrite (CH) structure. This means that the TED pattern of this figure can be interpreted assuming only Cu-Au ordering.

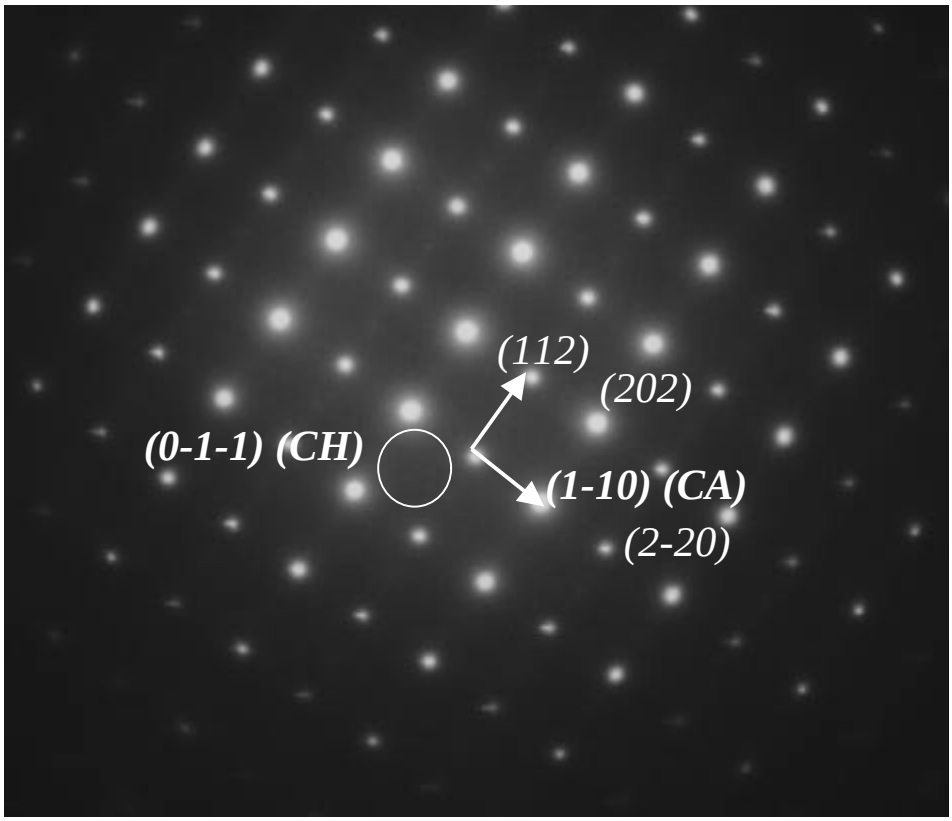

Figure 3. 15. $[11\bar{1}]$**-TED pattern for a $CuInS_2$ epitaxial sample.**

The previous TED patterns showing the existence of Cu-Au ordered phase in the epitaxial layers are in good agreement with both theoretical and experimental reports in literature. Furthermore, the quantification of the additional phase can not be accomplished by TED. For this reason, we have performed a more detailed XRD study on these samples. XRD measurements

have been carried on with a Philips MRD diffractometer using its parallel beam mode.

Chalcopyrite and Cu-Au ordering are characterised by their respective symmetry space group. Due to the existence of specific symmetry operations in each group, different extinction rules hold for each structure. In this sense, the Cu-Au space group $(P\bar{4}m2)$ corresponds to a group with a primitive tetragonal unit cell, in which no glide planes or screw axis occur. Therefore, no reflection conditions exist for this crystalline structure. On the other hand, the chalcopyrite structure $(I\bar{4}2d)$ is a more complex structure, and different reflection conditions can be found in the crystallographic tables for this structure, which are summarised in **[Eq. 3.17]**. First rule arises from the fact that the crystal unit cell is body-centred. This leads to the reflection condition *(h+k+l=2n)*. Moreover, screw dyads along the crystallographic axis require additional conditions for the reflections *(h00)* and *(00l)*. Finally, the glide planes normal to the {110} directions are responsible for the reflection condition involving the *(hhl)* planes.

(h k l): $h + k + l = 2n$
(0 0 l): $l = 4n$
(h 0 0): $h = 2n$
(h h 0): $h = 2n$
(h h l): $2h + l = 4n$ **[Eq. 3. 17]**

The differences in the XRD spectra of both structures can be observed at the following figure (*figure 3.16*), where the simulated patterns are presented.

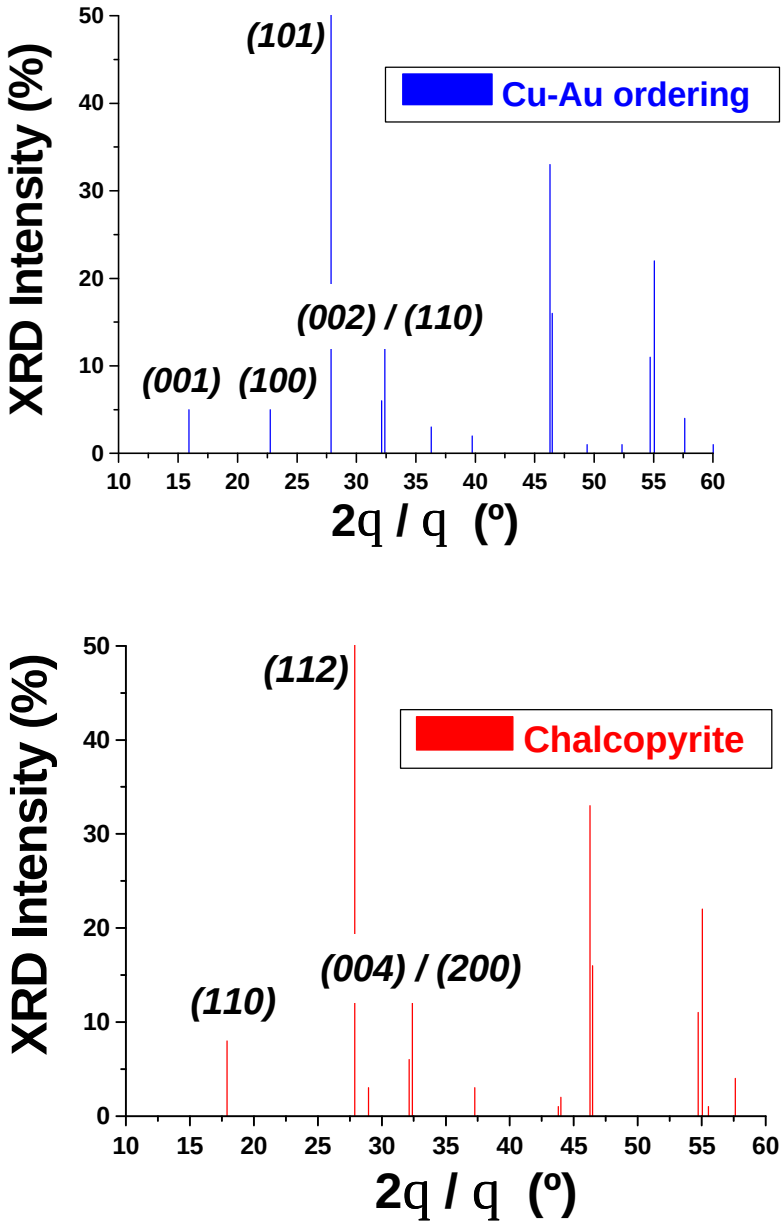

Figure 3. 16.- Cu-Au (top) and chalcopyrite (bottom) simulated XRD spectra.

Despite these differences, the detection of the presence of the Cu-Au phase and its quantification is not straightforward, due to the low relative intensity of the Cu-Au distinctive reflections. In the case of $CuInS_2$, this may be done by studying the intensity of the (001) Cu-Au reflection, which is the most intense Cu-Au reflection forbidden in the chalcopyrite structure. Notice that the relative intensity of this reflection is only about 5% the intensity of the (101) reflection, which is the more intense one in the Cu-Au structure, and which is equivalent to the (112) chalcopyrite one.

The XRD diffractograms of the analysed $CuInS_2$ epitaxial samples can be interpreted as due to the reflections corresponding to a mixture of chalcopyrite and Cu-Au ordered phases. In good agreement with the TED patterns, the additional not-allowed chalcopyrite reflections have been detected, at $2\theta=16.0^o$ and $2\theta=49.7^o$. Those peaks may be indexed as $(001)_{CA}$ and $(003)_{CA}$ in the Cu-Au tetragonal unit cell, and correspond to characteristic reflections of the Cu-Au structure. The identification of the Cu-Au phase can be done in a simple way in the case of the epitaxial samples grown on [001] oriented *Si* substrates. In this case, the chalcopyrite film is mainly [001] oriented. Therefore, by performing a simple $2\theta/\theta$ scan it is possible to detect the characteristic forbidden bands in chalcopyrite $CuInS_2$ (see *figure 3.17*).

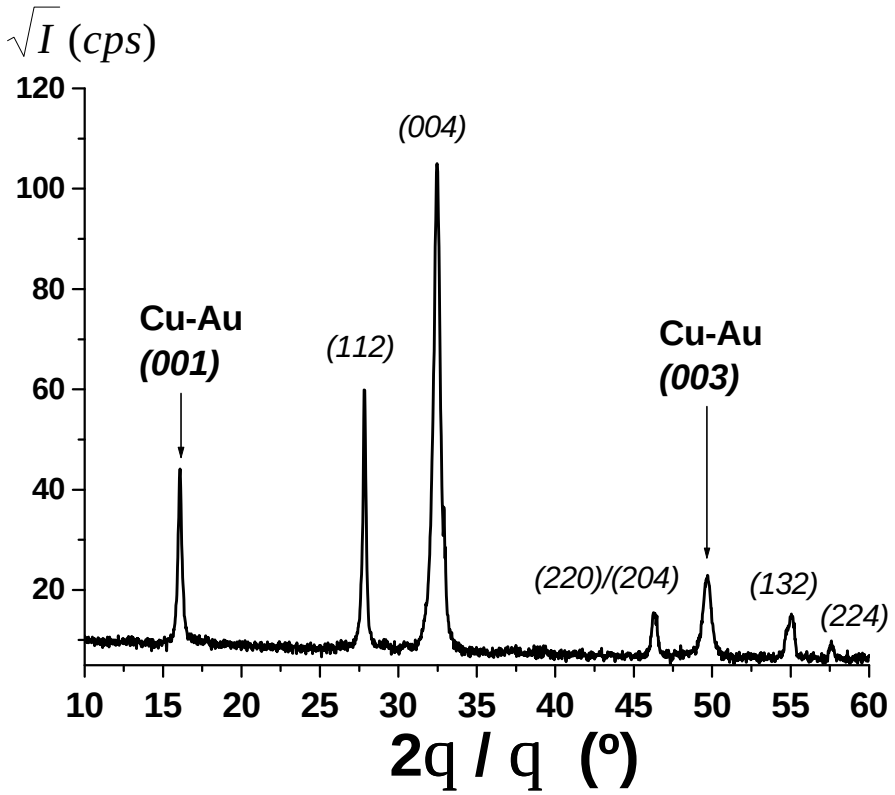

Figure 3. 17. 2q/q XRD spectrum of a $CuInS_2$ epitaxial layer grown on [001] oriented *Si* substrate.

From the previous spectrum it is clear that domains not oriented in the [001] direction exist in this sample. This is a consequence of the fact that the [221] growth direction of $CuInS_2$ on *Si* is more favourable, and therefore changes in the growth direction occur during the formation of the film, leading to the appearance of new reflections in the 2θ/θ spectrum. In the case of the films grown on [111] oriented substrates, the $CuInS_2$ domains are strongly oriented in the [221] chalcopyrite direction. This can be seen in the following plot corresponding to the 2θ/θ spectrum of a $CuInS_2$ film grown on [111] oriented *Si* substrate. Notice that the spectrum is characterised by the (112) chalcopyrite

reflection at about 27.8º, while the (004) chalcopyrite reflection at 32.1º is almost undetectable.

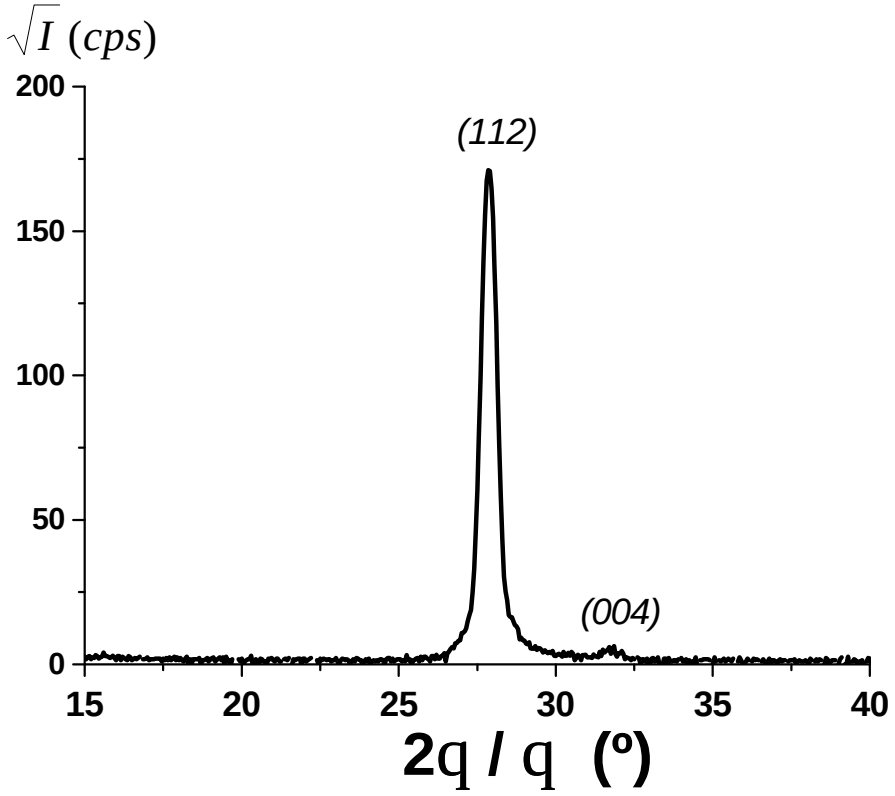

Figure 3. 18. XRD 2q/q scan of a $CuInS_2$ epitaxial film grown on [111] oriented *Si* substrate.

Due to the higher quality of the epitaxial samples grown on [111] *Si* substrates, these samples have been used for estimating the amount of Cu-Au content, rather that those grown on [001] substrates, in which different oriented domains coexist in the same sample. The estimation of the relative amount of each phase in every sample has been accomplished by comparing the diffracted intensity of the $(001)_{CA}$ reflection at 16.0º, and the equivalent $(002)_{CA}$ / $(004)_{CH}$ reflections at

32.3º (the subindex "CH" denotes "chalcopyrite"). For these measurements, the samples have been oriented in the [001] direction by optimising the $(002)_{CA}$ / $(004)_{CH}$ reflection with respect to the ϕ and ψ angles. Once this was done, standard $2\theta/\theta$ spectra have been recorded in order to obtain the integrate intensity of the $(001)_{CA}$ and $(002)_{CA}$ / $(004)_{CH}$ reflections. In the following figure it is represented the recorded XRD spectra for the samples with the highest and the lowest amount of Cu-Au ordered phase:

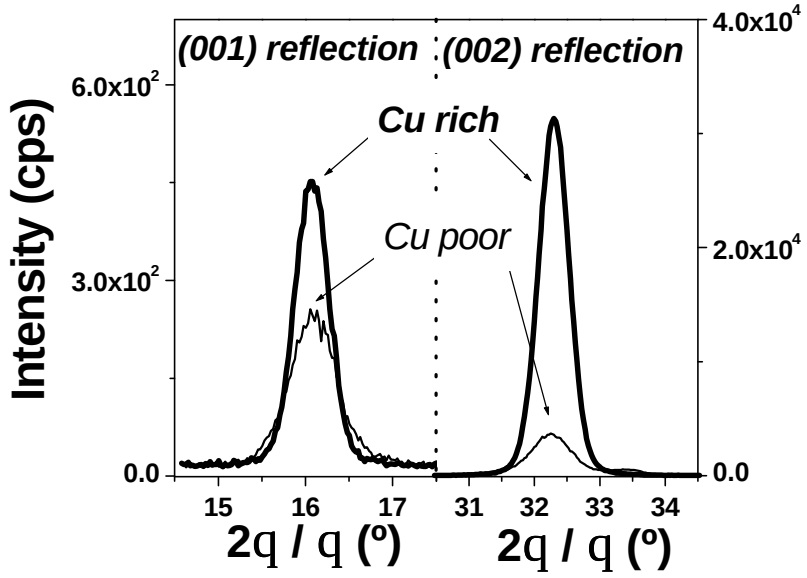

Figure 3. 19. XRD spectra corresponding to the $(001)_{CA}$ and $(004)_{CH}$ / $(002)_{CA}$ reflections. The spectra correspond to the samples with the highest and lowest relative intensity of the CA reflections.

It is well known that the intensity of the diffracted peaks is determined by the structure factor of the crystal lattice, given by:

$$S_K = \sum_{j=1}^{n} f_j \cdot e^{i\vec{K}\cdot\vec{d}_j}, \qquad \textbf{[Eq. 3. 18]}$$

where f_j and $\vec{d}_j$ are the atomic factor and the position of the atom *j* in the unit cell of the crystal, and $\vec{K}$ is a reciprocal lattice vector. Using the atomic factors provided by the crystallographic tables, or using a computer simulation program [153], the diffracted intensity for each atomic plane can be easily obtained for the crystallographic structures. From the parameters of the XRD patterns simulations, we find the relations $I_{004}^{CH} = I_{002}^{CA}$ and $I_{002}^{CA} = 1.163 \cdot I_{001}^{CA}$. Then, taking into account that the total intensity of the diffraction peak at 32.3º is given by the sum of the contributions arising from the chalcopyrite and Cu-Au phases, i.e. $I_{002}^{Tot} = I_{004}^{CH} + I_{002}^{CA}$, and that the XRD count rate depends on the illuminated area on the sample by a factor 1/sinθ, one obtains:

$$\frac{X^{CA}}{X^{CH}} = \frac{1.163 \cdot I_{001}^{CA}}{I_{002}^{Tot} \cdot \frac{\sin\theta_{001}}{\sin\theta_{002}} - 1.163 \cdot I_{001}^{CA}} \qquad \textbf{[Eq. 3. 19]}$$

From this equation, we have estimated the relative amount of the Cu-Au ordered phase in each sample (X^{CA} / X^{CH}). Accordingly, the total amount of Cu-Au phase in our samples $X^{CA} \big/ X^{CA} + X^{CH}$ is between 8% and 25%. These results allowed classifying the samples as a function of their relative Cu-Au phase content. Once the phase composition has been determined, we may plot the relative intensity of the 305 cm^{-1} Raman mode related to the chalcopyrite A_1 mode, versus (X^{CA} / X^{CH}), as shown in *figure 3.20*.

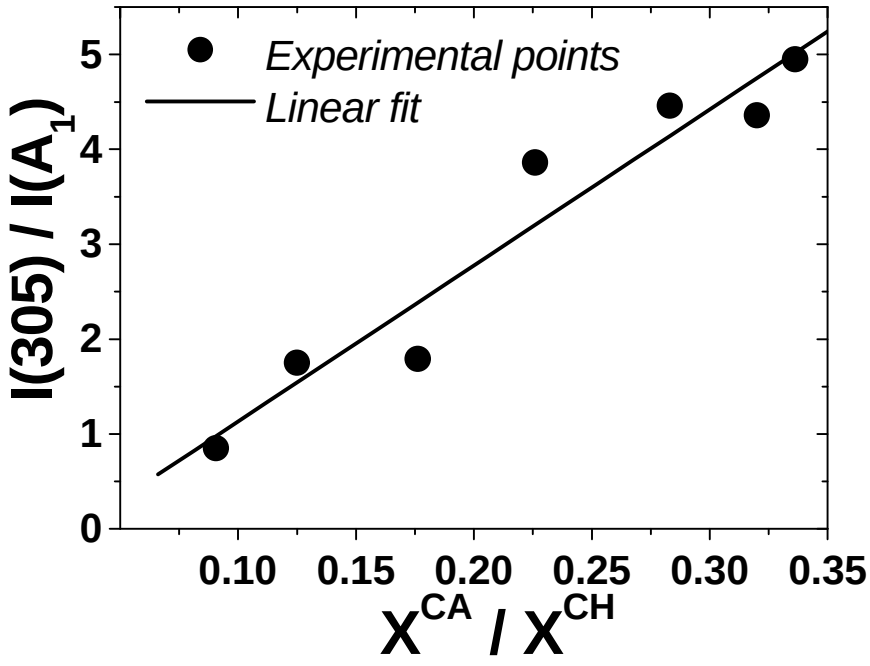

Figure 3. 20. Relative intensity of the 305 cm^{-1} mode with respect to the chalcopyrite A_1 mode, vs. the Cu-Au / chalcopyrite phase ratio (X^{CA}/X^{CH})

The experimental points indicate a linear relationship that reveals the existence of a direct correlation between both magnitudes. These results give a very strong experimental evidence for a direct relation between the additional Raman mode at 305 cm^{-1} in $CuInS_2$ and the Cu-Au ordered phase content within the samples.

3.4. Valence Force Field Model for $CuInS_2$

Theoretical investigations give also support to the assignment of the 305 cm^{-1} to the A_1^* Cu-Au zone-centre phonon. In this section group-theory analysis of the zone-centre phonons in the Cu-Au structure is presented and a Keating model is applied to calculate the expected frequency bands of this crystal. The theoretical results show the existence of a totally symmetric mode in the reducible representation of the Cu-Au crystal, which is expected to appear very close to the experimentally observed position, according to the results obtained from the Keating model.

Following the same procedure as for the determination of the normal modes of the chalcopyrite structure, the reducible representation for the zone-centre phonons in the Cu-Au crystal is determined. Consider the tetragonal unit cell of the Cu-Au structure, as shown in the following figure:

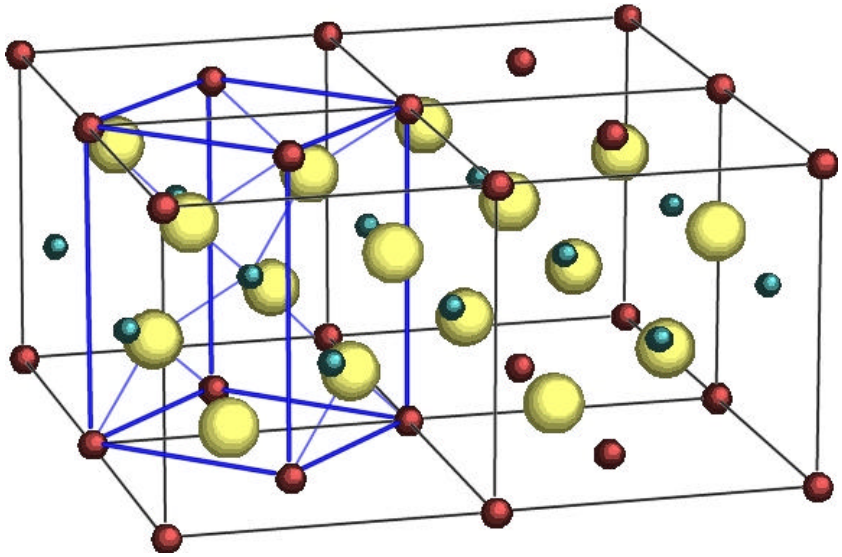

Figure 3. 21. Cu-Au $CuInS_2$ crystalline structure and unit cell

Now, we select an atomic basis with a single molecular unit with the following coordinates:

$R_I^{(Cu)} = (0\ 0\ 0)$ $\quad$ $R_{II}^{(In)} = (\ ½\ ½\ ½)$
$R_{III}^{(S)} = (\ 0\ \ ½¼\ )$ $\quad$ $R_{IV}^{(S)} = (\ \ ½0\ \ ¾)$

After applying the space group operations upon the atoms in the basis, and using the table of characters for the crystal (point group $\mathbf{D_{2d}}$), one finds the reducible representation for the crystal. Results are summarised in the following table:

$\mathbf{D_{2d}}$	**{E}**	**{2S$_4$}**	**{C$_{2Z}$}**	**{2C$_{XY}$}**	**{2s$_d$}**
$\mathbf{R_I}$	R_I	R_I	R_I	R_I	R_I
$\mathbf{R_{II}}$	R_{II}	R_{II}	R_{II}	R_{II}	R_{II}
$\mathbf{R_{III}}$	R_{III}	R_{IV}	R_{III}	R_{IV}	R_{III}
$\mathbf{R_{IV}}$	R_{IV}	R_{III}	R_{IV}	R_{III}	R_{IV}
c[R]	3	-1	-1	-1	1
N[R]	4	2	4	2	4
$\mathbf{c_R}$	12	-2	-4	-2	4

Table 3. 5. Calculation of the characters of the reducible representation for the Cu-Au structure

The number of times each irreducible representation in the point group appears in the crystal representation, $N(G_i)$, is obtained from the orthogonality relations:

$N(A_1) = 1/8\ (12 - 4 - 4 - 4 + 8\ ) = \mathbf{1}$
$N(A_2) = 1/8\ (12 - 4 - 4 + 4 - 8\ ) = \mathbf{0}$
$N(B_1) = 1/8\ (12 + 4 - 4 - 4 - 8\ ) = \mathbf{0}$
$N(B_2) = 1/8\ (12 + 4 - 4 + 4 + 8\ ) = \mathbf{3}$
$N(E) = 1/8\ (24 + 8) = \mathbf{4}$

Therefore:

$$G_T = A_1 \text{ Å } 3B_2 \text{ Å } 4E, \qquad \textbf{[Eq. 3. 20]}$$

which gives for the optical modes:

$$G_{opt} = A_1 \text{ Å } 2B_2 \text{ Å } 3E \qquad \textbf{[Eq. 3. 21]}$$

In this case, all the zone-center phonons are Raman-active, and only the A_1 mode is not Infrared-active. Notice that due to the fact that the number of atoms in the basis of the Cu-Au cell is half of that in the chalcopyrite cell, the number of optical modes is reduced from 21 to 9. Notice also that the representation of the Cu-Au structure includes a single totally symmetric mode, which is in well agreement with the experimental observations in these films. On the basis of the experimental results, one may assign the A_1 mode of the Cu-Au (A_1^*) to the additional mode at 305 cm^{-1}.

On the other hand, the displacement coordinates for the A_1^* mode have been also determined by applying the corresponding projector operator to the Cartesian coordinates. The result obtained is:

$$\mathbf{A_1^*: Z_4 - Z_3} \qquad \textbf{[Eq. 3. 22]}$$

Therefore, the normal coordinates for the A_1^* mode in the Cu-Au structure involves only the anti-phase motion of the anion atoms in the *Z* direction of the tetragonal cell, as can be seen in *figure 3.22*.

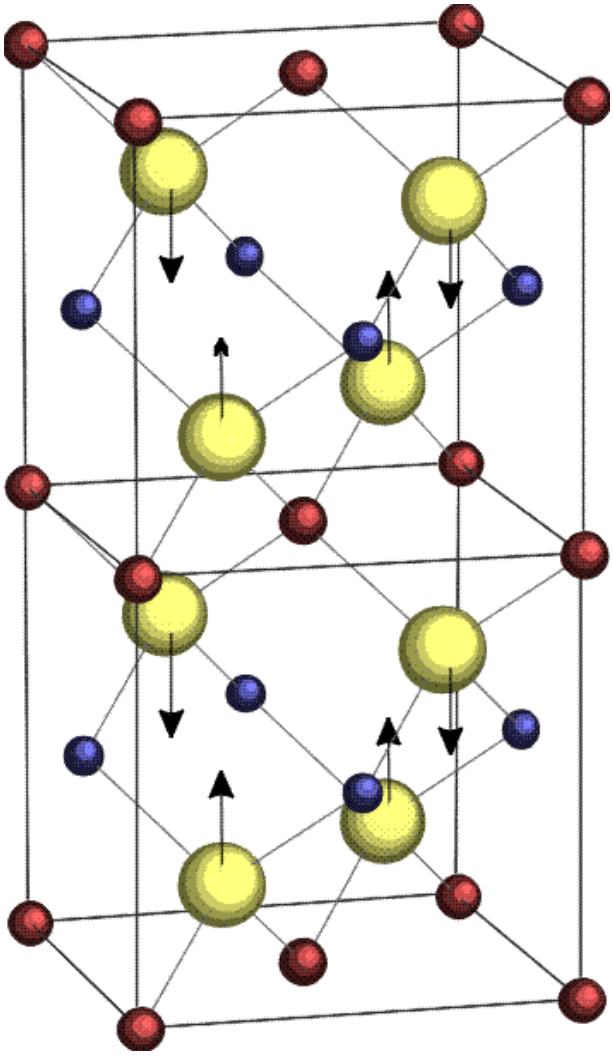

Figure 3. 22. Cu-Au cell showing the displacement of the atoms in the A_1^* vibration.

It is worth to remark that the totally symmetric vibrations are very similar in both the chalcopyrite and the Cu-Au crystals. These correspond to an alternative vibration of the anions against the monovalent and the trivalent cations, which remain at rest. Therefore, a similar spectral position is to be expected for both

modes (as experimentally observed). However, differences in the frequencies of the modes may be expected due to the different bond angle distortion. While in the chalcopyrite lattice the anions move along the *X* and *Y* crystallographic directions, in the Cu-Au crystal they move in the *Z* direction. As a result, for a fix anion displacement the *S-Cu-S* and *S-In-S* bond angle distortion for the Cu-Au lattice is larger, despite the fact that the bond lengths, as well as the *Cu-S-Cu* and *In-S-In* angles, are similar. According to this, the associated A_1^* vibration is expected to have also a higher frequency. This argument is consistent with the given interpretation for the experimental results, and the assignment of the 305 cm^{-1} mode to the A_1^* Cu-Au vibration.

Despite these considerations, a more accurate knowledge of the vibrational spectra of the Cu-Au ordered structure would be desirable to support the assignment of the 305 cm^{-1} experimental mode to the A_1^* Cu-Au zone-centre phonon. Unfortunately, up to now it has not been possible to grow $CuInS_2$ single crystals with Cu-Au crystallographic structure. Therefore, the determination of the vibrational spectra of this structure requires using a theoretical model. Several models may be applied to the determination of the normal modes of a crystal. For example, the "*Rigid Ion Models"* take into account [154] short-range interactions between neighbour atoms represented by elastic forces, and also the Coulomb interaction between ions. On the other hand, the *"Shell Models"* assume [155] that the ions are electrically and mechanically deformable, and that such deformations cause variations of the polarizability that result in interatomic forces. Other models such as the *"Overlap Shell Models"* and the *"Adiabatic Bond Charge Models"* have also been applied [156] to the calculation of the Dispersion Curves of several materials. However, all these models present the disadvantage of requiring a large number of parameters, and some of these parameters have a doubtful physical meaning.

The "*Valence Force Field" (VFF)* model represents a good alternative approach for the description of the zone-center vibrations in a crystal, involving a lower number of parameters with a direct physical interpretation. In this model, the

interactions between the atoms in the crystal are modelled by considering the elastic interactions between the atoms in the primitive unit cell. As a first approximation, the electrostatic interaction is neglected. This results in a reduction of an important number of parameters, but at the same time, this makes the VFF model useless for predicting the LO-TO splitting of the polar modes of the crystal. For a tetrahedrally coordinated crystal, the elastic potential between first neighbours may be written within this approach as:

$$U = \frac{1}{2}\cdot\sum_{i=1}^{4} k_r\cdot(Dr_i)^2 + \sum_{s=1}^{2}\left[\begin{array}{l} \frac{1}{2}\sum_{i,j>i} k_q^s\cdot(rDq_{ij}^s)^2 + \sum_{i,j\neq i} k_{rq}^s\cdot(Dr_i^s)\cdot(rDq_{ij}^s) + \\ + \sum_{i,j>i} k_{rr}^s\cdot(Dr_i^s)\cdot(Dr_j^s) \end{array}\right] \qquad \textbf{[Eq. 3. 23]}$$

Here, the subindex *s* refers to two given atoms (1,2), and *(i,j)* run over all the first neighbours of the atoms *s*. The equilibrium bond distance is described by *r*, while the change in the bond distance is given by *Dr*. The term Dq_{ij}^s corresponds to the change of the bond angle between the atoms (*i*-*s*-*j*). On the other hand, the force constants needed are stretching force constants (k_r and k_{rr}), bond-bending constants (k_q) and coupled stretching-bending constants (k_{rq}).

The *Keating* model is a particular case of the VFF models. The model was first developed by Keating [95], who applied invariance requirements to the strain energy of the Diamond crystal to derive a mathematical form for the elastic potential. Keating proposed that the elastic potential between atoms could be described within the VFF model by the squares of the variation of the dot products $D\left(\vec{r}_i^{\,s}\cdot\vec{r}_j^{\,s}\right)$. Here, the vectors $\vec{r}_i^{\,s}$ correspond to the vectors joining the atoms *s* and its first neighbour *i*. Therefore, Keating expressed the interatomic potential by:

$$U = \tfrac{1}{2}\cdot a\cdot\left(\frac{3}{4r^2}\right)\sum_{i=1}^{4}\left[D(r_i^l\cdot r_i^l)\right]^2 + \tfrac{1}{2}\cdot\sum_{s=1}^{s=2} b^s\cdot\left(\frac{3}{4r^2}\right)\sum_{i=1}^{4}\left[D(r_i^s\cdot r_j^s)\right]^2 \qquad \textbf{[Eq. 3. 24]}$$

In the Keating model, the a and b constants correspond to the stretching and bending force constants, respectively. These Keating constants can be related with the VFF ones by the following relations [96]:

$$k_r = 3a + \tfrac{1}{2}b \qquad k_q = \tfrac{2}{3}b$$
$$k_{rq} = \tfrac{1}{3\sqrt{2}}b \qquad k_{rr} = \tfrac{1}{12}b \qquad \textbf{[Eq. 3. 25]}$$

Given the interatomic potential, it can be calculated in a straightforward way the force constant between the pair of atoms *(i, j)*. The Keating potential gives rise to non-zero force constants up to first neighbours between anion-cation, anion-anion and cation-cation, which can be calculated as the second derivative of the potential energy with respect to the atomic displacement of the atoms $(x_m^{(i)})$ along two directions in the space:

$$C_{mn}(i,j) = \frac{\partial U(i,j)}{\partial x_m^{(i)} \cdot \partial x_n^{(j)}} \qquad \textbf{[Eq. 3. 26]}$$

We will apply now the Keating model to both chalcopyrite and Cu-Au structures. From the experimental frequencies for the chalcopyrite $CuInS_2$ compound, the force constants involved in the model can be extracted. Once the values of the force constants are known, they are used to calculate the expected frequencies in the case of the Cu-Au ordered crystal. We will assume that the bond distances and bond angles of both orderings are similar, and therefore it is not necessary to re-scale the force constants [157]. As a matter of fact, no important differences are expected due to the strong relationship between both structures, and because the atoms constituting the crystal are the same and they are tetrahedrally coordinated in both cases. Unfortunately, experimental results are not available to confirm this. However, it has been shown that the introduction of vacancies in the chalcopyrite structure leads to the formation of

OVC compounds which keep the same interatomic chalcopyrite distances within an error of 0.01Å, as determined by EXAFS [158]. It seems unlikely that the rearrangement of the cations in the cation sublattice could modify the bond parameters in a more important way than the introduction of vacancies.

As may be appreciated in **[Eq. 3.24]**, within the Keating approximation, only two force constants are needed to describe a diamond-like lattice [159]. This is especially important when dealing with more complex crystalline structures. Even in this approximation, the introduction of three types of atoms in the chalcopyrite structure leads to a considerable increase of the number of constants. Five bond-bending constants are needed in order to describe the interactions (*Cu-S-Cu, In-S-In, In-S-Cu, S-Cu-S, S-In-S*), while other two stretching constants are required for the stretching interactions between *Cu-S* and *In-S*. Therefore, it is important to be able to find physical arguments to achieve a further reduction in the number of constants of our model. This can be done by assuming the following hypothesis [160]:

- The bond-bending force constants for a given set of atoms including only two types of atoms, will be the same independently of which atom is in the center, and which atoms are in the edges. In this way, the interactions *Cu-S-Cu* and *S-Cu-S* are described by a single constant (b_1), and the interactions *In-S-In* and *S-In-S* by a constant b_2.

- For the sets of atoms of the type *Cu-S-In*, the bond-bending interaction is assumed to correspond to the arithmetic average of the bond-bending constants describing the sets *Cu-S-Cu* and *In-S-In*. Therefore, $b_{12} \approx \frac{1}{2} \cdot (b_1 + b_2)$.

This reduces the number of constants needed to describe the elastic interactions in the chalcopyrite lattice to two stretching constants for the A-C and B-C interactions (a_1 and a_2, respectively) and two bond-bending constants (b_1 and

b_2). The atomic interactions considered within the Keating approach are depicted in the following figure:

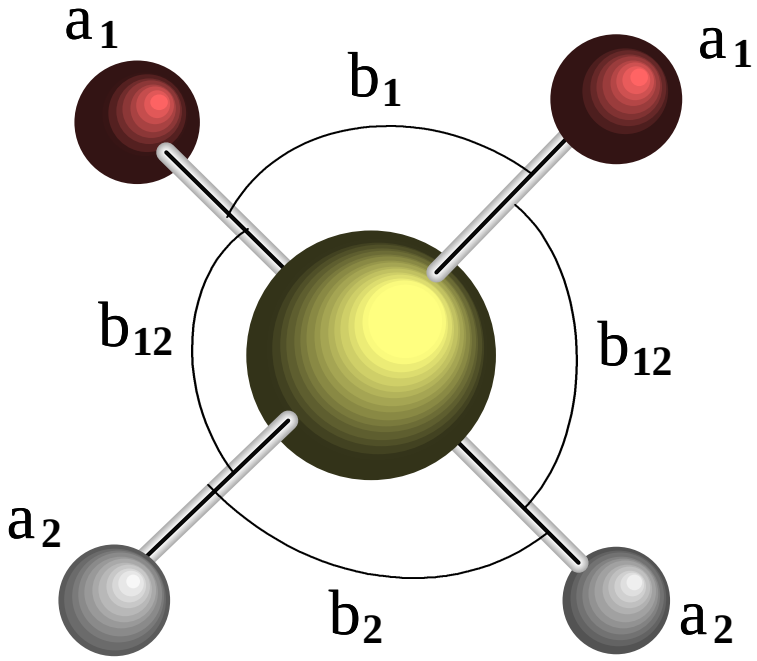

Figure 3.23. Force constants and atomic interactions for a fundamental tetrahedron in $CuInS_2$.

By this way, the dynamical matrix of the chalcopyrite crystal $D(\vec{k})$ can be expressed [161] in terms of only four parameters, which are included in the corresponding set of force constants C_{mn} .

$$D(\vec{k}) = D_{mn}\left(i, j \middle| \vec{k}\right) = \frac{1}{\sqrt{m_i \cdot m_j}} \cdot \sum_l C_{mn}\left(0\,i; l\,j\right) \cdot e^{i\vec{k}\cdot\vec{X}(l')} \qquad \textbf{[Eq. 3. 27]}$$

In the case of the chalcopyrite structure, this matrix corresponds to a 24x24 square matrix, whose eigenvalues correspond to the squares of the normal frequencies of the crystals. We will restrict ourselves to the study of the Zone-centre phonons of the crystal, which greatly simplifies the dynamical matrix. Under this conditions, three eigenvalues related to the acoustical modes of the crystal are zero, while the other 21 can be related to the optical zone-centre modes of the crystal. The determination of the force constants for the $CuInS_2$ compound can be accomplished by optimising their values in order to reproduce the experimental phonon spectra. Therefore, using the experimental values of the different modes reported in the literature [101], the problem restricts to the minimisation of the function c, defined as the quadratic deviation of all the experimental values with respect to the values predicted by the Keating model:

$$c(a_1, a_2, b_1, b_2) = \sum \left(w_j^{Experimental} - w_j^{Keating} \right)^2 \qquad \textbf{[Eq. 3. 28]}$$

Using the Simplex algorithm [162] for the minimisation of the above equation, the optimum values of the force constants for $CuInS_2$ are found to be:

$$\begin{aligned} a_1 &= 17.43 \cdot 10^3 \; dyn/cm & b_1 &= 1.24 \cdot 10^3 \; dyn/cm \\ a_2 &= 37.03 \cdot 10^3 \; dyn/cm & b_2 &= 1.71 \cdot 10^3 \; dyn/cm \end{aligned} \qquad \textbf{[Eq. 3. 29]}$$

The values obtained for the force constants are reasonable in terms of their physical meaning. First, they are all positive, which is expectable from their definition. Notice also that the values for the stretching force constants are one order of magnitude greater than the values for the bond-bending constants, which justifies neglecting the bond-bending interaction as a first approximation (see **[Eq. 3.15]** in section 3.1). Finally, the corresponding constants involving *In-S* interactions are greater than those involving *Cu-S* interactions, i.e, $a_2 > a_1$ and $b_2 > b_1$, as one may expect due to the higher strength of the *In-S* bond.

The experimental transversal optical frequencies are compared with the results obtained from the four parameters Keating Model in the following table. The modes are classified according to their symmetry, and the point in the Brillouin Zone of the Zincblende where they come from after folding it back is indicated into square brackets:

Transversal Optical modes in $CuInS_2$		
Mode	**$w_{EXPERIMENTAL}$ (cm^{-1})**	**$w_{KEATING}$ (cm^{-1})**
$G_4\ [G_{15}]$	321	330
$G_5\ [G_{15}]$	323	325
$G_2\ [X_1]$	- (silent)	297
$G_3\ [W_2]$	- (very weak)	294
$G_5\ [W_4]$	295	291
$G_4\ [W_2]$	234	253
$G_1\ [W_1]$	290	253
$G_5\ [X_5]$	244	244
$G_2\ [W_1]$	- (silent)	215
$G_3\ [X_3]$	157	157
$G_5\ [W_3]$	140	149
$G_5\ [W_4]$	88	87
$G_3\ [W_1]$	- (very weak)	83
$G_4\ [W_2]$	79	79
$G_5\ [X_5]$	67	68

Table 3. 6. Comparison of the transversal optical frequencies obtained from the Keating model with the experimental ones.

The previous table shows that the Keating model is able to reproduce with reasonable accuracy the experimental results, despite the low number of

parameters used for the description of the interactions. Most of the predicted frequencies agree with the experimental ones within an error of about 5%. The detailed properties of the different frequency bands and of each normal mode shall not be discussed, since they can be found in the literature for other analogue chalcopyrite semiconductors [93], and are not relevant for our objectives. Just as an example, notice that the four-parameters Keating model predicts the frequency splitting of the $(G_4\text{-}G_5)$ modes, which can not be explained using a two-parameters model. It also reproduces the formation of three groups of frequency. The group of low frequency modes appears well separated from the middle frequency group a gap of more than 60 cm^{-1}, while the middle and high frequency groups appear overlapped. The modes laying at the low frequency band involve mainly the displacements of *Cu* and *S* atoms, while for the modes at the high frequency band the contributions of the *In* and *S* displacements are the most important. For the middle frequency band, the three atoms contribute significantly to the corresponding vibrations. All these features are in fair agreement with the experimental observations of the position and symmetry of the different modes.

Obviously, the simplicity of the model leads to some limitations. For example, the predicted frequency splitting of the modes arising from the Zincblende G_{15} point leads to a higher frequency for the Γ_4 band. In fact, the experimental frequency of the Γ_5 band is higher than the Γ_4 one. On the other hand, the predicted position for the A_1 mode is significantly far away from the experimental position. The relative deviation for this frequency is the largest one, being almost 13%. This is a common limitation of this model, and has been already reported in the literature for other compounds [163]. It is clear that second neighbour interactions should be taken into account if one wishes to find with more accuracy the frequency of the A_1 mode.

Once the *Cu-S* and *In-S* force constants are known, the following step is finding the zone-centre frequencies for the Cu-Au crystal. Using the empirical values for the force constants shown in **[Eq. 3.29]**, the elastic interaction in the Cu-Au

ordered crystal can be described. In this case, the dynamical matrix of the crystal is a 12x12 square matrix, which can be taken into its diagonal form to obtain the crystal eigenfrequencies. The results of such calculation are summarised in the following table, where the transverse optical frequencies of the crystal are listed:

Transverse Optical phonons in Cu-Au $CuInS_2$	
Mode	**$w_{KEATING}$ (cm^{-1})**
$\Gamma_5^{(1)}$	325
$\Gamma_4^{(1)}$	295
Γ_1	265
$\Gamma_5^{(2)}$	246
$\Gamma_4^{(2)}$	157
$\Gamma_5^{(3)}$	82

Table 3. 7. Calculated zone-centre phonons in Cu-Au ordered $CuInS_2$

The previous calculation gives a different phonon spectra for the Cu-Au ordered $CuInS_2$ in relation to that of the chalcopyrite ordered one. In the case of the totally symmetric mode of the Cu-Au structure, its frequency appears at 265 cm^{-1}. In order to compare this value with the experimental results, one should bear in mind the intrinsic error on the frequency of the totally symmetric mode associated with the application of the Keating model. Furthermore, one may compare the relative shift of the frequency of the totally symmetric mode for both structures. Doing this, a corrected position for the A_1^* mode of the Cu-Au structure can be estimated taking into account the experimental frequency of the band for a chalcopyrite single crystal. Therefore:

$$w\left[A_1^*\right] \approx \frac{w_{Keating}^{Cu-Au}}{w_{Keating}^{Chalcopyrite}} \times 290\,cm^{-1} = 305\,cm^{-1} \qquad \textbf{[Eq. 3. 30]}$$

This result predicts that the position of the A_1^* Cu-Au mode should be close to the experimental observed frequency for the 305 cm^{-1} mode. Therefore, the application to the Keating model to both structures supports the assignment of the 305 cm^{-1} band in the Raman spectra of the films to the A_1^* band of the Cu-Au structure.

Another interesting result of the previous analysis is that the lowest frequency band of the Cu-Au crystal is estimated to be at 82 cm^{-1}. Since the Keating model seems to reproduce with good accuracy the low frequency region of the phonon spectra of the chalcopyrite $CuInS_2$ compound, this value is supposed to have a low uncertainty. Therefore, one should conclude that the assignment of the experimental band at 60 cm^{-1} to a Cu-Au zone-centre phonon is not possible, at least on the basis of the presented VFF model. Since the intensity of the additional modes at 305 cm^{-1} and 60 cm^{-1} appear to be correlated, one should think that the 60 cm^{-1} is somehow related to the existence of the Cu-Au ordered phase. At this point, several possible origins for the 60 cm^{-1} band can be imagined. First of all, one should take into account that Cu-Au ordered phase exists within these samples in the form of nanometric size domains. Therefore, differences may exist between the Raman spectra of these domains and a macroscopic crystal. In this sense, this mode could be due to the folding of an acoustical branch of the Cu-Au structure. Another possibility is the existence of a local mode appearing as a result of a certain defect configuration directly related to the chalcopyrite Cu-Au phase coexistence in the samples. It is well established that some solid state transformations in solids (such as order-disorder transformations) may give rise to the apparition of local or band modes in the spectra [164]. Nevertheless, the complexity of the problem makes difficult to elucidate the exact structure of the defect responsible for the observation of such band.

Even though the Keating model seems to be able to explain the experimental results, it yields errors for the frequency of the totally symmetric bands of these

structures, which lay in the range of 10%. A different approach for the calculation of the position of the totally symmetric bands of both structures has been carried out by S. Wei and co-workers. First-principle calculations have been performed in the National Renewable Energy Laboratory (NREL) in collaboration with our group and the Hahn-Meitner Institut. Their first-principle calculations used the frozen-phonon approach, which is based on density functional theory within the local density approximation as implemented by the general potential linearized augmented plane wave method. This method is based on the construction of a supercell by displacing the atoms of the crystal unit cell according to the displacement pattern of the phonon. The energy difference between the displaced and the equilibrium structures is used to evaluate the frequency of the phonon [165]. The calculated frequencies [166] for the A_1 and A_1^* modes were 296 and 315 cm^{-1} respectively, in agreement with the experimental observations. These values are closer to the experimental ones than those provide by the simple Keating model, and again reproduce fairly well the experimental frequency ratio:

$$w \approx \frac{315}{296} \times 290\,cm^{-1} = 308\,cm^{-1} \qquad \textbf{[Eq. 3. 31]}$$

3.5. Conclusions

In this chapter the vibrational properties of $CuInS_2$ have been described, together with experimental results concerning the existence of additional bands in polycrystalline and epitaxial films. These bands present analogue properties to the additional bands also observed in $CuInSe_2$ films. The determination of the origin of these peaks is of great importance for the better understanding of the properties of the material, as well as for the characterisation of the films.

The fundamental chemical properties of the *Cu-In-S* system have been also introduced in order to give an appropriate background for the comprehension of the possible origin of these additional bands. Experimental results point out that these peaks are not directly related to variations in the chemical composition of the films, but to structural differences. The intensity of the 305 cm^{-1} peak has been correlated with the amount of Cu-Au nanometric ordered domains in the films, which indicates a direct relationship between both features. Group theory analysis for the Cu-Au structure supports the assignment of the 305 cm^{-1} mode to this type of cation ordering in the $CuInS_2$ compound. Finally, the application of a four-parameters VFF model has been developed in order to estimate the phonon spectra of the Cu-Au $CuInS_2$ compound. These calculations are also in good agreement with the assignment of the 305 $CuInS_2$ to the A_1^* Cu-Au totally symmetric mode, and agree with alternative theoretical calculations performed by other groups.

4. Characterisation of coevaporated polycrystalline $CuInS_2$ films.

This chapter describes the detailed microstructural characterisation of polycrystalline $CuInS_2$ films for solar cell applications. The aim of the study has been the study of the structural and chemical properties of the films, due to their strong relationship with the efficiency of the final devices. Moreover, the presence of crystalline defects or secondary phases may lead to a reduction of the lifetime of the photogenerated carriers, therefore affecting the cell performance. In this sense, the stoichiometric conditions and the substrate temperature during the formation of the absorber have been found to directly influence the physico-chemical characteristics of the resultant material, which in turn determine its optoelectronic behaviour. The crystalline properties of the films have been analysed by micro-Raman spectroscopy and by XRD. Due to the relatively unknown vibrational properties of the films, special emphasis has been given to the micro-Raman characterisation task. As will be shown, it constitutes in fact a very useful tool for the characterisation of the material.

The chemical composition of the films has been studied by *Auger Electron Spectroscopy* (*AES*). This technique is very suitable for the characterisation of thin films and surface analysis, and it provides a high depth and lateral resolution. Furthermore, the combination of the *AES* with micro-Raman spectroscopy allows investigating simultaneously the chemical and structural properties of the film at different depths. This has made possible to identify the presence of different phases in the films, and their distribution across the samples.

4.1. Samples analysed and measurement conditions.

Co-evaporated samples

$CuInS_2$ absorbers are commonly obtained by a sequential process involving several steps. As already described in section ***1.4.2***, metallic precursors (*Cu* and *In*) are first sputtered onto a *Mo*-coated soda-lime glass. Then, the substrates are placed in a Vacuum chamber and subjected to a rapid thermal process (*RTP*) in a sulphur atmosphere. This process finishes after a few minutes. Usually, *Cu*-excess conditions are chosen because of its beneficial effects on the quality of the films. This process results in good quality absorber layers, with high lateral homogeneity. Despite this, there exist other growth techniques that may be more adequate for the study of the material properties. For example, coevaporation of the metallic precursors in a sulphur-containing atmosphere is a highly interesting growth method. This process takes place also in a Vacuum chamber. Due to the geometrical configuration of the evaporators, the coevaporated films present a lateral graded composition, being *Cu*-rich close to one edge, and Cu-poor close to the other. Therefore, although the film inhomogeneity may be inconvenient from the point of view of the device performance, this system offers the possibility of studying different stoichiometries in the same sample. Accordingly, respect the sequential process, the coevaporation technique avoids the necessity for growing different samples to study the effect of the stoichiometry. On the other hand, the coevaporation process can be easily adapted for the obtaining of homogeneous absorbers, just by introducing a rotating substrate holder. For these reasons, in this chapter we will focus on the study of samples grown by coevaporation. The details of the experimental results concerning the sequentially processed samples are presented in the next chapter.

We shall describe with more detail the coevaporation system used for the preparation of the samples. The experimental set-up corresponds to that used in the Hahn-Meitner Institut [167, 168]. In this system, four samples with dimensions of (0.8 x 5) cm can be grown in the same batch. Glass substrates are first placed into a pre-chamber and then transferred to a bigger chamber where the coevaporation takes place. For the process, high vacuum is required. A turbo-pump supplies the appropriate vacuum conditions, being the typical vacuum pressure during the sulphurisation reaction of around $3 \cdot 10^{-5}$ Torr. Four crucibles are distributed inside the chamber, which are heated through graphite resistances. For the formation of $CuInS_2$ films only three of them are needed. One evaporator is filled with *S*, while other two are filled with *Cu* and *In* respectively. The raw material used for the growth of the films is ultra-pure. A liquid nitrogen cooled stage is also placed inside the chamber in order to avoid the condensation of the sulphur vapour at the pumps. The evaporated elements react at the surface of the *Mo*-coated glass substrate with the sulphur vapour, leading to the formation of the film. During the sulphurisation, the substrate is heated up to a fix temperature with halogen lamps. The temperature of the glass substrate and the evaporators is monitored with the aid of thermocouples. Moreover, PID systems are used to properly control the temperature of each element during the thermal processes. A sketch of the system is shown in *figure 4.1.*

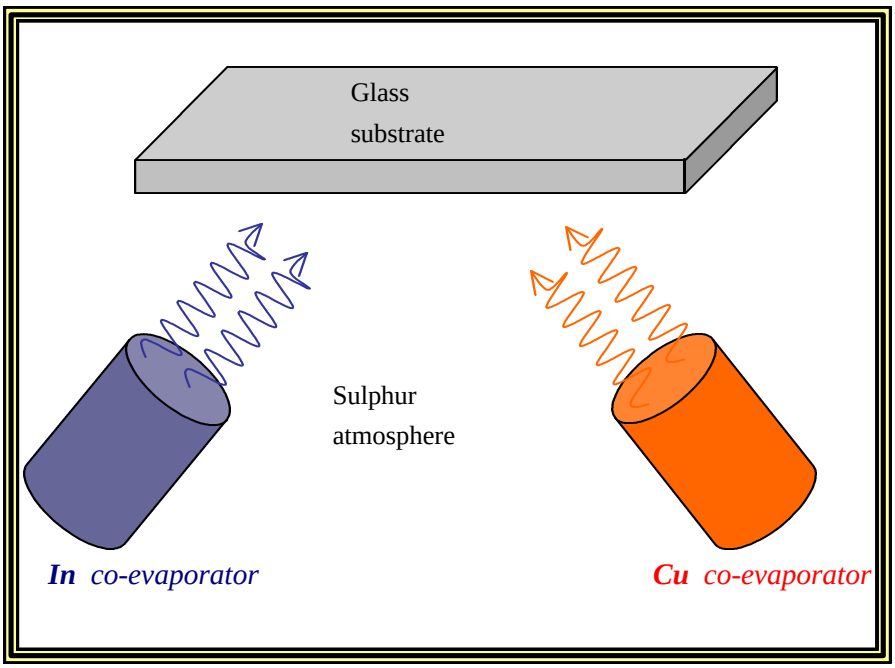

Figure 4. 1. Experimental set-up for the co-evaporation of $CuInS_2$

The graded composition in the samples is a consequence of the geometrical configuration of the evaporators. As may be appreciated in the figure, the edge of the sample closer to the *Cu* evaporator grows under *Cu*-rich conditions, while the edge closer to the In one grows under *Cu-poor* conditions.

The study of the effect of the substrate temperature and the chemical growth conditions has been performed by analysing samples grown at 370ºC, 420ºC, 470ºC and 520ºC. All the samples present a lateral Cu/In gradient.

Measurements: experimental conditions

Micro-Raman spectroscopy, AES and XRD techniques have been used for the characterisation of the polycrystalline samples. The standard conditions used for the Raman measurements were already given in detail in *section 2.3*. The AES experiments were carried out in a PHI Model 670 Scanning Auger Nanoprobe System with Schottky field emission source and multichannel detector. The energy of the electron beam was typically around 10keV, with a filament current of 10 nA. Despite the high lateral resolution of the technique, a 10 μm^2 square area has been scanned in order to avoid effects of possible local inhomogoneities. The AES equipment made possible the study of different points at the bulk of the samples by using an Ar^+ sputtering beam. The energy of the Ar^+ beam has been kept around 2 keV in order to minimise the damage induced in the samples. The composition of each point has been determined from the analysis of the AES spectra, using the data obtained from a $CuInS_2$ single crystal to calculate the atomic sensitivity factors.

On the other hand, the combination of the micro-Raman and AES techniques has been proved as a very powerful tool for the characterisation of the samples. The procedure used for the combination of both techniques was the following. After recording a micro-Raman spectrum of a concrete point of a given sample, the sample was moved to the AES chamber, where it was sputtered and its composition determined. The sample was then transferred back to the micro-Raman set-up to obtain another spectrum. This procedure was repeated until the *Mo* back contact was reached, after a certain number of sputtering steps. The sputtering time has been adjusted to about 200-300 nm per sputtering step. Therefore, after about 10 sputtering steps the 2-3 μm of the films are analysed. Although the depth resolution of the micro-Raman spectroscopy in $CuInS_2$ is, in principle, about 150 nm, reducing the sputtering time makes no sense due to the roughness of the films, which may be around 300 nm (as estimated from interferometric measurements).

Finally, the XRD analysis has been carried out in a Philips MRD diffractometer using the Cu $\boldsymbol{k_a}$ line at λ=1.541 Å. Standard 2θ/θ measurements have been performed in the polycrystalline films, mainly to determine the secondary phases present at the film and to study the crystalline quality of the chalcopyrite phase.

4.2. CuS segregation: Assessment of KCN etching

As-grown coevaporated samples have been analysed by micro-Raman spectroscopy. Different spectra have been recorded corresponding to equidistant points at the surface of the coevaporated samples. Due to the characteristics of the films, each spectrum corresponds to a different *Cu/(Cu+In)* ratio during growth of the film. The spectra obtained for the sample coevaporated at T = 520ºC are shown in next figure:

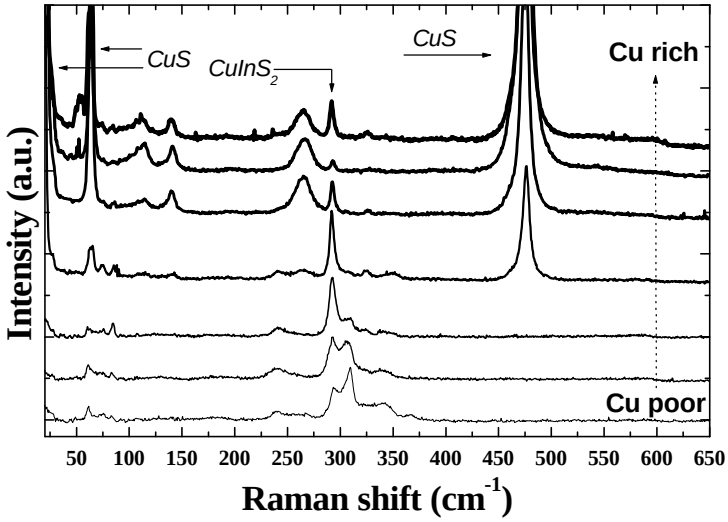

Figure 4. 2. Surface micro-Raman spectra for the as-grown coevaporated sample at T=520ºC.

In the figure, spectra at the bottom correspond to points closer to the *Cu*-poor edge of the sample, while the top spectra arise from points close to the *Cu*-rich edge. *Cu*-rich spectra can be interpreted as due to a phase mixture of the covellite phase CuS and the chalcopyrite phase of the $CuInS_2$. The most intense

peak of the chalcopyrite phase (A_1 mode) at 290 cm^{-1} is hardly visible due to its low relative intensity with respect to the CuS peaks. All the non-chalcopyrite peaks in the spectra have been identified as belonging to the covellite phase of the CuS, according to the reported spectra found in the literature [169, 170]. The highest intense modes of CuS found at 18 cm^{-1} (E_{2g}), 65 cm^{-1} (A_{1g}) and 473 cm^{-1}(A_{1g}) have been indicated in the figure. A Raman mapping of the Cu-rich region reveals that the CuS phase completely covers the surface of the sample at this region.

On the other hand, in the *Cu*-poor region the spectra are characterised by the presence of the dominant peaks at 290 cm^{-1} and 305 cm^{-1}, which may be assigned to the A_1 and A_1^* modes of the chalcopyrite and Cu-Au ordered phases of the $CuInS_2$ compound. The detailed chemical and structural characterisation of the films will be given in the next section. In this section we will study the reliability of the chemical etching process. This process is done in order to remove the CuS segregated at the surface of the *Cu*-rich films, and constitutes a required technological step for the fabrication of the solar cell devices. From the characterisation point of view, it is important to analyse the surface of the absorber layer after the chemical etching. The performance of the solar device critically depends upon the quality of the surface of the absorber, due to the fact that in the $CuInS_2$-based cell most of the photons are absorbed close to the surface. In the next figure, the Raman spectra of a *Cu*-rich point of a coevaporated sample after and before the chemical treatment are shown.

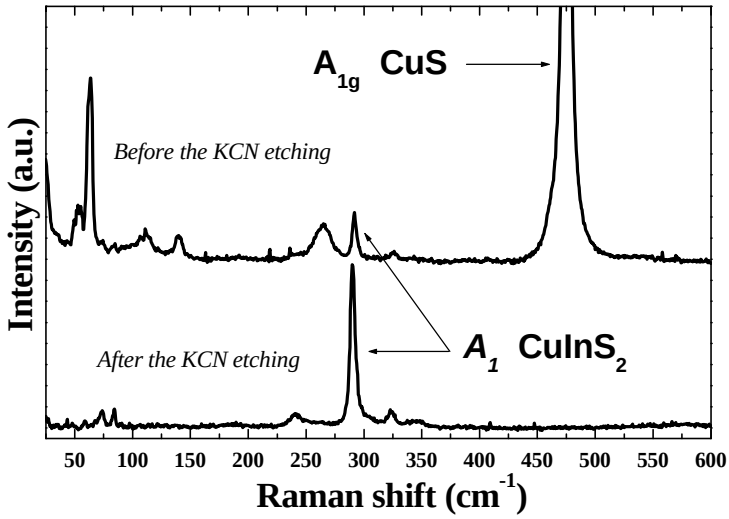

Figure 4. 3. Raman spectra of a *Cu*-rich point before and after the KCN etching.

As can be appreciated, the chemical etching is very effective in removing the CuS. This can be seen by the absence of the CuS related peaks after the etching. Notice that micro-Raman spectroscopy may be a valid technique for the assessment of the KCN etching step. This is related to the relatively high Raman scattering cross section of CuS, and makes the Raman technique very sensitive to the presence of this secondary phase. Moreover, the spatial resolution of the technique allows investigating the presence of possible CuS local segregation. On the other hand, no changes are observed in the spectral features of the $CuInS_2$ bands after the chemical etching. This strongly suggests that the chemical etching process does not have any effect upon the structural properties of the chalcopyrite phase. Accordingly, the KCN treatment does not cause any chemical damage at the chalcopyrite phase.

4.3. Effect of growth temperature and composition.

4.3.1. Surface analysis

The chemical etching of the films is the last step before the deposition of the CdS layer in the solar cell fabrication process. Therefore, a systematic investigation of the properties of the etched films is important for the comprehension of the electrical characteristics of the devices. As will be shown, growth temperature and growth stoichiometry have a direct influence on the properties of the films. In fact, Scanning Electron Microscopy (SEM) pictures already reveal that the Cu/In ratio strongly affects the microstructure of the polycrystalline material. These differences can be seen in next SEM photographs corresponding to a *Cu*-rich and a *Cu*-poor etched samples, grown at 520ºC.

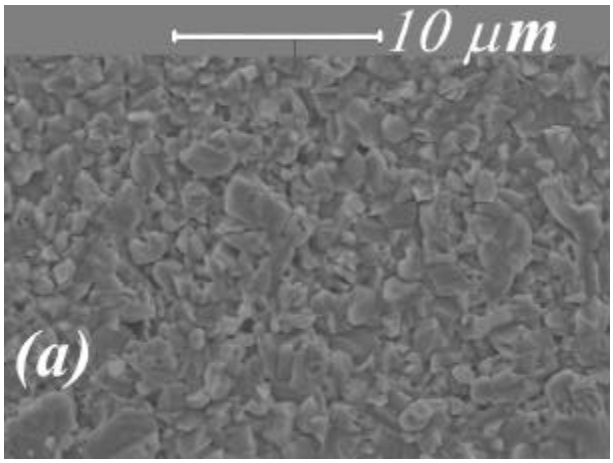

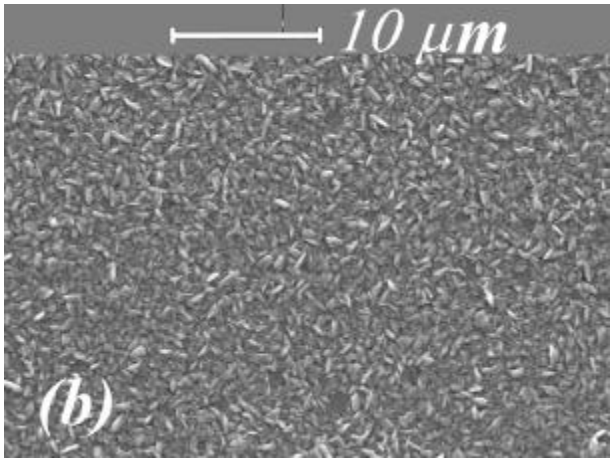

Figure 4. 4. SEM pictures of a *Cu*-rich (a) and a *Cu*-poor (b) samples grown at 520ºC, after been etched in KCN for the removal of the CuS.

The main difference between both samples is clearly the grain size of the $CuInS_2$ grains. *Cu*-excess conditions during growth results in a higher grain size (typically around 1 μm), which is attributed to the capability of the *Cu* atoms to promote the grain growth. In both cases the film looks dense and compact. Moreover, the morphology of the grains of both samples is also different. While grains in the *Cu*-poor sample present a droplet-like shape, the *Cu*-rich sample is characterised by much more spherical grains. More detailed TEM micro-structural characterisation of these films performed in our laboratory can be found in the literature [171, 172].

The results concerning the surface properties of the films will be presented first. As discussed above, the presence of defects or secondary phases at the surface of the absorber of a solar cell device may have a strong influence on the optical and electrical parameters of the heterojunction. As a matter of fact, the surface properties of the $CuInS_2$ semiconductor significatively differ from their bulk properties. This can be seen just by studying the composition at different points of the samples. AES measurements show that after the KCN etching, the

surface composition of the films becomes *Cu*-poor, even in the *Cu*-rich edge of the samples. The *In/(In+Cu)* ratio measured at different points of the surface of the samples is around *0.6*. The thickness of this surface *Cu* depleted region has been estimated to be around 200 nm. Nevertheless, the composition found for points at deeper positions is in good agreement with the chemical growth conditions. For points at the *Cu*-rich region the composition becomes slightly *Cu*-rich (most of the *Cu* segregates at the surface as CuS), while the points at the *Cu*-poor region keep their *Cu*-deficient composition. The bulk composition for the different analysed samples will be given in the next section, in which the AES depth profiles of these samples are shown.

Despite the chemical differences between the surface and the bulk of the samples, micro-Raman spectroscopy does not give any clear indication for the existence of a different ordering at the surface with respect to the bulk of the sample. Compositional values at the surface of the samples are close to those expected for the OVC $CuIn_2S_{3.5}$, although no other signs for the presence of this phase were found from the Raman and XRD analysis of the samples. Notice also that this *In/(In+Cu)* rate may also be achieved by a mixture of $CuInS_2$ and $CuIn_3S_5$ phases. Neither in this case it has been found any evidence for the presence of this phase in the samples from the XRD and Raman spectra. However, taking into account the chemical properties of the I-III-VI compounds, it is clear that the Cu deficiency at the surface should be accommodated by the introduction of complex defects involving ($2V_S^- + In_{Cu}^{2+}$) in the chalcopyrite lattice. Although the periodic repetition of this defects along the crystal would lead to the formation of the OVC crystalline phases, these defects may not involve long-range ordering, as suggested by C. Chang [173] et al. In this case, the existence of these non-periodically distributed defect complexes provides an explanation for the chemical stoichiometry deviation at the surface of the samples, as well as for the no detection of any surface crystalline phase.

On the other hand, the Raman spectra obtained at equidistant points at the surface of the set of etched coevaporated samples show the strong influence of

the growth temperature and composition upon the structural properties of the material. Next figure shows two characteristic Raman spectra of *Cu*-rich and *Cu*-poor points of the sample coevaporated at 520ºC.

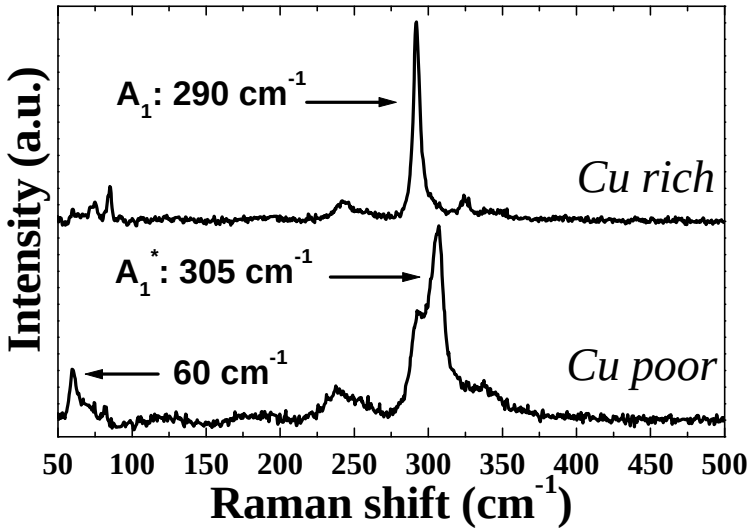

Figure 4. 5. Raman spectra of Cu-rich and Cu-poor points of the coevaporated sample grown at T = 520ºC.

The most significative difference between both spectra is the apparition at the *Cu*-poor region of the sample of the Cu-Au related mode at 305 cm^{-1} (A_1^*) and also the low-frequency mode at 60 cm^{-1}. As shown in the previous figure, these bands appear together with the chalcopyrite modes. This indicates that for points grown under *Cu*-poor conditions, chalcopyrite and Cu-Au ordering coexist in $CuInS_2$. In contrast with the *Cu*-poor region, the spectra from the *Cu*-rich region of the sample grown at this temperature present only chalcopyrite ordering. However, a small shoulder appearing close to the A_1 band, centred at around 305 cm^{-1}, may indicate the existence of a small residual fraction of Cu-Au ordered phase. In addition to the effect of the *Cu* deficiency, the growth temperature has also a direct influence on the cation ordering in the samples. For growth temperatures below 420ºC, Cu-Au ordering is observed even at the

Cu-rich region of the samples. In the case of the sample grown at the lowest temperature (370ºC), the A_1^* mode of the Cu-Au ordered phase dominates the spectra for all the measured points.

These experimental results are presented in *figure 4.6*, where the surface *Cu*-rich and *Cu*-poor Raman spectra for the four samples grown at different temperatures are plotted.

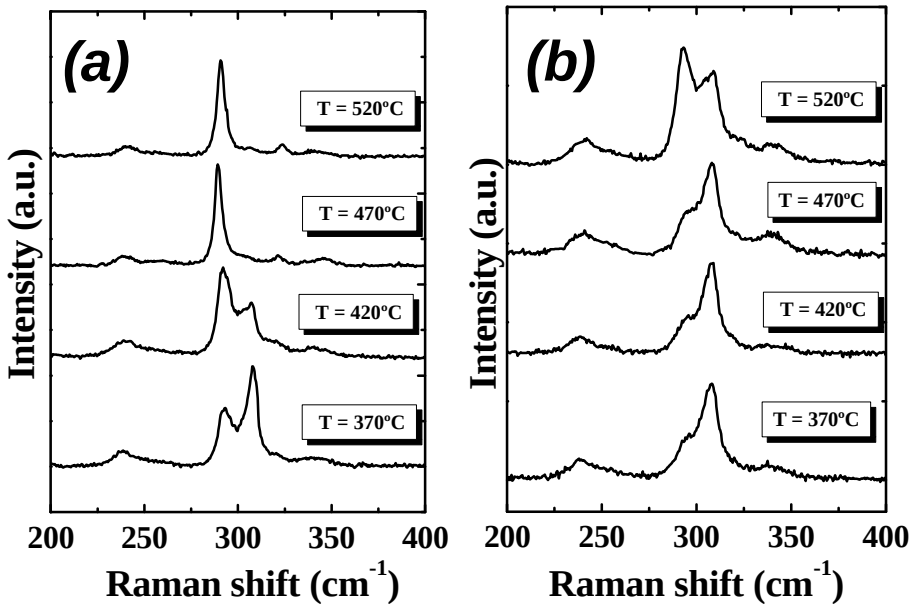

Figure 4. 6. Raman spectra of *Cu*-rich (a) and *Cu*-poor (b) points of samples grown at different substrate temperature.

Notice that although Cu-Au ordering in the *Cu*-poor region of the samples is observed for all the samples (*Figure 4.6b*), there is a decrease of the relative intensity of the A_1^* modes with the growth temperature. Therefore, the increase of the growth temperature tends to avoid the formation of Cu-Au ordering in the films, although in the *Cu*-poor region the highest growth temperature is not high enough in order to prevent its formation. Unfortunately, it has not been possible

to substantially increase the substrate temperature above this value, due to the softening of the glass substrate for temperatures over its glass transition temperature. Thus, according to the Raman results, Cu-Au ordering formation seems to be favoured by the low growth temperatures. This may be explained as due to a kinetic effect. Assuming that the formation of Cu-Au metastable domains occurs during the growth process, higher temperatures may be required in order to overcome the kinetic barrier for the transformation of that Cu-Au domains into chalcopyrite ordered ones. On the other hand, the *Cu* deficiency has also a clear effect on the formation of the Cu-Au phase. Cu-Au ordering may be obtained through the introduction of In_{Cu} antisites in the chalcopyrite lattice (which have a low formation energy in $CuInS_2$). *In/Cu* ratios higher than one clearly favour the formation of this type of defect, and therefore may result in the greater amount of Cu-Au ordered domains. In the case of the *Cu*-excess growth, one may think that high tendency to form $Cu_{2-x}S$ phases reduces the probability for the formation of Cu_{In} point defects.

The crystalline quality of the different samples has also been investigated by studying the spectral features of the A_1 chalcopyrite mode. Although the A_1 and the A_1^* bands overlap, they can be deconvoluted by their fitting with Lorentzian-shape peaks, obtaining accurate information about the position, width and intensity of the bands. The width of the Raman bands is generally expressed as the Full Width at Half Maximum (FWHM) of the peak. The fitting error for the position of the modes has been found always to be less than 0.2 cm^{-1}. The errors for the values of the FWHM of the peaks were around 5%, and the error in the intensities has been found to be greater (around 10%). It is well-known that although the crystallinity of the material has a strong influence on the absolute intensity of the Raman scattered intensity, this value is strongly sensitive to small variations of the measuring conditions (as slight defocusing or misalignments, and presence of dust particles in the samples or in the laser path). The most reliable parameter for the crystalline quality of the samples is probably the FWHM of the peaks, hereafter referred to as G. In the following figure (*figure 4.7*), the values of the G for the A_1 chalcopyrite mode measured at

different points of these samples are plotted. In the figure it is also indicated the stoichiometric line separating the Cu-rich and Cu-poor regions of the films. The experimental values may be compared with the G obtained for a $CuInS_2$ single crystal reference (G_{SC} = **3.5 cm^{-1}**).

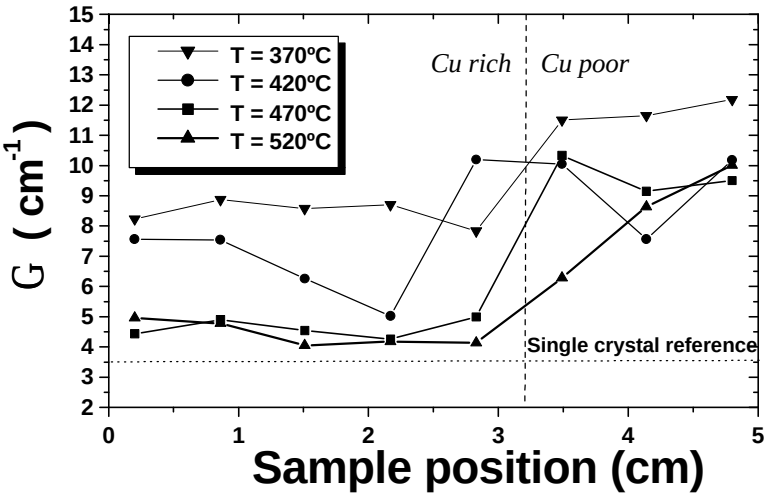

Figure 4. 7. FWHM (G) of the chalcopyrite A_1 mode for different points at the surface of the analysed samples.

The effect of the growth composition and temperature upon the crystalline quality of the chalcopyrite phase can be clearly appreciated. The higher material quality is achieved for the highest growth temperature under *Cu*-excess conditions. Even in this case, the G of the A_1 is still greater than that of the single crystal reference sample. This is attributed to the existence of crystalline defects in the polycrystalline films, which may affect the phonon lifetime, thus increasing the width of the Raman mode. Moreover, a decrease of the growth temperature also leads to an increase of the G of the A_1 band, which indicates the higher density of defects in samples grown at lower substrate temperatures. Notice also that for each sample, a deterioration of the crystalline quality of the chalcopyrite phase is observed at the *Cu*-poor region.

The crystallinity of the samples has been also studied by XRD and TEM for comparison. These experiments prove that, as one may expect, the behaviour of the G of the A_1 band clearly correlates with the evaluation done by XRD and electron microscopy. In the case of XRD, the intensity of the chalcopyrite reflections in the spectra has been observed to be lower for samples where the A_1 chalcopyrite band is wider and the relative intensity of the A_1 peak lower. In a similar way, the TEM analysis of the samples shows that the microstructure of bad crystallinity samples is characterised by high density of defects in the grains, including dislocations and stacking faults.

The Raman shift of the chalcopyrite A_1 mode is also affected by the growth conditions. Experimental results show that the broadening of the band is always accompanied by a blue shift of the mode with respect to the single crystal reference position. The magnitude of this shift is comprised between 0 and 5 cm^{-1}. To clarify the possible relationship of this shift with residual stress in the samples, XRD *($sin^2 y$ vs. d^2)* measurements have been performed at both *Cu*-rich and *Cu*-poor regions. The chalcopyrite (112) and (224) reflections have been selected for these measurements. From these results, no direct evidence for the existence of stress in the samples could be found, within an estimated range of ±100 MPa. Moreover, other factors may also affect the position of the Raman bands. The strong correlation between the shift of the A_1 mode and its broadening indicates that they are related. Therefore, some relation may exist between the crystalline defects and the shift of the mode. This can be understood by considering that under the presence of defects, phonons with $\vec{k} \neq 0$ may be activated. Under these conditions, the dispersion curves for each optical phonon should be considered. In the case of the $CuInS_2$ compound, ab-initio calculations performed by J. Lazewsky [174] have shown that the slope of the phonon dispersion curve for the A_1 mode is positive close to the centre of the Brillouin-Zone for different directions in the reciprocal space of the crystal. Therefore, the defect activation of phonons close to the G point of the Brillouin-

Zone provides a possible explanation for the experimental blue shift of the A_1 mode, and its close relation with the widening of the peak. On the other hand, if the *Cu* deficiency is partially compensated by the introduction of a small fraction of In_{Cu} anti-sites, the effective force constant for the A_1 vibration is expected to increase, which would also explain the observed blue shift of the mode.

Finally, it is worth to note the strong correlation between the degradation of the structural quality of the chalcopyrite phase and the existence of Cu-Au ordering in the material. This relation can be clearly seen in *Figure 4*.8, where the relative intensity of the A_1^* mode $\left[I(A_1^*)/I(A_1)\right]$ is plotted versus the frequency and G of the A_1 mode for different measured spectra.

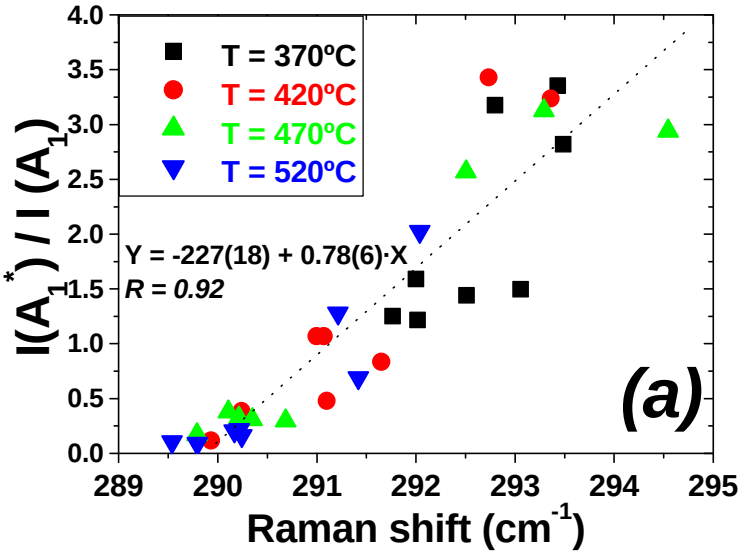

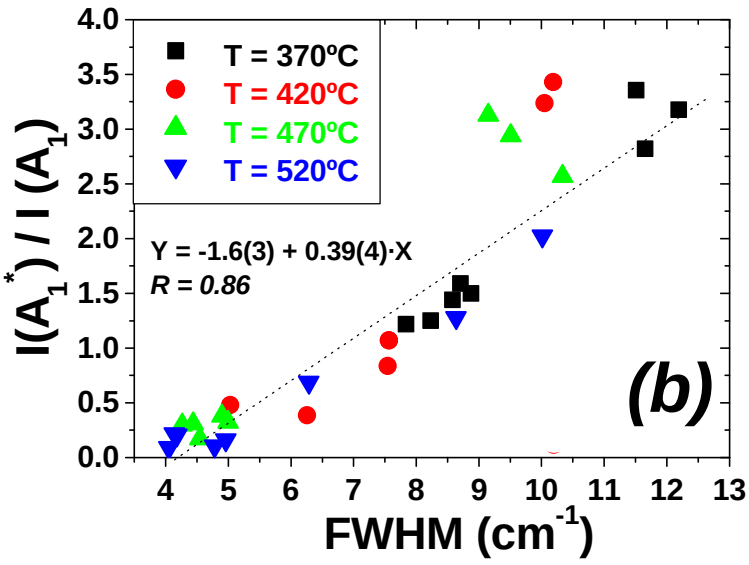

Figure 4. 8. - Correlation between the FWHM and Raman shift of the chalcopyrite A_1 mode, with the relative intensity of the A_1^* Cu-Au band.

The relation between the bad quality of the films and the existence of Cu-Au domains in the films may be explained as due to different factors. First, it is clear that although the electronic properties of both polytypes are expected to be very similar, the boundaries of the ordered domains may act as scattering centres, thus decreasing the phonon life-time. In any case, the coexistence of different ordered domains leads to the breakage of the long-range ordering of the crystalline material. On the other hand, it may be possible that the microscopic mechanism responsible for the formation of Cu-Au domains could involve the formation of some kind of defects in the material (such as In_{Cu} antisites or stacking faults), which at the same time would result in the deterioration of the chalcopyrite phase.

On the other hand, the comparison of the relative intensity data for the different samples suggest the existence of a transition growth temperature at 420ºC. For temperatures above this value, the films appear to be almost free of Cu-Au

domains, as long as *Cu*-rich growth conditions are chosen. The later may be seen in *Figure 4.9*, where the relative intensity of the A_1^* band is represented for surface points of the samples.

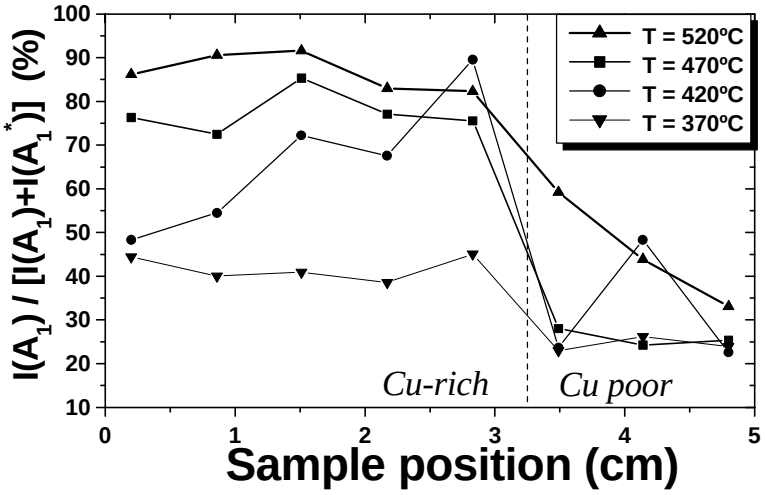

Figure 4. 9.- Relative intensity $\frac{I(A_1)}{I(A_1)+I(A_1^*)}$ for different surface points of each analysed coevaporated sample.

On the basis of these results, the relative intensity of the A_1^* Cu-Au band has been postulated as a quality indicator of the material, and in general, the presence of the A_1^* mode is always indicative of films resulting in solar cells with bad performance. For an industrial-scale process it is desirable to have tools for detecting errors in each technological step before the cells are completely processed and electrical measurements can be carried out on them. Needless to say, this leads to a reduction of fabrication costs and to a saving of raw material, thus reducing the unitary cost of the final cell, which is one of the main aims of the thin film solar cell technologies. Taking the experimental results into account, Raman spectroscopy may be a very useful tool for the on-line control of a production line of $CuInS_2$ solar cells. This technique would

easily allow detecting possible deviations of the optimal growth conditions during the growth of absorbers, which would lead to low efficient devices. Although the $CuInS_2$-based technology is currently under development, other more mature chalcopyrite-based technologies ($CuInSe_2$ mainly) could also implement Raman spectroscopy as a quality-control step for the absorbers.

4.3.2. "In-depth" Raman/AES study

The small penetration depth of the excitation light for Raman spectroscopy in $CuInS_2$ (around 150 nm) has the advantage that the information extracted from the surface spectra corresponds to the region of the film that absorbs most of the incident radiation in the solar cell device. Nevertheless, an accurate characterisation of the bulk properties of the films requires the possibility for investigating points at deeper positions. For this purpose, we have developed a systematic procedure for the analysis of these samples by combining micro-Raman and Auger Electron Spectroscopy, as discussed in the first section of the present chapter. These results will be compared with the results provided by XRD and TEM, which are presented on the next section of the present chapter.

***Cu*-poor region**

In order to study the effect of the growth temperature, we have investigated the bulk properties of the films coevaporated at 370ºC and 520ºC. *Figures 4.10 (a)* and *4.10 (b)* show the AES compositional depth profiles obtained for points at the *Cu-poor* region of these samples.

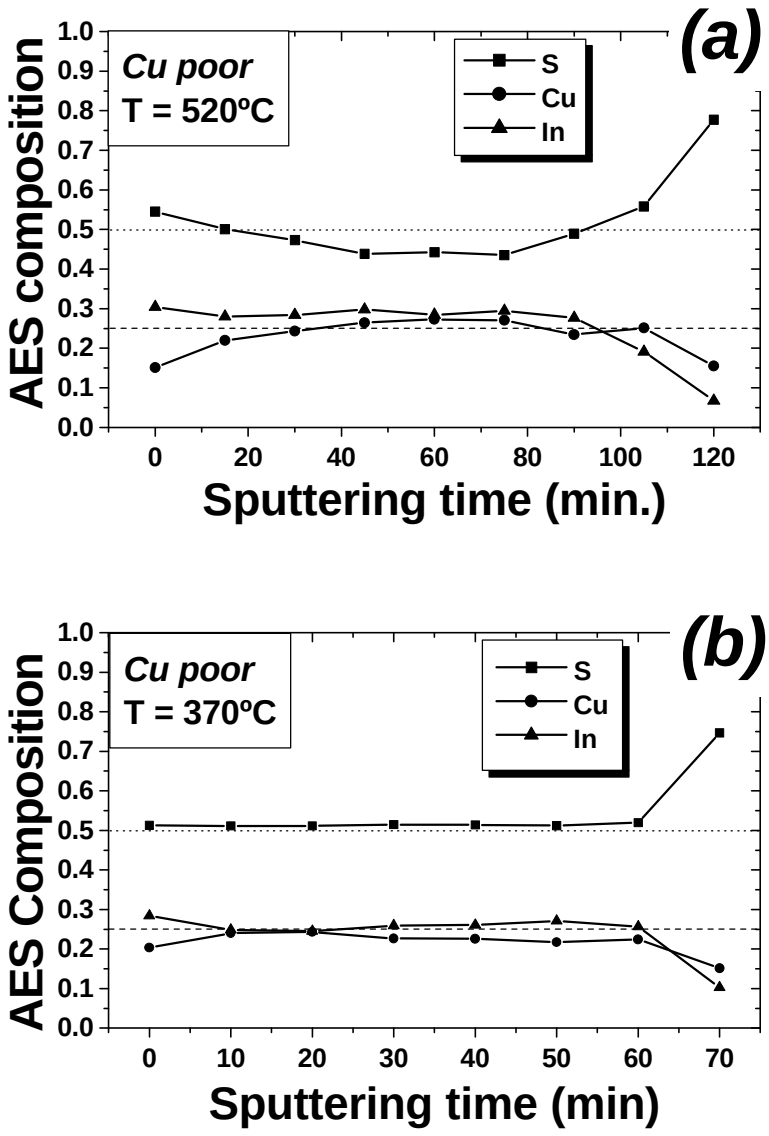

Figure 4. 10. AES depth profiles of *Cu*-poor edges of samples grown at 520ºC (a) and 370ºC (b).

In both cases the *Cu*/*In* ratio at the surface is lower than at the bulk, indicating the existence of a *Cu* depleted region at the surface of the samples. However, the *Cu*/*In* ratio is quite constant below the surface region. To describe the relative *In* to *Cu* ratio as, we may define a parameter ξ as: $x \equiv \frac{[In]}{[In]+[Cu]}$. The average values of this parameters for the bulk of both samples were $<\xi>$ = 0.54 and $<\xi>$ = 0.53 for the samples grown at 520ºC and 370ºC, respectively. As shown in the figure, the sample grown at the highest temperature has a more homogenous compositional profile.

The spectral series obtained in the combined Raman/AES measurements are shown in *figure 4.11*. The spectra have been vertically shifted in such a way that the spectrum at the bottom of each figure corresponds to the spectrum measured at the surface, whereas the spectrum at the top corresponds to the deepest point of the bulk (closest to the *Mo* back contact). The number of sputtering steps (***N***) before each spectrum was recorded has been indicated in the figures.

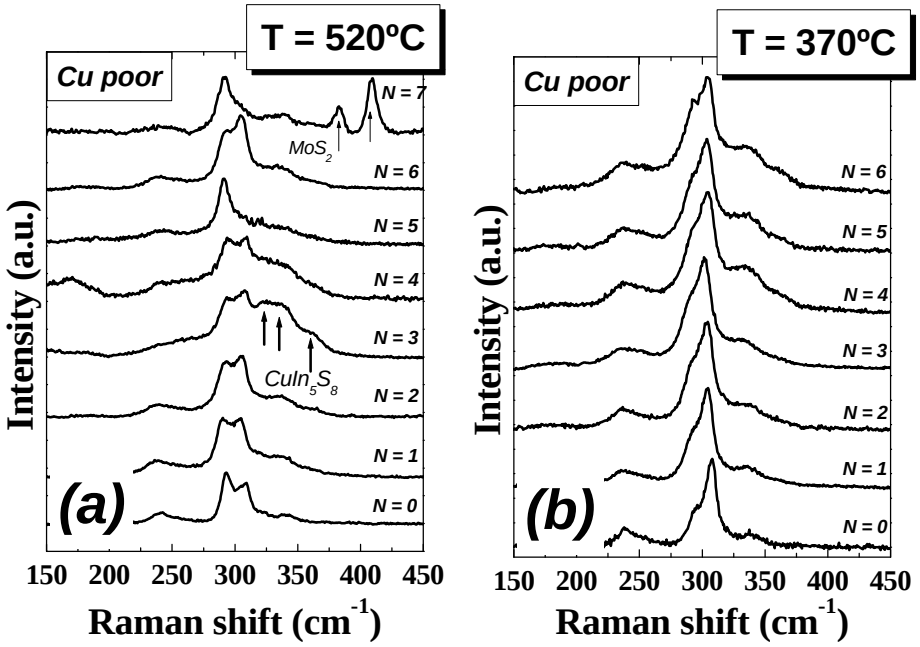

Figure 4. 11. Bulk Raman spectra for the *Cu*-poor edges of samples grown at 520ºC (a) and 370ºC (b).

The first important conclusion that may be extracted from these spectra is that the Cu-Au ordered phase in the *Cu*-poor region of the films is present through all the bulk of the samples, independently of the growth temperature of the sample, though a decrease of the relative intensity of the A_1^* is observed close to the back contact. Moreover, similarly to what was observed in the surface analysis, the A_1 band of the sample grown at the lowest temperature shows a bigger width and blue shift through the whole layer, when compared with the sample grown at the highest temperature. A second interesting feature is the apparition of new bands at 325 cm^{-1}, 340 cm^{-1} and 360 cm^{-1}, in some of the bulk spectra of the sample grown at T=520ºC. These bands can be related to the $CuIn_5S_8$ spinel phase [175], and show that the *In*-excess in this sample results in the formation of micro-precipitates of such *In*-rich phase. It is also worth to remark that the observation of these bands in the spectra is accompanied by a more

pronounced blue shift and broadening of the A_1 chalcopyrite band. These effects may be due to the existence of local residual compressive stresses in this region of the sample, due to the precipitation of the secondary phase. In the case of the sample grown at 370ºC, the formation of the spinel phase seems to be less favoured, and the $CuIn_5S_8$ Raman bands can not be clearly resolved, though in fact some contributions in that spectral range arise in the form of broad bands. All these results demonstrate the strong influence of the growth temperature upon the structural properties of the surface and the bulk of the films.

Finally, the Raman/AES combined measurements have been useful for the study of the $CuInS_2$/*Mo* interface region. The interface between the metallic back contact and the absorber is of great importance, not only because of its influence on the electronic properties of the device, but also because interface phenomena may be responsible for the adhesion failure problems frequently observed in these films. In this sense, the Raman spectrum of the sample grown at 520ºC measured at the point closest to the *Mo* interface shows new bands at about 383 cm^{-1} and 408 cm^{-1}. These bands have been identified as belonging to the MoS_2 compound, which is formed at the interface. The hexagonal layered structure of this compound is expected to be low resistant to mechanical shear stresses, and therefore it may have a direct negative influence on the adhesion of the films. The formation of the MoS_2 secondary phase at the interface may be inhibited by the *Cu*-excess growth conditions, since this phase is less detectable in *Cu*-rich points.

Cu-rich region

The structural properties of the *Cu*-rich region of the films are much more dependent on the growth temperature than those of the *Cu*-poor region. This can be seen by comparing the AES compositional depth profiles for points at the

Cu-rich region of the sample grown at 520ºC and at 370ºC, which are plotted in *figure 4.12*.

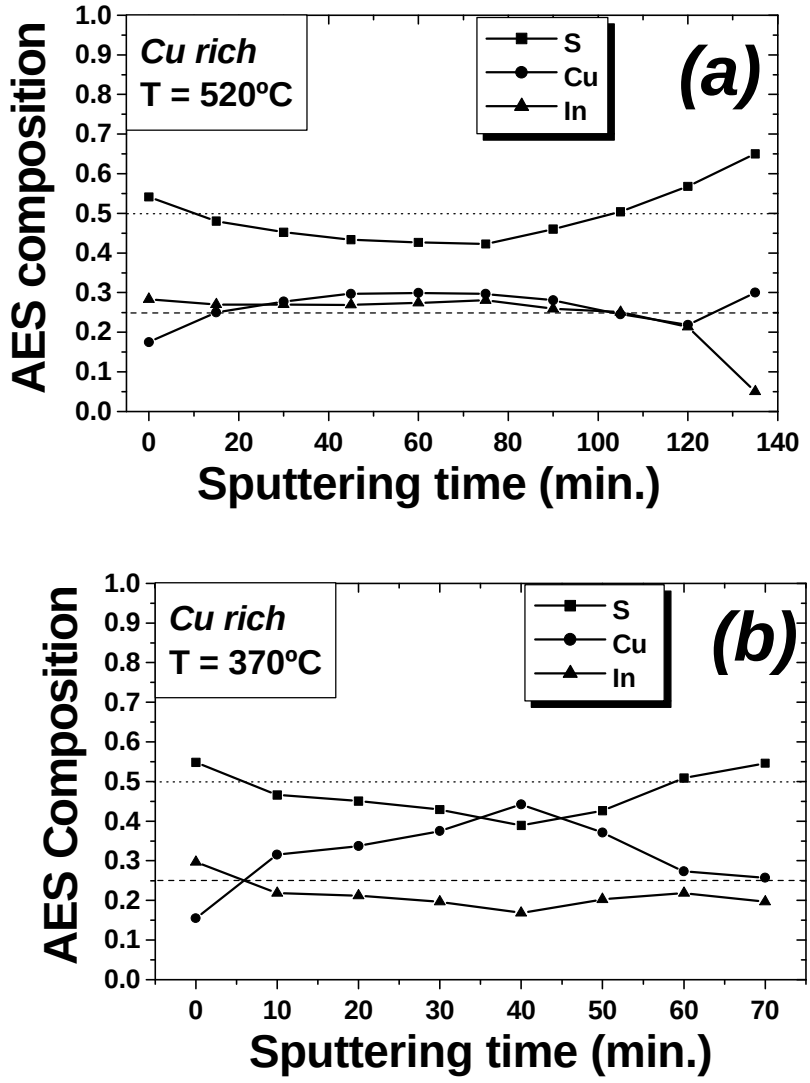

Figure 4. 12. AES depth profiles of *Cu*-rich edges of samples grown at 520ºC and 370ºC.

In the case of the sample grown at higher temperature, the composition of the bulk of the sample appears quite homogeneous and close to the stoichiometric values ($<\xi> = 0.49$). Only close to the surface the composition is *Cu*-deficient, and ξ is around 0.65. On the other hand, the sample grown at the lowest growth temperature presents a clear *Cu*-excess at the bulk. In this case, the low temperature seems to prevent segregation of all the *Cu*-excess at the surface of the sample. As a result, the bulk of the sample retains part of the *Cu*-excess, leading to a value for $<\xi>$ at the bulk of *0.35*. It is not clear the way in which the Cu-excess is present in the film. It does not seem very likely that a so high *Cu*-excess could be incorporated in the chalcopyrite lattice without affecting the stability of this phase. The most probable explanation is that the *Cu*-excess forms $Cu_{2-x}S$ precipitates (no metallic *Cu* has been detected by XRD). Due to the strong similitude of the XRD spectra of some these $Cu_{2-x}S$ phases with the spectra of the $CuInS_2$ chalcopyrite one, it is not evident to confirm this assertion. Moreover, one should bear in mind that the presence of a secondary phase in the films limits the validity of the AES sensitivity factors used for the quantification of the composition. Thus, one should be cautious when considering the quantitative values provided by AES under these conditions.

The Raman spectra from the bulk of both samples obtained by the Raman/AES measurements are shown in *figure 4.13*. Here again, the spectrum at the bottom of each figure corresponds to the surface of the samples, while the spectrum at the top arises from points closest to the *Mo* back contact. The number of sputtering steps (***N***) has also been indicated in the figures.

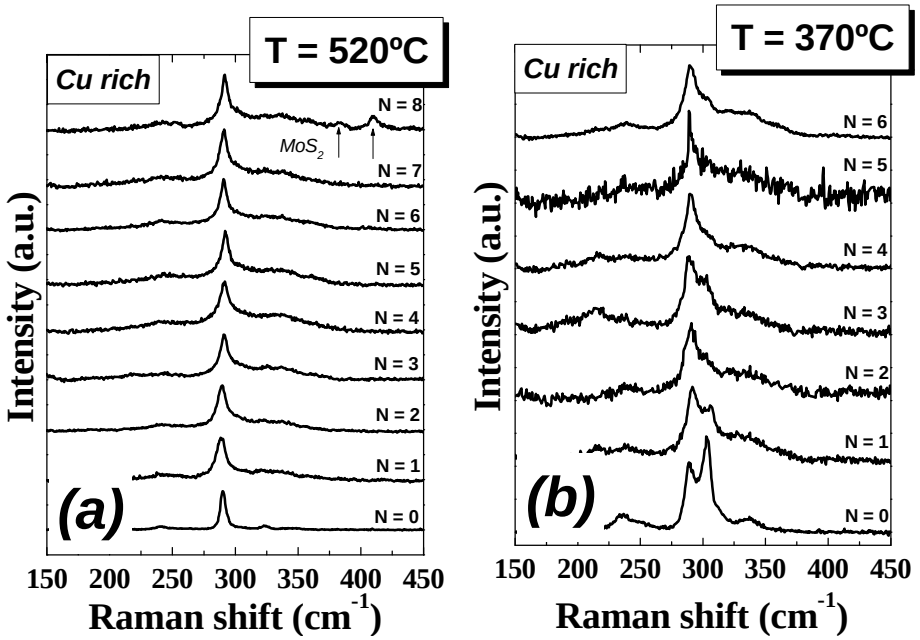

Figure 4. 13. Raman spectra from the bulk of points at the *Cu*-rich edge of the samples grown at 520ºC and 370ºC.

Significative differences exist between the spectra of the samples grown at 520ºC under *Cu*-rich and *Cu*-poor conditions. In the first case, the higher growth temperature makes possible the segregation of most of the *Cu*-excess to the surface of the film as CuS, which afterwards is eliminated. In addition to this, the high temperature together with the beneficial effect of the *Cu-excess* gives rise to a good quality chalcopyrite structure. Neither in the surface nor in the bulk of this sample, significative contributions of the Cu-Au phase can be detected. *Figure 4.13a* demonstrates the bulk homogeneity of this sample. Only at the point closest to the $CuInS_2$/*Mo* interface a secondary phase can be resolved, again in the form of MoS_2. This contrasts with the properties of the *Cu*-rich sample grown at 370ºC (*figure 4.13b*). In this case, a significant degradation of the crystalline quality of the chalcopyrite phase is observed from the widening of the A_1 mode, as well as from the appearance of the A_1^* Cu-Au

related band. The low crystalline quality of the layer is also responsible for the much lower intensity of the measured bands in the spectra, which show a much lower signal to noise ratio than in the previous case. However, it seems that the lower growth temperatures hinders the formation of the MoS_2 interface phae, as it was also observed for the *Cu*-poor region of the samples.

In summary, these experiments have allowed to determine the optimal growth conditions for the obtaining of high quality $CuInS_2$ absorbers. *Cu*-poor growth conditions give rise to bad crystalline quality chalcopyrite phase, favouring the formation of Cu-Au ordered domains and the precipitation of $CuIn_5S_8$ spinel phase. On the contrary, *Cu*-rich growth conditions are suitable for obtaining good crystalline quality $CuInS_2$ polycrystalline films, as long as the growth temperature is high enough. For low growth temperatures, *Cu*-excess does not completely segregate to the surface of the film as CuS, resulting in the formation of Cu-Au domains in the film, and probably some $Cu_{2-x}S$ precipitates.

4.3.3. XRD and TEM characterisation

In this section, the results about the structural properties of the material provided by Raman spectroscopy will be complemented with those extracted from XRD and TEM techniques.

XRD spectra of *Cu*-rich not-etched samples indicate that the samples are constituted by a mixture of CuS and $CuInS_2$. In this sense, XRD can be used also to evaluate the existence of residual CuS phase after the KCN treatment of the samples. However, the intensity of the CuS reflections is quite lower than that of the chalcopyrite reflections, which makes XRD a less sensitive technique than Raman spectroscopy for the detection of CuS phase. In the following plot the XRD spectra of an etched and not-etched *Cu*-rich samples are compared. In

good agreement with the Raman observations, after the chemical etching CuS is not detectable in the samples.

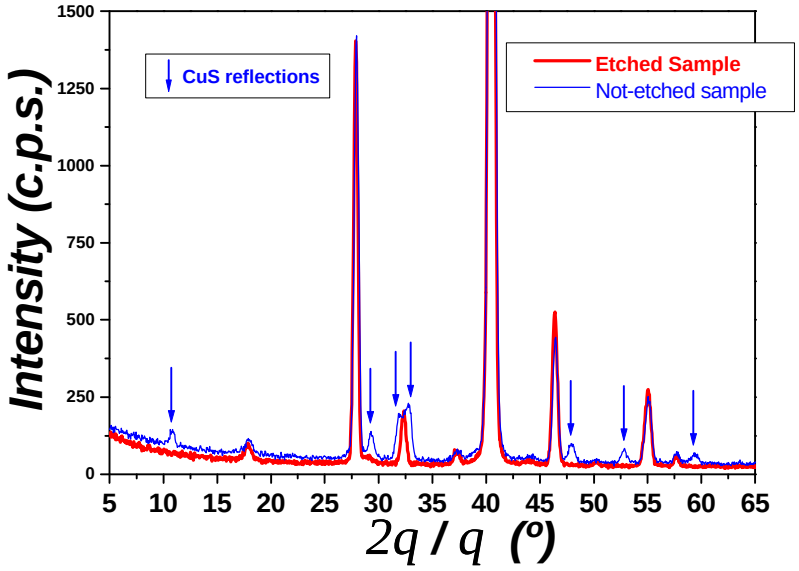

Figure 4. 14. XRD 2q/q diffractograms of a *Cu*-rich sample, not-etched and etched in KCN.

Moreover, there are important differences between the XRD spectra of the *Cu*-rich and *Cu*-poor samples. The most evident one is the confirmation of the existence of *In*-rich phases in *Cu*-poor samples. The identification of *In*-rich secondary phases is not easy by XRD. Many of these phases, such as β-In_2S_3, $CuIn_5S_8$ and other more complex phases as $CuIn_{11}S_{17}$ or In_6S_7 have a great number of reflections which overlap in the spectra. According to the XRD spectra, $CuIn_5S_8$ is detected in some of the *Cu*-poor films, while it has not been possible to confirm the presence of β-In_2S_3. This interpretation is supported by the previous Raman results. XRD spectra of the *Cu*-rich and *Cu*-poor sides of an etched sample grown at 520ºC are shown in the following figure.

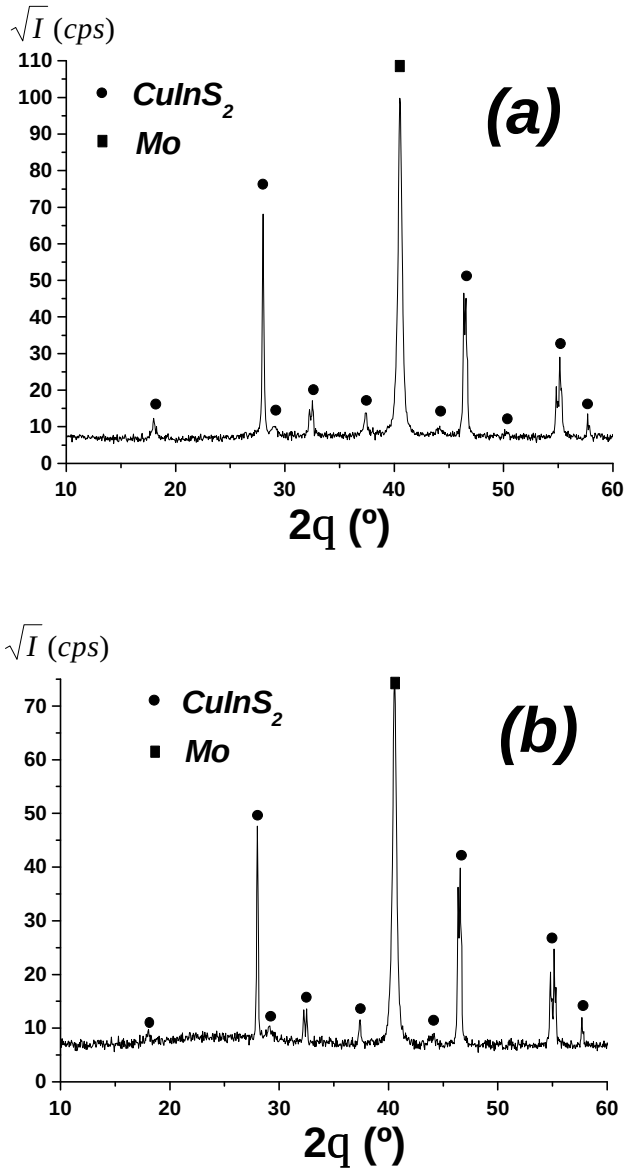

Figure 4. 15. XRD 2q/q diffractograms of a *Cu*-rich (a) and *Cu*-poor (b) samples grown at high temperature (520ºC).

In this case, the *Cu*-poor side of the film was only slightly *Cu*-poor, and therefore the $CuIn_5S_8$ bands are hardly detectable in the spectra. For comparison, we present the following plot corresponding to another co-evaporated sample grown at 520ºC under higher *In*-excess conditions. In this case, the existence of the spinel $CuIn_5S_8$ compound is much clearer:

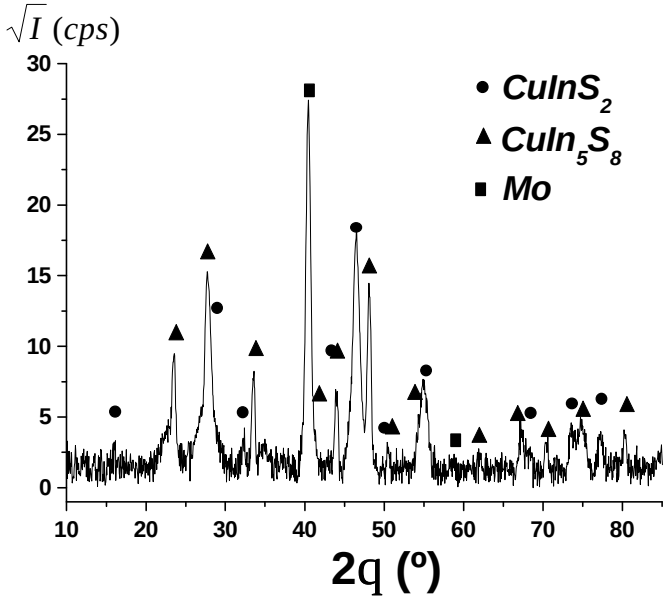

Figure 4. 16. XRD 2q/q diffractogram of a Cu-poor film grown at 520ºC.

The previous spectrum shows that the *Cu* deficient growth conditions give rise to the formation of the spinel compound, whose presence can be identified by XRD if the total amount of this secondary phase is high enough. From the previous Raman/AES combined measurements we know that even in the case of slightly *Cu*-poor growth conditions, the segregation of $CuIn_5S_8$ occurs, though its low concentration may make difficult its detection by XRD. Moreover, this phase segregates at the bulk of the samples, and can not be straightforwardly

removed as in the case of the CuS surface phase in the *Cu*-rich growth conditions.

Besides the precipitation of this *In*-rich phase, differences exist in the properties of the dominant chalcopyrite phase of the films. The strong difference in the diffracted intensity of the peaks is attributed to the lower crystalline quality of the *Cu*-poor sample, which was already observed by Raman. Moreover, the characteristic chalcopyrite splitting of the (004)/(200), which is also considered as a material quality indicator, is generally clearer in the *Cu*-rich sample. Another significative difference is the different texture of both samples. According to the intensity ratio of the different reflections, in the case of the *Cu*-rich film the grains are preferentially oriented in the [221] chalcopyrite direction, while in the case of the *Cu*-poor film this effect is much less evident.

On the other hand, Cu-rich and Cu-poor samples grown at 370ºC have also been investigated by XRD. The results reveal in this case a much lower crystallinity of the film. This is especially true in the case of the *Cu*-poor film in which signs of sphalerite ordering have been found, as will be discussed later. The following figure shows the spectra of both samples (*Cu*-rich and *Cu*-poor grown at 370ºC):

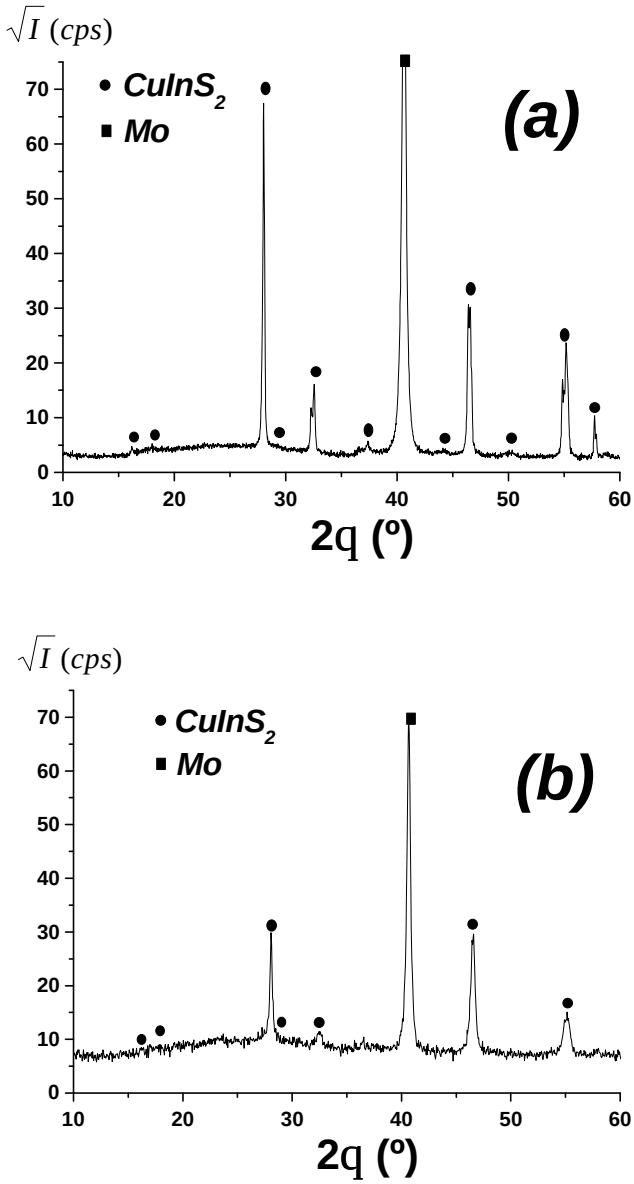

Figure 4. 17. XRD 2q/q spectra of *Cu*-rich and *Cu*-poor samples grown at low temperature 370ºC.

An interesting point concerns with the detection of the Cu-Au ordering by XRD. As can be seen in the XRD patterns, the intensity of the (001) characteristic Cu-Au reflection at $2\theta=16^{o}$ is very low for this set of polycrystalline samples. Only in the case of the samples grown at lower temperatures the peak can be detected using standard integration times (3 seconds per step). In the case of *Cu*-poor samples grown at high temperature, the (001) Cu-Au reflections has also be detected by increasing the integration time up 15 seconds per step. In contrast, the Raman spectra of these samples clearly present the additional Cu-Au characteristic bands. This fact is indicative that in the case of the polycrystalline samples, the coherent size of the Cu-Au domains is much lower than in the case of the epitaxial samples, analysed in *chapter 3*. The decrease of the size of the Cu-Au domains in the polycrystalline films leads to an increase of the width of the XRD peaks, together with a decrease in the maximum intensity of the peak, in order to keep the integral intensity constant. Under these conditions, the Cu-Au phase is likely present in the form of nanometric domains which are detectable by Raman spectroscopy. However, the corresponding XRD reflections are hardly visible by XRD, due to the different sensitivity of both techniques. As a matter of fact, Raman spectroscopy is much more sensitive to short-ordering in the material than XRD [176]. Moreover, the formation of extended Cu-Au domains in the epitaxial films seems to be favoured by the epitaxial growth, which makes easier their detection by XRD.

On the other hand, evidences for the existence of other $CuInS_2$ polytypes have been looked for in the XRD spectra of the polycrystalline films. Sphalerite ordering in $CuInS_2$ can be understood as an effect of disorder in the cation sublattice of the chalcopyrite crystal. Though sphalerite is not an equilibrium phase at room temperature, it may exist as a non-equilibrium phase. As a result of the change of symmetry in the crystalline structure, different XRD reflection conditions hold for the new structure [177], and some chalcopyrite allowed reflections are forbidden for the sphalerite ordering. These correspond to the *(hkl*) planes with par *k* even and (*h,l*) odd, and to planes with *h* even and (*k,l*)

odd. The most intense reflections of this type in $CuInS_2$ are given in the following table:

(h k l)	**2q (l = 1.5418 Å)**
(1 0 1)	17.9º
(1 0 3)	29.0º
(2 1 1)	37.3º
(2 1 3)	44.1º

Table 4. 1. Chalcopyrite reflections forbidden for the sphalerite structure.

The other important feature which allows identifying the sphalerite ordering is the absence of the characteristic chalcopyrite splitting between complementary reflections, due to the fact that the relation $c/2a \neq 1$ is no longer true. As a first approximation, the sphalerite unit cell is cubic, with lattice parameter given by $a_{sph} \approx \sqrt[3]{a_{ch}^2 \cdot c_{ch}}$. For the $CuInS_2$ compound, the most intense chalcopyrite splittings correspond to the following relations:

Sphalerite	***Chalcopyrite***	**2q (l = 1.5418 Å)**
(2 0 0)	(0 0 4) + (2 0 0)	32.2º / 32.4º
(2 2 0)	(2 2 0) + (2 0 4)	46.4º / 46.5º
(3 1 1)	(3 1 2) + (1 1 6)	54.8º / 55.1º

Table 4. 2. Relation of some of the characteristic chalcopyrite splittings.

Taking this into account and analysing the XRD spectra of the different samples, one should conclude that sphalerite ordering is not present either in the *Cu*-rich samples or in the *Cu*-poor sample grown at the highest temperature.

However, in the case of the *Cu*-poor sample grown at 370ºC, the chalcopyrite splittings given in **[table 4.2]** are hardly visible, and the distinctive chalcopyrite reflections are difficult to detect. Therefore, these results indicate that the *Cu*-deficient conditions during growth seem to favour the cation disordering in the lattice, thus resulting on the formation of the sphalerite non-equilibrium phase of the $CuInS_2$ compound, as far as the growth temperature is low enough. For film growth under high temperature conditions, formation of sphalerite ordering seems to be less favourable.

Regarding the possible existence of residual stresses in the grains, $sin^2 y \ \ vs. \ d$ XRD measurements have been performed at the *Cu*-rich and *Cu*-poor region of the samples grown at 520ºC and 370ºC, using the (112) and (224) chalcopyrite reflections. The measurements were performed for different values of the angle ϕ. It is well-known that the existence of a biaxial stress state in the film leads to a linear dependence of the interplanar distance *(d)* with the parameter $(sin^2 y)$. More complex stress states in the sample may lead to a more complicated relation between both parameters [178]. In our case, all the samples present important oscillations in the curve $sin^2 y \ \ vs. \ d$. However, these oscillations could be explained just as due to experimental errors. Therefore, all the co-evaporated samples appear to be stress free within the experimental error. By considering the dependence of $sin^2 y \ \ vs. \ d$, the maximum stress in the samples has been estimated to be no more than 100 MPa.

Finally, cross-section TEM images are presented in order to relate the structural properties of the films deduced by Raman and XRD, with their microscopic images. *Figure 4.18* shows cross-section TEM pictures of the *Cu*-rich and *Cu*-poor regions of the samples grown at 370ºC and 520ºC.

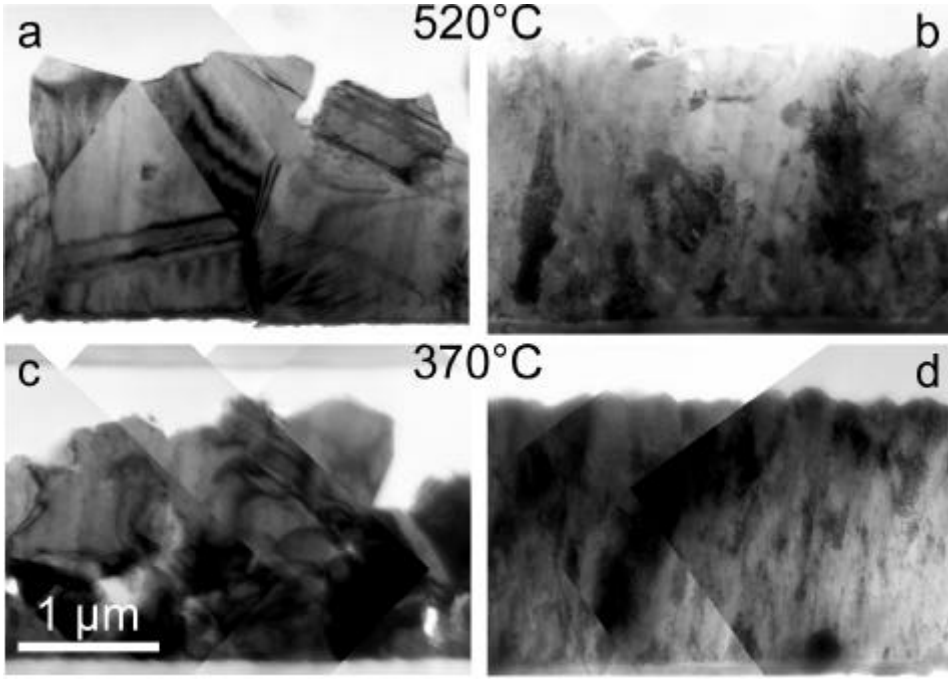

Figure 4. 18. Cross-section TEM images of the *Cu*-rich (left) and *Cu*-poor (right) coevaporated samples at 520ºC and 370ºC.

Differences in the morphology between the different samples become clearly visible from these TEM images. In the case of the samples grown under *Cu*-rich conditions, the resultant structure is constituted by big grains (the typical size for the sample grown at 520ºC is around 1 µm or even greater), in which different types of crystalline defects have been identified, such as dislocations, stacking faults and twins. In good correlation with Raman and XRD, the *Cu*-poor region of the samples presents a much lower grain size and a higher density of defects, which can be appreciated in the TEM images. Moreover, *Cu*-poor samples present a different morphology, with columnar-shaped grains. In both cases, the decrease of the growth temperature leads to a reduction of the grain size and to an increase of the density of defects in the material.

On the other hand, the crystalline structure of the samples has been investigated by TED. Cu-Au and chalcopyrite ordering have been found to coexist in these samples, corroborating the previous Raman results. Although Cu-Au has also been found in some regions of the samples grown at high temperature under *Cu*-rich conditions, Cu-Au ordering has been found to be characteristic of *Cu*-poor samples and *Cu*-rich samples grown at low temperature. Cu-Au is observed predominantly together with chalcopyrite ordering in the different grains of the films. Only for samples grown at low temperature under *Cu*-poor conditions, it has been detected small nanometric grains (~50 nm) in which Cu-Au ordering is the only order observed. The estimation of the size of these domains in the polycrystalline films by HRTEM has not been possible up to now, due to the great difficulty to identify the orientation of the small grains of the samples.

4.4. Conclusions

In this chapter, the characterisation of co-evaporated $CuInS_2$ polycrystalline films by means of Raman and XRD has been presented. Special emphasis has been given to he effect of the growth stoichiometric variations and to the growth substrate temperature. A good correlation between the XRD, TEM and Raman data has been obtained. For samples grown at high enough substrate temperature under *Cu*-excess conditions, the co-evaporation process leads to the formation of a chalcopyrite phase with good crystalline quality. In this case, *Cu*-excess segregates to the surface in the form of the hexagonal-type CuS phase, which can be effectively removed with a KCN chemical treatment. On the other hand, films obtained under *Cu*-poor growth conditions consist of a mixture of chalcopyrite and Cu-Au ordered $CuInS_2$ polytypes, while *In*-excess has been found to precipitate in the form of $CuIn_5S_8$. In this case, the $CuInS_2$ crystalline phase presents a much higher density of defects, which is responsible for the poorer performance of the cells obtained from *Cu*-poor films. Furthermore, the decrease of the growth temperature has a similar effect upon the chalcopyrite phase that the growth under *Cu*-deficient conditions. Also in this case, the formation of Cu-Au domains and the decrease of the crystalline quality of the material can be appreciated, even in the case of *Cu*-rich films.

Raman/AES combined measurements have allowed to identify the presence of MoS_2 phase close to the $CuInS_2$/Mo interface, in the samples grown at higher substrate temperature. The formation of this layered compound close at the interface of the solar device may affect the electronic properties of the device, and it may also be responsible for the adhesion failure problems observed in some of these films.

When the growth conditions are not optimum for single-phase chalcopyrite growth (*Cu*-poor or low temperature growth conditions), the coevaporation

process leads to the formation of Cu-Au ordered metastable domains, which coexist with chalcopyrite ordered domains. The coexistence of both polytypes leads to a worsening of the crystallinity of the chalcopyrite phase, due to the breakage of the translational symmetry of the crystal. Therefore, the Raman spectra of the films reveal a good correlation between the structural properties of the chalcopyrite phase and the relative intensity of the A_1^* Cu-Au band. As a result of this, the relative intensity of the A_1^* band with respect to the A_1 chalcopyrite one can be used as a crystalline quality indicator for the evaluation of the structural quality of $CuInS_2$ films. The correlation between this parameter and the final efficiency of the solar cell device has led to propose Raman Spectroscopy as a reliable technique for the on-line quality control of chalcopyrite-based solar cell production line.

5. Baseline sequentially processed films.

5.1. Structural properties of sequentially processed $CuInS_2$ films.

The selection of *Cu*-rich growth conditions for the preparation of $CuInS_2$ films is very advantageous from the point of view of the properties of the resulting material. As presented in the previous chapter, the sulphurisation process under *Cu*-excess conditions gives rise to high quality chalcopyrite films. Moreover, at high enough substrate temperatures it is possible to inhibit the formation of Cu-Au ordered domains in the grains and the precipitation of secondary phases at the bulk of the layers. On the other hand, the large window process offered by the *Cu*-rich preparation recipe is very convenient for the large-scale production of these films. Local *Cu*/*In* stoichiometric variations do not have important repercussions on the final properties of the baseline processed $CuInS_2$ films, which constitutes a significative difference with respect to $CuInSe_2$ films.

The sequential baseline process is based on the sulphurisation of the metallic precursors at around 500ºC, which are previously sputtered onto the *Mo* coated glass substrate. The details of the process were already given in *section **1.4.2***. The reproducibility of the process and the surface homogeneity of the baseline samples have been analysed by micro-Raman spectroscopy. The results indicate a good reproducibility of the baseline process, as well as a high homogeneity of the samples analysed (in their surface and bulk).

A Raman mapping of the surface of a baseline sample has been done in order to analyse in detail the homogeneity of the layer. A series of 16 spectra have been recorded at different points of the surface of the sample, with dimensions 5.0x1.2 cm. No traces of secondary phases were found at any of the spectra.

Moreover, the Raman spectra indicate that the samples are constituted by a single chalcopyrite phase of $CuInS_2$. A slight asymmetry of the shape of the A_1 band is observed, which may be due to the existence of a broad contribution around 305 cm^{-1} related to some residual contribution of the Cu-Au band. The following figure plots a characteristic baseline Raman spectrum:

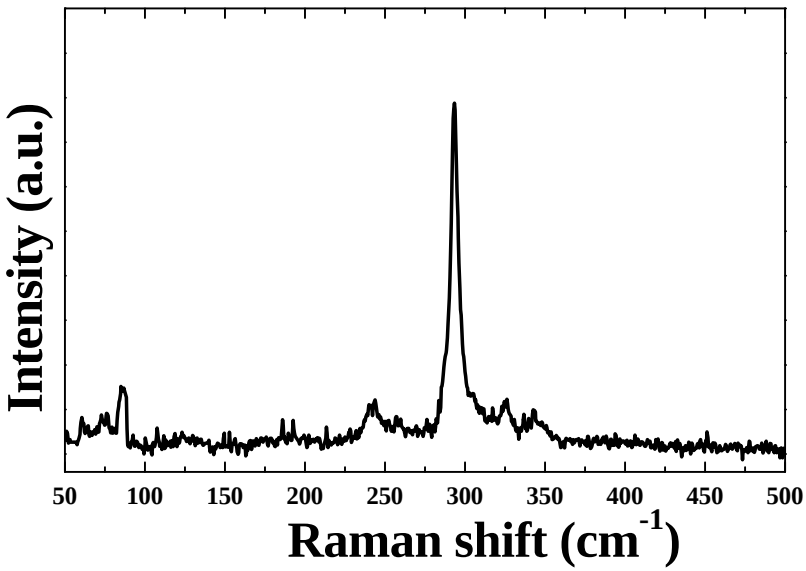

Figure 5. 1. Raman spectrum of a sequentially processed baseline sample.

On the other hand, a low dispersion of the position and the width of the chalcopyrite A_1 mode has been found for the different surface points analysed. The average value for the position and width of the band were $\langle\omega\rangle$ = 290.0 cm^{-1} and $\langle\Gamma\rangle$ = 6.0 cm^{-1}, with standard deviations of 0.6 cm^{-1} and 0.8 cm^{-1}, respectively. Although the average frequency of the band corresponded to the single crystal reference, the average width of the mode was significantly higher than the value obtained for the $CuInS_2$ crystal (G_{SC} = *3.5* cm^{-1}). Also in this case, the relative dispersion of the values was higher. This result indicates that the crystalline properties of the film are still not equivalent to the single crystal

case, as well as the existence of some statistical fluctuations in the crystalline quality of the different grains in the sample. As a matter of fact, the width of the A_1 band of the *Cu*-rich side of the coevaporated samples was closer to the single crystal one.

In addition to the surface analysis, combined Raman/AES measurements were also performed on baseline samples. As in the coevaporated samples, MoS_2 has been found also to be present in these samples at the CIS/*Mo* interface. No other secondary phases could be found at the bulk of the film by Raman Spectroscopy, in good agreement with XRD analysis. An interesting feature is the evolution of the position and width of the A_1 mode with the depth, which can be appreciated in the following plot:

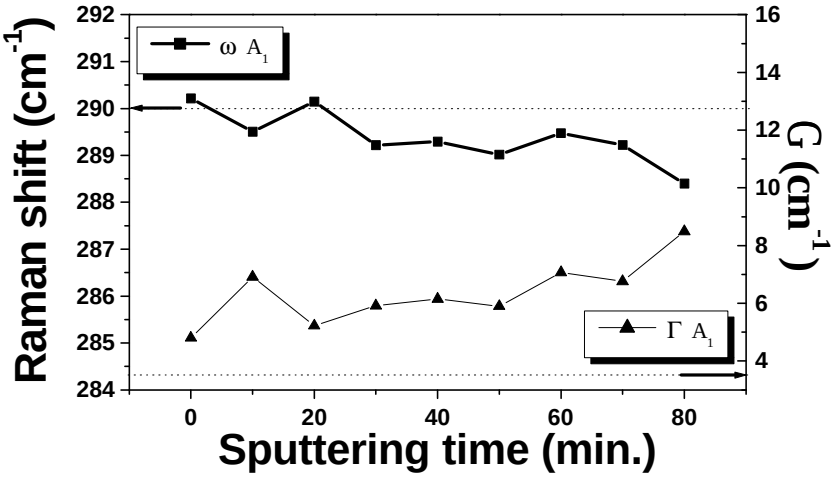

Figure 5. 2. Frequency and width of the chalcopyrite A_1 band for points corresponding to different depths in a baseline sample.

Figure 5.2 shows a broadening and a red shift of the band for points closer to the CIS/*Mo* interface. A first interesting aspect concerns with the red shift of the band at the bulk of the film. The magnitude of this shift is comprised between 1

and 2 cm^{-1}. XRD measurements have been performed at the same sample in order to investigate the possible existence of residual stress in the material, which may induce this shift. The (112) chalcopyrite reflection has been used for obtaining the dependence of the interplanar distance, as a function of the angle ψ. The following figure plots the values obtained from these measurements, for *f* values of 0º and 180º.

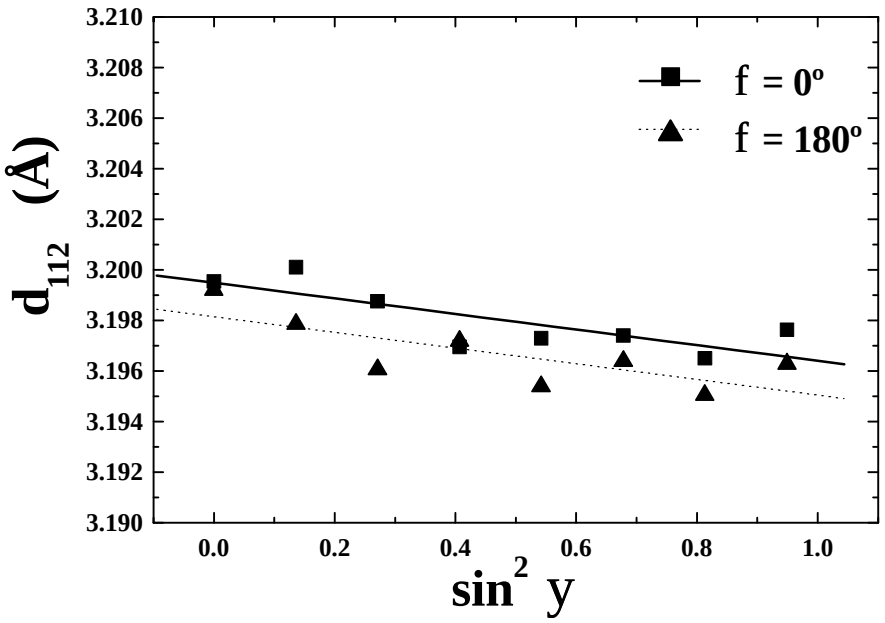

Figure 5. 3. XRD stress measurements (sin^2 y vs. d) for a baseline sample

The linear dependence of the interplanar distance on the parameter [sin^2 ψ] reveals the existence of a tensile stress in the sample. The numerical value of the stress can be extracted from the slope of the linear fit of the data. Assuming the material being isotropic, and a biaxial stress state in the sample, the following expression may be used for the calculation of the stress [178]:

$$\frac{d_{yf}-d_0}{d_0}=\frac{1+n}{E}\cdot s_f\cdot sin^2 y-\frac{n}{E}\cdot(s_{11}+s_{22}) \qquad \textbf{[Eq. 5. 1]}$$

In the previous equation, d_{yf} and d_0 refer to the interplanar distances for a given reflection *(hkl)* of a strained and an unstrained lattice, n is the Poisson coefficient, E is the Young's module, s_f is the stress component along a direction forming an angle f with the axis *X* of the sample, and s_{11} and s_{22} are the components of the corresponding stress tensor. The values obtained from the data of *Figure 5.3* are:

$$s(0^o)=-170\pm 40\,MPa$$
$$s(180^o)=-170\pm 60\,MPa$$

The existence of this tensile stress provides an explanation for the red shift of the A_1 Raman band. Unfortunately, to our knowledge, the behaviour of the frequency of the A_1 mode under biaxial stress conditions has not been reported. In order to estimate the magnitude of the stress corresponding to the observed Raman shift, one may use the empirical expression for the dependence of the A_1 phonon frequency with the hydrostatic pressure in a $CuInS_2$ crystal, which is given by [179]:

$$w\left[cm^{-1}\right]=w_0+a\cdot P[GPa]=290.7+5.03\cdot P[GPa] \qquad \textbf{[Eq. 5. 2]}$$

Therefore, taking into account that the relative shift of the A_1 mode observed at the bulk of the sample is in the range of 1-2 cm^{-1}, one finds that the equivalent hydrostatic stress value indicated by the Raman red shift to be amid 200-400 MPa. This is in reasonably good agreement with the magnitude of the stress value obtained by XRD, assuming a biaxial stress state in the film. Due to the fact that the shift of the A_1 mode increases towards the CIS/*Mo* interface, one may thought that this stress is induced by the substrate, because of the different

thermal expansion coefficient of both. In addition, the residual stress may be at least in part responsible for the broadening of the band. In fact, in *Figure 5.2* a parallel trend is observed for the variation of the width and the frequency of the mode across the sample. Therefore, although the broadening of the mode towards the back contact may indicate a worsening of the structural quality of the material, this broadening may be caused by the tensional state in the grains.

5.2. Incorporation of *Ga* in the sequential process

Several elements may be incorporated in the $CuInS_2$ ternary system as isovalent and non-isovalent substitutional atoms. This is a means to modify the electronic and structural properties of the material, because of the potential capability of these added elements to modify the electronic band structure, the carrier concentration and the growth mechanisms and chemical reactions. The incorporation of new elements may result in a poorer performance of the final device, as in the case of the aluminium, but in general they can improve at least some aspects of the device characteristics. One of the most promising elements to be successfully incorporated into the $CuInS_2$ ternary system is *Ga*. By introducing *Ga* it is possible to increase the V_{OC} of the cell, maintaining the solar efficiency. In general, the addition of *Ga* leads to an increase of the bandgap of the absorber, which in the case of $CuInS_2$ is not so necessary as in the case of $CuInSe_2$ for reaching the optimum value. However, it has been observed that if the amount of *Ga* is low enough, the increase of V_{OC} exceeds that related to the bandgap widening. Moreover, higher *Ga* concentrations may be used in order to achieve high values of V_{OC} (even above 800 mV). Another interesting potential benefit of the *Ga* alloying may be the improvement of the film adhesion. Finally, the possibility to control the *Ga* concentration in order to achieve a bandgap grading in the samples offers new possibilities for bandgap engineering on these devices.

The incorporation of *Ga* to the sequential baseline process can be carried out just introducing *Ga* as a third metallic precursor before the sulphurisation process. Nevertheless, the low melting point of *Ga* complicates the process of sputtering from *Ga* targets. Therefore, evaporation has been selected as the deposition method for the precursors, and good results have been achieved by this procedure. Metallic precursors are sequentially evaporated (*Cu/In/Ga*) onto

the *Mo*-coated glass. Then, the samples are sulphurised using either S or H_2S reactive atmosphere. Different sulphurisation temperature profiles can also be used. The Conventional Thermal Process ("CTP") includes a linear temperature ramp of about 30 minutes, which takes the substrate to the sulphurisation temperature (T_S). This temperature is then held for some minutes, until the sulphurisation process is finished. Alternatively, a faster ramp can be used to raise the substrate temperature from room temperature to T_S. This process is referred to as Rapid Thermal Process ("RTP"). Both methods provide good results in terms of the performance of the final devices.

5.3. Influence of the *Ga* content in films processed by CTP

The influence of the *Ga* content on the microstructural properties of the films has been investigated on CTP processed samples. The sulphurisation of the samples has been performed within a sulphur atmosphere. A set of five *Ga* containing baseline samples have been prepared from precursor samples with different values of *R* [*R = Ga/(Ga+In)*]. Absorption Atomic Spectroscopy (AAS) measurements were performed on the samples in order to accurately determine the value of *R*. The sulphurisation temperature used for the preparation of these samples was 550ºC. The *Cu/(In+Ga)* ratio was kept around 1.3 in order to ensure *Cu*-excess growth conditions. After the sulphurisation, the CuS of the samples segregated at the surface was removed by a KCN treatment.

The existence of a non-homogeneous distribution of *Ga* through these samples has been proved by using several techniques [180] (AES, SNMS, XRD and EDX). Despite the stacking sequence of the precursors, the final microstructure of these samples consists [181] of a top and a back region with composition close to $CuInS_2$ and $CuGaS_2$, respectively. For the formation of a single quaternary phase, higher annealing times are likely required in order to permit the interdiffusion between both regions. Moreover, surface Raman measurements have provided information about the structural properties of the $CuInS_2$ top region. The following figure shows the surface spectra corresponding to the five *Ga* containing samples.

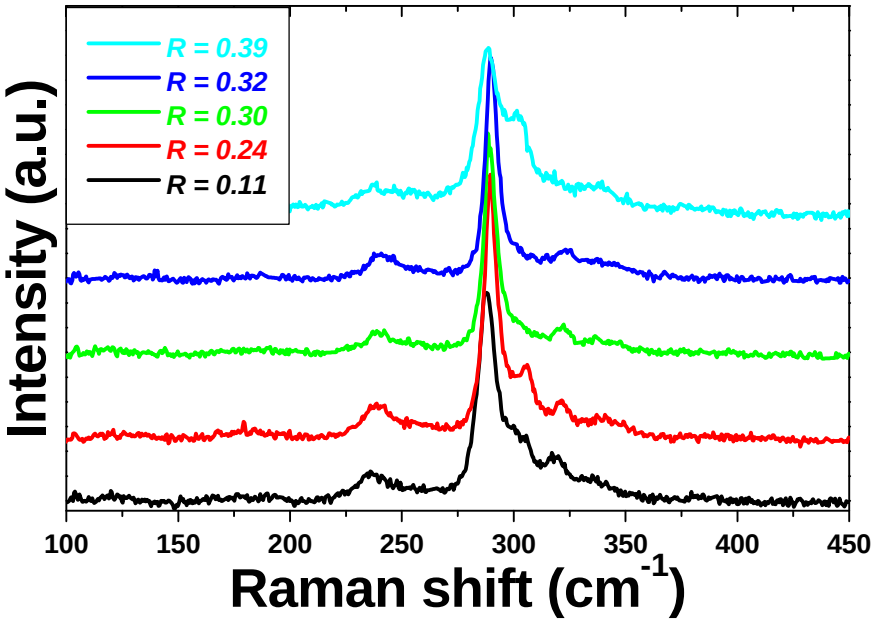

Figure 5. 4. Surface Raman spectra of the sequentially processed (CTP) *Ga* containing samples.

In principle, a shift towards high frequency of the A_1 $CuInS_2$ mode could be indicative of some degree of alloying of both $CuInS_2$ and $CuGaS_2$ ternaries. As will be discussed later, the A_1 mode of the $Cu(In_{1-x}Ga_x)S_2$ quaternary system presents an unimodal behaviour through all the compositional range [182], and the frequency of the mode shifts almost linearly with *x* between the positions for the $CuInS_2$ crystal (290 cm^{-1}) and $CuGaS_2$ (310 cm^{-1}) [183]. The frequency and FWHM (*G*) of the A_1 mode from the spectra of the previous figure are plotted in *figure 5.5*. In this case, almost all the spectra present a blue shift of the A_1 mode, which cannot be explained due to *Ga* incorporation in the $CuInS_2$ lattice. This indicates that the amount of *Ga* incorporated in the surface region has to be very small (if any). However, the relative amount of *Ga* is found to have a direct influence upon the structural quality of the $CuInS_2$ surface phase, as can be seen

by comparing the width of the chalcopyrite A_1 mode for the different samples (see *figure 5.5*).

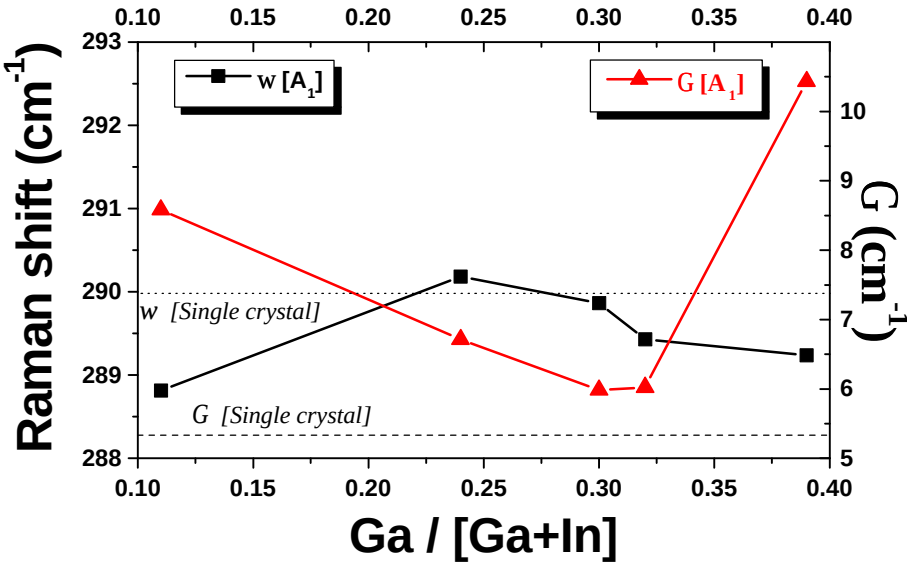

Figure 5. 5. Frequency and G of the chalcopyrite A_1 mode for the set of CTP samples.

Notice from the previous figure that the optimum crystallinity of the $CuInS_2$ surface phase occurs for values of *R* around 0.30, and the width of the A_1 mode increases for higher or lower *Ga* concentrations. As in the case of *Ga*-free samples, the improvement of the crystallinity of the chalcopyrite phase appears together with the decrease of the intensity of the A_1^* Cu-Au related mode. Furthermore, the best efficiency of the solar cells derived from these CTP absorbers corresponds to this value of *R* around 0.30, which is a clear indication of the strong sensitivity of the cell parameters to the surface properties of the film (see table [184] below). Once again, Raman spectroscopy reveals itself as a valid tool for the assessment of the absorber quality of this type of chalcopyrite cells.

Ga/(Ga+In)	**h (%)**	**J_{SC} (mA/cm^2)**	**V_{OC} (mV)**	**FF (%)**	**Raman: G [A_1] (cm^{-1})**
0.11	9.1	18.2	708	71	8.6
0.24	9.0	17.7	736	69	6.7
0.30	*9.4*	*17.3*	*752*	*72*	*6.0*
0.39	0.3	4.0	287	22	10.4

Table 5. 1. Correlation between solar cell electrical parameters and structural properties of the $CuInS_2$ films.

5.4. Effect of the sulphurisation temperature in CTP process

As already shown in previous sections, the sulphurisation temperature is a fundamental parameter which directly influences the properties of the final absorber. In this section, we will focus our attention on the study of absorbers with R = 0.30, i. e, with the optimum *Ga* content in terms of solar efficiency of the final device. Three CTP samples have been analysed corresponding to sulphurisation temperatures of 500ºC, 550ºC and 600ºC. *Figure 5.6* shows the *Ga*/(*Ga*+*In*) compositional profiles obtained from these samples, as determined by AES:

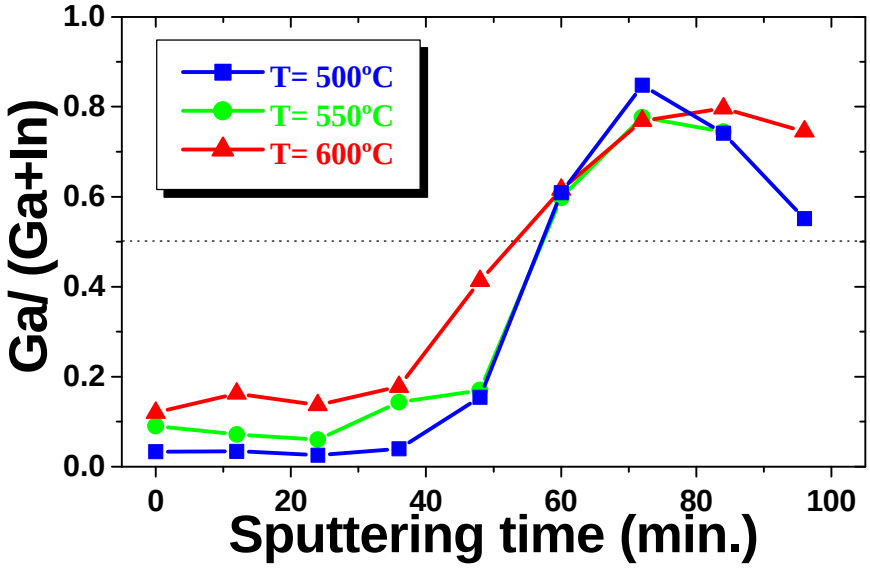

Figure 5. 6. AES depth profiles of CTP *Ga*-containing samples (*R*=0.30) grown at different temperatures.

Notice that the above profiles clearly show a characteristic bilayer structure of the CTP *Ga*-containing samples: a top region with composition close to $CuInS_2$

and a back region with composition similar to $CuGaS_2$. Besides, the compositional profiles show an important feature related to temperature: the lower the sulphurisation temperature, the steeper the transition between both regions. Therefore, higher sulphurisation temperatures are favourable for inducing the interdiffusion of *Ga* and *In* and the formation of a single quaternary phase in the samples. This temperature effect is also noticeable by comparing the Raman spectra from the bulk of the three samples, obtained from combined Raman/AES. The following spectra depicted in *figure 5.7* were obtained from the samples grown at 500ºC and 600ºC, respectively.

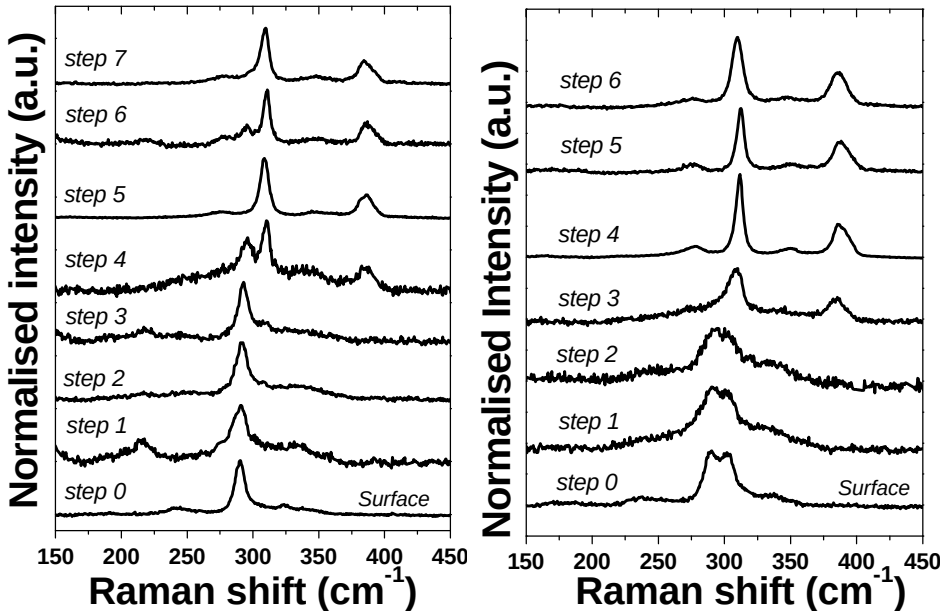

Figure 5. 7. Raman spectra from the depth of samples grown at 500ºC (right figure) and 600ºC (left figure). The corresponding number of sputtering steps is indicated.

In both cases, spectra from the bottom of the figures are similar to those from *Ga*-free $CuInS_2$ films. For deeper points, the spectra turns into $CuGaS_2$ characteristic spectra, confirming the existence of a bilayer structure in the

samples. The transition between both regions appears to be quite abrupt, especially for the sample grown at lower temperature. In *figure 5.8* the frequency of the mode for the points corresponding to different depths is shown.

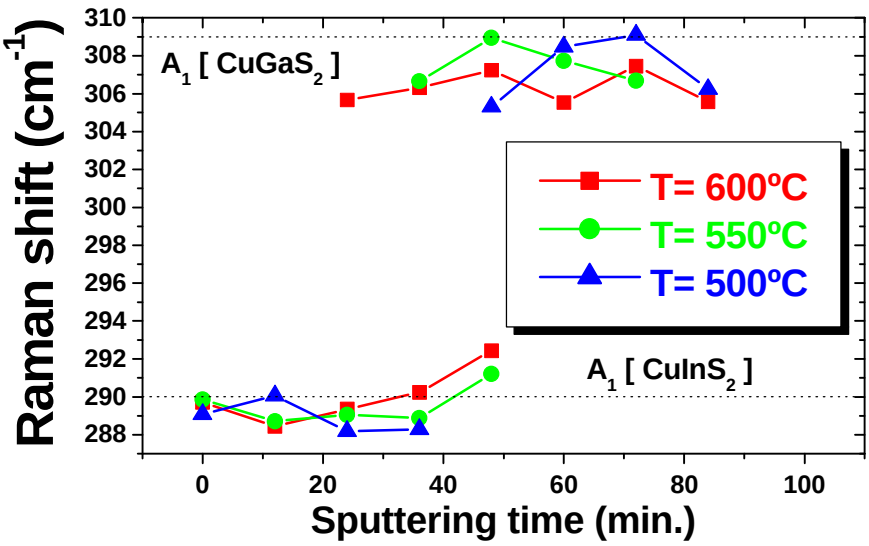

Figure 5. 8. Spectral position of the A_1 mode through the three samples.

As a result of the higher interdiffusion between $CuInS_2$ and $CuGaS_2$ regions in the sample grown at the highest temperature, the chalcopyrite A_1 mode from this sample tends to shift towards higher frequencies in relation to the mode from the other samples, mainly at the region close to the back $CuGaS_2$ layer. This is also accompanied by a more homogeneous shift of the $CuGaS_2$ A_1 mode at the back region towards lower frequencies, which indicates the more uniform distribution of incorporated *In* at this region.

A more detailed analysis of the spectra allows to estimate the relative composition of the chalcopyrite phases, through the dependence of the frequency of the A_1 chalcopyrite mode with *R*. The composition of the $Cu(In_xGa_{1-x})S_2$ quaternary phase at each region may be estimated through the

dependence of the frequency of the band on the force constants. Within the virtual crystal approximation, one may assume an effective force constant depending linearly on the composition:

$$K_{eff} = K_{In} \cdot (1 - x) + K_{Ga} \cdot x \qquad \textbf{[Eq. 5. 3]}$$

Therefore, using the Neumann expression for the frequency of the A_1 chalcopyrite mode **[Eq. 3.15]**, one finds an analytical expression which predicts an almost linear variation of the frequency of the mode with the composition of the alloy, from 290 cm^{-1} for $x = 0$ ($CuInS_2$), to 310 cm^{-1} for $x = 1$ ($CuGaS_2$).

$$w(A_1) = \sqrt{\frac{K_{Cu} + K_{In} \cdot (1 - x) + K_{Ga} \cdot x}{m_S}} \qquad \textbf{[Eq. 5. 4]}$$

From the above expression and *Figure 5.8*, one should conclude that the degree of alloying in the sample grown at 600ºC, which is the sample with the highest interdiffusion between both regions, is only around 10% of *Ga* incorporated in the top region ($CuIn_{0.8}Ga_{0.2}S_2$), and 15% of *In* incorporated in the back region ($CuIn_{0.2}Ga_{0.8}S_2$). Certainly, the quantification of the composition in the case of the top region is more complex due to the red shift of the mode (already observed in *Ga*-free baseline samples).

The previous Raman/AES "in-depth" analysis shows the failure of the CTP process for producing chalcopyrite absorbers with homogeneous *Ga* distribution. Accumulation of Ga close to the back contact is not positive, even in the case that one would like to make a controlled graded film. Even in such a case, better results are expectable for a graded absorber in which Ga was concentrated at the top. In any case, best absorbers provided by the CTP process are produced by using values of *R* around 0.30, and high sulphurisation temperatures. As previously shown this value of *R* optimises the structural

properties of the surface of the absorber, while the high temperature favours interdiffusion. The incorporation of Ga in the top region of the absorber leads to a bandgap increase, which in turn results in an increase of the V_{OC}.

5.5. Ga-containing samples obtained by RTP process

RTP process is advantageous in front the CTP process due the time reduction for absorber formation, which does not cause the degradation of their quality. In the present section, the introduction of *Ga* in the RTP process will be studied. Sulphurisation process involving elemental sulphur as well as in H_2S/Ar atmosphere will be both considered. Raman/AES results are compared in both cases, and also with the data obtained from CTP samples.

"In-depth" Raman/AES measurements have been performed in sulphurised samples in *S* and H_2S, with precursor compositions given by $Cu/(In+Ga) = 1.7$ and $R = Ga/(Ga+In) = 0.3$. The sulphurisation temperature was 500ºC, which corresponds to the standard temperature for the RTP baseline process. The Raman/AES experiments show that neither in this case is possible to prevent the accumulation of *Ga* close to the back contact.

As in the case of CTP samples, the Raman spectra of the top region of the samples resembles the $CuInS_2$ reference spectrum, while the back region of the samples is constituted by a *Ga*-rich $Cu(In_{1-x}Ga_x)S_2$ quaternary alloy. Moreover, it is worth to note that the degree of interalloying between the top (*In*-rich) region and the back region (*Ga*-rich) is higher than for the CTP processed samples, mainly at the back region. This is reflected in the Raman spectra by a higher shift of the A_1 mode towards the position estimated for the perfect quaternary alloy ($CuIn_{0.5}Ga_{0.5}S_2$), especially in the back region of the samples. The following figure plots the spectral position of the A_1 mode at the back region of both samples:

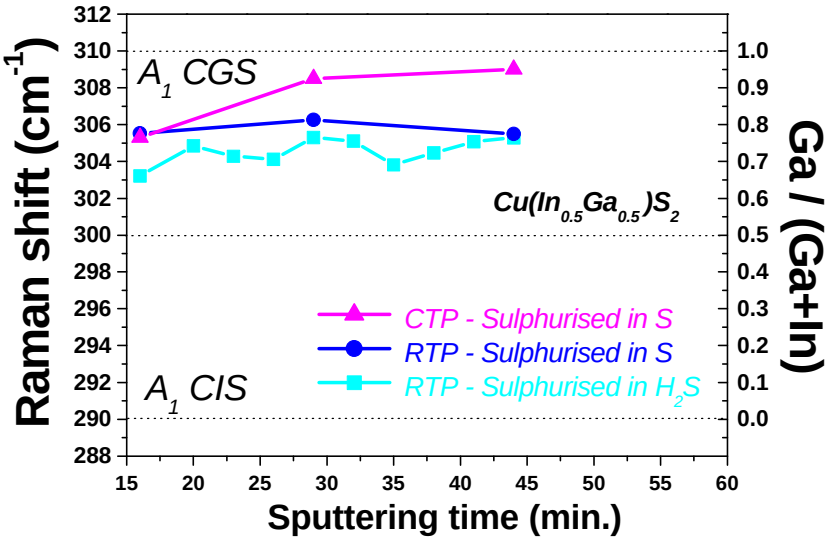

Figure 5. 9. Frequency of the A_1 mode for the samples sulphurised in elemental sulphur and in H_2S.

A comparison of the RTP sulphurisation processes in S and in H_2S is also possible on the basis of the above plot. According to these results, by processing the samples using a RTP process in H_2S one achieves a maximum incorporation of *In* in the quaternary phase at the back region of the film, with composition around $Cu(In_{0.3}Ga_{0.7})S_2$. Furthermore, the composition at the top region of both samples appears more similar to the results obtained using the CTP process. Also in this case, the incorporated *Ga* to the $CuInS_2$ lattice appears to be only around 10%.

5.6. Study of sulphurisation

The current understanding of the sulphurisation reaction paths which give rise to the formation of the final films is still very limited. Needless to say, the comprehension of the different aspects of the chemical reaction are of great importance if one wishes to modify the growth conditions in order to optimise the film properties. In this section the results concerning the study by Raman/AES of several series of quenched RTP processed samples are presented. The samples have been obtained by aborting the sulphurisation process at a certain time after the sulphurisation started, and then cooling down the sample to room temperature. Each set of samples has been analysed ex-situ in order to study the microstructure of the film at each stage of the sulphurisation process. The whole results have provided a consistent picture of the different steps of the reaction.

Ga-free samples

First of all, we will analyse the RTP sulphurisation process in elemental sulphur of the standard *Cu*-rich metallic precursors (Cu/In = 1.8). Results involving equivalent experiments concerning *Cu*-poor precursors can be found in literature [185, 186]. We have analysed five samples ("**A**", "**B**", "**C**", "**D**" and "**E**") corresponding to different instants of the process, as indicated in the following figure showing the heating ramp of the process.

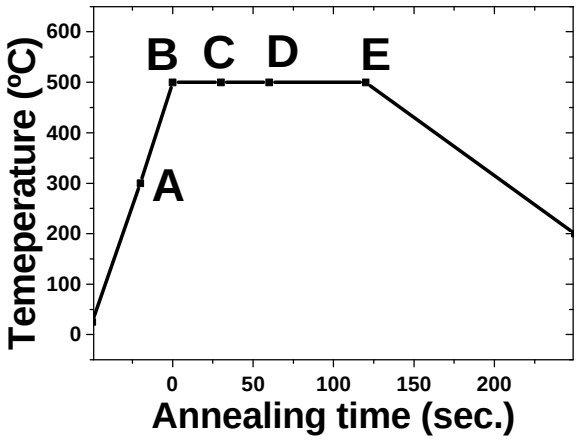

Figure 5. 10. Heating ramp and set of quenched samples analysed.

Surface Raman analysis of the samples already provides interesting information about the sulphurisation process. Sample **A** presents no Raman signal, which indicates that when the substrate temperature is 300ºC the sulphurisation process has not started, and therefore the sample is still constituted by metallic phases. Moreover, the first indications of the beginning of the sulphurisation are found at sample **B**, whose surface spectrum is characterised by a broad contribution in the region about 300 cm^{-1} (see *figure 5.11a*). The apparition of these broad bands close to the most intense $CuInS_2$ characteristic peaks is attributed to the formation of this compound. Furthermore, the shape and width of the bands reveal the bad crystallinity of this phase at the first stages of the process. An enhancement of the crystallinity of the $CuInS_2$ is observed for sample **C**, in which no traces of CuS binary phases are still detected. The narrowing of the bands in the spectrum corresponding to this sample permits to resolve the presence of the chalcopyrite and Cu-Au modes. These observation show that $CuInS_2$ does not crystallise directly in an ordered chalcopyrite structure, but in a disordered lattice in which chalcopyrite and Cu-Au ordered domains coexist. Similar observations have been recently reported by M. Gossla et al [187]. Finally, longer sulphurisation times lead to the formation of the characteristic CuS phase at the surface of the sample, as indicated in the Raman

spectra of samples **D** and **E**. Due to this, it has been necessary to sputter the sample in the AES machine for the study of the properties of the $CuInS_2$ phase underneath the CuS. By this procedure, the spectra corresponding to the subsurface region of the films were also obtained (see *figure 5.11b*). In the case sample **D**, its spectrum is similar to the one of the sample **C**. A detailed look of the spectrum shows a slight improvement of the crystalline quality of the chalcopyrite phase. It is worth to note that still in this case, the A_1^* Cu-Au related peak is clearly visible in the spectrum. In contrast, the peak disappears for the sample **E.** As will be shown later, for this sample the sulphurisation reaction is completed. Therefore, these results indicate that time is required not only to completely sulphurise the precursors, but also to induce a recrystallisation of the Cu-Au metastable domains formed during the reaction. After this recrystallisation, the film is constituted by a single $CuInS_2$ chalcopyrite phase, besides the CuS segregated phase.

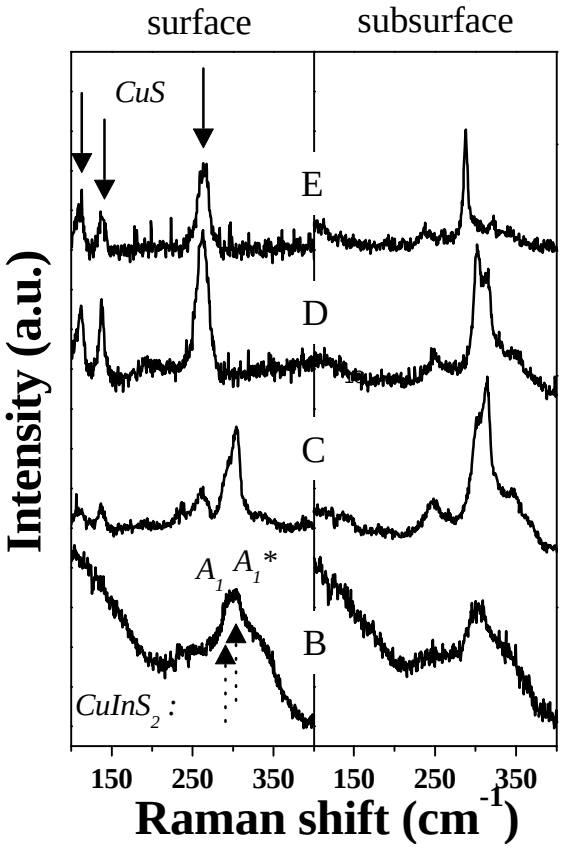

Figure 5. 11. Surface (*a*) and subsurface (*b*) Raman spectra of the set of quenched samples (no Raman signal was found for sample A)

The improvement of the crystallinity of the chalcopyrite phase in the subsurface region of the samples is also observed through the whole sulphurised layer by increasing annealing time. The analysis of the Raman spectra of the bulk of the samples obtained through combined Raman/AES measurements shows that the shift and width of the A_1 mode decreases with the sulphurisation time, as indicated in *figure 5.12*. This figure shows the spectral features of the A_1 mode versus the sputtering time normalised to the total time for which the sulphurised layer is fully sputtered, for samples **C**, **D** and **E**.

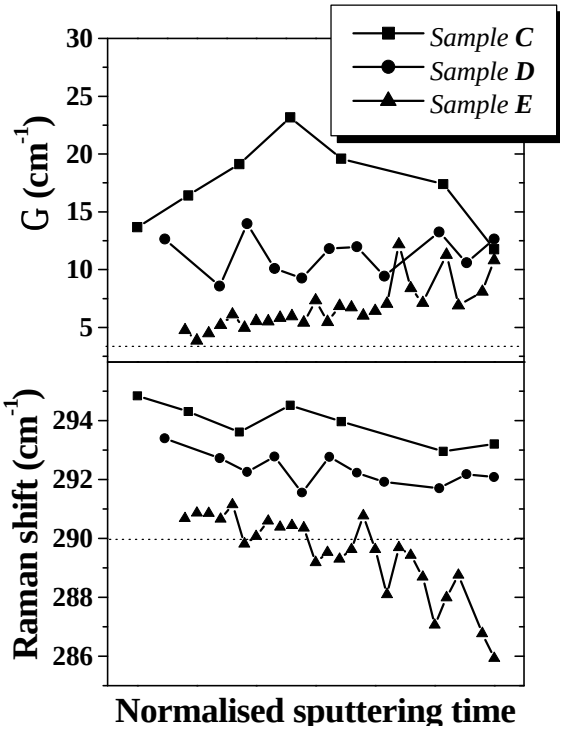

Figure 5. 12. Raman shift and FWHM (G) of the A_1 chalcopyrite mode for points at the bulk of samples C, D and E.

AES profiles provide also interesting information about the details of the sulphurisation reaction. Due to its good sensitivity, AES is able to detect the presence of small amounts of elements in a thin film, and therefore it has been used to confirm the absence of sulphur at the surface of sample **A**, thus confirming that the sulphurisation reaction has not started at this point. Moreover, the AES profile of sample **A** indicates that *In* is concentrated mainly at the top of the film. In this top region, the estimated composition of the film is close to $CuIn_2$, according to AES. On the other hand, *Cu*-excess remains at the back region of the film. Further XRD analysis of this sample has confirmed that sample **A** consists mainly of a mixture of $CuIn_2$ and elementary *Cu*. *Figures 4.13* show the AES profiles corresponding to samples **B**, **C**, **D** and **E**. Sulphur is

detected for the first time in sample **B**. The sulphur concentration is maximum at the surface of the sample and decreases towards the bulk of the sample. This supports the previous Raman results which indicated that the sulphurisation reaction starts at the surface of the film. Beneath the sulphurised region, the metallic precursors are found. As in the case of sample **A**, Cu-excess seems to accumulate at the back region of the film, close to the Mo back contact. Moreover, phase composition of the metallic precursors of this sample is more complex. XRD analysis shows that $Cu_{11}In_9$ metallic phase forms, while $CuIn_2$ disappears, in good agreement with experimental observations reported in the literature [188, 189]. Moreover, accordingly to XRD, $Cu_{11}In_9$ and metallic *Cu* are the dominant phase present in the precursors of the samples during the annealing process, although they may coexist with some $Cu_{16}In_9$ phase. On the other hand, the AES profiles of these two samples can be interpreted analogously to those of sample **B**. As a result of the incorporation of sulphur in the sample, the thickness of the sulphurised region increases, while the not sulphurised metallic region keeps at the back region. Notice that for sample **D,** corresponding to 60 seconds annealing time, the sulphurisation process is not finished and an important amount of *Cu* remains at the back region of the sample. Finally, for sample **E** the sulphurisation process is completed, and the profiles are in well agreement with the existence of the characteristic bilayer structure consisting of the CuS surface segregated phase and $CuInS_2$.

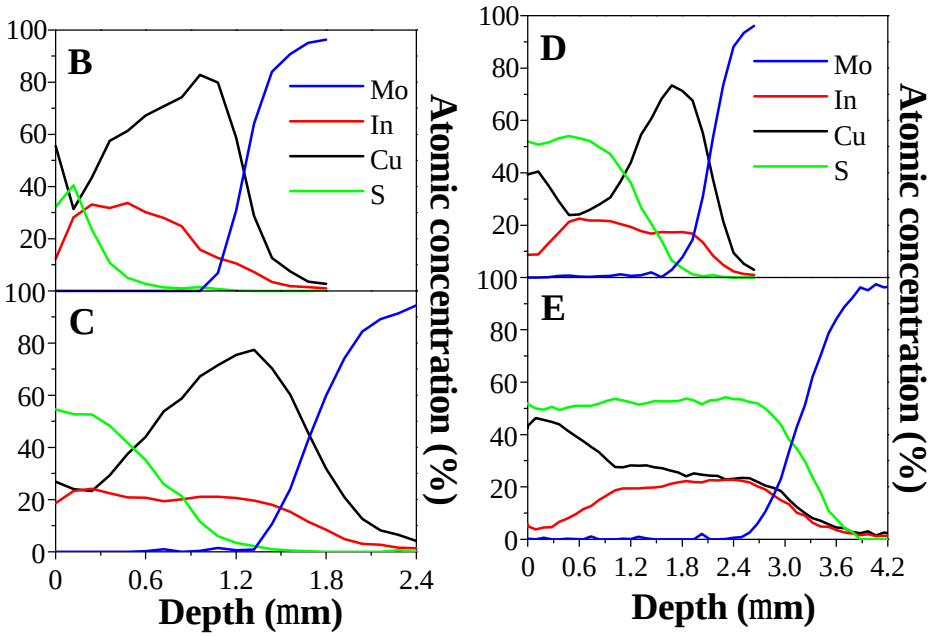

Figure 5. 13. AES profiles corresponding to samples B, C, D and E.

XRD and TEM analysis of the samples are in good agreement with these results presented [190, 191], confirming the overall picture of the chemical reaction [192].

Ga-containing samples

Quenching experiments have been also carried out on *Ga*-containing samples. The sulphurisation reaction in elemental *S* and in H_2S have been both analysed. Although no important differences exist between both sulphurisation procedures when using *Ga*-free precursors, some remarkable aspects where found for Ga-containing precursors. The different samples of each set were obtained following an analogous procedure to that described for the obtaining of the *Ga*-free baseline samples. Each sample was obtained by cooling down the sample

after aborting the sulphurisation process at different times. The characteristics of the thermal process used for each analysed sample are described in the following picture:

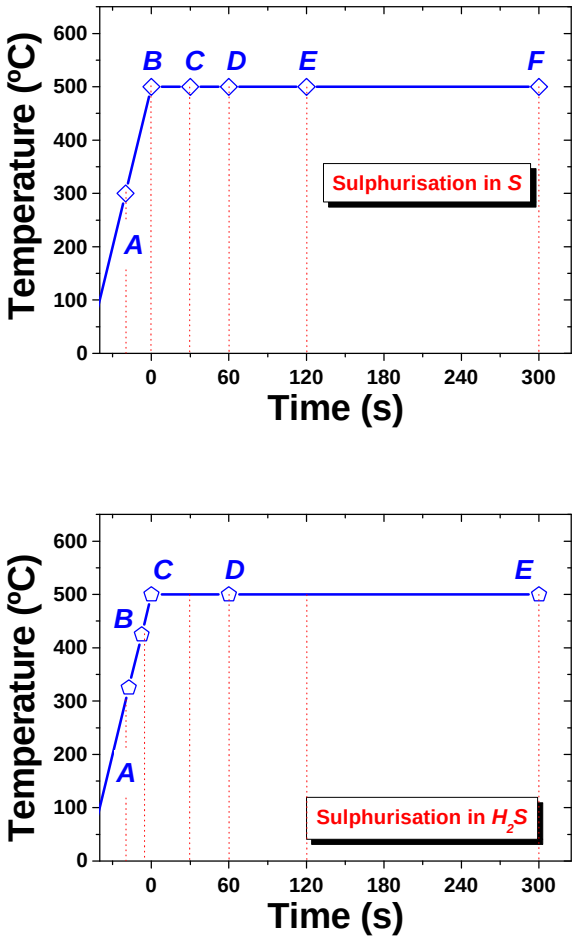

Figure 5. 14. Thermal process used for the sulphurisation of the quenched samples. Samples were obtained by interrupting the process at the corresponding points indicated in the plots.

We will consider first the case of the sulphurisation reaction in elemental *S*. The presence of *Ga* in the precursor layer strongly affects the reaction mechanisms and the intermediate phases formed during the reaction. XRD analysis of the precursors show that at room temperature the film consists of $CuGa_2$, metallic *Cu* and metallic *In*. Moreover, in contrast to *Ga*-free films, metallic *In* is still present during the heating up process [193]. This is thought to favour the formation of $CuIn_5S_8$ phase during the first stages of the sulphurisation reaction in *S* atmosphere. The presence of this phase can be clearly seen at the series of the "in-depth" Raman spectra of the different samples, which were obtained by performing combined Raman/AES measurements. Evidences for the starting of the sulphurisation were found neither at sample **A** nor at sample **B**. Sulphur containing phases are already present at sample **C**, as indicated by the Raman spectra presented in the next figure:

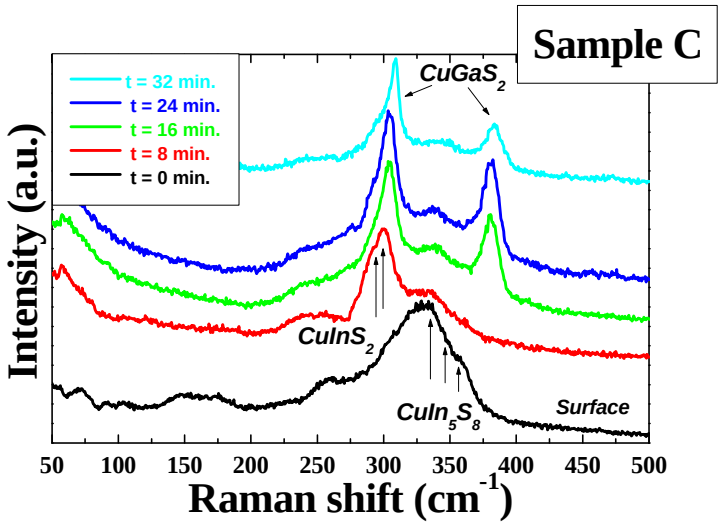

Figure 5. 15. *"In-depth"* Raman spectra obtained from the sample C grown in elemental sulphur.

The previous series of spectra shows that $CuIn_5S_8$ and $CuInS_2$ constitute the surface of the sample. Below this surface region, the sample consists of chalcopyrite $CuGaS_2$ ternary phase. This microstructure is thought to be the result of the following process. The sulphurisation of the *Ga* containing precursor phases occurs during the first seconds after the maximum temperature is reached. This is just a consequence of the fact that at the sulphurisation temperature, the surface of the precursor layer consists mainly of $CuGa_2$. Moreover, the formation enthalpy [194] of the $CuGaS_2$ chalcopyrite phase is lower than the one for $CuInS_2$. Formation of $CuGaS_2$ chalcopyrite phase seems to occur directly from the precursors (no other *Ga* containing phases were observed). Subsequently, the outdiffusion of *In* and *Cu* through the $CuGaS_2$ chalcopyrite phase leads to the formation of $CuIn_5S_8$ and $CuInS_2$ on the top of the $CuGaS_2$ grains. The fact that the *In*-containing phases grow on top of $CuGaS_2$ gives support to the idea that the reaction occurs by the out-diffusion of the metallic species, rather than by the in-diffusion of the sulphur gas. Further evidences for the occurrence of this mechanism were provided by selenization experiments of films which had been previously partially sulphurised [195]. This microstructure persists at samples **D** and **E**. In addition, CuS was also observed at the top of these samples. The following picture plots the *"in-depth"* Raman spectra obtained for sample **E** (t_{sulph} = 120 s.). The figure shows that the sulphurisation process continues through the formation of *In*-containing phases onto the $CuGaS_2$ phase.

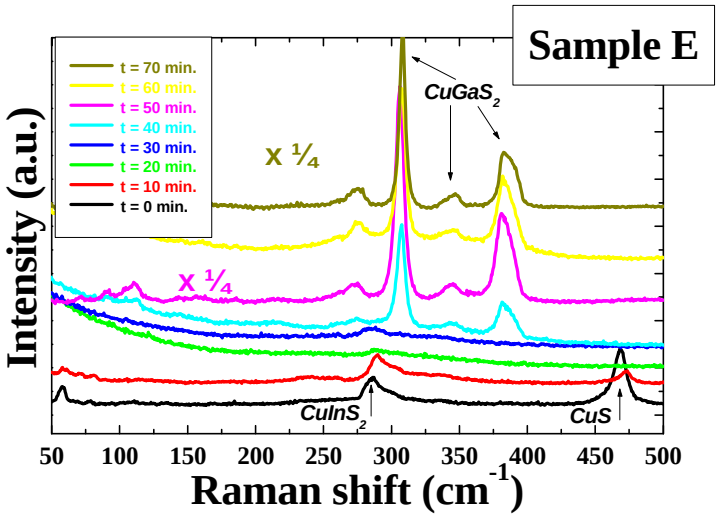

Figure 5. 16. "In-depth" Raman spectra obtained for sample E (sulphurisation in elemental sulphur).

It is worth to note that despite the crystalline quality of the $CuGaS_2$ is good, the bad Raman signal of the top region indicates that the $CuInS_2$ and $CuIn_5S_8$ phases that form onto the $CuGaS_2$ phase present a very poor crystalline quality. After the end of the sulphurisation process (sample **F**), the sample consists of the typical bilayer structure: $CuGaS_2$ at the back and $CuInS_2$ at the top. As can be shown in the next figure, even after the sulphurisation process is finished, any significant enhancement of the crystallinity of the $CuInS_2$ chalcopyrite phase occurs:

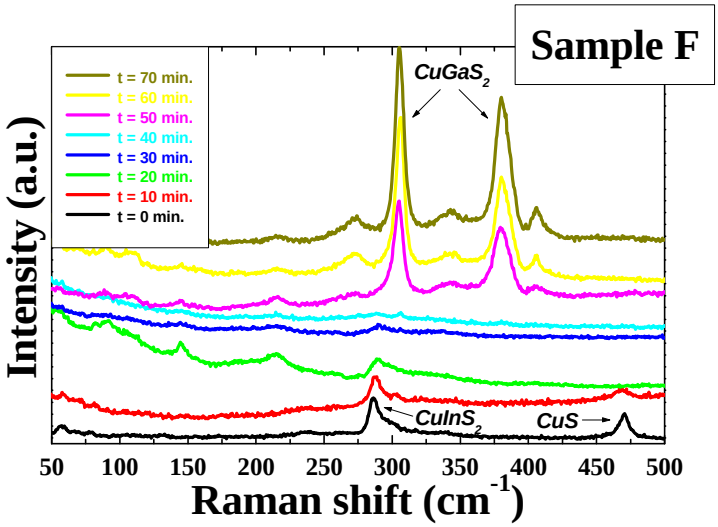

Figure 5. 17. "In-depth" Raman spectra corresponding to sample F (sulphurisation in elemental sulphur)

The interdiffusion of *Ga* and *In* after the formation of the ternary phases leads to the incorporation of small amounts of *In* and *Ga* into the $CuGaS_2$ and $CuInS_2$ lattices, respectively. The formation of the quaternary seems not to occur directly through a reaction from the metallic precursors, due to the extremely fast formation of the $CuGaS_2$ ternary phase. On the other hand, the appearance of the $CuIn_5S_8$ intermediate phase avoids the formation of the chalcopyrite $CuInS_2$ phase directly from the precursors. Consequently, the interdiffusion process which leads to the alloying between both ternaries is delayed, and can be accomplished only partially.

In terms of the formation of an homogeneous quaternary phase through all the film, better results are achieved by performing the sulphurisation process in H_2S. We will analyse now the differences between both sulphurisation processes. As in the previous case, the sulphurisation in H_2S atmosphere leads first of all, to the formation of $CuGaS_2$ chalcopyrite phase at the surface of the

film. However, in this case $CuGaS_2$ is already detected during the heating up stage of the process, which indicates the higher reactivity of H_2S with the precursors. "In-depth" Raman analysis of samples **A** and **B** show that the surface region of the films is constituted by this single phase. Next figure shows the Raman spectra obtained from sample **A**:

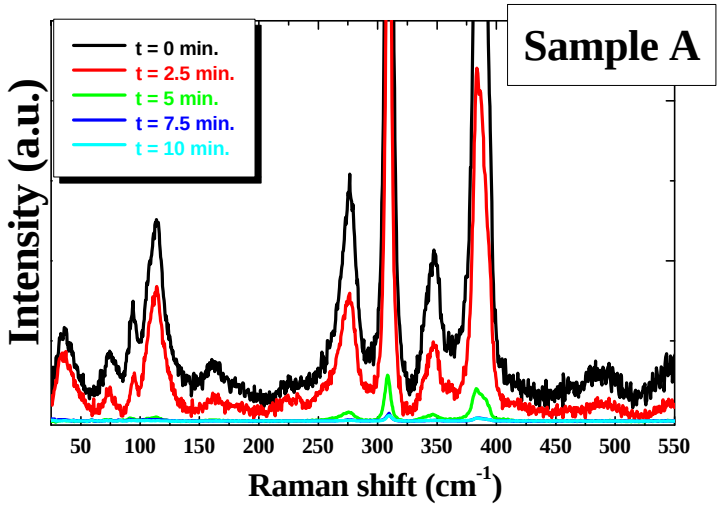

Figure 5. 18. Raman spectrum obtained from the sample A sulphurised in H_2S.

For sample **C**, the formation of $CuInS_2$ onto the $CuGaS_2$ phase is already detected (see *figure 5.19*). Unlike in the case of the samples sulphurised in *S*, the sulphurisation reaction does not result in the formation of $CuIn_5S_8$, but only in $CuInS_2$ chalcopyrite phase (Cu-Au ordering is not detectable, either). In addition, the crystalline quality of the chalcopyrite phase is significantly improved with respect to the sulphurisation in *S*.

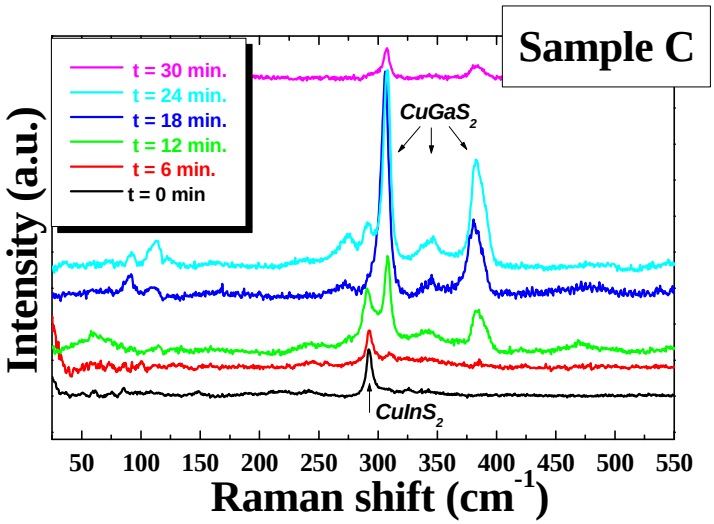

Figure 5. 19. "In-depth" Raman spectra obtained for sample C, sulphurised in H_2S.

At this point, further annealing times lead to the sulphurisation of the whole metallic precursors. Moreover, since the reaction in H_2S allows a fast formation of the $CuInS_2$ phase without $CuIn_5S_8$ as intermediate phase, the quaternary phase formation is favoured through a solid-state diffusion process. As shown in *section 5.5*, after the conclusion of the reaction (sample **E**) the film presents the characteristic bilayer structure with a *Ga*-rich and an *In*-rich quaternary phases at the bottom and at the top of the film, respectively. Next figure plots the corresponding "in-depth" spectra for the fully sulphurised sample:

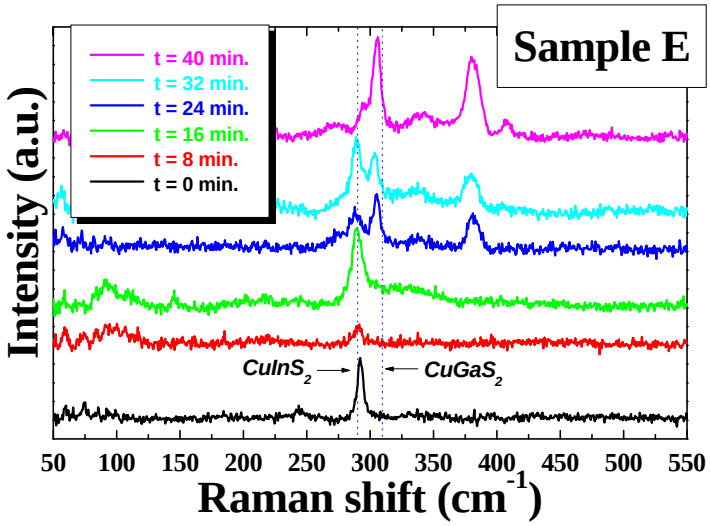

Figure 5. 20. "In-depth" Raman spectra corresponding to the point at the end of the sulphurisation process (sample E)

5.7. Conclusions

In this chapter we have deepen into the structural properties which characterise the sequentially processed samples. Sulphurisation of *Cu*-rich metallic precursors by RTP provides a fast method for obtaining good quality $CuInS_2$ absorbers. Quenching experiments have provided a picture for the sulphurisation reaction, which can be described in terms of subsequent steps:

1) Alloying of the precursors. Formation of $Cu_{11}In_9$ phase.
2) Sulphurisation of the surface of the film, which gives rise to the formation of $CuInS_2$. Chalcopyrite and Cu-Au metastable ordered phase coexist.
3) Out-diffusion of the metallic species through the $CuInS_2$ phase. At the surface they react with the *S* gas forming more $CuInS_2$ phase.
4) Recrystallisation of the $CuInS_2$ phase. This process leads to the formation of a single chalcopyrite phase in $CuInS_2$, which presents a good crystallinity.

Moreover, the sulphurisation of *Ga* containing precursors has been also studied. In this case, it has been shown that the formation of a single quaternary phase is difficult due to the fast formation of the $CuGaS_2$ phase. This leads to a characteristic bilayer structure: $CuInS_2$ at the top of the film, and $CuGaS_2$ beneath. Raman spectroscopy has been used for the assessment of the crystalline quality of the films. It has been found that for CTP processed samples there exists an optimum *Ga* concentration, which provides a minimum in the FWHM of the A_1 chalcopyrite band. The amount of *Ga* leading to the best crystallinity of the $CuInS_2$ phase coincides with the one which leads to best efficiencies in the final solar cell devices.

The ex-situ investigations of quenched samples have allowed understanding the differences observed between the sulphurisation processes in *S* and in H_2S. In both cases, the reaction path starts by the fast formation of the $CuGaS_2$ ternary

phase. Moreover, *In*-containing phases form onto the $CuGaS_2$ grains. When the sulphurisation process is performed in *S*, $CuIn_5S_8$ intermediate phase formation occurs, which may be favoured by the presence of free metallic *In* in the *Ga*-containing precursors. The formation of this intermediate phase delays the chalcopyrite formation, thus hindering the interdiffusion process which makes possible the quaternary formation. In front of this, the reaction in H_2S prevents the formation of this intermediate phase, favouring the interdiffusion process. As a result, samples processed in H_2S present a higher degree of interalloying than the ones processed in *S*. In addition, the crystalline quality of the top region of the films is substantially improved by processing the samples in H_2S instead of in elementary *S*.

6. Conclusions

In this work, the vibrational properties of $CuInS_2$ films have been investigated in detail, which has allowed characterising the polycrystalline films used for solar cell applications. The Raman spectra of these films are characterised by the presence of the totally symmetric band of the chalcopyrite structure, appearing at around 290 cm^{-1}. Moreover, some of the films present additional bands at 60 cm^{-1} and 305 cm^{-1}, whose origin was unknown up to now. The comprehension of the appearance of these bands was necessary in order to understand the structural properties of the material. Consequently, different experimental techniques were used to investigate the crystalline structure of these films. The TED and XRD results presented in *chapter 3* have proved that these films are constituted by a phase mixture of two $CuInS_2$ polymorphic phases. These phases correspond to the equilibrium chalcopyrite phase and the metastable Cu-Au ordered phase. In addition, combined XRD/Raman measurements have shown that the intensity of the additional Raman bands in the spectra correlate with the total amount of Cu-Au ordered phase in the films. The calculated symmetry and frequency of the zone-centre phonons of the Cu-Au ordered structure support this assignment. Group theory predicts the existence of a totally symmetric mode in the Raman spectra of the Cu-Au crystalline structure, appearing at higher frequencies than the A_1 mode of the chalcopyrite structure. A 4-parametres Keating model has been used in order to calculate the phonon spectra of the Cu-Au structure, using the empirical force constants extracted from the chalcopyrite crystal. The results provided by this model are in good agreement with the experimental frequency and symmetry of the additional band at 305 cm^{-1}. However, this model failed to explain the low frequency band at 60 cm^{-1}. This could be due to an intrinsic limitation of this phenomenological model. Another possibility is that this band arises because of some local defect (localised phonon) and it is not a normal mode of the Cu-Au crystal.

The interpretation of these features in the Raman spectra made possible to characterise and to understand the structural properties of the polycrystalline films grown either by coevaporation or by a sequential process. The results presented in *Chapter 4* deal with the analysis of coevaporated films. The combined use of AES and Raman has provided detailed information about the surface and bulk structure of the films. It has been shown that the variation of the growth stoichiometry leads to the formation of secondary phases (CuS in *Cu*-rich films, and $CuIn_5S_8$ in *Cu*-poor ones). Moreover, although CuS segregates at the surface of the film and is effectively removed by a KCN chemical treatment, $CuIn_5S_8$ forms microprecipitates in the bulk of the film, which can not be removed in an easy way. In addition, MoS_2 has been detected in the CIS/*Mo* interface of the films. The formation of this phase maybe responsible for the adhesion failure problems which sometimes affect these films. On the other hand, the crystalline quality of the $CuInS_2$ phase has been investigated by Raman spectroscopy. It has been shown that for films grown either under *Cu*-poor conditions or at lower growth temperatures, Cu-Au ordered domains coexists with chalcopyrite ones. In this sense, the experimental results points out the existence of a transition growth temperature which depends on the film preparation conditions. For growth temperatures above it, the amount of Cu-Au ordering in the samples seems to be drastically reduced. On the contrary, lower growth temperatures promote the coexistence of both ordered domains. In addition, the characterisation of the films by Raman reveals the existence of a strong correlation between the intensity of the A_1^* Cu-Au band and the structural quality of the films. As a matter of fact, the formation of different ordered nanometric domains results in a polycrystalline material in which the crystal lattice periodicity is partially broken. This leads to an impoverishment of the crystalline quality of the films, which makes these films bad quality photovoltaic absorbers. On the other hand, films in which the A_1^* Cu-Au band is absent at the spectra, lead in general to good efficiency cells. Therefore, for practical purposes, it has been shown that the optimisation of the

properties of the absorber films requires high growth temperatures and *Cu*-excess conditions.

Sequentially grown films, described in *chapter 5*, present also good crystalline quality when *Cu*-excess conditions and high substrate temperatures are used for growing them. In this case, these films present structural characteristics similar to those of the coevaporated samples grown under the same conditions. Moreover, the RTP sequential process offers the advantage of being capable to produce films with good homogeneity, together with a fast formation of the absorber. On the other hand, the *Ga* can be incorporated into the absorber in order to modify the bandgap of the films, thus increasing the V_{OC} of the solar device. Moreover, *Ga* doped films are characterised by a bilayer structure, in which the top of the film is constituted by an *In*-rich quaternary phase and the back region by a *Ga*-rich quaternary one. The degree of interalloying is favoured by higher growth temperatures, and by the sulphurisation process in H_2S instead of *S* atmosphere. Therefore, the sequential process is not able to produce an homogeneous quaternary phase in the whole film. However, it has been shown that the crystalline quality of the *In*-rich quaternary phase of the top of the films is optimum for relative concentrations of *Ga* given by $Ga/(Ga+In) = 0.30$.

The sulphurisation reaction process has been investigated through the analysis of quenched samples. Sulphurisation reaction of *Ga*-free precursors starts by the formation of $CuInS_2$ phase at the surface of the precursors. Afterwards, the reaction proceeds with the out-diffusion of cations through the sulphurised layer until they reach the surface, where they react with the sulphur atmosphere to form more $CuInS_2$ phase. Furthermore, it has been shown that the sulphurisation reaction leads to the formation of $CuInS_2$ phase with bad crystalline quality, in which Cu-Au and chalcopyrite domains coexist. Longer annealing times are necessary in order to induce a recrystallisation that yields a good quality polycrystalline material, mainly constituted by $CuInS_2$ chalcopyrite phase, and CuS secondary phase, which segregates at the surface as a result of the *Cu*-

excess conditions. On the other hand, the introduction of *Ga* in the precursors alters the reaction mechanisms. In this case, the extremely fast formation of the $CuGaS_2$ phase avoids the direct formation of a quaternary phase in the films. Therefore, $CuGaS_2$ phase forms first, while afterwards $CuInS_2$ phase grows on top of it. This mechanism is responsible for the bilayer structure of the *Ga*-containing films. Moreover, the formation of the quaternary phase can only be accomplished by interdiffusion, promoted by temperature and longer annealing times. The main difference between the sulphurisation reaction in S and in H_2S atmospheres is the formation of $CuIn_5S_8$ intermediate phase in the former case. This leads to a delay in the formation of the $CuInS_2$ phase, which hinders the interdiffusion process necessary for the formation of the quaternary phase.

Finally, it is worth to mention that Raman spectroscopy has proved itself as a valid tool for the quality control of the absorber films. This may be accomplished just by taking profit of the relationship existing between the cell efficiency, the crystalline properties of the material and the relative intensity of the A_1^* band, as indicated in the following scheme:

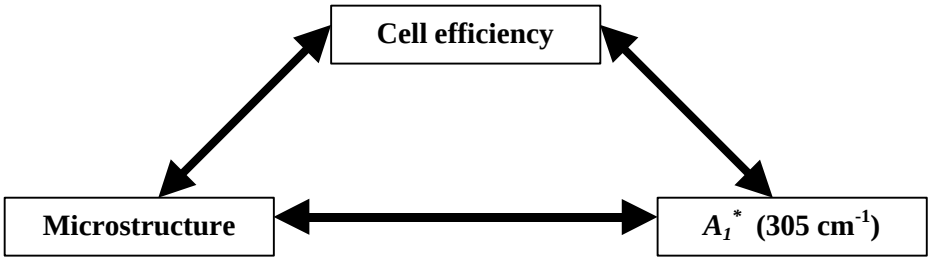

This strong sensitivity of the Raman spectra to structural variations of the material, and to the presence of CuS in the films, makes it useful for the "on-line" analysis of the absorbers. Moreover, it offers the important advantage in front of other techniques, such as conductivity measurements, of being a non-destructive technique, and it does not require any especial sample preparation. The utilisation of Raman spectroscopy as an "on-line" technique may be extended also to other chalcopyrite-based technologies, mainly $CuInSe_2$.

A. "Caracterización de capas de $CuInS_2$ para células solares mediante espectroscopia Raman" (Resumen)

Introducción

Sin duda, el sol constituye la mayor fuente de energía de la que dispone el ser humano. Existen diferentes sistemas mediante los cuales se ha intentado aprovechar esta energía (sistemas de calefacción, energía fotovoltaica, etc.). Sin embargo, la viabilidad económica de estos sistemas ha limitado en gran medida su utilización generalizada. En los últimos años, el creciente interés por desarrollar sistemas de generación de energía no contaminantes ha propiciado importantes inversiones en nuevas tecnologías. Una de las alternativas que ha despertado mayor interés es la utilización de células fotovoltaicas de bajo coste para la producción de energía eléctrica.

Las células fotovoltaicas son dispositivos electrónicos cuya finalidad es la generación de energía eléctrica a partir de la radiación solar incidente. La célula solar más simple consiste en una estructura tipo diodo. Los pares de portadores fotogenerados en el material son separados por el potencial interno de la unión semiconductora, dando lugar a una diferencia de potencial entre los dos extremos de la unión. Los parámetros más relevantes que definen las propiedades eléctricas de una célula solar son su eficiencia (h), su voltaje en circuito abierto (V_{OC}) y su intensidad en cortocircuito (I_{SC}). La eficiencia de una célula se define como el cociente entre la potencia eléctrica máxima que puede ser generada por el dispositivo y la potencia de la radiación incidente (P_{in}). Además, es frecuente utilizar un parámetro adicional "factor de llenado" (FF)

que relaciona la potencia máxima que puede proporcionar una célula ($V_M \cdot I_M$) con el productor $I_{SC} \cdot V_{OC}$:

$$FF = \frac{V_M \cdot I_M}{I_{SC} \cdot V_{OC}} \qquad \textbf{[Eq. A 1]}$$

A través de este parámetro, la eficiencia de una célula voltaica se expresa como:

$$h = \frac{FF \cdot V_{OC} \cdot I_{SC}}{P_{in}} \qquad \textbf{[Eq. A 2]}$$

Por otro lado, la expresión de la intensidad de corriente (I) en función del potencial (V) para una célula solar se puede escribir como:

$$I = I_L - I_0(T) \cdot \left(e^{\frac{eV}{AkT}} - 1 \right) \qquad \textbf{[Eq. A 3]}$$

En la expresión anterior, I_L es la intensidad fotogenerada, $I_0(T)$ es la corriente de saturación en inversa del diodo y A es el coeficiente de idealidad del diodo. Con esta expresión, los parámetros V_{OC} y FF se pueden expresar como:

$$V_{OC} = \frac{A \cdot k \cdot T}{e} \cdot \ln\left(\frac{I_L}{I_0(T)} \right) \qquad \textbf{[Eq. A 4]}$$

$$FF = \frac{n_{OC} - \ln(n_{OC} + 0.72)}{n_{OC} + 1} \text{ , con } n_{OC} \equiv \frac{e \cdot V_{OC}}{A \cdot k \cdot T} \qquad \textbf{[Eq. A 5]}$$

Cabe destacar, a la vista de las ecuaciones anteriores, que dado que la corriente de saturación del diodo es proporcional a la concentración intrínseca de portadores en el material, V_{OC} depende de manera lineal con el gap del material (E_g). Pese a ello, la utilización de materiales con un gap excesivamente grande hace que la corriente de portadores fotogenerados sea menor. Estos efectos antagónicos hacen que exista un valor de E_g óptimo que maximiza la eficiencia de la célula solar. Utilizando el Principio de Balance Detallado se ha estimado que la eficiencia teórica máxima que una célula de unión simple puede producir es de 32.5%, la cual se obtiene para un material con E_g = 1.13 eV. Sin embargo, en los dispositivos reales es necesario tener en cuenta la existencia de determinados mecanismos de recombinación que modifican los resultados anteriores. Teniendo esto en cuenta, la eficiencia límite se estima entorno al 30%, y ésta se obtiene para un material con E_g = 1.5 eV. En cualquier caso, el valor de la eficiencia máxima varía lentamente para valores de E_g entre 1.1 y 1.5 eV. Además de la dependencia de la eficiencia con el gap del material seleccionado, hay que tener en cuenta la influencia de otros parámetros del material, tales como su calidad cristalina o su coeficiente de absorción óptico.

Actualmente existen numerosas tecnologías fotovoltaicas. De manera general, pueden clasificarse en dos grandes grupos: las tecnologías monocristalinas y las tecnologías de capa delgada policristalina. Las células monocristalinas ofrecen los mejores valores de eficiencia, por lo que son especialmente adecuadas para aplicaciones aerospaciales, si bien su alto coste representa un serio inconveniente para sus aplicaciones terrestres. Se han conseguido excelentes resultados con células monocristalinas de *Si* y de materiales III-V tales como el GaAs, GaAlAs, GaInAsO, InAs, InSb e InP. Por ejemplo, se han logrado eficiencias récord de 24.4% en células de *Si* de unión simple, y de hasta un 33.3% en multiuniones de materiales III-V. Por otro lado, las tecnologías de capa delgada ofrecen una interesante alternativa para la producción de células solares de bajo coste, lo cual compensa sus menores eficiencias. Entre las tecnologías de capa delgada que actualmente existen en el mercado cabe

destacar las basadas en *Si* amorfo y policristalino, las tecnologías II-VI (CdS, CdTe, etc.) y las tecnologías basadas en calcopiritas I-III-VI_2 ($CuInSe_2$, etc.).

El gran potencial de los compuestos de tipo calcopirita en el campo de la energía fotovoltaica ha despertado un enorme interés por conocer en detalle sus complicadas propiedades físico-químicas. Dentro de esta familia de materiales, el $CuInSe_2$, el $CuInS_2$ y el $CuInTe_2$ tienen un gap directo bien adaptado al espectro solar, y son susceptibles de ser dopados dando lugar a materiales tipo *n* y tipo *p*. Además, poseen coeficientes de absorción óptica muy elevados, tienen una buena estabilidad química, y pueden ser modificados de manera controlada para dar lugar a compuestos cuaternarios y multinarios, con propiedades bien definidas. Hasta este momento, el $Cu(In,Ga)Se_2$ es la aleación que ha proporcionado mejores resultados en términos de eficiencia, con valores récord por encima del 18% y con una excelente estabilidad. Por todo ello, estos materiales son candidatos ideales para ser utilizados en aplicaciones a gran escala.

Pese a los buenos resultados obtenidos por las anteriores tecnologías de capa delgada, todavía es necesario resolver muchos problemas fundamentales, así como lograr una reducción significativa de los costes de producción que las haga más competitivas frente a los sistemas tradicionales de producción de energía. Por ello, es especialmente interesante el estudio detallado de nuevos materiales que puedan dar lugar a mejores tecnologías. El $CuInS_2$ es uno de los materiales más prometedores de cara a su utilización como capa absorbente en dispositivos fotovoltaicos. Respecto de su competidor más directo, el $CuInSe_2$, este material tiene un gap mejor adaptado al espectro solar (E_g = 1.5 eV), que además proporciona mayores valores de V_{OC} en los dispositivos. La substitución del *Se* por *S* en el material es de gran interés desde el punto de vista medioambiental, dada la gran toxicidad de los compuestos químicos involucrados en los procesos de selenización. Además, existen sistemas para el crecimiento de las capas de $CuInS_2$ que presentan enormes ventajas tecnológicas respecto a los necesarios para el crecimiento de capas de $CuInSe_2$.

La tecnología que denominaremos “baseline” para la producción de células solares de $CuInS_2$ involucra diferentes procesos, muchos de los cuales son análogos a los que se utilizan en las tecnologías para células de $CuInSe_2$. En este proceso, las capas policristalinas se obtienen mediante un proceso rápido de sulfurización (RTP) de los precursores metálicos (*Cu* e *In*) a unos 500ºC, que son depositados sobre substratos de vidrio recubierto de *Mo*. El *Mo* constituye el contacto metálico posterior de la célula, mientras que la capa de $CuInS_2$ actúa como parte *p* del dispositivo. A continuación, se deposita una capa de CdS mediante un proceso de deposición en baño químico (“Chemical Bath Depostition”), que hace de capa intermedia entre la capa de $CuInS_2$ de tipo *p*, y la capa de ZnO de tipo *n*. Esta última se crece sobre la capa de CdS mediante pulverización catódica magnetrón DC. Finalmente, se depositan los contactos metálicos frontales, constituidos por Al/Ni depositado mediante un cañón de electrones, y se encapsula el dispositivo en polímero EVA. Las dimensiones típicas de cada una de las capas son: 1 μm la capa de *Mo*, unas 2-3 μm la capa de $CuInS_2$, alrededor de 50 nm la capa de CdS y 0.5 μm la capa de ZnO. Cabe destacar que después del proceso de sulfurización de la capa de $CuInS_2$ es necesario realizar un tratamiento químico superficial de las capas en KCN, que tiene como objeto la eliminación de la fase secundaria CuS que segrega en la superficie. La formación de esta fase se debe a que los precursores utilizados presentan un exceso de Cu, el cual ha demostrado ser beneficioso para la calidad de las capas finales. Tal como se describirá en los siguientes apartados, precursores con composiciones dadas por [Cu/In = 1.2-1.8] permiten obtener capas policristalinas de $CuInS_2$ con buena estructura cristalina, y tamaños de grano superiores a 1 μm. Además, este sistema de preparación asegura la correcta estequeometría de las capas, ya que el exceso de Cu utilizado es eliminado mediante el ataque químico en KCN. Por esta misma razón, las capas obtenidas son altamente homogéneas, y sus propiedades son poco influenciadas por pequeñas inhomogeneidades locales durante el crecimiento. Esto hace que dicho proceso sea de gran interés para la producción de módulos fotovoltaicos de mayores dimensiones.

Appendix

En términos de eficiencia máxima, los resultados obtenidos hasta el momento con células de $CuInS_2$ (11.4%) todavía distan de los conseguidos en $CuInSe_2$. Esto se debe en parte, al desconocimiento de las propiedades físico-químicas de las capas de $CuInS_2$ utilizadas para la fabricación de las células, así como la influencia que sobre éstas tienen los parámetros fundamentales de crecimiento. Por ello, se ha llevado a cabo el presente trabajo con el objetivo de caracterizar dichas capas mediante espectroscopia Raman. Esta técnica ha sido ampliamente utilizada en la caracterización de otros semiconductores, y es de gran utilidad para el estudio de las propiedades vibracionales de los materiales, el estudio de su calidad cristalina y para la identificación de fases secundarias. La utilización de la espectroscopia Raman con otras técnicas tales como difracción de rayos-X (XRD), espectroscopia de electrones Auger (AES) y difracción de electrones (TED) ha permitido abordar un análisis detallado de las propiedades estructurales de las capas, así como su dependencia en los parámetros tecnológicos de crecimiento.

Propiedades vibracionales de capas de $CuInS_2$

El $CuInS_2$ es un compuesto cuya fase cristalina termodinámicamente estable a temperatura ambiente es la estructura calcopirita. Aunque las propiedades vibracionales de los compuestos con estructura calcopirita han sido ampliamente estudiadas durante estas últimas décadas, el espectro Raman de las capas de $CuInS_2$, al igual que las de $CuInSe_2$, presentan características especiales que hasta el momento no habían sido entendidas en detalle. La siguiente figura muestra un espectro Raman característico de un cristal de $CuInS_2$. El espectro ha sido obtenido en un equipo Jovin-Yvon T64000, en la configuración substractiva y utilizando un microscopio para focalizar la luz de un láser de Ar^+ (λ= 514.5 nm). La potencia incidente sobre todas las muestras analizadas en este trabajo ha sido siempre de 1.0 mW, valor suficientemente bajo como para evitar la aparición de efectos térmicos en el espectro.

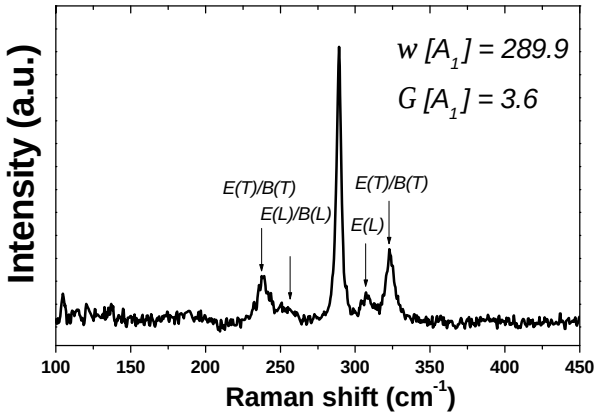

Figura A. 1. Espectro Raman de un cristal de $CuInS_2$.

La estructura calcopirita ($I\bar{4}2d$) es una estructura tetragonal centrada, con un total de 8 átomos por celda unidad. La descomposición de la representación reducible para los modos normales de vibración del cristal viene dada por:

$$\Gamma_{opt} = A_1 \oplus 2A_2 \oplus 3B_1 \oplus 3B_2 \oplus 6E$$
$$\Gamma_{ac} = B_2 \oplus E \qquad \textbf{[Eq. A 6]}$$

De los anteriores modos, todos los modos, excepto los modos A_2 que son modos silenciosos (no activos ni por Raman ni por Infrarrojo), son activos por Raman. Los modos B_2 y E son modos polares. Sin embargo, pese al gran número de modos de vibración que presenta esta estructura, el espectro Raman de estos compuestos generalmente está caracterizado por la presencia de un modo dominante, mucho más intenso que el resto, y que corresponde a la representación totalmente simétrica del cristal (A_1). En la *figura A.1*, este modo aparece a una frecuencia de 290 cm^{-1}. De cara a la caracterización del material, este modo es de gran importancia ya que su posición y características espectrales dependen en gran manera de las propiedades cristalinas del material. Por otro lado, resulta difícil realizar una caracterización del material basándose en el estudio del comportamiento de cualquier otro modo, ya que su intensidad es muy pequeña, y además aparecen solapados, lo cual dificulta un análisis preciso.

Experimentalmente se ha observado que el espectro Raman de algunas capas delgadas de $CuInS_2$ difiere notablemente del esperado para un monocristal volúmico. La siguiente figura muestra espectros micro-Raman de una capa epitaxial de $CuInS_2$ crecida por coevaporación sobre un substrato de *Si* orientado en la dirección [111]. Los espectros han sido obtenidos utilizando dos configuraciones de polarización. En una de las configuraciones, el modo A_1 de la calcopirita esta prohibido, mientras que en la otra no lo está:

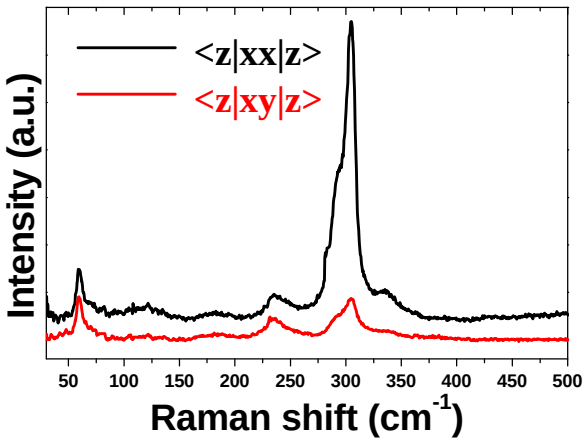

Figura A. 2. Espectros Raman en polarización obtenidos a partir de una muestra epitaxial de $CuInS_2$.

En la figura anterior se puede observar la existencia de modos adicionales en los espectros de estas capas, a frecuencias de 60 cm^{-1} y a 305 cm^{-1}. Este último es especialmente intenso, incluso más que el modo A_1 de la calcopirita a 290 cm^{-1}. Los experimentos realizados en diferentes configuraciones experimentales demuestran que el modo adicional a 305 cm^{-1} es un modo totalmente simétrico, tal y como se puede comprobar a partir de la drástica reducción de su intensidad en el espectro en el que las reglas de selección prohiben la observación de modos A_1. Hasta la realización del presente trabajo, el origen de estos modos adicionales no había sido esclarecido. Tal y como se verá posteriormente, la comprensión del origen de estos modos es de gran importancia, ya que se ha observado experimentalmente que su intensidad está correlacionada con un empeoramiento de la calidad cristalina del material, que conduce a una degradación de la eficiencia del dispositivo fotovoltaico.

El análisis de muestras crecidas bajo diferentes condiciones llevó a la conclusión de que estos modos no estaban necesariamente relacionados con la formación de una fase secundaria en las capas con diferente estequeometría. Por ello, se realizaron diversos experimentos con el objetivo de estudiar las

propiedades cristalinas de las capas. Los estudio de XRD y TED demostraron que la estructura cristalina de estas capas epitaxiales no corresponde únicamente a la fase calcopirita, sino que se identificaron también dominios cristalinos con orden catiónico Cu-Au $(P\bar{4}m2)$. Esta estructura cristalina corresponde a una fase metaestable a temperatura ambiente del compuesto $CuInS_2$, y su existencia ya había sido predicha teóricamente por cálculos termodinámicos "ab-initio". Esto llevó a plantear la posible relación entre esta fase cristalina y la aparición de las bandas adicionales en los espectros Raman. Para poder establecer esta posible relación, se realizó un análisis cuantitativo sobre muestras epitaxiales crecidas bajo diferentes condiciones. Se estudió la intensidad relativa del modo a 305 cm^{-1} respecto del modo A_1 a 290 cm^{-1}, y se comparó con la fracción de fase Cu-Au estimada a partir de XRD. Tal como se puede observar en la *figura A.3*, los resultados experimentales demuestran la existencia de una correlación prácticamente lineal entre la intensidad del modo a 305 cm^{-1} y la cantidad de $CuInS_2$ con orden Cu-Au en las muestras.

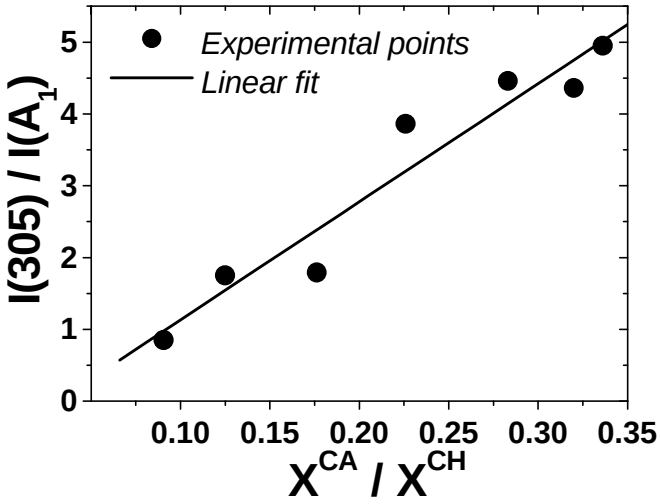

Figura A. 3. Intensidad relativa del modo a 305 cm^{-1} respecto al modo A_1 vs. la fracción de orden Cu-Au respecto a la fracción de fase calcopirita. (fig. 3.20)

Estos resultados experimentales han sido apoyados por diferentes consideraciones teóricas. En primer lugar, se han calculado las representaciones irreducibles para los modos normales de la estructura Cu-Au, obteniéndose como resultado:

$$G_{opt} = A_1 \oplus 2B_2 \oplus 3E \qquad \textbf{[Eq. A 7]}$$

La existencia de un modo totalmente simétrico en la representación de la estructura Cu-Au (que designaremos como A_1^*) está de acuerdo con la simetría observada experimentalmente para el modo a 305 cm^{-1}. Por otro lado, se ha calculado la frecuencia de los modos normales de vibración para la estructura Cu-Au utilizando un modelo de Keating de cuatro parámetros. Dentro de esta aproximación, el potencial de interacción entre átomos queda descrita por cuatro constantes de fuerza: dos constantes para las interacciones tipo "stretching" entre los átomos *Cu-S* e *In-S* (α_1 y α_2), y dos más para las interacciones tipo bending entre los átomos *Cu-S-Cu* e *In-S-In* (β_1 y β_2). De esta forma, el potencial interatómico para cada átomo en el cristal se expresa como:

$$U = \tfrac{1}{2}\cdot a \cdot \left(\frac{3}{4r^2}\right)\sum_{i=1}^{4}\left[D(r_i^l \cdot r_i^l)\right]^2 + \tfrac{1}{2}\cdot\sum_{s=1}^{s=2} b^s \cdot \left(\frac{3}{4r^2}\right)\sum_{i=1}^{4}\left[D(r_i^s \cdot r_j^s)\right]^2 \qquad \textbf{[Eq. A 8]}$$

En la expresión anterior, $\{r_i\}$ son los vectores que unen el átomo central con cada uno de sus vecinos. De esta forma, es posible construir la matriz dinámica del cristal y calcular sus valores propios, que corresponden directamente al cuadrado de las frecuencias de los modos normales de vibración. Sin embargo, el modelo de Keating es un modelo fenomenológico, que no proporciona a priori ninguna información sobre el valor de las constantes de fuerza del cristal. Por ello, se ha aplicado previamente este modelo a la estructura calcopirita, y se ha realizado un ajuste por mínimos cuadrados para calcular los valores de las constantes de fuerza que mejor reproducen el espectro de frecuencias

experimental del cristal. Los valores obtenidos para las constantes de fuerza mediante este procedimiento son:

$$a_1 = 17.43 \cdot 10^3\ dyn/cm \qquad b_1 = 1.24 \cdot 10^3\ dyn/cm$$
$$a_2 = 37.03 \cdot 10^3\ dyn/cm \qquad b_2 = 1.71 \cdot 10^3\ dyn/cm \qquad \textbf{[Eq. A 9]}$$

Las siguientes tablas muestran los valores de las frecuencias de los modos normales para las estructuras calcopirita y Cu-Au. Los valores experimentales utilizados para el ajuste han sido también incluidos:

Modos transversales ópticos en $CuInS_2$ (calcopirita)		
Modo	**$W_{EXPERIMENTAL}$ (cm^{-1})**	**$W_{KEATING}$ (cm^{-1})**
$G_4\ [G_{15}]$	321	330
$G_5\ [G_{15}]$	323	325
$G_2\ [X_1]$	- (silencioso)	297
$G_3\ [W_2]$	- (muy débil)	294
$G_5\ [W_4]$	295	291
$G_4\ [W_2]$	234	253
$G_1\ [W_1]$	290	253
$G_5\ [X_5]$	244	244
$G_2\ [W_1]$	- (silencioso)	215
$G_3\ [X_3]$	157	157
$G_5\ [W_3]$	140	149
$G_5\ [W_4]$	88	87
$G_3\ [W_1]$	- (muy débil)	83
$G_4\ [W_2]$	79	79
$G_5\ [X_5]$	67	68

Tabla A. 1. Frecuencias experimentales y calculadas para el $CuInS_2$ con estructura calcopirita.

Transverse Optical phonons in Cu-Au $CuInS_2$	
Mode	**$W_{KEATING}$ (cm^{-1})**
$\Gamma_5^{(1)}$	325
$\Gamma_4^{(1)}$	295
Γ_1	265
$\Gamma_5^{(2)}$	246
$\Gamma_4^{(2)}$	157
$\Gamma_5^{(3)}$	82

Tabla A. 2. Frecuencias estimadas a partir del modelo de Keating, para el $CuInS_2$ con estructura Cu-Au.

Tal como se puede observar en la *tabla A.1*, el modelo de Keating reproduce razonablemente bien el espectro de frecuencias experimental. La mayoría de las frecuencias calculadas se corresponden con los valores experimentales, dentro de un margen de discrepancia de entorno al 5%. La máxima desviación ocurre para el modo A_1, con un error del orden del 13%. Pese a ello, es posible comparar las frecuencias de los modos A_1 y A_1^* en las estructuras calcopirita y Cu-Au. De esta forma se observa que la frecuencia del modo A_1^* es mayor que la del modo A_1, lo cual es predecible si tenemos en cuenta sus cooredenadas normales de desplazamiento. A partir de esta relación de frecuencias, y del valor experimental real de la frecuencia del modo A_1, podemos determinar un valor corregido para la frecuencia de A_1^* dado por:

$$w\left[A_1^*\right] \approx \frac{w_{Keating}^{Cu-Au}}{w_{Keating}^{Chalcopyrite}} \times 290\,cm^{-1} = 305\,cm^{-1} \qquad \textbf{[Eq. A 10]}$$

A la vista de estas consideraciones, el modo a 305 cm^{-1} se puede asignar al fonón del modo A_1^* de centro de zona de la estructura Cu-Au. Esta asignación está apoyada por otros cálculos teóricos basados en modelos dinámicos más complejos, que proporcionan resultados similares.

Caracterización de capas de $CuInS_2$ obtenidas por coevaporación.

Con el objetivo de estudiar las propiedades estructurales de las capas policristalinas de $CuInS_2$ crecidas bajo diferentes condiciones, se han analizado diversas muestras crecidas mediante coevaporación. Debido la geometría de la propia cámara de coevaporación, estas muestras presentan un gradiente lateral de composición, lo que facilita el estudio de la influencia de la estequeometría sobre el material. Para ello, se han realizado medidas de espectroscopia Raman, AES y XRD sobre muestras crecidas a diferentes temperaturas.

Los resultados demuestran que las muestras crecidas a alta temperatura (T=520ºC) bajo condiciones de exceso de *Cu* dan lugar a capas policristalinas de buena calidad. El exceso de Cu da lugar a la formación de CuS como fase secundaria, que segrega en la superficie de la capa, y que puede ser fácilmente eliminada mediante un tratamiento en KCN. En el caso de utilizar temperaturas de crecimiento inferiores (por debajo de 470ºC), la calidad cristalina de las capas empeora drásticamente, tal como se puede deducir a partir del ensanchamiento del modo A_1 en el espectro Raman y en la disminución de la intensidad difractada en XRD. Esta degradación de la calidad cristalina de la fase calcopirita tiene lugar simultáneamente con la formación de dominios con orden Cu-Au en el material, lo cual se manifiesta por la aparición de la banda A_1^* en los espectros Raman.

Por otro lado, en zonas en las que el crecimiento ha tenido lugar en condiciones de exceso de *In* se ha comprobado la formación de precipitados de fase secundaria $CuIn_5S_8$ en el interior de las capas, que a diferencia de la fase CuS en el caso de crecimiento en exceso de *Cu*, no puede ser eliminado de manera simple. Además, el exceso de *In* favorece la formación de dominios con orden Cu-Au en el material, dando lugar a una degradación de la calidad cristalina de

la fase calcopirita. En este caso, no es posible mejorar significativamente la calidad cristalina de las capas mediante el aumento de la temperatura de substrato, dentro del rango de temperaturas estudiado (370ºC-520ºC). En la siguiente figura se puede observar la influencia de la temperatura de crecimiento sobre los espectros Raman superficiales de muestras ricas en *Cu* y en *In* (después de realizar el tratamiento químico en KCN para la eliminación del CuS):

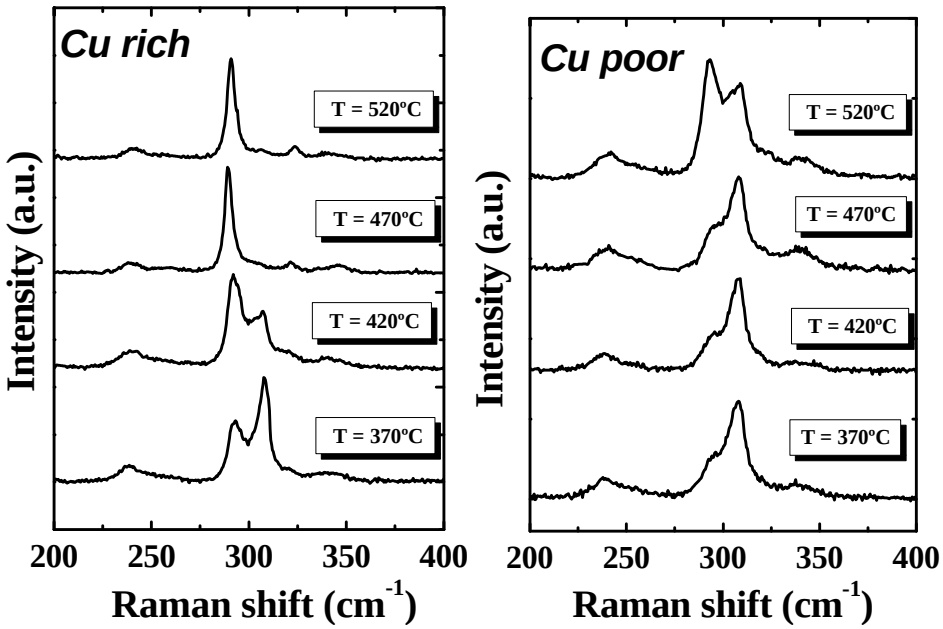

Figura A. 4. Espectros micro-Raman superficiales obtenidos en diferentes muestras crecidas en exceso de *Cu* ("*Cu*-rich") y exceso de *In* ("*In*-rich").

Cabe destacar de la anterior figura que para el caso de las muestras crecidas en condiciones de exceso de Cu parece existir una temperatura de transición de aproximadamente 470ºC, por encima de la cual la formación de dominios con orden Cu-Au resulta muy desfavorable. Por debajo de 470ºC la coexistencia de

dominios de fase calcopirita y de fase metaestable Cu-Au da lugar a una mala calidad cristalina de las capas, que se refleja también en los espectros de XRD. Para el caso de la muestra crecida a la temperatura más baja (370ºC) en condiciones de exceso de In, los efectos locales de desorden son tan importantes que dan lugar a un espectro de XRD con características propias de un cristal con estructura tipo esfalerita, en la que los átomos están distribuidos aleatoriamente dentro de la sub-red de cationes.

Por último, la utilización combinada de las técnicas de espectroscopia Raman y AES ha permitido detectar la formación de MoS_2 en la interficie $CuInS_2$/Mo de las capas. La estructura hexagonal de este compuesto hace suponer que se trata de un compuesto fácilmente exfoliable, lo que podría ser la causa de los problemas de adhesión que frecuentemente afectan a estas capas policristalinas.

Caracterización de muestras "baseline" obtenidas mediante proceso secuencial.

El proceso secuencial constituye una tecnología de crecimiento de capas de $CuInS_2$ alternativa a la de coevaporación. En esta tecnología, la formación de la capa tiene lugar mediante una reacción de sulfurización de los precursores metálicos que son previamente depositados sobre el substrato. El proceso secuencial ofrece la ventaja de ser un proceso altamente reproducible y capaz de dar lugar a capas de gran homogeneidad, por lo que tiene un gran interés tecnológico a escala industrial.

Para la tecnología "baseline" se utilizan precursores metálicos (*Cu* e *In*) con una relación de *Cu*/*In* entorno a 1.8. Al igual que en el caso de las capas crecidas por coevaporación, esto permite obtener capas policristalinas de buena calidad cristalina, a la vez que el exceso de *Cu*, que segrega a la superficie en forma de CuS, es fácilmente eliminable mediante un ataque químico selectivo en KCN. En este sentido, para condiciones de crecimiento de exceso de *Cu*, las propiedades estructurales de las capas policristalinas obtenidas por el proceso secuencial son análogas a las de las capas crecidas por coevaporación.

Uno de los elementos que ha suscitado mayor interés de cara a su utilización como aleante dentro del compuesto $CuInS_2$ es el *Ga*. Se ha comprobado que la incorporación de *Ga* aumenta el valor de V_{OC} sin deteriorar la eficiencia de los dispositivos. Además, puede resultar beneficioso para la mejora de la adhesión de las capas, a la vez que ofrece la posibilidad de obtener capas con variaciones estequeométricas controladas. El estudio del efecto de la incorporación de *Ga* sobre la calidad cristalina de las capas se ha iniciado sobre una primera serie de muestras crecidas por proceso secuencial a 550ºC, utilizando diferentes valores de concentración de *Ga*. El análisis de estas muestras demuestra que la sulfurización de los precursores metálicos no da lugar a una única fase

cuaternaria homogénea, sino a una estructura "bicapa" en la que el Ga se acumula preferentemente en la región cercana al *Mo*. Como resultado, la composición de las capas en la zona cercana a la superficie está próxima a la del $CuInS_2$, mientras que cerca del *Mo* la composición corresponde prácticamente a $CuGaS_2$. Sin embargo, la cantidad de *Ga* introducida ha demostrado tener una influencia relevante sobre la calidad cristalina de la región superficial de las capas (ver *figura A.5*)

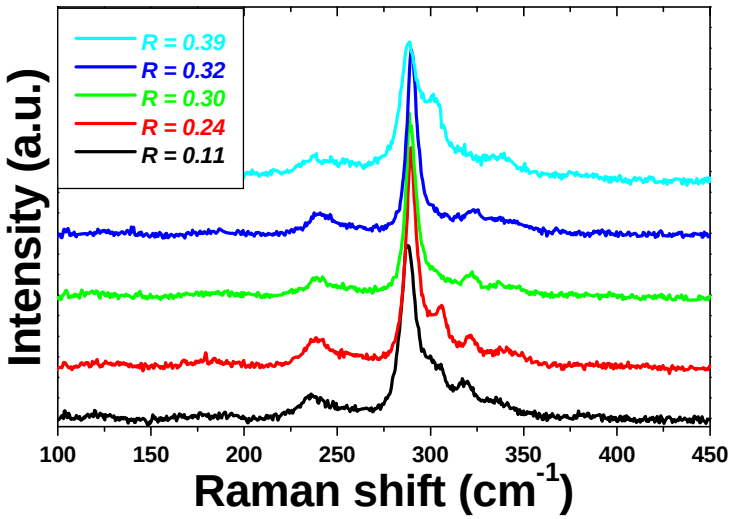

Figura A. 5. Espectros micro-Raman superficiales de muestras con diferentes concentraciones de R [R=Ga/(Ga+In)]

Tal como se puede apreciar en la figura anterior, la contribución de la banda A_1^* en los espectros superficiales es mínima para valores de *R* de 0.30. De manera similar, la calidad cristalina de la fase cristalina es óptima para esta concentración, tal como se puede concluir a partir del análisis de la anchura del modo A_1 (*G*) para las diferentes muestras (ver *figura A.6*).

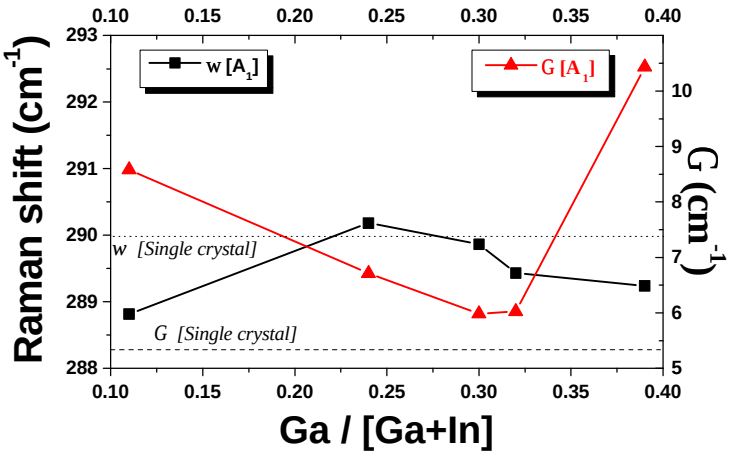

Figura A. 6. Dependencia de la posición y anchura del modo A_1 con la concentración de *Ga* en las muestras.

Estos resultados obtenidos en capas aleadas con *Ga* se correlacionan con las eficiencias obtenidas en los dispositivos finales. También en este caso, las eficiencias máximas obtenidas corresponden al caso en el que R = 0.30, demostrando la influencia que tienen las propiedades microestructurales sobre el comportamiento de los dispositivos fotovoltaicos. Como consecuencia de todo ello, las muestras "baseline" utiliza estos mismos valores de R para producir capas aleadas con *Ga*.

El efecto de la temperatura de crecimiento también tiene un efecto significativo sobre la microestructura de las capas aleadas con *Ga*. Los experimentos combinados de Raman/AES han demostrado que la temperatura favorece la interdifusión entre la región superficial y la región posterior de las capas, dando lugar a mayor presencia de *Ga* y de *In* en las regiones superficial y posterior, respectivamente. La estructura bicapa que presentan estas muestras con Ga, resulta evidente a la vista de los espectros Raman obtenidos a diferentes profundidades por medio de la utilización combinada de Raman/AES. Teniendo en cuenta que el modo A_1 para el compuesto cuaternario $Cu(In,Ga)S_2$ presenta

un comportamiento unimodal, variando de forma prácticamente lineal entre 290 cm^{-1} y 310 cm^{-1}, los espectros obtenidos para puntos correspondientes a diferentes profundidades claramente demuestran la existencia de dos fases cuaternarias con composiciones diferentes, incluso cuando la sulfurización se realiza a 600ºC (ver *figura A.7*).

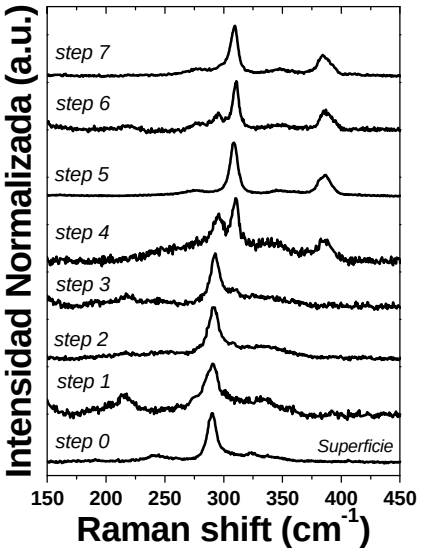

Figura A. 7. Espectros Raman obtenidos en diferentes profundidades de la muestra con R = 0.30 y T=600ºC, mediante medidas combinadas Raman/AES.

Cuando el proceso de sulfurización tiene lugar en un sistema RTP ("Rapid Thermal Process"), la tecnología secuencial presenta la ventaja adicional de ser capaz de dar lugar a capas de alta calidad en ciclos de tiempo muy cortos. Es por ello que el sistema de sulfurización rápida de los precursores se ha impuesto progresivamente al proceso de sulfurización estándar CTP ("Conventional Thermal Process"). La utilización del proceso RTP en lugar del proceso CTP da lugar a modificaciones en las propiedades estructurales de las capas cuando se

utilizan precursores con *Ga*. Si bien el proceso RTP da lugar igualmente a capas con estructura "bicapa", experimentalmente se observa una mayor interdifusión entre las dos regiones que en el caso de la sulfurización en CTP, especialmente en la región posterior. La interdifusión es aun mayor cuando la sulfurización se realiza en atmósfera de H_2S. Estas diferencias se pueden apreciar comparando la posición del modo A_1 del cuaternario $Cu(In,Ga)S_2$ para las muestras crecidas mediante los diferentes procesos. Todas las muestras corresponden a valores de R = 0.30 y T = 500ºC.

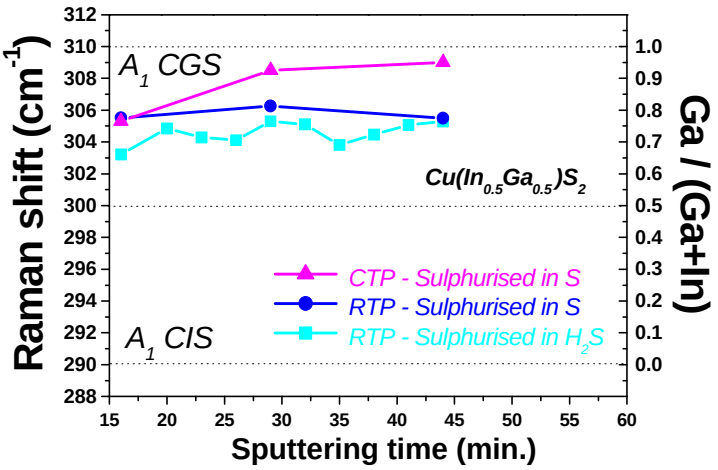

Figura A. 8. Variación de la posición del modo A_1 del sistema cuaternario para la región posterior de muestras "baseline" crecidas por CTP, RTP (S) y RTP (H_2S)

Tal como se puede observar a partir de los resultados anteriores, el proceso de sulfurización RTP en H_2S ofrece los mejores resultados en términos de interdifusión entre las dos regiones de la capa, si bien su composición estimada todavía dista de la que cabría esperar para una capa perfectamente homogénea.

Con el objetivo de profundizar en el análisis de la reacción de sulfurización se han llevado a cabo experimentos de "quenching". Se han analizado tres grupos

de muestras: *(i)* muestras sin *Ga* sulfurizadas por RTP en *S*, *(ii)* muestras con *Ga* sulfurizadas por RTP en *S* y *(iii)* muestras con *Ga* sulfurizadas por RTP en H_2S. En todos los casos se han utilizado precursores con composiciones con exceso de *Cu*. En cada caso, se han analizado diversas muestras correspondientes a diferentes estadios del proceso de sulfurización. Cada muestra ha sido obtenida deteniendo bruscamente la reacción de sulfurización, y enfriándola rápidamente, con el objetivo alterar lo menos posible la microestructura correspondiente a cada momento del proceso.

El estudio de la sulfurización de los precursores sin *Ga* ha permitido establecer las diferentes etapas de la reacción. Los resultados muestran que la sulfurización se inicia en la superficie de la muestra con la formación directa de $CuInS_2$, y continúa gracias a un proceso de difusión de los elementos metálicos a través de la región sulfurizada hasta que alcanzan la superficie, donde reaccionan con la atmósfera reactiva. Sin embargo, la reacción de sulfurización inicial no da lugar directamente a granos cristalinos de buena calidad cristalina, tal y como lo demuestran la observación del modo A_1^* y el ensanchamiento del modo A_1 (ver *figura A.9*). El proceso de sulfurización continúa dando lugar a la segregación del exceso de *Cu* hacia la superficie en forma de CuS, a la vez que se inicia un proceso de recristalización que se traduce en una mejora significativa de la calidad cristalina de la fase calcopirita y a la prácticamente total desaparición de la fase Cu-Au.

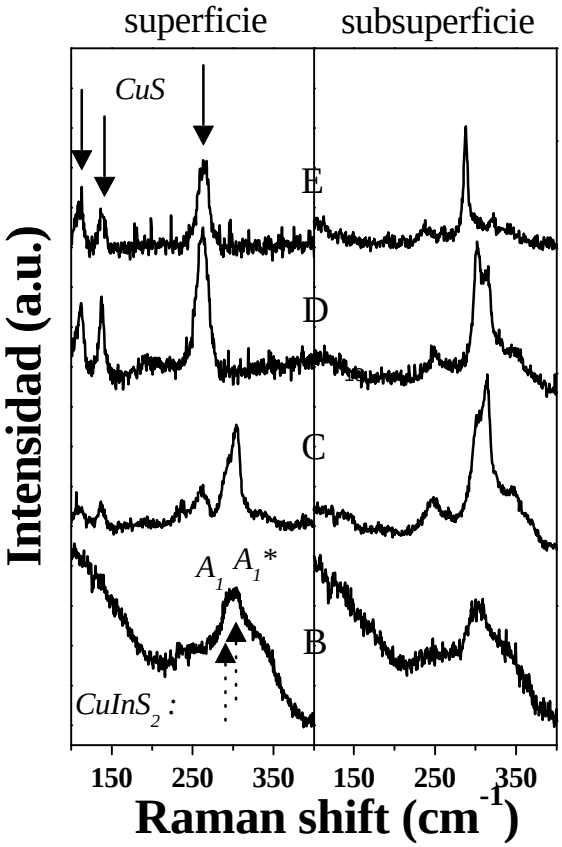

Figura A. 9. Espectros Raman superficiales y sub-superficiales para muestras RTP sin Ga, correspondientes a diferentes estadios del proceso: muestras *B* (T=500ºC, t = 0 s), *C* (T=500ºC, t = 30 s), *D* (T=500ºC, t = 60 s) y *E* (T=500ºC, t = 120 s)

El segundo grupo de muestras analizadas corresponde a precursores con *Ga* sulfurizados en *S*. En este caso, los resultados obtenidos indican que la reacción se inicia, al igual que en el caso anterior, en la superficie de la capa. Sin embargo, debido a que la formación del $CuGaS_2$ es extraordinariamente rápida, la sulfurización da lugar a la formación de una capa de $CuGaS_2$, tras la cual tiene lugar un proceso de difusión hacia la superficie del *In* y del *Cu* a través de esta fase sulfurizada. El resultado de este proceso es el crecimiento fases ternarias $CuIn_xS_z$ sobre la fase $CuGaS_2$. Este fenómeno es el responsable de que,

finalizada la sulfurización, el *Ga* se acumule en la región posterior de las capas. La formación de la fase cuaternaria solamente puede tener lugar mediante un proceso de interdifusión entre la fase superficial (rica en *In*) y la fase de la región posterior de la capa (rica en *Ga*). Además, en el caso del proceso de sulfurización en *S*, la reacción de sulfurización del *In* no da lugar únicamente a $CuInS_2$, sino también a una determinada fracción de $CuIn_5S_8$, tal y como se puede apreciar en la *figura A.10*. Esto retrasa el final de la formación de la fase $CuInS_2$, dificultando aun más la formación de la fase cuaternaria.

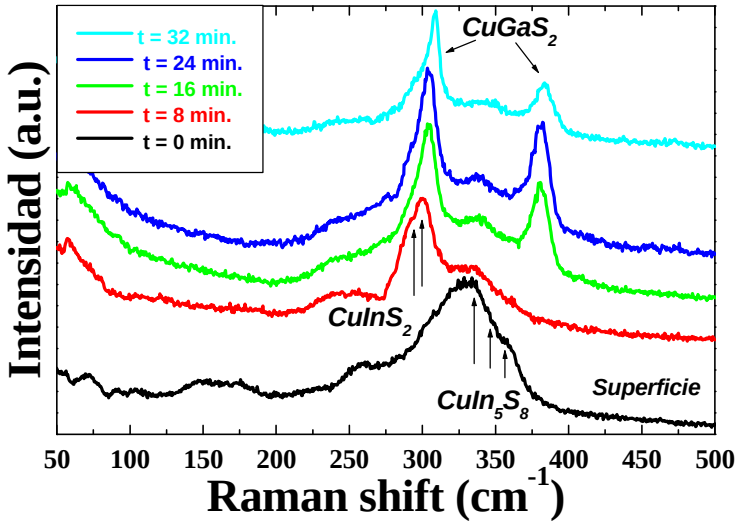

Figura A. 10. Espectros micro-Raman procedentes de puntos a diferentes profundidades para una muestra correspondiente a los instantes iniciales del proceso de sulfurización en *S*. La figura muestra el crecimiento de $CuInS_2$ y $CuIn_5S_8$ sobre la fase $CuGaS_2$.

Por último, se ha analizado también el proceso de la sulfurización en H_2S. En este caso, la diferencia más significativa respecto es que no se detecta la fase intermedia $CuIn_5S_8$. Por esta razón, el proceso de interdifusión entre las dos regiones es más efectivo, ya que no es necesaria la transformación previa

$CuIn_5S_8$ → $CuInS_2$. El resultado es un mayor grado de incorporación de *In* en la región posterior, tal como se refleja en la *Figura A.8*.

Conclusiones

En este trabajo se han investigado las propiedades vibracionales de capas de $CuInS_2$, lo que ha permitido realizar una caracterización microestructural detallada de las capas policristalinas utilizadas para la fabricación de dispositivos fotovoltaicos. Los espectros Raman de estas capas se caracterizan por la presencia de una banda dominante, correspondiente al modo A_1 de la estructura calcopirita, que aparece a 290 cm^{-1}. Sin embargo, algunas de las capas de este material crecidas bajo determinadas condiciones, presentan también bandas adicionales a 60 cm^{-1} y 305 cm^{-1}, cuyo origen no había sido establecido hasta la realización del presente trabajo. La comprensión del origen de dichos modos era necesaria para poder comprender las propiedades estructurales del material. Por ello, en primer lugar se llevaron a cabo diversos experimentos de TED, XRD y Raman, con el objetivo de estudiar las propiedades cristalinas de las capas. Estos experimentos demostraron que las capas estudiadas están constituidas por una mezcla de fases polimórficas del compuesto $CuInS_2$: la fase calcopirita y la fase con orden Cu-Au. Por otro lado, se pudo comprobar que la cantidad relativa de fase Cu-Au presente en las muestras está correlacionada con la intensidad del modo adicional a 305 cm^{-1}, lo que indica la relación existente entre ambos. La simetría y frecuencia observadas experimentalmente para el modo a 305 cm^{-1} concuerdan con los resultados teóricos predichos por teoría de grupos para uno de los modos de vibración de la fase Cu-Au. De acuerdo con esto, se ha llevado a cabo una modelización de las estructuras para realizar el cálculo de sus modos normales de vibración, mediante un modelo de Keating de 4 parámetros. Los resultados obtenidos a partir de dichos cálculos apoyan la identificación del principal modo adicional a 305 cm^{-1} con el modo A_1^* de la estructura Cu-Au.

La interpretación del origen de esta banda adicional en los espectros ha permitido realizar una caracterización detallada de las propiedades estructurales

de las capas, tanto las crecidas por coevaporación como las crecidas a través del proceso secuencial. Mediante la utilización combinada de espectroscopia Raman y AES en muestras coevaporadas se ha estudiado el efecto de la temperatura de crecimiento y de la estequeometría utilizada para la preparación de las capas. En muestras crecidas en condiciones de exceso de Cu, se ha demostrado la segregación superficial de dicho exceso en forma de CuS, el cual es eliminado de forma efectiva mediante un ataque químico en KCN. En el caso de muestras crecidas a partir de precursores con exceso de *In* ("Cu-poor"), el defecto de *Cu* da lugar a la formación de precipitados de $CuIn_5S_8$ en el interior de las capas. Por otro lado, también se ha detectado la presencia de MoS_2 en la interficie $CuInS_2$/Mo, que puede ser responsable de los problemas de adhesión que a veces presentan las capas. Por otro lado, se ha estudiado la calidad cristalina de la fase $CuInS_2$ mediante espectroscopia Raman y XRD. Se ha observado que el crecimiento de las capas tanto en condiciones de defecto de *Cu*, como en condiciones de baja temperatura de substrato, favorecen la formación de dominios de Cu-Au en la fase $CuInS_2$, que se traducen en el deterioro de la calidad cristalina del material. La utilización de exceso de *Cu*, junto con temperaturas de crecimiento por encima de un cierto valor crítico, favorece la existencia de un único orden (calcopirita), dando lugar a capas con buenas propiedades estructurales de cara a su aplicación en dispositivos fotovoltaicos.

De manera similar, las capas crecidas mediante el proceso secuencial presentan buenas propiedades cristalinas cuando se utilizan precursores con *Cu* en exceso y temperaturas de crecimiento elevadas. Cuando se incorpora Ga en los precursores, la estructura final de las capas se ve modificada. En este caso, se ha comprobado que las capas presentan una estructura "bicapa" constituida por dos fases cuaternarias $Cu(In,Ga)S_2$: una rica en *Ga* en la parte posterior, y otra rica en *In* más próxima a la superficie. La utilización de elevadas temperaturas de crecimiento, así como la sulfurización de los precursores mediante RTP en atmósfera de H_2S, favorece la interdifusión de *Ga* e *In* entre ambas capas. Así

mismo, la calidad cristalina de la fase cuaternaria superficial es óptima cuando se utilizan concentraciones de *Ga* dadas por la relación *Ga*/(*Ga*+*In*) = 0.30.

El estudio del proceso de sulfurización en RTP se ha llevado a cabo mediante el análisis de muestras "quenched". Para precursores sin *Ga*, la reacción de sulfurización se inicia en la superficie con la formación de $CuInS_2$ desde los primeros momentos de la reacción. A continuación, la reacción tiene lugar gracias a un proceso de difusión de los elementos metálicos a través de la capa sulfurizada hasta alcanzar la superficie, donde reaccionan con la atmósfera reactiva. La reacción de sulfurización da lugar a una estructura inicialmente desordenada, caracterizada por la coexistencia de dominios con orden calcopirita y Cu-Au. Gracias al proceso de recocido, está estructura inicial evoluciona hacia la estructura definitiva, predominantemente formada por orden calcopirita. Por otro lado, la introducción de *Ga* en los precursores modifica algunos aspectos de la reacción. En este caso, la reacción se inicia también en la superficie de la capa dando lugar a la formación de la fase ternaria $CuGaS_2$. Una vez formada esta fase, la reacción continúa a través de la difusión hacia la superficie de las especies metálicas no sulfurizadas (*Cu* e *In*). Como resultado, tiene lugar un crecimiento de una fase ternaria de $CuInS_2$ sobre la fase $CuGaS_2$, lo que origina la característica estructura final en forma de "bicapa". La formación de la fase cuaternaria tiene lugar gracias a la interdifusión entre las fases ternarias. La diferencia esencial entre la sulfurización en S y en H_2S es que en el primer caso la sulfurización da lugar a la formación de $CuIn_5S_8$ como fase intermedia, lo cual retarda el proceso de interdifusión de *Ga* e *In* entre ambas capas.

Finalmente, cabe destacar que el presente trabajo ha demostrado que la espectroscopia Raman es una técnica de gran interés para su utilización como técnica de control de calidad en una línea de producción de dispositivos fotovoltaicos basados en $CuInS_2$. Esto se debe a la gran correlación existente entre las propiedades estructurales de las capas (que condicionan la eficiencia de los dispositivos) con las características de los espectros Raman

(ensanchamiento del modo A_1, aparición de bandas adicionales, detección de posibles fases secundarias, etc.). Además, la espectroscopia Raman posee la ventaja frente a otras técnicas de ser una técnica no destructiva, que ha demostrado ser extremadamente sensible a las condiciones tecnológicas de crecimiento de las capas (temperatura, estequeometría, etc.). Todo ello justifica el interés de esta técnica de caracterización como sistema de control de calidad para este tipo de capas.

Acknowledgements

I would like to express my gratitude to all the members of the Department of Electronics of the University of Barcelona for offering me the possibility to perform this work. Specially, I am very grateful to Dr. Alejandro Perez, who has been my supervisor during all these years, and to Dr. Albert Romano, Beatriz Barcones and Jordi Marcos, who have performed all the TEM experiments, part of which are presented in this thesis work.

I would like to acknowledge also all the other people who participated in the SULFURCELL project, and particularly, to Dr. Roland Scheer, Dr. Reiner Klenk and Dr. Ilka Luck, for their stimulating discussions.

Finally, I would like also to thank Sandra, my family and all my fellows from the University, for encouraging me during the performance of this work.

References

[1] Contract JOR-CT98-0297 (Non Nuclear Energy Programme, Joule III)
[2] *M. Ohnishi, A. Takeoka, S. Nakano, Y. Kuwano*: Renewable Energy V**6**(3), pp. 275-282 (1995)
[3] *E. Becquerel, C. R. Hebd. Séanc*: Acad. Sci. **9**, p. 145 (1839)
[4] *E. Becquerel*: Ann. Phys. Chemie **54**, p. 18 (1841)
[5] *W. G. Adams, R. E. Day*: Proc. R. Soc. A**25**, p. 113 (1877)
[6] *C. E. Fritts*: Proc, Am. Ass. Adv. Sci. **33**, p. 97 (1833); *C. E. Fritts*: Am. J. Sci. **26**, p. 465 (1883)
[7] *D. M. Chapin, C. S. Fuller, G. L. Pearson*: J. Appl. Phys. **25**, p. 676 (1954)
[8] *W. Shockley and H.J. Queisser*: J. Appl. Phys. **32**, pp. 510-519 (1961)
[9] *G. L. Araújo, A. Martí*: Sol. Ener. Mat. Sol. Cells **33**, pp. 213-240 (1995)
[10] *G. L. Araújo, A. Martí*: Sol. Ener. Mat. Sol. Cells **43**, pp. 203-222 (1996)
[11] *A. V. Shah, R. Platz, H. Keppner*: Sol. Ener. Mat. Sol. Cells **38**, pp. 501-520 (1995)
[12] "Solar Cells", *M. A. Green.* Prentice Hall (New York, 1982)
[13] *F. Treble*: Renewable Energy **15**, pp. 473-478 (1998)
[14] *J. Zhao, A. Wang, M. A. Green, A. Ferrazza*: Appl. Phys. Lett. **73**, p. 991-993 (1998)
[15] *L. L. Kazmerski*: Renewable and Sustainable Energy Reviews, **V1** (1/2), pp. 71-170 (1997)
[16] *T. Takamoto, E. Ikeda, T. Agui, H. Kurita, T. Tanable, S. Tanaka*: Proc. of the 26th IEEE Photovoltaic Specialists Conference. New York IEEE, p. 1031 (1997)
[17] *R. C. Chittick, J. H. Alexander, H. F. Sterling*: J. Electrochem. Soc. **116**, p. 93 (1969)
[18] A. J. Lewis, G. A. N. Connell, W Paul, U.J.R. Pawlik, R. J. Temkin. Proc. Conf. on Tetrahedrally-Bonded Amorphous Semiconductors. AIP, New York, p. 27 (1974)

[19] *D. E. Carlson, C. R. Wronski*: Appl. Phys. Lett. **28**, p. 671-673 (1976)
[20] *D. L. Staebler, C. R. Wronski*: Appl. Phys. Lett. **31**, p. 1977-1979 (1976)
[21] *T. Matsuyama, T. Baba, T. Takahama, K. Wakesaka, S. Tsuda*: Optoelectronics.Devices and Technologies **9** (3), p. 391 (1994)
[22] *H. Keppner, J. Meier, P. Torres, D. Fischer, A. Shah*: Appl. Phys. A **69**, pp. 169-177 (1999)
[23] *A. Rohatgi, S. Narasimha, S. Kamra, P. Doshi, C. P. Khattak, K. Emery, H. Field*: Proc. 25th Photovoltaic Specialists Conf. IEEE New York, pp. 741-744 (1996)
[24] *D. Cusano*: Solid-State Electronic **6**, p. 217 (1963)
[25] *D. Bonnet, H. Rabinhorst*: Proc. 9th IEEE Photovoltaic Specialists Conf. IEEE New York, pp. 129-132 (1972)
[26] *H. Uda, H. Matsumoto, N. Nakayama, S. Ikegami*: Jap. J. Appl. Phys. **15**, p. 1575 (1976)
[27] *C. Ferekides, J. Britt*: J. Solar Energy Materials and Solar Cells **35**, p. 255 (1994)
[28] *A. Hanafusa, T. Aramoto, M. Tsuji, T. Yamamoto, T. Nishio, P. Veluchamy, H. Higuchi, S. Kumazawa, S. Shibutani, J. Nakajima, T. Arita, H. Ohyama, T. Hibino, K. Omura*: Sol. Ener. Mat. & Sol. cells **67**, pp. 21-29 (2001)
[29] *R. A. Mickelson, W. S. Chen*: Appl. Phys. Lett. **30**, pp. 371-373 (1980)
[30] *J. R. Tuttle, J. S. Ward, A. Duda, R. A. Berens, M. A. Contreras, K. R. Ramanathan, A. L. Tennant, J. Keane, E. D. Cole, K. Emery, R. Noufi*: Proc. MRS Spring Meeting, Pittsburg (1996)
[31] *M. Eron, A. Rothwarf*: Appl. Phys. Lett. **44**, pp. 131-133 (1984)
[32] *U. Rau, M. Schmidt, A. Jasenek, G. Hanna, H. W. Shock*: Sol. Ener. Mat. & Sol. Cells **67**, pp. 137-143 (2001)
[33] *D. Braunger, S. Zweigart, H. W. Schock*: Proc. 2nd World Conf. on Photovoltaic Energy Conversion, p. 413 (1998)
[34] *L. Kronik, D. Cahen, H. W. Schock*: Adv. Mater **10**, p. 31 (1998)
[35] *D. Schmid, M. Ruckh, F. Grunwald, H. W. Shock*: J. Appl. Phys. **73**(6), pp. 2902-2909 (1993)

[36] *C. Rincón, S. Mahanty, M. León, R. Díaz, F. Rueda, J.L. Martín de Vidales*: J. Appl. Phys. **87**(5), pp. 2293-2296 (2000)

[37] *R. Schäffler, D. Hariskos, M. Kaiser, M. Ruck, U. Rühle, H. W. Shock*: Crys. Res. Technol. **31**, p. 543 (1996)

[38] *S. H. Wei, S. B. Zhang, A. Zunger*: Appl. Phys. Lett. **72**, p. 3199-3201 (1998)

[39] *T. Nakada, H. Ohbo, T. Watanabe, H. Nakazawa, M. Matsui, A. Kunioka*: Sol. Ene. Mater. & Sol. Cells **49**, p. 285 (1997)

[40] *J. R. Tuttle, J. S. Ward, T. A. Berens, M. A. Contreras, K. R. Ramanathan, A. L. Tennant, J. Keane, E. D. Cole, K. Emery, R. Noufi*. Proc. Mat. Res. Soc. Symp. **426**, p. 143 (1996)

[41] *D. Cahen, R. Noufi*: Appl. Phys. Lett. **54**, p.558-560 (1989)

[42] *R.R.Gray*: "Status and Prospects for CIS-Based photovoltaics", http:\\www.siemenssolar.com

[43] *J. E. Jaffe, A. Zunger*: Phys. Rev. B **28** pp. 5822-5847 (1983)

[44] *J. E. Jaffe, A. Zunger*: Phys. Rev. B **29** pp. 1882-1906 (1984)

[45] *K. Siemer, J. Klaer, I. Luck, J. Bruns, R. Klenk, D. Braünig*: Sol. Ener. Mat. & Sol. Cells **67**, pp. 159-166 (2001)

[46] *R. Scheer*: Private communication.

[47] *J. Klaer, K. Siemer, I. Luck, D. Braünig*: Thin Solid Films **387**, pp. 169-171 (2001)

[48] *R. Scheer*: Private communication

[49] *I. Luck, J. Kneisel, K. Siemer, J. Bruns, R. Scheer, R. Klenk, N. Janke, D. Braünig*: Sol. Ener. Mater. & Sol. Cells **67**, pp. 151-158 (2001)

[50] *J. Reiß, J. Malmström, A. Werner, I. Hengel, R. Klenk, M. Ch. Lux-Steiner*: Proc. Mat. Res. Soc. Symp. **V668**, Materials Research Society (2001).

[51] *R. Klenk*: Thin Solid Films **387**, pp. 135-140 (2001)

[52] *I. Hengel, A. Neisser, R. Klenk, M. Ch. Lux-Steiner*: Thin Solid Films **361-362**, pp. 458-462 (2000)

[53] SULFURCELL: "Efficient Thin Film Solar Cells Based on $CuInS_2$" [Ref: JOR3CT980297]

[54] *R. Klenk, P. Dobson, M. Falz, N. Janke, J. Klaer, I. Luck, A. Pérez-Rodríguez, A. Romano-Rodríguez, R. Scheer, E. Terzini*: 16th European Photovoltaic Solar Energy Conference, 1-5 May 2000, Glasgow (U.K.)

[55] *Th. Riedle, Th. M. Matthes, A. Neisser, R. Klenk, C. Hinrichs, N. Esser, W. Richter, M. Ch. Lux-Steiner*: 16th European Photovoltaic Solar Energy Conference, 1-5 May 2000, Glasgow (U.K.)

[56] *K. Siemer, J. Klaer, I. Luck, J. Bruns, R. Klenk, D. Braünig*: Sol. Ener. Mater. & Sol. Cells **67**, pp. 159-166 (2001)

[57] *U. Störkel, M. Aggour, C. P. Murrell, H. J. Lewerenz*: Thin Solid Films **387**, pp. 182-184 (2001)

[58] *U. Störkel, M. Aggour, M. Webber, R. Scheer, H. J. Lewerenz*: 16th European Photovoltaic Solar Energy Conference, 1-5 May 2000, Glasgow (U.K.)

[59] *I. Luck, U. Störkel, W. Bohne, A. Ennaoui, M. Schmidt, H. W. Schock, D. Bräunig*: Thin Solid Films **387**, pp. 100-103 (2001).

[60] *A. M. Chaparro, R. Bayón, M. T. Gutiérrez, J. Herrero*: 16th European Photovoltaic Solar Energy Conference, 1-5 May 2000, Glasgow, U.K.

[61] D. Braunger et al. "An 11.4% efficient polycrystalline thin film solar cell based on $CuInS_2$ with a Cd-free buffer layer", Sol. Ener. Mat. & Sol. Cells **40**, pp. 97-102 (1996)

[62] *Rayleigh Lord*: Phil. Mag. **47**, p. 375 (1899)

[63] *T. Andrews*: Phil. Trans. Roy. Soc. **159**, p. 575 (1869)

[64] *M. Smoluchowski*: Ann. Phys. **25**, p. 205 (1908)

[65] L. Brillouin: Ann. Phys. (Paris) **17**, p. 88 (1922)

[66] *Sir C. V. Raman, K. S. Krishnan*: Nature **121**, p. 501 (1928)

[67] *G. Landsberg, L. Mandelstam*: Naturwiss. **16**, p. 557 (1928)

[68] *A. Smekal*: Naturwiss. **11**, p. 873 (1923)

[69] "Quantum Theory of light", *R. Loudon*. Clarendom Press (Oxford, 1973)

[70] "Scattering of light by crystals", *W. Hayes, R. Loudon*. John Wiley & Sons (New York, 1978).

[71] "Light Scattering in Solids I", *M. Cardona*. Spring-Verlarg Heidelberg (New York, 1975)

[72] *D. L. Rousseau, R. P. Bauman, S. P. S. Porto*: Journal of Raman Spectroscopy **10**, pp. 253-289 (1981)

[73] "Theory of groups and its application to physical problems", *S. Bhagavantan, T. Venkataraudu*. Academic Press (New York, 1969)

[74] "Dynamical Properties of Solids", *G. K. Horton, A. A. Maradudin*. North-Holland Publishing Co (Amsterdam, 1974)

[75] "Quantum chemistry", *H. Eyring, J. Walter, G. E. Kimball*. John Willey (New York, 1944)

[76] *M. Saad, S. Bleyhl, T. Ohashi, Y. Hashimoto, K. Ito, B. Mertesacker, A. Jager-Waldau, W. Woletz, M. Ch. Lux-Steiner*:. 2nd World Conference on Photovoltaic Solar Energy Conversion V**1**, pp. 1149-1152 (1998)

[77] *W. Hausheng, L. Pudong, W. Jiangen, Q. Fengyuan*: Extended Abstract Book. pp. 419-422, 18th Conf. Solid State Devices Mater, Tokyo, Japan (1986)

[78] *K. Mizoguchi, S. Nakashima, A. Fujii, A. Mitsuishi, H. Morimoto, H. Onoda, T. Kato*: Japan. J. Appl. Phys. **26**, pp. 903-907 (1987)

[79] *J. Wagner*: Appl. Phys. Lett. **52**, pp. 1158-1160 (1987)

[80] *K. Yamazaki, R. K. Uotani, K. Nambu, M. Yamada, K. Yamamoto, K. Abe*: Jpn. J. Appl. Phys. **23**, pp. L403-L405 (1984)

[81] *S. Nakashima*: Extended Abstract Bood. pp. 415-418. 15th Conf. Solid State Devices Mater. Tokyo, Japan (1983)

[82] *H. Richter, Z. P. Wang, L. Ley*: Sol. State Comm. **39**, p. 625 (1981)

[83] *R. Tsu, J. Gonzalez-Hernandez, J. Doehler, S. R. Ovshinsky*: Sol. State Comm. **46**, p. 79 (1983)

[84] *T. Pearsell, R. Carles, J. C. Portal*. Appl. Phys. Letts. **42**, p. 436-438 (1983)

[85] B. Jusserand, J. Sapriel: Phys. Rev. B **24**, p. 7194 (1981)

[86] "Estudio de capas pesudomórficas de $Si_{1-x-y}Ge_xC_y$ mediante difracción de Rayos X y espectroscopia Raman", *O. Gonzalez*. Thesine work (1998)

[87] *A. Mooradian, T. C. Haran*: Proc. Conf. Physics of Semimetals and Narrow-Gap Semiconductors, p. 297, Dallas (1970)

[88] *M. F. Limonov, A. I. Rykov, S. Tajima*: Phys. Rev. B **61**(18), pp. 12412-12419 (2000)

[89] *J. E. Jaffe, A. Zunger*: Phys. Rev. B **28**(10), pp. 5822-5847 (1983)
[90] J. E. Jaffe, A. Zunger: Phys. Rev. B **29**(4), pp. 1882-1906 (1984)
[91] "Infrared and Raman Selection Rules for Molecular and Lattice Vibrations: The correlation Method", *W. G. Fateley, F. R. Dollish, N. T. McDevitt, F. F. Bentley*. John Wiley & Sons, (USA, 1972)
[92] *J. Camassel, L. Artus, J. Pascual*: Phys. Rev. B **41**(9) pp. 5717-5726 (1990)
[93] *J. Camassel, L. Artus, J. Pascual*: Phys. Rev. B **41**(9) pp. 5727-5734 (1990)
[94] *L. Artus, J. Pascual, J. Pujol, J. Camassel*: Phys. Rev. B **43**, pp. 2088-2096 (1991)
[95] *P. N. Keating*: Phys. Rev. B **145**(2), pp. 637-645 (1966)
[96] *R. M. Martin*: Phys. Rev. B **1**(10), pp. 4005-4011 (1970)
[97] *F. W. Ohrendorf, H. Haeusler*: Crys. Res. Technol. **34**(3) pp. 339-349 (1999)
[98] *F. W. Ohrendorf, H. Haeusler*: Crys. Res. Technol. **34**(3) pp. 351-362 (1999)
[99] *F. W. Ohrendorf, H. Haeusler*: Crys. Res. Technol. **34**(3) pp. 339-349 (1999)
[100] *G. D. Holah, J. S. Webb, H. Montgomery*: J. Phys. C: Solid State Phys. **7**, pp. 3875-3890 (1974)
[101] *W. H. Koschel, M. Bettini*: Phys. Stat. Sol. (b) **72**, pp. 729-737 (1975)
[102] *M. Saad, S. Bleyhl, T. Ohashi, Y. Hashimoto, K. Ito, B. Mertesacker, A. Jager-Waldau, W. Woletz, M. Ch. Lux-Steiner*: 2nd World Conference on Photovoltaic Solar Energy Conversion (1998), V**1**, pp. 1149-1152.
[103] *C. Rincón, S. M. Waso,. G. Marín. J. R. Huntzinger, A. Zwick, J. Galibert*: J. Appl. Phys. **85**(7) pp. 3925-3927 (1998)
[104] "Analytical Raman Spectroscopy", *J. G. Grasselli, B. J. Bulkin*. Wiley Cop. (New York, 1991)
[105] "Fundamentals on semiconductors", *P. Y. Yu and M. Cardona*. Springer Cop. (Berlin, 1996)
[106] *H. Tanino. T. Maeda, H. Fujikake, H. Nakanishi, S. Endo, T. Irie*: Phys. Rev. B **45** (23), pp. 13323-13330 (1992)
[107] *H. Haeuseler, F. W. Ohrendorf*: 11th Int. Conf. On Ternary and Multinary Compounds, ICTMC-11, Salford (8-12 September 1997).

[108] "Solid State Physics", *R. Kubo, T. Nagayima*. McGraw-Hill Book Co. (New York, 1968)

[109] "Teoría del Sólido", *A. S. Davidov*. Editorial Mir (Moscú, 1981)

[110] *H. Matsushita, S. Endo, T. Irie*:, Jpn. J. Appl. Phys. **31**, pp. 18-22 (1992)

[111] *H. Neumann*: Helv. Phys. Acta **58**, pp. 337-346 (1985)

[112] *C. Rincón, F. J. Ramírez*: J. Appl. Phys. **72**(9), pp. 4321-4324 (1992)

[113] *T. Terasako, N. Tsuboi, H. Uchiki, S. Iida*: Jpn. J. Appl. Phys. **36** pp. 997-1005 (1997)

[114] *H. Metzner, M. Brüssler, K. D. Husemann, H. J. Lewerenz*: Phys. Rev. B **44**(21), pp. 11614-11623 (1991)

[115] *Chr. Dzionk, M. Brüssler, H. Metzner*: Nuc. Inst. and Methods in Phys. Res. B **63**, pp. 231-235 (1992)

[116] *M. L. Fearheiley, N. Dietz, H. J. Lewerenz*: J. Electrochem. Soc. **139**(2), pp. 512-517 (1992)

[117] *M. Brüssler, H. Metzner, K. D. Husemann, H. J. Lewerenz*: Phys. Rev. B **38**(13), pp. 9268-9271 (1988)

[118] *J. M. Merino, S. Mahanty, M. León, F. Rueda, J. L. Martin de Vidales*: Thin Solid films **361-362** pp. 70-73 (2000)

[119] *A. J. Nelson, G. S. Horner, K. Sinha, M. H. Bode*: Appl. Phys. Lett. **64**(26), pp. 3600-3601 (1994)

[120] *A. N. Tiwari, S. Blunier, M. Filzmoser, H. Zogg*: Appl. Phys. Lett. **65**(26), pp. 3347-3349 (1994)

[121] *H. P. Wang, I. Shih, C. H. Champness*: Thin Solid Films **361-362,** pp. 494-497 (2000)

[122] *H. Z. Xiao, L. C. Yang, A. Rockett*: J. Appl. Phys. **76**(3), pp. 1503-1510 (1994)

[123] *T. Negami, N. Kohara, M. Nishitani, T. Wada*: Jpn. J. Appl. Phys. Part 2, V**33**(9A) pp. L1251-1253 (1994)

[124] *S. B. Zhang, Su-Huai Wei, A. Zunger, H. H.-Yoshida*: Phys. Rev. B **57**(16), pp. 9642-9656 (1997)

[125] *G. Morell, R. S. Katiyar, S. Z. Weisz, T. Walter, H. W. Schock, I. Balberg*: Appl. Phys. Lett. **69**(7), pp. 987-989 (1997)
[126] *J. C. W. Folmer, H. F. Franzen*: Phys. Rev. B**29**(11), pp. 6261-6265 (1983)
[127] *S. –H. Wei, L. G. Ferreira, A. Zunger*: Phys. Rev. B**45**(5), pp. 2533-2537 (1992)
[128] A. Zunger: Phys. Rev. B **50**(3), pp. 164-166 (1986)
[129] C. Rincón: Phys. Rev. B **45**(22), pp. 12716-12719 (1992)
[130] *D. S. Su, W. Neumann, R. Hunger, P. Schuber-Bischoff, M. Giersig, H. J. Lewerenz, R. Scheer, E. Zeitler*: Appl. Phys. Lett. **73**(6), pp. 785-788 (1998)
[131] *D. S. Su, W. Neumann, M. Giersig*: Thin Sol. Films **361-362**, pp. 218-222 (2000)
[132] *D. S. Su, S. -H. Wei*: Appl. Phys. Lett. **74**(17), pp. 2483-2485 (1999)
[133] *S.- H. Wei, S. B. Zhang, A. Zunger*: Phys. Rev. B Rapid Comm. **59**(4), pp. R2478-R2481 (1999)
[134] *H. Metzner, Th. Hahn, J. –H. Bremer, M. Seibt, B. Plikat, I. Dirnstorfer, B. K. Meyer*: Thin Sol. Films **361-362,** pp. 504-508 (2000)
[135] *T. Hahn, H. Metzner, B. Plikat, M. Seibt*: Thin Solid Films **387**, pp. 83-85 (2001)
[136] *J. Alvarez-Garcia, J. Marcos-Ruzafa, A. Perez-Rodriguez, A. Romano-Rodriguez, J. R. Morante, R. Scheer*: Thin Solid Films **361-362**, pp. 208-212 (2000)
[137] *S. Yamanaka, M. Konagai, K. Takahashi*: Jpn. J. Appl. Phys. **28**(8), pp. L1337-L1340 (1989)
[138] *S. Nomura, S. Ouchi, S. Endo*: Jpn. J. Appl. Phys. **36**, Part 2, pp. L1075-L1077 (1997)
[139] *J. Alvarez-Garcia, A. Perez-Rodriguez, A. Romano-Rodriguez, T. Jawhari, J. R. Morante, R. Scheer, W. Calvet*: Thin Solid Films **387**, pp. 216-218 (2001)
[140] *K. Kambas, J. Spytidelis, M. Balkanski*: Phys. Stat. Sol. (b) **105**, pp. 291-296 (1981)
[141] K. Kondo, S. Nakamura, K. Sato: Jpn. J. Appl. Phys. Part I **37**(10), pp. 5728-5729 (1998)

[142] *R. Hunger, M. Wilhelm, K. Diesner, J. Brunns, G. Lippold, K. Hinrichs, N. Esser, H. J. Lewerenz, R. Scheer*: Presented at the 2nd World Conference on Photovoltaic Solar Energy Conversion (Vienna, 6-10 July 1998)

[143] *J. H. Park, I. S. Yang, H. Y. Cho*: Appl. Phys. A **58**, pp. 125-128 (1994)

[144] *S. Shirakata, H. Kubo, C. Hamaguchi, S. Isomura*: Jpn. J. Appl. Phys. Part 2 **36**(10B), pp. L1394-1396 (1997)

[145] *S. Shirakata, Y. Kannaka, H. Hasegawa, T. Kariya, S. Isomura*: Jpn. J. Appl. Phys. Part 1 **38**(9A) pp. 4997-5002 (1999)

[146] *M. Winkler, O. Tober, J. Penndorf, K. Szulzewsky, S. Röser, G. Lippold, K. Otte*: Presented at the European Materials Research Society Spring Meeting, June 1-4 1999, Strasbourg, France.

[147] *J. Alvarez-Garcia, A. Perez-Rodrigyez, A. Romano-Rodriguez, J. R. Morante, L. Calvo-Barrio, R. Scheer, R. Klenk*: J. Vac. Sci. Technol. A **19**(1), pp. 232-239 (2001)

[148] *C. Rincon, S. M. Wasim, G. Marin, J. M. Delgado, J. R. Huntzinger, A. Zwick, J. Galibert*: Appl. Phys. Lett. **73**(4) pp. 441-443 (1998)

[149] *C. Rincon, S. M. Wasim, G. Marin, E. Hernandez, J. M. Delgado, J. Galibert*: J. Appl. Phys. **88**(6), pp. 3439-3444 (2000)

[150] *C. Rincon, S. M. Wasim, G. Marin, E. Hernandez, G. Sanchez Perez, J. Galibert*: J. Appl. Phys. **87**(5), pp. 2293-2296 (2000)

[151] *H. Metzner, Th. Hahn, J. -H. Bremer, J. Conrad*: Appl. Phys. Lett. **69**(13), pp. 1900-1903 (1996)

[152] *R. Hunger, R. Scheer, K. Diesner, D. Su, H.J. Lewerenz*: Appl. Phys. Lett. **69**(20), pp. 3010-3012 (1996)

[153] Computer simulation program: CaRIne Crystallography v. 3.1

[154] *F. Herman*: J. Phys. Chem. Solids **8**, p. 405 (1959)

[155] *W. Cochran*: Phil. Mag. **4**, p. 1082 (1959)

[156] *K. Kunk, M. Balkanski, M. A. Nusimovici*: Phys. Status Sol. (b) **72**, p. 229 (1975)

[157] *L. Artus, J. Pascual*: J. Phys: Cond. Matt. **4**, pp. 5835-5844 (1992)

[158] *C. -H. Chang, S. -H. Wei, S. P. Ahrenkiel, J. W. Johnson, B. J. Stanbery, T. J. Anderson, S. B. Zhang, M. M. Al-Jassim, G. Bunker, E. A. Payzant, R. Duran*:, Mat. Res. Soc. Symp. Proceedings V**668**, p. H4.3 (2001)

[159] *E. O. Kane*: Phys. Rev. B **31**, pp. 7865-7876 (1985)

[160] "Modes de vibració atòmica en semiconductors tetraèdricament coordinats: influència de les sustitucions catiòniques i de les vacants ordenades", *S. Royo* (Thesine work, 1996)

[161] "The Physics of phonons", *G. P. Srivasta, Adam Hilger*. (Bristol, England, 1990).

[162] "Càlcul numèric", *M. Grau Sánchez, M. Noguera Batlle*. Edicions UPC, (Barcelona, 1993).

[163] *J. Pascual, J. Pujol, L. Artus, J. Cassamel*: Phys. Rev. B **43**(12), pp. 9831-9841 (1991)

[164] "Crystal Physics", *G. Zhdanov*. Edited by A. F. Brown (Edinburgh, Scotland, 1965)

[165] *M. T. Yin, M. L. Cohen*: Phys. Rev. B **26**, pp. 3259-3272 (1982)

[166] *J. Alvarez-Garcia, A. Perez-Rodriguez, B. Barcones, A. Romano-Rodriguez, A. Janotti, S. -H. Wei*: Appl. Phys. Lett. **80**(4), pp. 562-565 (2002).

[167] *R. Scheer, H. J. Lewerenz*: J. Vac. Sci. Technol. A **12**(1), pp. 51-55 (1994)

[168] *R. Scheer, M. Alt, I. Luck, H. J. Lewerenz*: Sol. Ener. Mat. & Sol. Cells **49**, pp. 423-430 (1997)

[169] *I. Mareen, N. R. De Tacconi, K. Rajeshwar*: J. Electroanal. Chem. **453,** pp. 187-195 (1998)

[170] *M. Ishii, K. Shibata, H. Nozaki*: J. Sol. State Chem. **105**, pp. 504-511 (1993)

[171] *J. Alvarez-Garcia, A. Perez-Rodriguez, A. Romano-Rodriguez, J. R. Morante, L. Calvo-Barrio, R. Scheer, R. Klenk*: J. Vac. Sci. Tech. A **19**(1), pp. 232-238 (2001)

[172] *J. Marcos-Ruzafa, A Romano-Rodríguez, J Álvarez-García, A Pérez-Rodríguez, J R Morante, J Klaer and R Scheer*. International Conference on Microscopy of Semiconducting Materials 1999. Oxford University, England (March 1999).

[173] *C. -H. Chang, S. -H. Wei, S. P. Ahrenkiel, J. W. Johnson, B. J. Stanbery, T. J. Anderson, S. B. Zhang, M. M. Al-Jassim, G. Bunker, E. A. Payzant, R. Duran*: Mat. Res. Soc. Symp. Proc. V**668** (2001)

[174] Not published results.

[175] *N. M. Gasanly, S. A. El-Hamid, L. G. Gasanova, A. Z. Magomedov*: Phys. Stat. Sol (b) **169**, pp. K115-K118 (1992)

[176] *J. Kreisel, S. Pignard, H. Vincent, J. P. Senateur, G. Lucazeau*: Appl. Phys. Lett. **73**(9) pp. 1194-1197 (1998)

[177] *R. Scheer, K. Diesner, H. –J. Lewerenz*: Thin Solid Films **268**, pp. 130-136 (1995).

[178] "Residual Stress", *I. C. Noyan, J. B. Cohen*. Springer-Verlag (New York, 1987)

[179] *Roland Scheer*: Private communication

[180] *A. Neisser, I. Hengel, R. Klenk, Th.W. Matthes, J. Alvarez-García, A. Pérez-Rodríguez, A. Romano-Rodríguez, M.-Ch. Lux-Steiner*: Sol. Ener. Mat. & Sol. Cells **67**, pp. 97-104 (2001)]

[181] *J. Alvarez-Garcia, J. R. Morante, A. Perez-Rodriguez, A. Romano-Rodriguez, L. Calvo-Barrio, R. Scheer, R. Klenk, A. Neisser*: Asian J. Phys. Soc. **9**, pp. 809-821 (2000)

[182] *V. F. Agekyan, N. V. Orekhova, D. Rajab, A. Y. Serov*: Sov. Phys. Solid State **34**(7), pp. 1215-1217 (1992)

[183] *I. -H. Choi, P. Y. Yu*: "Optical investigation of defects in $AgGaS_2$ and $CuGaS_2$". J. Phys. Chem. Solids V**57**(11), pp. 1695-1704 (1996)

[184] Electrical measurements performed at the Hahn-Meitner Institut.

[185] *I. V. Luck, J. Alvarez-Garcia, L. Calvo-Barrio, A. Werner, A. Perez-Rodriguez, J. R. Morante and D. Bräunig*. Proc. Materials Research Society Spring Meeting, San Francisco (2001), V**668**, p. H1.4.

[186] *B. Barcones, A Romano-Rodríguez, J Álvarez-García, L Calvo-Barrio, A Pérez-Rodríguez, J R Morante, R Scheer, R Klenk, I Luck, K Siemer, O Van der Biest*: International Conference on Microscopy of Semiconducting Materials 1999. Oxford University, England (March, 2001).

[187] *M. Gossla, H.-E. Mahnke, H. Metzner*: Thin Solid Films **361-362**, pp. 56-60 (2000)

[188] *M. Gossla, H. Metzner, H. -E. Mahnke*: J. Appl. Phys. **86**(7), pp. 3624-3632 (1999)

[189] *C. Dzionk, H. Metzner, S. Hessler, H. -E. Mahnke*: Thin Solid Films **299**, pp. 28-44 (1997)

[190] *K. Siemer, J. Klaer, I. Luck, J. Alvarez-Garcia, A. Romano-Rodriguez, D. Bräunig*: Presented at the PVSEC'11 Conference, Glasgow, U.K. (2000)

[191] *L. Calvo-Barrio, A. Perez-Rodriguez, J. Alvarez-Garcia, A. Romano-Rodriguez, B. Barcones, J. R. Morante, K. Siemer, I. Luck, R. Klenk, R. Scheer*: Vacuum **63**, pp. 315-321 (2001)

[192] *J. Alvarez-Garcia, A. Perez-Rodriguez, A. Romano-Rodriguez, L. Calvo-Barrio, B. Barcones, J. R. Morante, K. Siemer, I. Luck, R. Klenk*: Thin Solid Films **387**, pp. 219-221 (2001)

[193] *A. Neisser, J. Alvarez-Garcia, L. Calvo-Barrio, R. Klenk, T. W. Matthes, I. Luck, M. Ch. Lux-Steiner, A. Perez-Rodriguez, J. R. Morante*: Proc. Materials Research Society Spring Meeting (2001), V**668**, p. H1.3.

[194] *E. García víllora, S. Fiechter, R. Klenk and M. Ch. Lux-steiner*: Presented at the ICTMC-12 Conference, 13-17th March 2000, Hsin-Chu (Taiwan)

[195] Not published results